MBE Growth, Characterisation and Physics of Antiferromagnetic Copper Manganese Arsenide

Victoria Anne Hills

Department of Physics and Astronomy

University of Nottingham

This dissertation is submitted for the degree of

Doctor of Philosophy

November 2016

Abstract

Research into antiferromagnetic materials for application in spintronics has rapidly expanded in recent years. The prediction and observation of spin based phenomena with antiferromagnets as the active components, has expanded the field and there is a need for high quality materials that are compatible with existing III-V semiconductor systems to expand this research. Copper manganese arsenide is one such material and will be the subject of this thesis. Early studies had shown that this material grows epitaxially on both gallium arsenide and gallium phosphide substrates by molecular beam epitaxy. This thesis builds on this early work by further characterising CuMnAs, improving the techniques used to grow it, and enhancing our understanding of the material. A key result of this thesis is that the Néel temperature of CuMnAs can be studied using temperature dependent transport measurements. This method allows for a range of layer thickness (from between 5 and 140 nm) to be studied. We find that the Néel temperature of CuMnAs is suppressed by around 100K when the layer thickness is less than 10nm. At the thicknesses studied there is agreement (around (480$\pm$5)K) with the more established neutron diffraction technique for measuring Néel temperature, which was also used to determine the magnetic structure of the CuMnAs studied. In addition to measurement of the Néel temperature of CuMnAs, a detailed study is made in this thesis of the ideal growth conditions for ultrathin (sub 10nm) films of CuMnAs. Post-growth examination of ultrathin layers of CuMnAs showed that significant portions of material were missing due to poor adhesion. This thesis shows the results of the development of several different nucleation and growth methods, which were used to

improve the adhesion of the CuMnAs layer to the substrate. These methods are evaluated using atomic force microscopy, x-ray diffraction, magnetometry and transport measurements. CuMnAs has previously shown to strongly prefer growth under stoichiometric conditions, as non-stoichiometric conditions have tended to favour the formation of clusters of the excess material. In excess Mn conditions these clusters are ferromagnetic MnAs inclusions that are conducting and contribute to the magnetic behaviour. This thesis presents the results of a simulation study of the conductivity of ferromagnetic elements in a non-ferromagnetic medium. This approach could be extended to allow the number of inclusions in a CuMnAs layer to be approximated from transport measurements.

Finally, this thesis will also look at the effects of alloying CuMnAs with phosphorous. This reduces the lattice constants of the material while retaining the same crystal and magnetic structure. In thick films of the alloy the Néel temperature increases from that of CuMnAs.

Acknowledgements

The work is this thesis would not have been possible without the help and encouragement of many people. I would first like to thank Professor Bryan Gallagher, Dr. Richard Campion and Dr. Peter Wadley for their advice, support and encouragement throughout my PhD.

I would like to thank everyone who collaborated on these projects or who taught me how to use the many different techniques that have been used including: -Dr V. Novàk for coming over from Prague for MBE growth runs, -Dr K. Edmonds for organising beam times and advising on transport measurements and results, - S. Tabreham, A. Stuart and A. Soloman for designing and manufacturing the high temperature system, - Dr A. Rushforth, Dr M. Wang and S. Bowe for teaching and helping me to use the SQUID, -Dr D. Parkes for teaching me to use the AFM and helping with coding issues, -Professor T. Foxon for advice on every aspect of MBE growth -J. Chauhan and D. Taylor for teaching me how to use the clean room and process devices -Dr. D. Khalyavin and Dr. P. Manuel on the WISH beamline at ISIS, -Dr B. Ouladdiaf on the D10 beamline at ILL, -Professor T. Jungwirth and other collaborators for the opportunity to discuss results at the Lanna meetings.

I would like to thank everyone who has helped make my time at Nottingham so fun, especially my C26 office mates (Mu, Duncan, Stuart, Eduardo, Lucy, Debi, Michal, Carl, Mo, Mohammed and Bryn), the tea room team, Sarah Heywood, Richard Cousins and the university of Nottingham Taekwondo club.

Finally I would like to thank my nearest and dearest for their support and putting up with me during the last six months.

Publications

V. Hills, P. Wadley, R. P. Campion, V. Novak, R. Beardsley, K. W. Edmonds, B. L. Gallagher, B. Ouladdiaf, and T. Jungwirth. Paramagnetic to antiferromagnetic transition in epitaxial tetragonal CuMnAs (invited). *Journal of Applied Physics*, 117(17):172608, 2015.

P Wadley, V Hills, MR Shahedkhah, KW Edmonds, RP Campion, V Novák, B Ouladdiaf, D Khalyavin, S Langridge, V Saidl, et al. Antiferromagnetic structure in tetragonal CuMnAs thin films. *Scientific Reports*, 5:17079, 2015.

P. Wadley, B. Howells, J. Železný, C. Andrews, V. Hills, R. P. Campion, V. Novák, K. Olejník, F. Maccherozzi, S. S. Dhesi, S. Y. Martin, T. Wagner, J. Wunderlich, F. Freimuth, Y. Mokrousov, J. Kuneš, J. S. Chauhan, M. J. Grzybowski, A. W. Rushforth, K. W. Edmonds, B. L. Gallagher, and T. Jungwirth. Electrical switching of an antiferromagnet. *Science*, 351(6273):587–590, 2016.

Table of contents

Glossary

$\Delta\mathbf{c}$ change in the lattice parameter from CuMnAs/GaP.

$\Delta x_{\mathrm{Incl,gap}}$ Distance that inclusions must be from each other.

Δx_{V} Distance along the x axis were voltage is measured across.

$\Delta y_{\mathrm{Incl,gap}}$ Distance that inclusions must be from each other.

η scattering factor.

$\frac{\mathbf{d}\rho_{\mathbf{xx}}}{\mathbf{dT}}$ derivative of the longitudinal resistivity with temperature.

$\rho_{\mathbf{xy}}$ Transverse Resistivity.

σ Conductivity.

$\rho_{\mathrm{U},xx,\mathrm{s}}$ Longitudinal resistivity of a bulk medium that has been scaled to compare to the longitudinal resistivity of a non uniform medium.

ρ_{U} Resistivity for a uniform medium.

$\rho_{xx,\mathrm{H}}$ Hereman Resistivity.

$\rho_{xx,\mathrm{m}}$ Measured Resistivity.

$\rho_{xx,\mathrm{p}}$ Predicted Resistivity.

ρ_{xx} Longitudinal Resistivity.

$\rho_{xy,\mathrm{p}}$ Predicted Resistivity.

ρ Resistivity.

σ_{Ba} Conductivity for a background of a non uniform model with inclusions.

σ_{Incl} Conductivity for an inclusion with in a non uniform model.

σ_{U} Conductivity for a uniform medium.

σ_{xx} Longitudinal Conductivity.

σ_{xy} Transverse Conductivity.

θ_{eq} Angle of equipotential lines.

2DEG 2 Dimensional Electron Gas.

a Lattice Constant.

AF Antiferromagnetic.

AFM Atomic Force Microscopy.

AHE Anomalous Hall Effect.

AlAs Aluminium arsenide.

b Lattice Constant.

Ba Background.

BCC Body Centered Cubic.

BEP Beam Equivalent Pressure.

BFM Beam Flux Monitor.

c Lattice Constant.

CO Carbon monoxide.

CuMn($As_{(1-x)}P_x$) Copper manganese arsenide phosphide, *x* is the percentage of phosphide flux.

CuMnAs Copper manganese arsenide.

CuMnP Copper manganese phosphide.

E_g Band gap.

FCC Face Centered Cubic.

FEA Finite Element Analysis.

FM Ferromagnetic.

FWHM Full Width Half Maximum.

GaAs Gallium arsenide.

GaMnAs Gallium manganese arsenide.

GaP Gallium phosphide.

GMR Giant Magnetoresistance.

H_2O Water (deionised).

H_2O_2 Hydrogen peroxide.

H_3PO_4 Orthophosphoric acid.

HCl Hydrochloric acid.

ILL Institut Laue-Langevin.

IMR Isotropic Magnetoresistance.

Incl Inclusion.

IrMn Iridium manganese.

j Current Density (Amps per unit length).

$\mathbf{k_B}$ Boltzmann constant.

LAOS Low angle optical scattering.

LiMnAs Lithium manganese arsenide.

$\mathbf{M_R}$ Magnetisation from Wikberg [1].

$\mathbf{M_{sat}}$ Saturation Magnetisation.

MBE Molecular Beam Epitaxy.

MBMS Modulated Beam Mass Spectrometry.

MFM Magnetic Force Microscopy.

$\mathbf{Mn_2Au}$ Manganese-2 gold.

MnAs Manganese arsenide.

MnP Manganese phosphide.

MR Magneto Resistance.

$\mathbf{n_i}$ Intrinsic carrier concentration.

NHE Normal Hall Effect.

NS Non-stoichiometric.

$\mathbf{p}_{\mathrm{Incl}}$ Percentage of inclusions (%).

PBN Pyrolytic boron nitride.

PDE Partial Differential Equations.

PEEM Photoemission Electron Microscopy.

PID proportional integral derivative controller.

PM Paramagnetic.

$\mathbf{R}_{\mathrm{A}}$ Anomalous Hall coefficient.

$\mathbf{R}_{\mathrm{H}}$ Hall coefficient.

$\mathbf{R}_{\mathbf{xx}}$ Longitudinal Resistance.

$\mathbf{R}_{\mathbf{xy}}$ Transverse Resistance.

RHEED Reflection High Energy Electron Diffraction.

RMS Root Mean Square.

S Stoichiometric.

s Distance vector (m).

SL Seeding layer of Cu and Mn at the beginning of the layer growth.

SQUID Superconducting Quantum Interference Device.

STEM Scanning Transmission Electron Microscopy.

t reduced temperature.

$\mathbf{T_{sub}}$ substrate temperature.

$\mathbf{T_{TC}}$ substrate thermocouple temperature.

$\mathbf{T_B}$ Blocking Temperature.

$\mathbf{T_C}$ Curie Temperature.

$\mathbf{T_c}$ Critical Temperature.

$\mathbf{T_N}$ Néel Temperature.

TAMR Tunnelling Anisotropic Magneto Resistance.

TMR Tunnelling Magnetoresistance.

UHV Ultra High Vacuum.

V Voltage (Volts).

$\mathbf{V_{CuMnAs/Mn}}$ Volume of orthorhombic CuMnAs per Mn in the unit cell.

$\mathbf{V_{MnAs/Mn}}$ Volume of hexagonal MnAs per Mn in the unit cell.

$\mathbf{V_{UC/Mn}}$ Volume of unit cell per manganese.

$\mathbf{V_{UC}}$ Volume per Unit Cell.

$\mathbf{x_0}$ Initial position of the outer edge of the box along the x axis and the position from which a two terminal measurement is made.

$\mathbf{x_1}$ Final position of the outer edge of the box along the x axis and the position from which a two terminal measurement is made.

$\mathbf{x}_{4t,0}$ Initial position of the measurement for a four terminal measurement.

$\mathbf{x}_{4t,1}$ Final position along the x axis for a four terminal measurement.

XMLD X-ray magnetic linear dichroism.

XRD X-Ray Diffraction.

List of samples used in this thesis

This section contains a set of tables detailing the samples used in this thesis. Each table contains a series of samples as discussed in the following work. Sample series S represents layers that were grown at stoichiometry, while NS represents samples that were grown in non-stoichiometric conditions. Samples labelled SL were grown with seeding layer at the start of the growth. Samples will be referred to by their table number and then the sample number in that table. Samples in a series with sequential sample numbers were not necessarily grown sequentially. Samples Sample:3-1and Sample:4-1are the same sample that has been used in two different series.

Sample:1-1, Sample:1-3, Sample:1-10and Sample:2-1were grown by R.P. Campion and V. Novàk. All other samples were grown with the authors involvement.

Sample Number	Substrate	Layer	Capping Layer
1	GaP (N type)	46nm CuMnAs (S)	None
2	GaP (N type)	250nm CuMnAs (S)	None
3	GaP (N type)	140nm CuMnAs (S)	None
4	GaAs (undoped)	80nm CuMnAs (S)	2nm Al
5	GaP (undoped)	80nm CuMnAs (S)	2nm Al
6	GaP (undoped)	SL + 5nm CuMnAs(S)	2.5nm Al
7	GaP (N type)	10n CuMnAs(S)	2nm GaAs
8	GaP (undoped)	SL+ 20nm CuMnAs(S)	2nm Al
9	GaP (undoped)	50nm CuMnAs(S)	2nm Al
10	GaP (N type)	138nm CuMnAs (S)	None

Table 1 A table of the sample discussed for stoichiometric CuMnAs.

Sample Number	Substrate	Layer	Capping Layer
1	GaAs (S-I)	337nm CuMnAs (NS)	None

Table 2 A table of the sample discussed for non-stoichiometric CuMnAs.

Sample Number	Substrate	Layer	Capping Layer
1	GaP (undoped)	10nm CuMnAs (S)	2nm Al
2	GaP (undoped)	10nm CuMnAs (S)	2.7nm GaAs
3	GaP (undoped)	10nm CuMnAs (S)	30nm GaP

Table 3 A table of samples discussed in ultra thin films with varying capping layers.

Sample Number	Substrate	Layer	Capping Layer
1	GaP (undoped)	10nm CuMnAs (S)	2nm Al
2	GaP (undoped)	5nm CuMnAs (S)	2nm Fe / 2nm Al
3	GaP (undoped)	4nm CuMnAs (S)	2mm Al
4	GaP (undoped)	2nm CuMnAs (S)	2mm Al

Table 4 A table of all the samples used in the ultra thin thickness series.

Sample Number	Substrate	Layer	Capping Layer
1	GaP (undoped)	1ML Cu / 10nm CuMnAs(S)	2nm Al
2	GaP (undoped)	1ML Mn / 10nm CuMnAs(S)	2nm Fe / 2nm Al
3	GaP (undoped)	As terminated GaP / 10nm CuMnAs(S)	2mm Al
4	GaP (undoped)	0.7nm Cu+Mn then As exposed, 10nm CuMnAs(S)	2mm Al
5	GaP (undoped)	10nm CuMnAs(S) (Low growth Temeperature)	2mm Al

Table 5 A table of the samples used for investigating different possible growth methods for ultra thin film CuMnAs.

Sample Number	Substrate	Layer	P flux (Torr)	Capping Layer
1	GaP (N type)	214nm CuMn($As_{(\mathbf{1-x})}P_{\mathbf{x}}$)	1×10^{-8}	None
2	GaP (N type)	200nm CuMn($As_{(\mathbf{1-x})}P_{\mathbf{x}}$)	2×10^{-8}	None

Table 6 A table of the samples for CuMn($As_{(\mathbf{1-x})}P_{\mathbf{x}}$) - first growth series.

Sample Number	Substrate	Layer	P flux (Torr)	Capping Layer
1	GaP (undoped)	50nm CuMn($As_{(\mathbf{1-x})}P_{\mathbf{x}}$)	1×10^{-8}	None

Table 7 A table of the samples for CuMn($As_{(\mathbf{1-x})}P_{\mathbf{x}}$) - second growth series.

Sample Number	Substrate	Layer	P flux (Torr)	Capping Layer
1	GaP (undoped)	0.7nm Cu+Mn seeding layer, 40nm CuMn($As_{(\mathbf{1-x})}P_{\mathbf{x}}$)	0.5×10^{-8}	2mm Al
2	GaP (undoped)	0.7nm Cu+Mn seeding layer, 40nm CuMn($As_{(\mathbf{1-x})}P_{\mathbf{x}}$)	1×10^{-8}	2mm Al
3	GaP (undoped)	0.7nm Cu+Mn seeding layer, 40nm CuMn($As_{(\mathbf{1-x})}P_{\mathbf{x}}$)	1.5×10^{-8}	2mm Al
4	GaP (undoped)	0.7nm Cu+Mn seeding layer, 8nm CuMn($As_{(\mathbf{1-x})}P_{\mathbf{x}}$)	2×10^{-8}	2mm Al

Table 8 A table of the samples for CuMn($As_{(\mathbf{1-x})}P_{\mathbf{x}}$) - Third growth series.

Chapter 1

Introduction and Background Theory

1.1 Introduction and Motivation

1.1.1 Spintronics

Spintronics is a combination of the word spin and electronics. The field is based on the principle of using the spin of an electron in place of or with the charge of an electron to create different functionalities [2, 3] that can replace traditional charge based devices in data processing and storage. Memory storage works on the principle of recording a bit of data as a 1 or 0 on an element. A device needs to be able to write the data on to the element and read it off without rewriting the state. Memory elements ideally need to be resistant to accidental erasure of data, rewritable and able to retain their state without additional energy inputs for a prolonged period of time. Spintronic devices offer all of the above and the possiblity of shorter read / write times, being radiation hard (unaffected by charge perturbations) and non volatile [4, 5].

Giant Magnetoresistance (GMR), discovered separately by [6] and [7], was one of the first technically applicable spintronics phenomena and originally used for read head technology. There are many other key devices in spintronics such as magnetic tunnelling junctions and

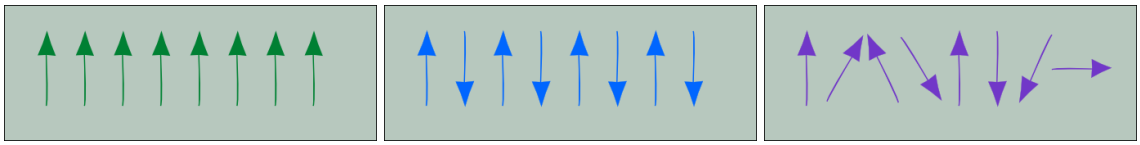

(a) Ferromagnetism (b) Antiferromanetism (c) Paramagnetism

Fig. 1.1 Schematics showing an idealised spin arrangement in different types of magnetic ordering. In 1.1a the spins are aligned in one direction, in 1.1b the spins are aligned anti-parallel to one another and in 1.1c there is no alignment between the spins and they point in random directions independent of each other.

spin valves. Many recent spintronic technologies have looked at building devices with the capability of not needing external fields to write or read the magnetic element. The write element can be set using spin transfer torques [2, 8, 9] and spin orbit torques [3].

The majority of spintronic devices are based on Ferromagnetic (FM) materials to read or write elements of the device. Antiferromagnetic (AF) layers have previously been used as pinning layers for exchange bias [10] but there has been recent interest in developing spintronic devices that do not contain FM elements and rely solely on AF, which will be discussed later in the chapter.

1.1.2 Types of Magnetism

There are three types of magnetic ordering relevant to this thesis: FM, AF and Paramagnetic (PM), which are shown in figure 1.1. The arrows in the figures represents the direction of magnetic moments within the material. The different magnetic moment alignments are caused by the exchange interaction of a material [11]

Exchange interaction

The alignment of magnetic moments to form an ordered system needs to be energetically favourable to occur. The exchange energy, from the exchange interaction, dictates the magnetic order with lowest energy for direct exchange magnetic materials. The exchange energy is due to the electrostatic forces between electrons, and is dependent on the distance

between them and their relative spin alignment [11]. The exchange interaction arises from the fact that electrons with identical physical location and spin alignment can not exist due to the constraint that their wave functions must be antisymmetric. The exchange interaction is described by the Heisenberg model,

$$U = -2J_{\text{ex}}\mathbf{s_1}.\mathbf{s_2} \tag{1.1}$$

where U is the exchange energy, $\mathbf{s}$ is the magnetic moment of the electron and J_{ex} is the exchange integral [12, 13].

The sign of the exchange integral can indicate what type of magnetic ordering will occur. If it is positive then parallel spins are preferred leading to FM, if it is negative then anti-parallel spins are preferred leading to AF.

Paramagnetism

In paramagnetism there is no spontaneous alignment of the magnetic spins as the exchange interaction is too weak for either FM or AF, however the magnetic moments will have a net alignment when there is an applied magnetic field. The effect is very weak at room temperature as the thermal energy is greater than the magnetic energy aligning the moments [14]. If the thermal energy and the magnetic energy are comparable then the effect is strong.

Ferromagnetism

In a FM material the spins align parallel to each other forming a net magnetisation. The direction of this net magnetisation of the material can be manipulated by applying a sufficiently strong external field. The sensitivity of a magnetic material to external fields means that data in a memory or storage device can be written to or erased from a FM. Materials lose their FM ordering at a Critical Temperature (T_c) known as the Curie Temperature (T_C). Figure 1.2 shows the temperature dependence of the magnetisation. The magnetisation is

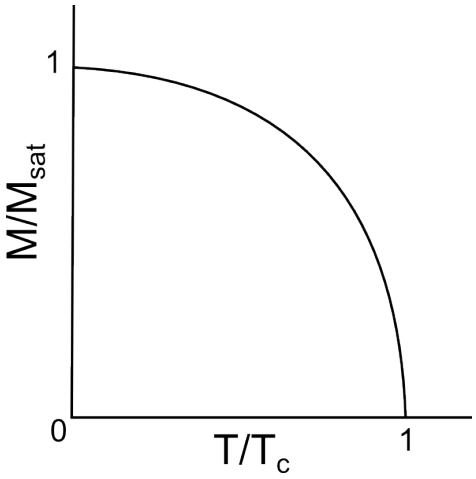

Fig. 1.2 An ideal spontaneous magnetisation against temperature for a FM transitioning into a PM. At low $\frac{T}{T_c}$ the Bloch $\frac{3}{2}$ scheme dominates, at high ratios of $\frac{T}{T_c}$ critical behaviour dominates

at a maximum at low temperatures as all the spins are aligned, where the material obeys Bloch's $\frac{3}{2}$ power law, which solves the Shrodinger equation for an exchange Hamiltonian to explain why spontaneous magnetisation occurs in the presence of spin waves[15]. The Bloch $\frac{3}{2}$ power law is:

$$M(T) = M(0)\left(1 - \left(\frac{T}{T_c}\right)^{\frac{3}{2}}\right) \tag{1.2}$$

where M(T) is the temperature magnetisation and M(0) is the magnetisation at 0K.

Just below the T_c the thermal energy of the spins means that the magnetisation has decreased the material displays critical behaviour, which is a power law relationship with a critical exponent (β):

$$M \propto (T_c - T)^{\beta} \tag{1.3}$$

The critical exponent is predicted to have a value of $\frac{1}{2}$ from mean field theory but different experimental values have been observed[11]. In between these two regions the magnetisation slowly decreases as the thermal energy increases but the spins stay principally ordered. After the T_c a material can transition into a different magnetic order but in figure 1.2 the magnetic order has transitioned into a PM so there is no magnetisation.

The exchange energy between magnetic moments in a FM is minimised when the spins are aligned parallel. The magnetostatic energy of a system is the energy stored in the generation of an external magnetic field. It is minimised by the non parallel alignment of magnetic moments, which will tend towards the system having zero net external magnetisation. These two conflicting energies are balanced by the generation of FM domains. The spins within a domain are aligned parallel, locally minimising the exchange energy, while the direction and configuration of the individual domains can minimise the magnetostatic energy. The boundaries between domain are called domain walls. In order to transition between two locally saturated, and internally parallel, domains it is necessary for the spins to be aligned non parallel to either domain. This non parallel alignment has an associated energy cost, the magnitude of which depends on the spin stiffness. The number and configuration of domains is then limited by the energy cost of each domain wall.

Antiferromagnetism

AF ordering can be considered to be two interlaced FM lattices in the case of a collinear AF as demonstrated in figure 1.1b. Materials can have more complicated spin sublattices including more than 2 spins, such as Iridium manganese (IrMn), which are non-collinear. In a collinear AF the spin axis will be described as the axis or plane in which the anti-parallel spins lie, shown in figure 1.3.

AF ordering does not produce any net magnetisation. It is difficult to manipulate the spins of AF materials, small tilting of the spins can be achieved when an external field is applied parallel to the sub-lattice magnetisation, however there is almost no magnetic susceptibility when an external field is applied parallel to the spin sub-lattice [11].

The T_c for an AF is known as the T_N. The spontaneous magnetic order has a similar dependence to a FM with a decrease in the strength of the magnetisation with temperature until T_N. Any phenomena that is an even function of the magnetisation that has been observed

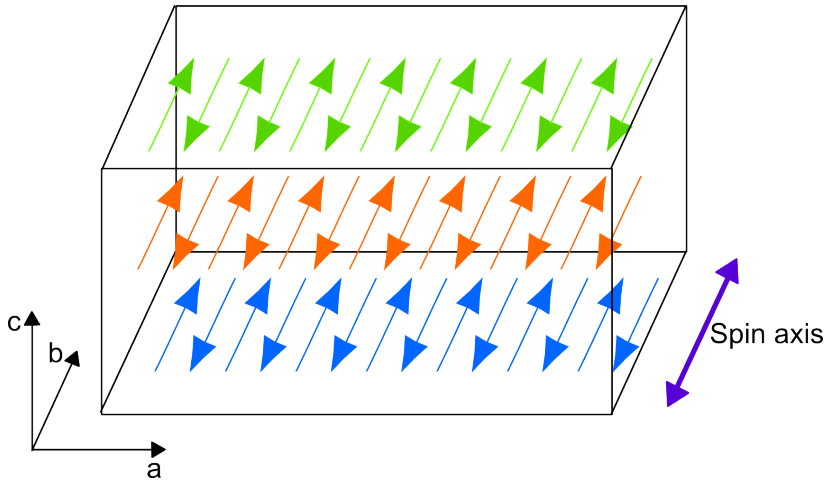

Fig. 1.3 Schematic showing the direction of the spin axis in a collinear AF. The different coloured arrows highlight the different layers along the *c* direction. The purple arrow depicts the direction the spin axis lies in.

in a FM should have a corresponding AF phenomena [5]. One that has been proven in Copper manganese arsenide (CuMnAs) is using a current pulse to switch the direction of the spin axis [16, 17] using the inverse spin galvanic effect, and will be discussed in detail in section 1.2.2

Exchange Bias

Exchange bias occurs when there is an interface between an AF layer and a FM layer. The spins at the interface couple together as shown in figure 1.4. Exchange anisotropy is caused by interface coupling between the layers and occurs when a sample is cooled from below the T_C through the T_N [10] with an applied external magnetic field. When a hysteresis loop is performed on an exchange biased system there is a shift in the hysteresis loop as shown in figure 1.5. Exchange biased layers are used in some spin valve devices [18] and in read head devices [19] to fix the direction of a FM layer.

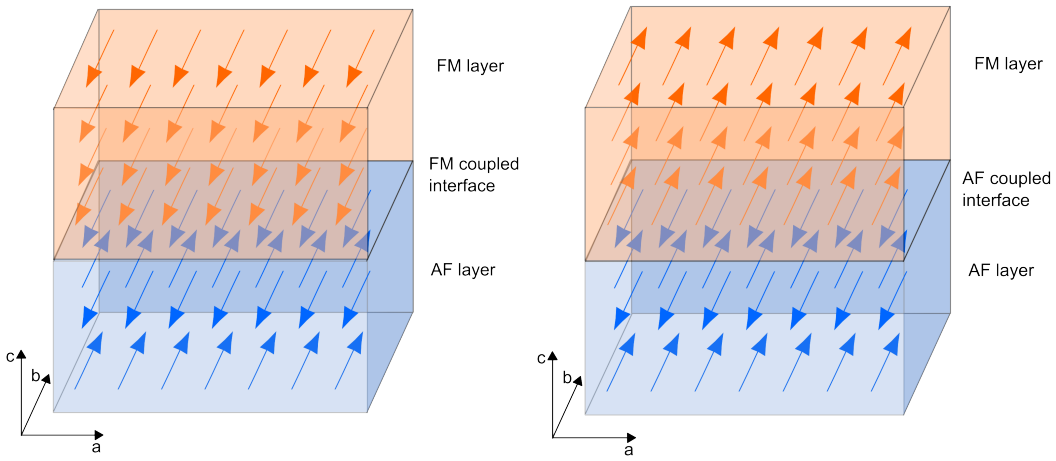

(a) FM coupled (b) AF coupled

Fig. 1.4 Schematic showing the interface coupling between a FM and AF layers. The AF is formed from FM layers in the *ab* plane coupled AF in the *c* plane.

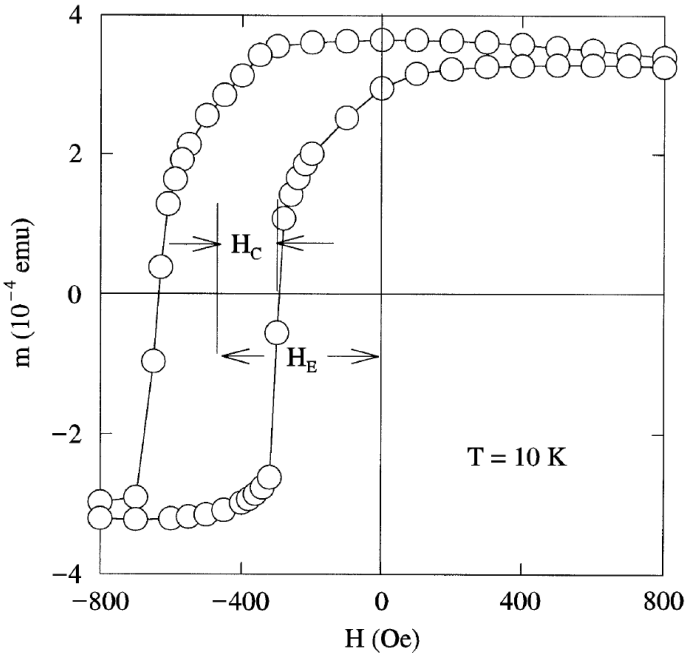

Fig. 1.5 An example of an exchange biased hysteresis loop. H_C is the coercive field and H_E is the exchange field. Image taken from [10].

1.1.3 Types of crystalline materials

Within a crystalline material electrons form different energy bands. The bands are separated by a band gap (E_g), where the energy values for the electrons are forbidden as there are no corresponding electron orbitals [12]. The bands on either side of the E_g are the conduction and valence band as shown in figure 1.6. The flat energy bands are a simplification of the situation. The allowed energies vary with the wave vector and can overlap each other, which occurs in semimetal and metals. The lowest allowed energy state on the conduction band will be less than the highest allowed energy state on the valence band so electrons will begin to fill the conduction band before the valence band is full.

An insulator (figure 1.6a) has a completely filled valence band and an empty conduction band. The E_g is too large for electrons to be easily excited across. In a semiconductor (figure 1.6b) the E_g is smaller and it is possible for electrons to be thermally excited into the higher band or by doping the material. Semiconductors typically have an intrinsic electron concentration less than 10^{17} cm^{-3}. In a semimetal (figure 1.6c) there is a small overlap in the conduction and valence band so that the conduction band is not full and the valence band is not empty. A semimetal may have an electron concentration in the range of $10^{18} - 10^{21}$cm^{-3}. A metal (figure 1.6d) has partly filled conduction and valence bands. A metal can have a electron concentration above 10^{22} cm^{-3} [12].

1.1.4 Antiferromagnetic Spintronics

In recent years there has been a spur of interest in creating spintronic devices that utilise AF materials for the principle elements rather than relying on FM elements [5]. This is due to the lack of stray fields generated by AF and their insensitivity to applied fields. An external field needs to be of the same magnitude as the exchange fields ($\sim$ 100T) compared to FM which are effected by fields greater than the coercive field ($\leqslant$ 1T) [20].

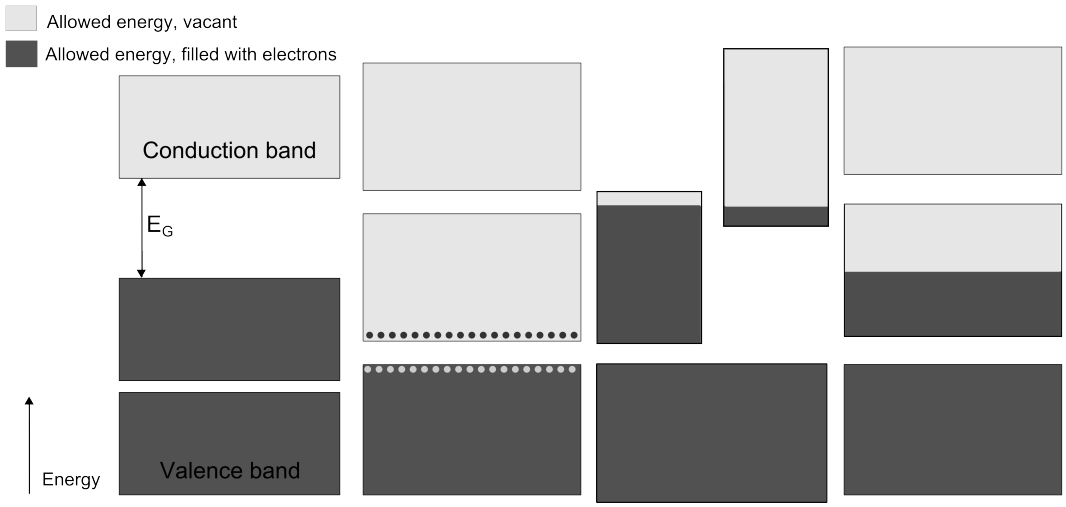

(a) Insulator (b) Semiconductor (c) Semimetal (d) Metal

Fig. 1.6 Simplified band structure schematics for different types of materials. Light grey areas are allowed energy states that are vacant, dark grey areas are allowed energy states filled with electrons. White areas between boxes are forbidden energy states. Image adapted from [12].

There are several different proposed devices including the exchange spring [21, 22], heat assisted magneto-recording [20] and current induced switching [16, 17, 23] (discussed later in section 1.2.2). There have also been several key phenomena such as Tunnelling Anisotropic Magneto Resistance (TAMR), spin Hall effect [24] and spin transfer torques [25] observed in AF. Below, the basis for several of the devices will be explained as examples of the emerging technologies.

The exchange spring works by having a FM element coupled to a thin AF and rotating the FM element causing a torque in the AF spins which rotate round as demonstrated in figure 1.7. The different directions of the applied field cause different states which have been observed in X-ray magnetic linear dichroism (XMLD) [21], resistivity [26] and SQUID [22] measurements.

Marti et. al. [20] created a room temperature AF memresistor from iron rhodium (FeRh), which has a $T_N \sim 400K$ and above this temperature it transforms into a FM. The different electrical resistance were achieved by heating the sample above the T_N and applying a

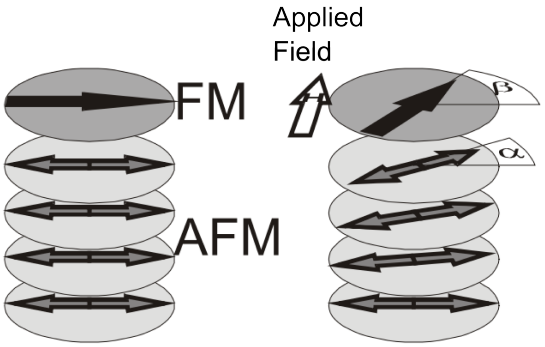

Fig. 1.7 Schematic showing the twisting of spins in an exchange spring between the FM and AF layer. α is the angle the FM layer rotates from its original axis. β is the angle that the top layer of the AF rotates from its easy axis. Image taken from [21].

magnetic field to align the FM moments. The sample is then cooled under the applied field, as it transitions to an AF the spins align perpendicular to their direction when FM. The sample remains in this AF state after the applied field is removed.

A spin valve is constructed of two FM layers seperated by a non magnetic spacer. If the FM layers are aligned parallel then the system is in a low resistance state and if they are aligned anti-parallel then a high resistive state is caused for a current passing throught the structure. If the non magnetic spacer is an insulator then the conduction is by tunnelling and the effect is termed Tunnelling Magnetoresistance (TMR). The difference in resistivity is caused by the electrons tunnelling across the barrier maintaining their spin, when the spins are parallel on both FM layers the density of states for each spin direction is similar, whereas when they are anti-parallel there is a difference in the available density of states for each spin direction [27, 28].

Initially AF layers were used to pin the one of the FM layers in spin valves but AF controlling devices were shown to produce an AF-TAMR [5]. Several groups [29–31] showed a spin valve like signal with a device layered as FM/AF/Insulator/Non magnetic metal. The FM layer was exchange coupled to the thin layer of AF material (IrMn) to cause

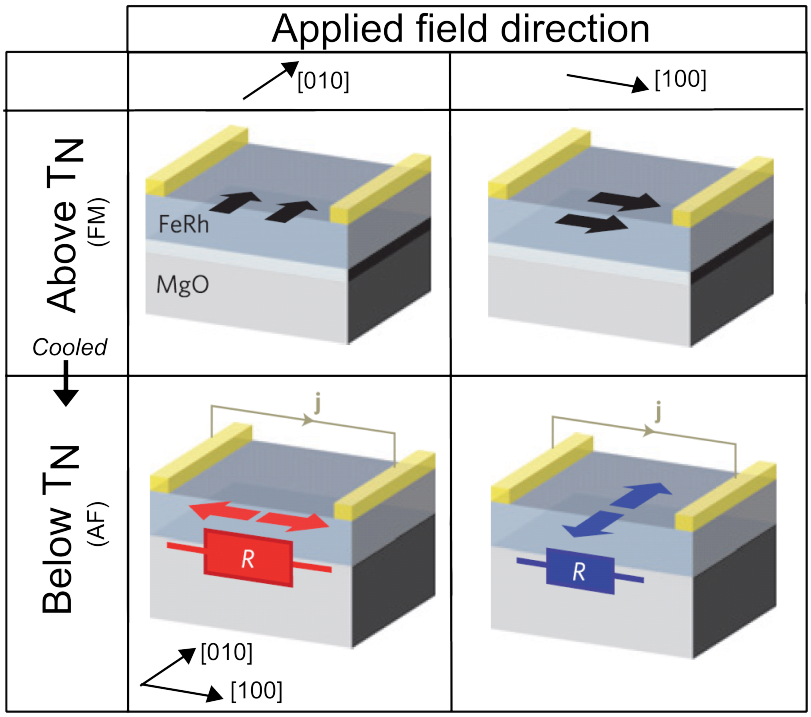

Fig. 1.8 Schematic showing the spin alignment for the FeRh resistor using field cooling to set states. The top row of boxes are for the material in a FM state and the bottom row are for when the material has been cooled into a AF state. The two columns represent the different field directions. Image adapted from [20].

an exchange spring. Petti et. al. [32] were able to prove a TAMR effect without a FM layer to set the direction of the AF, instead field cooling the AF into different spin axis orientations.

I-II-V semiconductors

Single element semiconductors are from the group IV elements (e.g. Si). However a wider range of elements can be used to make semiconductors and other crystalline materials such as the III-V (e.g. GaAs, GaP and InAs) or II-VI (e.g. MgO and CdTe) semiconductors. These semiconductors are predicted from the proton transfer rules, where the sum of the group elements in the material totals eights [33, 34]. The proton transfer rules can be expanded to ternary systems such as the I-II-V semiconductors, where a proton inhabits an interstitial site in the primitive cell [33]. I-II-V semiconductors were initially considered as a means of achieving higher T_C in FM semiconductors as the carrier concentration and Mn doping levels could be controlled independently [35]. Of the magnetic semiconductors that have been measured there are more with AF ordering than FM and they typically have higher T_N than the corresponding T_C [5].

Lithium manganese arsenide (LiMnAs) was investigated as a promising AF semiconductor when grown epitaxially on InAs [33, 36]. The layers were shown to grow in a 2D manner with X-Ray Diffraction (XRD) confirming similar lattice parameters to the bulk tetragonal material and Fabry-Pérot oscillations and scanning tunnelling spectroscopy demonstrating it is a semiconductor [33, 36]. Li has known problems with ageing in atmosphere making the grown layers susceptible to oxidation in atmosphere [36].

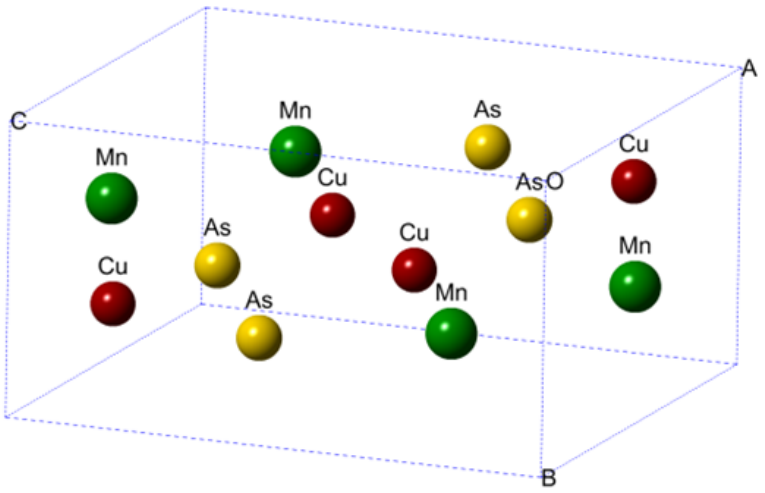

Fig. 1.9 The unit cell for CuMnAs with an orthorhombic structure.

1.2 Copper Manganese Arsenide - Previous Experimental and Theoretical Studies

In the bulk CuMnAs is an AF with an orthorhombic crystal structure [37] as seen in figure 1.9 and a T_N above room temperature [38]. CuMnAs was first considered for AF spintronics after work done by [33] into I-Mn-V compounds as AF semiconductors including LiMnAs. Due to the reactive nature of Li as a Molecular Beam Epitaxy (MBE) source the IB-Mn-As compounds were considered for epitaxial growth, as the IB elements (copper, silver and gold) have a similar outer electron configuration to the group I elements but are significantly less reactive.

When grown epitaxially on III-V substrates of GaAs or GaP it was found by Wadley et. al. [39] that CuMnAs forms a tetragonal unit cell as illustrated in figure 1.11. The epitaxially grown layers were found to have a high level of chemical ordering from Z contrast Scanning Transmission Electron Microscopy (STEM) shown in figure 1.10.

The in plane lattice parameters (a,b) of the unit cell of zinc blende [40] Gallium arsenide (GaAs) and Gallium phosphide (GaP) are significantly larger than those of CuMnAs so the

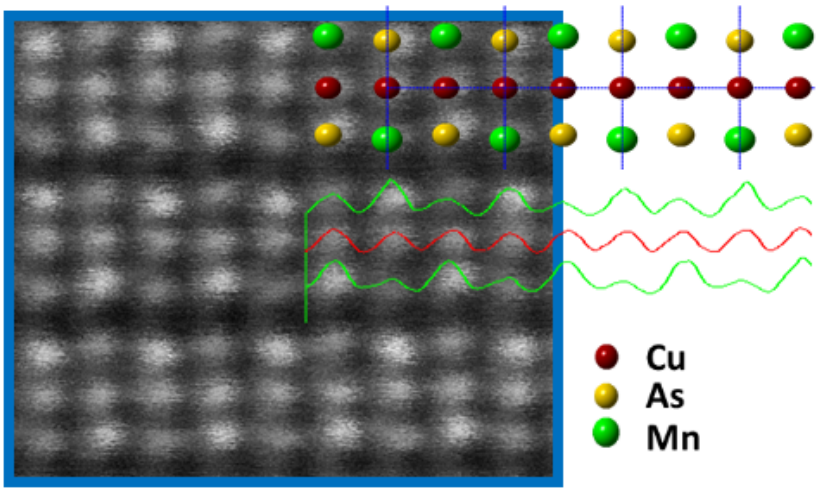

Fig. 1.10 Z-contrast STEM image showing the chemical ordering of CuMnAs where red spheres are copper, green are manganese and yellow are arsenic. Image taken from [39].

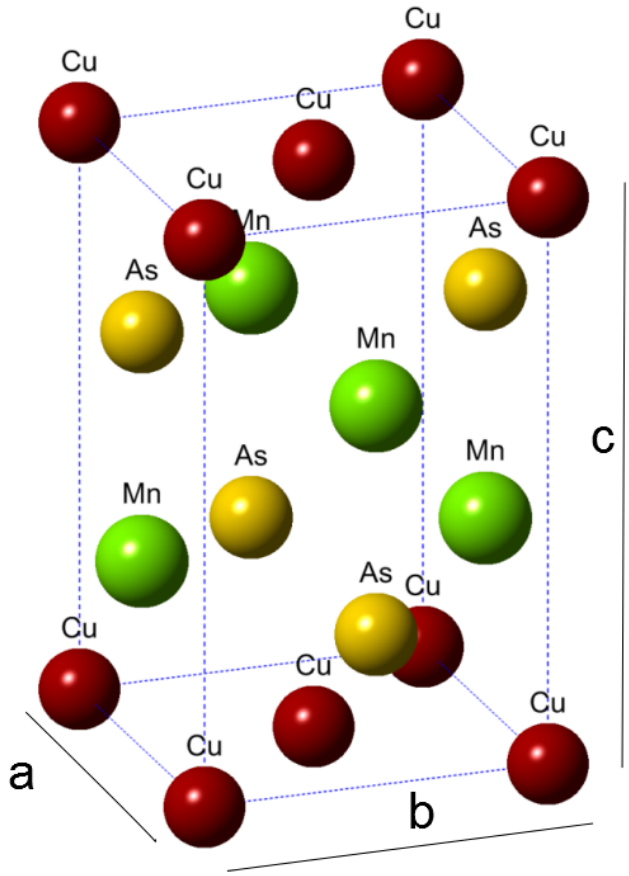

Fig. 1.11 The tetragonal unit cell structure of CuMnAs [39]. The red spheres are copper, green are manganese and yellow are arsenic.

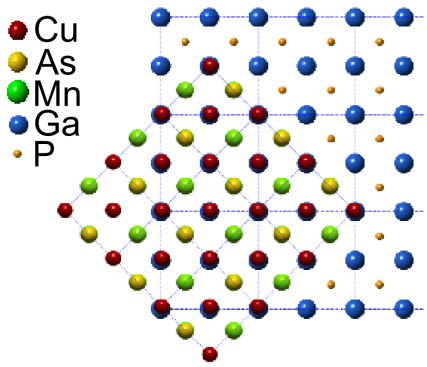

Fig. 1.12 Diagram of how the unit cells for CuMnAs aligns on the GaP substrate [39]. The red spheres are copper, green are manganese and yellow are arsenic. The blue and orange spheres are gallium and phosphorous of the substrate.

unit cell aligns along half of the diagonal of the substrate unit cell, example on GaP figure 1.12.

The zinc blende structure has a cubic unit cell so the lattice constants are equivalent, $a = b = c$. The lattice constant for GaAs is 5.6533Å and for GaP is 5.4505Å. When CuMnAs is grown on GaAs the unit cell structure of CuMnAs has a 1.5% mismatch. GaP has a significantly smaller lattice mismatch than GaAs, of only 0.3% [39], the alignment is shown in figure 1.12.

CuMnAs has been shown to exchange couple to an epitaxial layer of iron and exhibit reproducible exchange bias at room temperature [39]. The exchange bias caused a large change in the coercive field of iron (compared to a control sample of GaAs/Fe), however if the sample was heated above 440K then irrecoverable changes were caused at the interface [39].

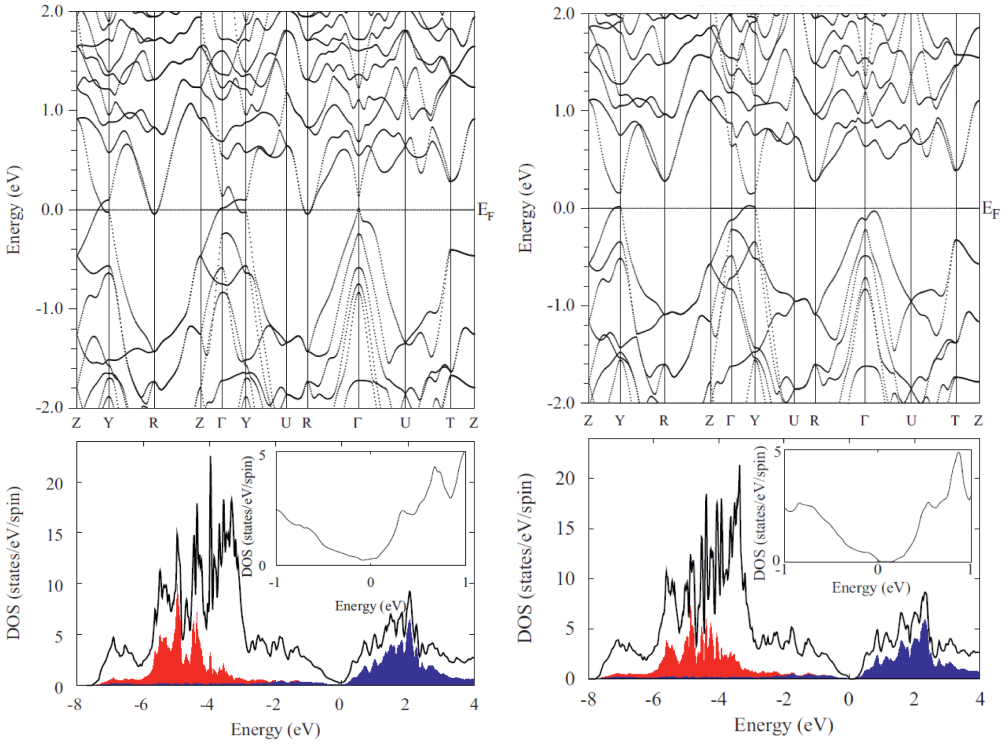

(a) CuMnAs (b) CuMnP

Fig. 1.13 The predicted band structure and density of states by [38] for CuMnAs and CuMnP with an orthorhombic structure. Images taken from [38].

1.2.1 CuMnAs Band Gap Predictions

Collaborators in Prague have used density functional theory[1] to predict the band structure of CuMnAs and several related compounds. The models were initially tested by predicting the structure for CuMnSb, which had been previously studied [41, 42].

Band structures were calculated for orthorhombic CuMnAs and Copper manganese phosphide (CuMnP) by [38]. The band structures are shown in figure 1.13. For CuMnAs the band structure predicts overlapping regions of holes and electrons, with a very small density of states at the Fermi energy. CuMnP has a band gap of ~ 0.1eV predicted. The difference in the band structures implies that CuMnP is a semiconductor while CuMnAs could lie at the transition between semimetal and semiconductor.

[1]Using the packages of: Full-potential linearized-augmented-plane-wave method (WIEN2K) and generalized-gradient approximation (GGA)

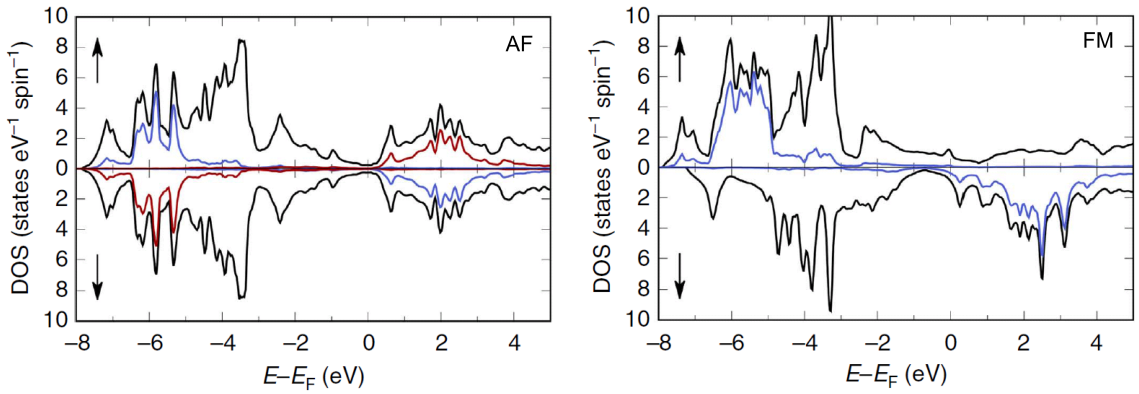

Fig. 1.14 Density of states calculations for tetragonal CuMnAs from GGA + U. Left is for AF coupling and right is for FM coupling. The coloured lines represent the spin sublattices and the black line is the total density of states. Image taken from [39].

Predictions were made for CuMnAs in a tetragonal structure. The density of states predictions are shown in figure 1.14. The predictions found that the AF coupling was energetically favourable and that the CuMnAs was still on the boundary between semimetal and semiconductor.

1.2.2 Current Switching

Železný et. al. [16] predicted that in AF, where the two spin sublattices individually have a broken inversion symmetry, that a lateral electrical current would generate Néel-order spin orbit torques. The current causes the spin axis of the AF to rotate so that it is perpendicular to the applied current.

In [17] it was shown in epitaxial layers of CuMnAs that current pulses could cause a change in the resistivity creating two resistance states that it was possible to read using a smaller probing current. Figure 1.15 shows the change in the resistance state for switching the direction of the current pulse. The CuMnAs layer needs to not be strongly uniaxial for the switching to occur.

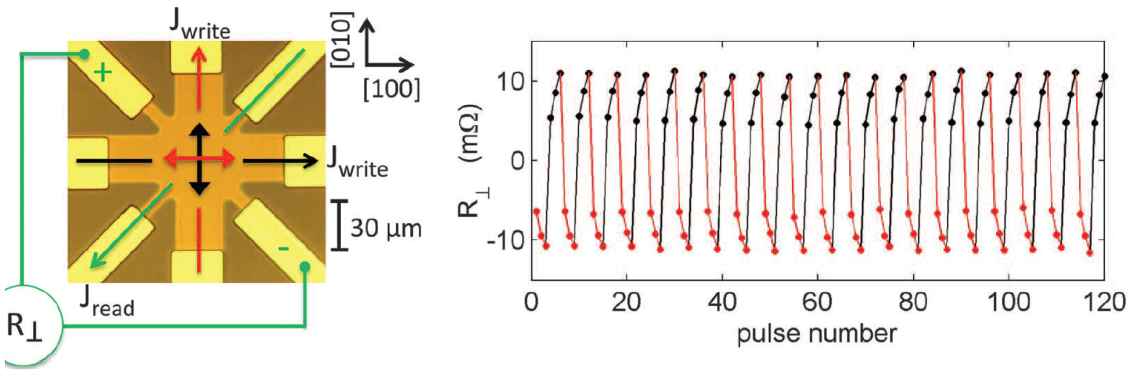

Fig. 1.15 Current Switching in a CuMnAs device. On the left is a schematic showing the applied current, spin axis and probing current direction and measurement. The double headed red and black arrows represent the two different magnetic states. The single headed arrow in either colour represents the direction of the applied current pulse, the double headed arrow represents the direction of the aligned spin axis. The green arrow represents the probing current. The right hand panel shows the change in the transverse resistance for writing the current state three times and then writing the alternate state. Image taken from [17].

1.3 Theory: Critical behaviour phenomena in electrical transport measurements

Transport measurements use the measurements of the resistivity against temperature to observe phenomena in metals and semiconductors. Different materials have different models of magnetism depending on how the magnetic order is coupled. The coupling can be caused by either localised electrons or itinerant electrons. Localised magnetic moments (or electrons) are associated with a specific lattice site and the interaction can be described by a Weiss molecular field, insulators can have magnetic order from localised electrons [43]. Itinerant electrons are non localised valence electrons, which behave like an electron gas. The exchange interaction causes the magnetic ordering and is often seen in metals and semiconductors [43]. Critical behaviour is observed as a material undergoes a phase transistion to a different magnetic state, at this point long range thermal effects have a larger effect on the system than the shorter range interactions considered in magnetic models [13]

There are several models for magnets where the spins are localised with an exchange interaction, such as the Ising and the Heisenberg models. In the Ising model the spins are aligned and can point in either an up or down direction. In Heisenberg model magnets the spins are aligned and can point in any direction [44], there is a peak in $\frac{\mathbf{d}\rho_{\mathbf{xx}}}{\mathbf{dT}}$ from the scattering of carriers by fluctuations in magnetic moments. The $d\rho_{xx}/dT$ peak has the same functional form as the specific heat [45, 46]. This behaviour has been observed in FM metals [45, 47] and dilute FM semiconductors [48]. It has also been shown that the $\frac{\mathbf{d}\rho_{\mathbf{xx}}}{\mathbf{dT}}$ can be used to determine T_C experimentally [48, 49]. In materials like Gallium manganese arsenide (GaMnAs) the magnetic interaction is caused by itinerant spins inducing the magnetic order between themselves [50]. In some semiconductors the peak at the magnetic transition appears in the resistivity [51] and is due to interaction between itinerant spins and lattice spins.

The $\frac{\mathbf{d}\rho_{\mathbf{xx}}}{\mathbf{dT}}$ and the cusp in the resistivity for different materials or layers can be compared by scaling the temperature to a new variable called the reduced temperature t [48, 52]:

$$t = \frac{T - T_c}{T_c} \tag{1.4}$$

T_c is the magnetic transition temperature which can be either T_C or T_N. $d\rho_{xx}/dT$ is also scaled for the reduced temperature to $d\rho_{xx}/dt$:

$$\frac{d\rho_{xx}}{dt} = \frac{d\rho_{xx}}{dT}\frac{dT}{dt} = \frac{d\rho_{xx}}{dT}T_c \tag{1.5}$$

1.4 Theory: Strain and relaxation in epitaxial layers

Epitaxial layers are crystals that grow with a lattice aligned in registery with the lattice of the underlying substrate [53]. The process of growing epitaxial layers can be split into homoepitaxy, where the same material as the substrate is grown and heteroepitaxy where a different material is grown on top of the substrate [54].

In homoepitaxy the main growth material does not change between the structure and the device for instance with a GaAs substrate growing a GaAs structure on top with varying levels of doping. In this scenario the crystal lattice of the substrate will replicate upwards and any stress in the material will be from distortions caused by dopants. One example of this is GaMnAs where Mn, typically less than 12% substitutes in the Ga position of the crystal lattice [55, 56].

However in heteroepitaxy a completely different material is grown on top of the substrate and the layer material and this can have a different lattice, lattices constants, expansion coefficients and other properties to the substrate with related crystal orientation [57]. The most well known form of heteroepitaxy is GaAs and Aluminium arsenide (AlAs) where there is less than a 0.15% mismatch between the lattice constants [58]. This can be used to form a 2 Dimensional Electron Gas (2DEG) [59].

Another technologically significant form of heteroepitaxy is the growth of single crystal iron on GaAs to create magnetic elements in device technologies [60–63]. Iron has a Body Centered Cubic (BCC) unit cell with a lattice constant of 2.87Å and GaAs has a zinc blende unit cell, which consists of two displaced Face Centered Cubic (FCC) unit cells with a lattice constant of 5.65Å [12]. This means that two unit cells of iron align along one of the GaAs [64, 65] with a lattice mismatch of 1.4% [63]. Iron was initially successfully grown on GaAs(110) [64] and then on GaAs(001) [60, 61]. All these initial growths were performed above room temperature ($175 - 225°C$), these layers suffered with large dead layers, that were partly attributed to As diffusion at the interface. The dead layers were decreased by reducing the growth temperature, changing the GaAs surface to Ga rich [65] or sulphur passivation of the interface to prevent As diffusion [66]. CuMnAs is an example of heteroepitaxy where the unit cell of the tetragonal CuMnAs rotates to align along the diagonal of the zinc blende GaAs or GaP. The unit cell of CuMnAs forms a tetragonal lattice

when grown epitaxially rather than orthogonally, as in bulk, to better match the underlying lattice.

Heteroepitaxy can cause antiphase boundaries at the interface, which can propagate to the surface of a material. They are formed at step edges on the substrate where the unit cell of the deposited layer is unable to arrange it's unit cell around them. One example of this is GaAs on Si substrates. GaAs has a zinc blende unit cell (two interlaced FCC) whereas Si has a FCC unit cell. If the Si has a double step then the GaAs unit cell can compensate, however where there is a single step then an antiphase boundary is formed [53].

Strain can be caused in a crystal by difference in lattice parameters, especially at an interface. At an interface of two crystals the surface layer of atoms, and the following layer underneath, will distort to minimise the lattice mismatch [67], which is known as pseudomorphism. A thin film will elastically strain to the substrate lattice until a critical thickness at which point dislocations will form to reduce the energy of the lattice. A layer can remain strained if the lattice mismatch is small enough and the layer thickness is below the critical thickness [67]. When an epitaxial layer is deposited on a significantly thicker substrate it can either stretch to the underlying substrate causing elastic tensile strain and if the substrate lattice is smaller than the epitaxial layer then compressive strain will be caused [53]. In some cases if a layer remains strained it can cause bowing of the underlying substrate [68].

If the energy to keep a layer strained is not energetically favourable then it will relax to the natural lattice parameters. The relaxation process can cause several different types of defects, such as threading dislocations and micro cracks. In some conditions when the layer relaxes it will form islands on the surface, which is one method of forming quantum dots. Threading dislocations can be caused from the surface down or from the interface up and will travel in a straight path at an angle to the interface. They will be aligned to a crystallographic axis of the sample. Threading dislocations are caused by a plane in the lattice slipping.

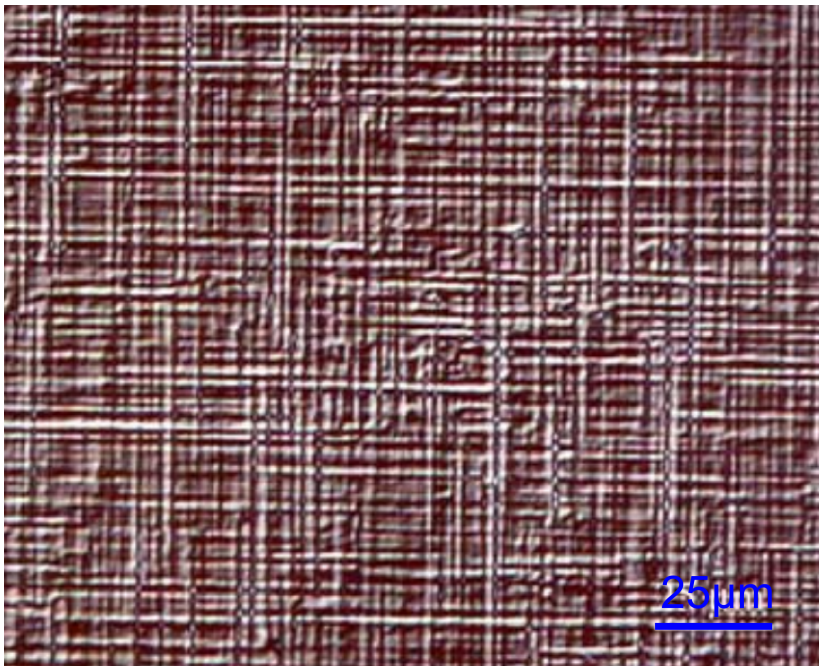

Fig. 1.16 Optical picture of a sample of Ge/$Si_xGe_{(1-x)}$/Si, where the lattice mismatch changes due to expansion causes threading dislocations through the layer resulting in a distinctive cross hatching pattern [71]. Image taken from [71].

The slip results in dangling bonds possibly reconstructing within the material; the dangling bonds can change the carrier transport and acts as scattering centres [69]. There are two types of threading dislocation: glide and shuffle in which the dangling bonds are parallel and perpendicular to the plane respectively [70]. In thin film crystals dislocations are formed by plastic deformation currently believed to result in predominantly glide dislocations [69, 70]. Figure 1.16 shows a distinctive cross hatching pattern formed by threading dislocations in a heteroepitaxy system. The two layers have different thermal expansions of the lattices [71]. This mismatch causes the layers to have dislocations that propagate to the surface from the interface.

1.4.1 Strain and magnetism

Thin film epitaxial layers can affect the magnetic order of a material. If a layer is grown strained then it causes a distortion in the lattice parameters and interatomic spacing. The

magnetic coupling is very sensitive to the interatomic spacing [62], an example of this is the magnetic coupling weakening with increased atomic spacing, however there are several energy factors that determine what type of magnetic ordering is favourable. Another effect that epitaxial layers can have on the magnetic properties of a layer is to cause a material to grow with a different crystal unit cell [62].

1.5 Thesis

In this thesis we will discuss results from the growth, characterisation and T_N of CuMnAs and copper manganese arsenide phosphide ($CuMn(As_{(\mathbf{1-x})}P_{\mathbf{x}})$). These are promising materials for AF spintronics and there have been significant developments in the field during this work including the proof of current induced switching of the spin sub lattices. The next chapter will explain the experimental and calculation techniques used throughout this thesis. In chapter 3 we will discuss the growth conditions for stoichiometric and non-stoichiometric CuMnAs and then characterise the layers to show the similarities and differences in lattice parameters and topology for layers grown on different III-V substrates. The spin axis and T_N of CuMnAs will be determined by neutron diffraction. For non-stoichiometric CuMnAs grown with an excess of Mn the material exhibits a FM secondary phase which will be characterised by SQUID and Magnetic Force Microscopy (MFM) to identify the presence of Manganese arsenide (MnAs) inclusions. Chapter 3 will also discuss techniques for growing continuous films of 10nm CuMnAs on GaP. Layers will be initially analysed with Atomic Force Microscopy (AFM) and successful continuous films will be characterised further. In chapter 4 we will discuss alloying CuMnAs with phosphorous to grow $CuMn(As_{(\mathbf{1-x})}P_{\mathbf{x}})$, the effect of the growth conditions on the lattice parameters and other characteristics will be discussed. The effect of the magnitude of the phosphorous flux in a systematic series of samples will also be discussed. The T_N of $CuMn(As_{(\mathbf{1-x})}P_{\mathbf{x}})$ is measured from neutron diffraction and compared to the value from CuMnAs where there has been a clear increase in the T_N. Chapter 5 is

about determining the T_N through transport measurements. The ρ_{xx} shows a distinct kink around the T_N, which results in a cusp in the temperature derivative ($d\rho_{xx}/dT$), that can be compared to the measured value of T_N from neutron diffraction. This technique will then be applied to several different variations in CuMnAs and CuMn($As_{(\mathbf{1-x})}P_{\mathbf{x}}$). We will see that the T_N of CuMnAs is suppressed by a layer thickness of 5nm, that there is a difference in transport behaviour for CuMnAs/GaAs or CuMnAs/GaP due to the increasing carrier concentration of the substrates, that it is possible to measure in a non-stoichiometric system the transition temperatures of the two phases and other features. In chapter 6 we will discuss magneto transport measurements for a sample of non-stoichiometric CuMnAs with MnAs inclusions to show how the FM inclusions (estimated at 13% of the layer) dominate the magneto transport. Finite Element Analysis (FEA) will be used to simulate a system with non uniform conductivity. The system will contain randomly placed inclusions that will be the only element in the system with a σ_{xy}. The chapter will conclude by comparing the calculated trends from the model with the magneto transport results. Finally in chapter 7 we will discuss the conclusions of this work and future areas of interest.

Chapter 2

Growth, Experimental and Computational Techniques

2.1 Crystal Growth Techniques - Molecular Beam Epitaxy

2.1.1 Principles

MBE is a powerful crystal growth technique that is used to grow device such as lasers, Hall sensors and high electron mobility transistors [72]. MBE is used to grow these structures as it allows precise control of doping levels, atomic interfaces and the growth of single crystal thin films [53, 73]. It was initially pioneered in the 1960's [74] by growing on Si surfaces with SiH_4. The technique then rapidly expanded in its understanding and application to its present state.

MBE works by exposing a crystalline substrate to fluxes of molecular beams of different molecules, when the molecules arrive on the surface they become known as adatoms. An adatom can be either a single atom or a oligmer of multiple atoms forming a stable state. The molecules deposited on the surface migrate until they find a site to bond to. Under the right conditions, materials will grow with a crystal structure aligned to the crystal structure of the

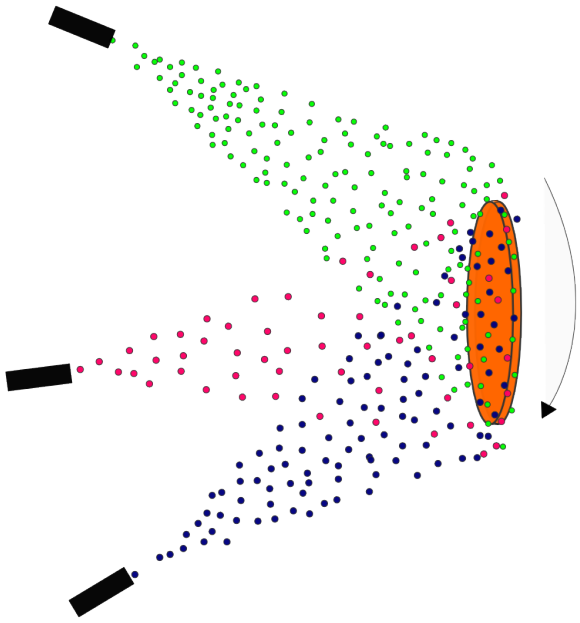

Fig. 2.1 A simplified schematic of atomic fluxes (coloured spheres) from three different sources (black rectangles) incident on a substrate (orange disk).

substrate, which is known as epitaxial growth. Figure 2.1 is a simplified schematic of how fluxes are incident on a substrate. The sources are arranged in a ring and aligned so that there is a direct line of sight between the source and the substrate holder, which is shown in more detail in the machine schematic in figure 2.2. To prevent a non-uniformity in how the flux of each material is distributed around a wafer it is necessary to rotate the sample during growth, ideally at a rate such that there is at least one revolution per monolayer deposited. There can be a radial difference in the flux which must be considered for larger diameter growth wafers but this is normally combated in commercial systems by the design of the source positions. An important consideration for the incident fluxes is the sticking coefficient of the molecule, which is the percentage of particles that remain on a surface without re-evaporating. The sticking coefficient of a molecule is dependent on several factors, for example the substrate material [75] and the temperature of the substrate the molecule is interacting with. Group V elements like As and P can have a low sticking coefficient, depending on factors such as their

oligomer, and are applied in an excess of the necessary incorporation flux. Different growths can require different ratios of material fluxes to attain the optimum growth conditions.

Typically, molecular fluxes are produced from effusion (or Knusden) cells, in which an ultra pure atomic material is heated until a vapour is formed in the confined space of the cell. There is a small opening in the cell from which a beam of particles can emerge [76]. Some materials, such as As, emerge as an oligmer for example a dimer (As_2) or tetramer (As_4). The oligmer can be controlled by having a high temperature cracker attached to the front of the cell, at lower temperature the tetramer will be the dominant species and at higher temperatures the dimer. Another type of cell now being incorporated in MBE systems are E-beam sources for the deposition of metals without the need for running very high temperature effusion cells.

MBE machines are designed to achieve Ultra High Vacuum (UHV), the main growth chamber of the system ideally has a background vacuum of 10^{-10}Torr. This is achieved by the design of the system and the pumping on the systems. Typically a system uses cryo, turbo molecular and ion pumps to achieve this vacuum. These pumps have different strengths and are able to achieve different levels of vacuum.

The vacuum of the system is further improved by cryopanels encasing the growth chamber. When the cryopanels are cool, gases and volatile species stick to the surfaces of the panel. This means that during growth gases emitted by the heated substrate and excess material from the sources are quickly removed [54]. The cryopanels also act to remove the heat dissipated by the heater and the individual sources [54].

The UHV conditions are necessary to reduce the chances of impurities impinging on the surface of the substrate, preventing gas phase collisions of the species on the way to the substrate and to prevent the species reimpinging on the substrate if they are desorbed. To ensure these conditions the mean free path of a molecule in the system needs to be greater than the size of the chamber, if this is true then the only particles likely to be incident on

a substrate are those from the sources and any impurities or desorbed particles will not be incident on the substrate. The mean free path ($\tilde{l}$) can be expressed as [77]:

$$\tilde{l} = \frac{k_{\mathrm{B}}T}{\sqrt{2}\pi d_{\mathrm{g}}^2 p_{\mathrm{s}}} \tag{2.1}$$

where k_{B} is the Boltzmann constant, T is the temperature, d_{g} is the diameter of gas particles (that are assumed to be hard spheres) and p_{s} is the pressure of the system. If we take T as room temperature (20°C) for a background pressure of 10^{-10} Torr and the diameter of N_2 for d_g as 0.378nm this gives a $\tilde{l} = 1.567 \times 10^3$km which is significantly greater than the size of the chamber so the chance of a particle to particle collision is minuscule [54].

A schematic of the MBE system is shown in figure 2.2. It shows the cryopanels (Blue) encircling the sample holder. It also shows a simplified arrangement for the *in-situ* measuring techniques that will be discussed in section 2.1.2.

To reduce contaminants in the system samples are loaded into the growth chamber through a series of introductory chambers. This means that it is possible to maintain the conditions in the growth chamber for an extended period of months or years [54]. Typically a small load lock chamber is brought to air to introduce multiple new samples into the system. This is then pumped down and heated to bake the substrate and holder to reduce contamination. After baking out in the load lock samples may be transferred into a buffer chamber through a gate valve where they may be stored until growth. This chamber also typically contains a heated stage on which individual sample may be heated to a higher temperature to further remove contaminants. By this point the substrates will have been heated for several hours to a temperature just below 450°C to remove water vapour and some Carbon monoxide (CO). The buffer chamber also has a gate valve to the main growth chamber.

Modern epitaxy ready samples are designed to have oxidised layers that have known desorption properties [78]. The final layer of this is removed when the sample is brought into the growth chamber and heated. This means that Reflection High Energy Electron Diffraction

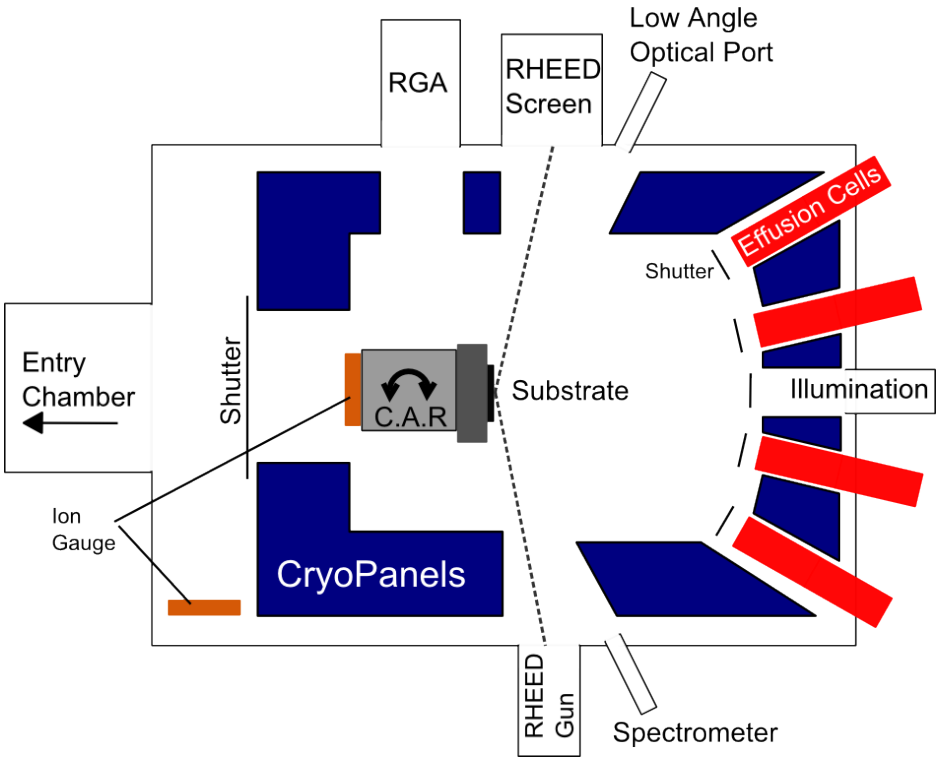

Fig. 2.2 A Schematic of the MBE growth chamber. The blue areas represent the areas with cryopanels and the red areas are different effusion cell which would be aligned along the circumference of a ring at the end of the chamber. The port providing illumination is at the centre of that ring. C.A.R stands for continuous aximuthal rotation, it contains the sample holder, heater and opposing beam flux monitor. The whole device can rotate by 180° so that either the sample or beam flux monitor faces the cells.

(RHEED) can be used to monitor the desorption to ensure the best possible surface before growth [54, 79]. Before any active device layer is grown ideally a buffer layer will be grown to further smooth the surface.

The epitaxial substrates are typically cuts from boules and can have a variety of orientations [80]. In this thesis we will use wafers of GaP and GaAs cut for the (001) face of the crystal. The cut of the crystal can change the growth conditions needed as different surface reconstructions form, which can be confirmed by RHEED.

Machine set up

A Veeco Gen III MBE machine was used to grow all the samples discussed in this thesis. This system had a background pressure of the order of 10^{-10}Torr. The machine had 14 different ports for cells including several gated cells that could be easily switched without bringing the main chamber to atmosphere. Within this thesis several different types of cells were used. A Mark IV Veeco cracker that had been well characterised for the ratios of As_2 and As_4 at different cracker temperatures [81], was used to provide an As flux. The phosphorus was from a decomposition effusion source from MBE Komponent, which was filled with GaP crystals. The cell is set up so that the tip was cooler than the base, without a direct path from the base to the tip so that at standard operating temperatures only the phosphorous was volatile enough to escape the cell. The source was in a differentially pumped port separated from the main chamber with a gate valve to minimise cross contamination when the source is not in use. The copper, manganese and aluminium were deposited from standard high temperature effusion cells.

The machine was also equipped with several devices for monitoring the system and growths in-situ, these included Beam Flux Monitor (BFM) gauges, a residual gas analyser (RGA) mass spectrometer, 15keV RHEED and a k-Space Associates BandiT [82, 83] for measuring growth temperatures on GaAs. During the work of this thesis a lower wavelength

spectrometer was adapted to measure the growth temperature for samples grown on GaP. The system has several different pumps to achieve the UHV conditions. The main chamber is pumped by a cryopump, an ion pump and a turbo pump. The buffer chamber is pumped by an ion pump and the load lock chamber is pumped by a turbo pump. Turbo pumps are especially suited to pumping standard air gases such as nitrogen, oxygen and water.

Epitaxy ready substrates were used and mounted on holders with a Pyrolytic boron nitride (PBN) backing plate. They were then introduced to the load lock and heated to 150°C to remove water vapour and other contaminants. When the samples were out-gassed sufficiently they were moved into the buffer chamber. Samples were further out-gassed on a heated stage up to 450°C before they were introduced into the growth chamber where they were heated until the final desorption was seen on the RHEED at around substrate thermocouple temperature (T_{TC}) of 700°C. For growths of all samples in this thesis the tetramer of Arsenic (As_4) was used.

Growth Mechanisms

There are three main growth models for MBE: Frank and Van der Merwe [84], Volmer - Weber [85] and Stranski-Krastanov [86].

Frank and Van der Merwe describes 2D growth systems where the material grows layer by layer or by step flow. In layer by layer growth, the arriving adatoms have a migration length that is shorter than the average distance between monolayer islands, as is demonstrated in figure 2.3. This form of growth can occur in GaAs and leads to oscillations in the intensity of the RHEED signal, which are a well established method of measuring the growth rate [87, 88] (discussed in further detail in section 2.1.2). In step flow growth, the molecule has sufficient mobility to migrate to a step edge where it will bond and expand the mono layer.

In the 3D growth model of Volmer - Weber, islands form on the surface of a layer and grow outwards and upwards from there. This form of growth occurs when molecules have

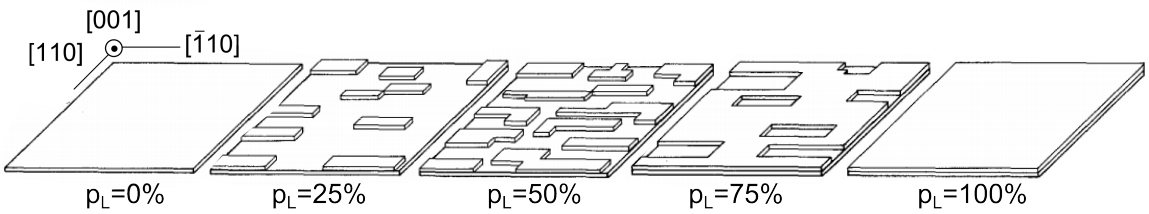

Fig. 2.3 A highly idealised schematic showing the growth of a monolayer by layer growth. p_L is the percentage of layer covered, at p_L is 50% the surface is roughest due to the split between the two surfaces. Image based on [87].

a low surface migration length. The Stranski - Krastanov growth mode is a mix of 2D and 3D growth where islands nucleate on the surface but the base layer of the material also continues to increase. It often occurs in strained layers that have passed a critical thickness and relaxation of the lattice has occurred [89, 90].

The different growth modes can also be considered from the perspective of the energy of the surface, deposited material and the interface between them. If these three energies are minimised by forming a large interface between the layers then the surface will 'wet' and the deposited material will spread across the surface of the substrate enabling layer by layer growth. At the other extreme if the energy is minimised by having the smallest interface possible between the substrate and deposited material then the deposit material will form into droplets on the surface to minimise the area in contact with the substrate, which will contribute to 3D growth. Between these two extremes 2D-3D growth will occur. At low growth temperatures metastable situations can occur, where the surface is not in a thermodynamic minimum but is kinetically limited to a local minima.

Doping and alloying

Dopants are used to change the properties of the material to increase (or decrease) the carrier concentration of either holes or electrons. Dopants can be used to counteract any unintentional background doping. By changing the dopants in different layers of a sample, devices such as PIN junctions can be made. Dopants can be incorporated substitutionally

or interstitially in a substrate by applying an additional dopant flux, that is smaller than the principal material fluxes, on a substrate during a layers growth. The doping profile can be sharply controlled by opening and closing the shutter [91] or a graded doping level incorporated by changing the temperature of the dopant cell [92]. Different doping sources are used for MBE to create p [93, 94] or n [95–97] type GaAs. Some dopants, such as Ge [79] and Si on (311)a GaAs [98], are amphoteric dopants and will be either p or n type depending on the growth conditions of the material. This can be caused by the dopant atom replacing different elements. Different materials such as GaAs, GaP and GaN require different dopant sources.

Alloying occurs when a significant proportion of a dopant is used so that an epitaxial layer has lattice coefficients that are proportional to both components [99]. Some common systems are $(Al_{1-x},Ga_x)As$ and $(In_{1-x},Ga_x)P$. Alloying can be used to tune the properties of a layer [100] from the lattice parameters, the band gap or magnetic properties. Alloying is used to create quantum wells such as in the structure $(Al_{1-x},Ga_x)As/GaAs/(Al_{1-x},Ga_x)As$ [91, 101], where the change in band gap between the layers causes a quantum well [102]. A graded layer of a changing alloy can be grown to change the lattice parameters of a substrate towards those of the active layer [103].

2.1.2 In situ growth monitoring

A major advantage of MBE is the ability to monitor the growth in-situ with RHEED and other techniques to provide instant feedback for the growth conditions. There are several tools for different purposes to allow this that will be discussed in the following section. They all monitor different aspects; mass spectrometry is used to monitor the purity of the chamber; RHEED is used to monitor the surface crystal structure across the substrate; band edge measurements are used to measure the substrate temperature independently of the

substrate heater and shallow angle optical observations provide additional information about the surface.

Mass spectrometry

Mass spectrometry is a tool to analyse the ambient compounds in a vacuum system. In an MBE system the mass spectrometer is positioned so that it is connected to the central chamber but not with a direct incident path of the molecular flux beam. This set-up allows for the mass spectrometer to be sensitive to the background of the MBE chamber, which means that it can be used to monitor the level of contaminants in the system. Another use of mass spectrometry, in a seperate system, is in characterising the behaviour of sources before they are used for growth [81].

Figure 2.4 shows a schematic of the layout of a mass spectrometer. Gas particles initially enter the system and are ionised. The ionised particles then travel on down into the quadrupole where the trajectory of the charge particles is deflected depending on the charge to mass ratio of each particle. The deflection caused by the magnetic field is varied with time so that different mass particles are registered at different points in each sweep.

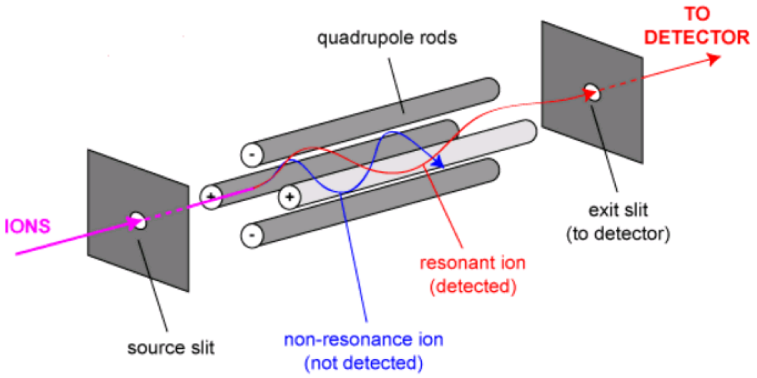

Fig. 2.4 Schematic diagram of a quadropole mass spectrometer. The diagram shows two different paths that an ion entering the through slit could take, one of which is the path of a resonant ion that is detected. Image taken from [104].

During the ionisation of the particles several phenomena occur. Compound particles can split into different particles or elements can become singly or doubly ionised by losing two electrons. The splitting of compounds is a common effect and aids in the determination of the compound when there are multiple possible options. For example, a peak at the atomic weight of 28 could indicate carbon monoxide (CO) or gaseous nitrogen (N_2), however by looking at the fracturing pattern of N, at 14, and C, at 12, it is possible to calculate the relative proportion of each compound in the 28 peak.

When using mass spectrometry to characterise sources, such as with Modulated Beam Mass Spectrometry (MBMS), it is possible to determine natural contaminants in a source or which oligomer of a material is released under certain conditions [81].

RHEED

RHEED is a powerful tool for studying the surface of a material in UHV. It uses a beam of high energy (15keV) electrons to diffract from the surface of a substrate. The electron beam is incident at a grazing angle to maximise the effect and is diffracted onto a fluorescent screen which emits light when an electron is incident on it and thus creates a 2D image of the reciprocal space. This technique is sensitive to periodic structure over the length of the wafer. The set up is demonstrated in figure 2.5. The angle of incidence for the electron gun can be varied in the range of $0.5^\circ - 5^\circ$.

The RHEED image is formed from the points that fall on the Ewald sphere [105]. The Ewald sphere is a sphere with a radius of $\frac{2\pi}{\lambda}$ where λ is the wavelength of the electrons. The Ewald sphere is a construct in reciprocal space and when overlaid on the reciprocal space diffraction pattern for the crystal, there will be a bright spot (high intensity) where the edge of the Ewald sphere intersects a reciprocal space point. Figure 2.6 demonstrates this for reciprocal lattice rods, which cause streaks on a RHEED screen [53]. An epitaxial surface will appear streaky if it has a smooth surface which is not causing disruption with the

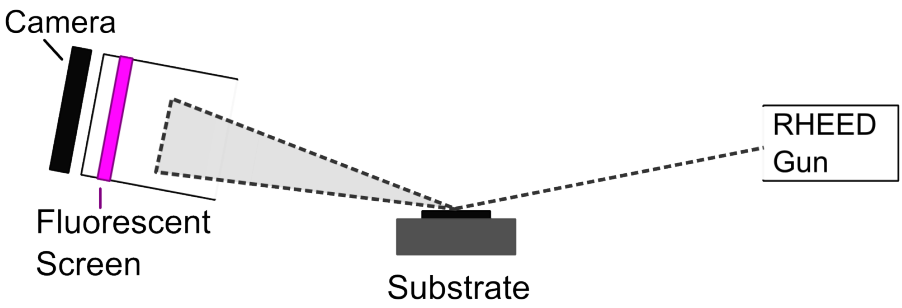

Fig. 2.5 Schematic showing the path of electrons (dashed line) in a RHEED system. The camera is mounted outside of the vacuum, but the fluorescent screen is mounted inside the vacuum.

diffraction. For an amorphous surface where there is no crystal alignment the RHEED image will appear as a continuous haze with no features (figure 2.7a). For a polycrystalline material there will be bright arcs on the RHEED screen (figure 2.7b) as there is some alignment to the crystal but there is not a single direction so it creates a band of points at which the criteria for diffraction is met. Finally in an epitaxial single crystal material there will be rods of points that meet the criteria for diffraction. In a perfect 2D surface the bands would narrow until they became tight spots but due to noise interference, surface disorder and step edges this is unlikely to occur [106]. For an imperfect 2D surface where there is roughness on the surface the RHEED image will appear as large dots. The distinctive RHEED reconstructions seen

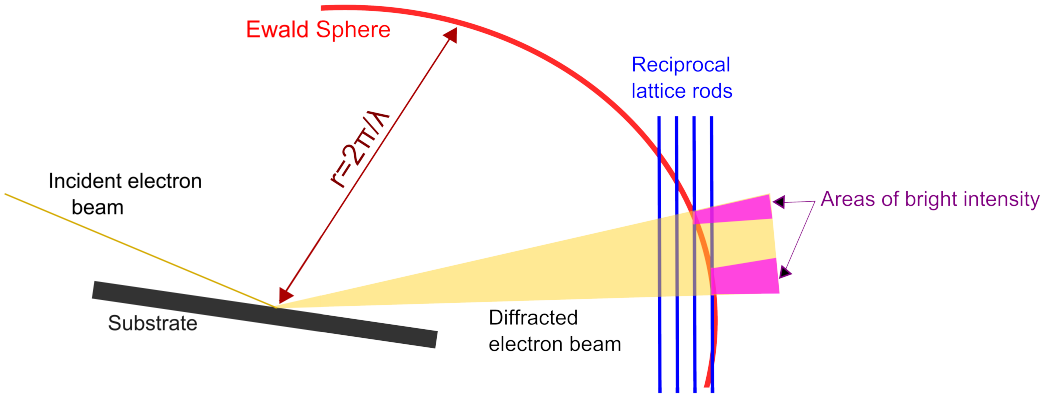

Fig. 2.6 A schematic showing how the positions where the reciprocal space rods intersect the Ewald sphere appear on the fluorescent screen forming a RHEED reconstruction of the surface.

(a) Amorphous material (b) Polycrystalline (c) Single crystal (2x)

Fig. 2.7 schematics of RHEED reconstructions for different crystals. In (a) the amorphous material that has no crystal alignment there is a continuous haze. In (b) the material is made up of small crystals that are aligned in different direction so diffraction occurs in bands. In (c) a single crystal is present causing streaks from the surface which varies with the alignment of the crystal and the RHEED beam.

from a crystalline 2D surface are due to the incomplete crystal structure on the top layer [105]. To minimise the energy of the surface the atoms will bond together to form a lower energy state [106]. This causes distortions in the top layers of the crystal structure that the electron beam is sensitive to.

For the growth of GaAs it is possible to use the intensity of the RHEED signal to determine the growth rate [87]. When a material is growing layer by layer, as shown in figure 2.3, the intensity of the RHEED signal is at a maximum when there is a complete layer on the surface and the intensity of the signal is at a minimum when the layer has 50% of the next layer deposited [87] as this has the most disorder on the surface. These changes cause an oscillation in the intensity of the diffraction lines along the RHEED screen without changing the background illumination.

The measurement of growth rates is important as this provide an independent means of checking the fluxes of source materials. The growth rate can be used as a reference point to scale the fluxes to known points and calibrate to sources to accurately replicate conditions from previous growths.

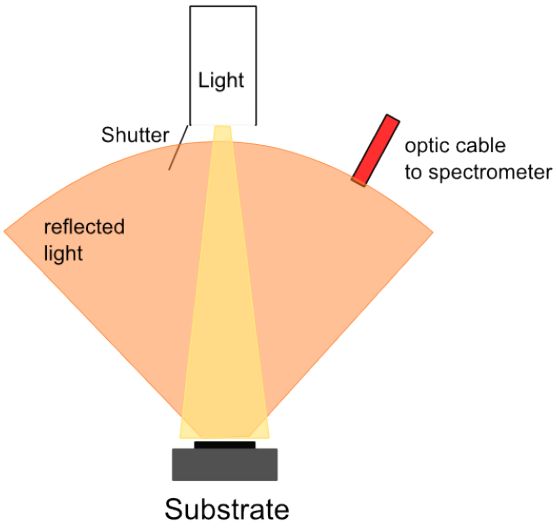

Fig. 2.8 Schematic of the set-up of a band edge measurement. The lamp provides the incident yellow light on the sample and the orange reflected light is detected by the spectrometer.

Band Edge Temperature Measurements

The substrate temperature (T_{sub}) is an important growth parameter and is most reliably obtained from measuring the temperature independently of the thermocouple that controls the heating. The band gap of a semiconductor is dependent on the temperature of the material, therefore the wavelength of the band gap can be used to calculate the T_{sub} using a known calibrated value.

The k-Space Associates BandiT [82, 83] technology allows the measurement of the band gap and temperature to be performed in real time for GaAs substrates. For GaP substrates a spectrometer with a different range is required, but our BandiT is a GaAs only unit and so a separate spectrometer was used, which is unable to provide real time updates on the temperature. The band edge measurements are set up as in figure 2.8, where a white lamp provides a focused beam of light of different wavelengths. The spectrometer records the light reflected from the sample.

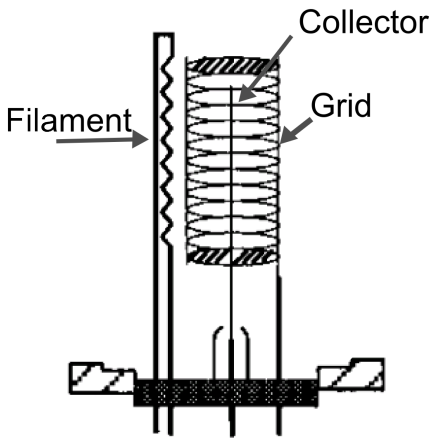

Fig. 2.9 Schematic of a hot cathode ion gauge that is used to monitor fluxes or background pressure. Image taken from [108].

The band edge technique measures the temperature from the bulk of the substrate. However there can be loss of signal during growth if the growth layer is more conductive than the substrate as the number of carriers in the material increases.

Beam flux monitors

The MBE system described in this work uses Bayard Alpert ion gauges, which are hot cathode ionisation gauges used to measure pressures in UHV conditions [107]. A schematic of a typical gauge is shown in figure 2.9. The system is made up of a filament which emits electrons that are accelerated into the grid and ionise gas particles in there. The ions are then incident with the collector rod in the center of the grid. One of the ion gauges is aligned so that when rotated in position it occupies the same location as a sample during growth, this allows the ion gauge to be used to calibrate growth fluxes against growth rates for samples.

There are several considerations that must be made when measuring fluxes with an ion gauge. The geometry of the cells will effect the reading. The gauge will be able to ionise different percentages of a flux depending on the atomic weight of the atom. The history of

the gauge will be important, for example with group V elements it is necessary to saturate the gauge with the growth species before taking a reading [53].

When comparing the background pressure of the system measured with ion gauges and the mass spectrometer, it is necessary to consider what elements are contributing to the background pressure. Heavy elements such as As and its oligmers will be easily ionised by the gauge, but the mass spectrometer has a reduced sensitivity at those atomic weights. Hydrogen on the other hand is easily detected by the mass spectrometer and not the ion gauge. Both systems of measurement are calibrated against nitrogen.

The Beam Equivalent Pressure (BEP) is often quoted for the fluxes from a cell. It is the pressure of a particular species with the background pressure removed. BEP is often quoted in literature but should be used with care as it makes no allowances for the geometry of a system, which can have large effects on the flux [106] or the sensitivity of the gauge to different speicies [72]. Within a system the BEP should be used with care and not be assumed to be comparable if a source was moved to a different port. Within a system with the same configuration and a calibrated growth rate for each source the BEP can be used to achieve the desired pressure for a growth, say returning to known stoichiometric conditions.

Shallow angle optics

Using the lamp from the band edge temperature measurements and a window with a view of the substrate at a shallow angle it is possible to visually inspect the sample to approximate characteristics such as temperature, surface roughness and the presence of some types of adatoms on the substrate. This will be referred to as Low angle optical scattering (LAOS). The position of the port is shown in figure 2.2. One of the features that can be observed is roughly checking the temperature of GaP substrates. At room temperature GaP is a pale orange colour but as it heats up to appropriate buffer growth temperatures it turns a deep red colour. If this change does not happen at an expected thermocouple temperature it is

indicative of poor coupling between the substrate and thermocouple possibly due to problems with the mounting. Another clear effect with the LAOS is the build up of group III, or metal, adatoms on the surface of a substrate. At the beginning of this process the surface will appear matt and silver, which is most apparent on GaP wafers, and then there will be the appearance of droplets on the surface. It is possible to see this process recover with a change of conditions to group V rich. Surface roughness is also apparent on the surface, at its best a surface will be a perfect mirror and it will be possible to see reflections of inner elements of the machine. As the surface becomes rougher then regions or the whole surface could have increased unidirectional scattering rather than reflecting the light or diffuse scattering. This cloudiness can be dependent on the direction of the aximuthal and will cause flashing during rotation. The flashing will be particularly on any aligned defects on the sample which can meet the conditions for constructive interference to occur.

2.2 Measuring crystal structure by diffraction

Diffraction is a powerful technique to study crystalline materials. Diffraction is based on Braggs law,

$$2d\sin(\theta) = n_{\mathrm{o}}\lambda \tag{2.2}$$

where d is the lattice spacing, θ is the angle between the plane and the beam, n_{o} is an integer for the order of diffraction, and λ is the wavelength [11, 12]. This means that constructive interference from planes of the crystal lattice will only occur when the path difference between the planes is equal to an integer multiple of the wavelength as demonstrated in figure 2.10. By choosing photons in the X-ray region or particles, such as electrons or neutrons, it is possible to probe different aspects of a crystal structure. X-rays are sensitive to the inter atomic spacing and are diffracted by atomic electrons, neutrons are diffracted by the atomic nucleus and are sensitive to elemental isotopes, lighter nuclei and also magnetic moment

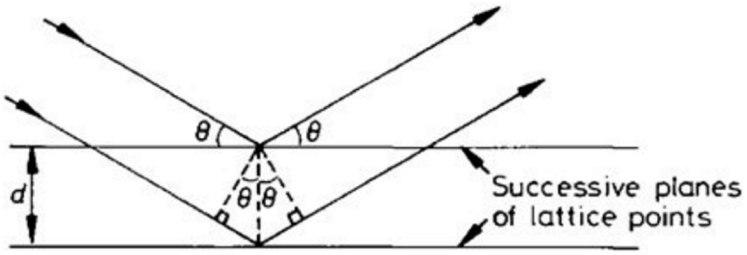

Fig. 2.10 Schematic demonstrating Braggs law (equation 2.2) for diffraction from two crystal planes. Image taken from [11].

orientation. Electrons are used to image the surface of materials (see RHEED - section 2.1.2) and can be easily focused onto specific areas [11].

2.2.1 X-ray diffraction

XRD measurements were performed on a Philips X'pert Material Research Diffractometer by Dr. P Wadley. The system used x-rays generated by a Cu$K_{\alpha 1}$ anode. The sample mounting was able to move in the three orthogonal dimensions (x,y,z) and to rotate(ϕ) and tilt(ψ). The technique is non destructive and allowed for measurement of the out of plane lattice parameter, crystal quality and thickness depending on the set-up.

The Miller indices of (h k l) were used to describe which planes of a crystal lattice cause the constructive interference. The Miller indices are defined as the reciprocal of the intercept of the plane with the crystal axes [11]. The Miller indices are related to the lattice spacing in a cubic unit cell by equation 2.3, where a is the lattice parameter.

$$d = \frac{a}{\sqrt{h^2 + k^2 + l^2}} \tag{2.3}$$

By using the miller indices it is possible to predict for a crystal structure at what angle the diffraction peak will occur. This can be used in reverse to determine the crystal structure of a material from the angle of the diffraction peaks for different peaks.

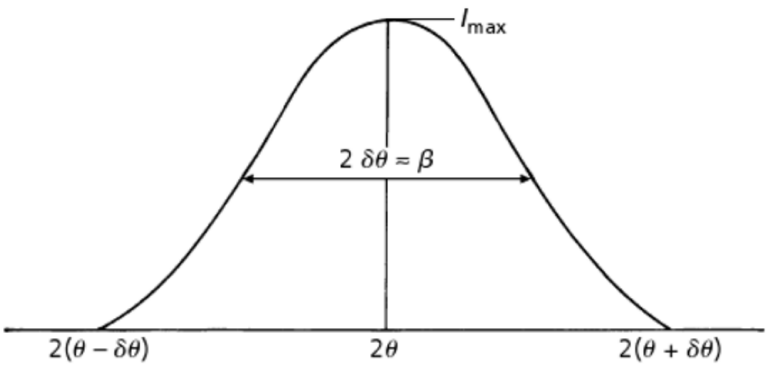

Fig. 2.11 Schematic demonstrating the broadening caused by a finite thickness. β is the full width half maximum of the peak. Image taken from [109].

In a perfect crystal the diffraction peak would be infinitely sharp, occuring at an infinitismally small angle. However due to disorder or lattice mismatching in real crystals the diffraction peak will extend beyond occuring precisely at a single angle as the Bragg condition will be satisfied at a wider range of angles. The peak will also be broadened due to effects from the finite thickness of the sample, which is shown in figure 2.11. The Scherrer equation,

$$\beta = \frac{K\lambda}{t_{th}\cos\theta} \tag{2.4}$$

where β is the full width half maximum of the diffraction peak, K is a correction factor for the particle shape and t_{th} is the film thickness, is derived from the Bragg equation (equation 2.2) by considering the constructive and destructive interference of a finite number of planes with a small perturbation in the angle[109].

Another feature that can be observed on thin films are small thickness fringes next to the diffraction peak. The fringes are caused by the limited number of planes to diffract from in a finite thickness film. By using fittings programs these fringes can be used to accurately calculate the thickness of a thin film.

2.2.2 Neutron Diffraction

Neutron diffraction can be used to study the crystal structure and the magnetic structure of a material. The nucleus of an atom scatters the neutrons by the strong nuclear force allowing the determination of the crystal structure. Scattering from the magnetic structure occurs from the interaction of magnetic moment of the neutron and the local magnetic flux density. The magnetic moment of the nucleus is ignored as it is normally 2000 times smaller than the electron magnetic moment [11]. If the atoms of a material have no magnetic moments then diffraction peaks only occur due to the crystalline order. If the atoms of a material have magnetic moments which are aligned randomly, as in the paramagnetic state, then magnetic scattering of the neutrons is random and incoherent. A coherent diffraction pattern will occur only if there is an alignment of the magnetic moments within the material. In an AF material the structured order of the magnetic moments causes a magnetic unit cell, which can generate diffraction peaks separate to the structural peaks of the material. These peaks occur as the magnetic unit cell can be larger than the structural unit cell [11]. If the magnetic and structural unit cells are the same size then the diffraction peaks will overlay

There are two types of neutron source: the fission source and the spallation source. The Institut Laue-Langevin (ILL) (figure 2.12) uses a fission reactor source whereas ISIS (figure 2.13) uses a spallation source. High energy neutrons released from a fission source are slowed within a moderator and form a beam of neutrons at different wavelengths. Monochoromators are then used to select a single wavelength. A monochromator works by only reflecting specific wavelengths onto a target with all other wavelengths passing though or reflecting on to shielding and being absorbed [11].

In a spallation source charged particles are accelerated to a large proportion of the speed of light. At ISIS the protons are accelerated to 84% of the speed of light [110] and then fired into a tungsten target to produce a burst of neutrons [110]. The neutrons arrive in a packet, they are at a variety of wavelengths, which will have varying times that it has taken them

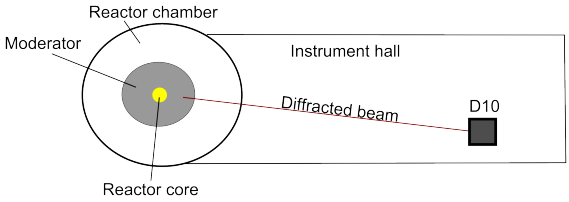

(a) ILL

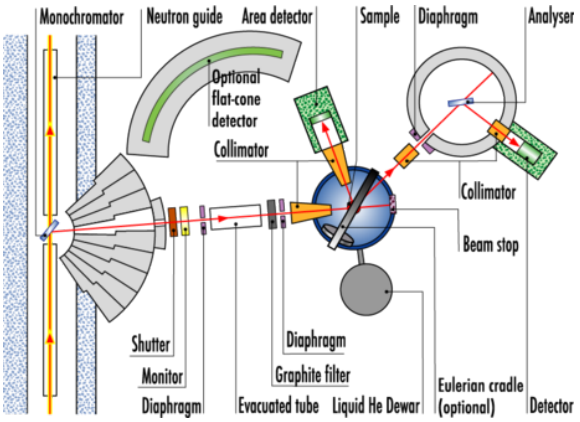

(b) D10

Fig. 2.12 Schematics of a) the layout of the ILL and b) the single crystal four circle diffractometer instrument used on the D10 beam line (image taken from [112]).

to travel from target to sample. Time of flight measurements are used to calculate the many diffracted wavelengths by equation 2.5, where t_d is the time taken to reach the detector from the source, M_n is the mass of the neutron, L is the distance from the source to the detector and h is Planck's constant.

$$t_{\mathrm{d}} = \frac{M_{\mathrm{n}} L}{h} \frac{2d}{n_{\mathrm{o}}} \sin(\theta) \tag{2.5}$$

Neutrons have a very low interaction rate so care needs to be taken to maximise the diffracted signal measured. ^{3}He detectors are used to measure neutron signals. When a neutron interacts with the ^{3}He it causes a nuclear reaction releasing energy (equation 2.6 [111]).

$$^3_2He + ^1_0n \rightarrow ^1_0P^+ + ^3_1H + e^- \tag{2.6}$$

The proton and elctron are from the ionisation of a hydrogen atom with 764keV from the energy realsed in the reaction. These charged particles are accelerated in an electric field to be detected at an anode and cathode causing a signal to be detected. On the D10 beamline at ILL a movable detector is used whereas at WISH a bank of ^{3}He detectors that cover 320° [111] are used to measure each pulse.

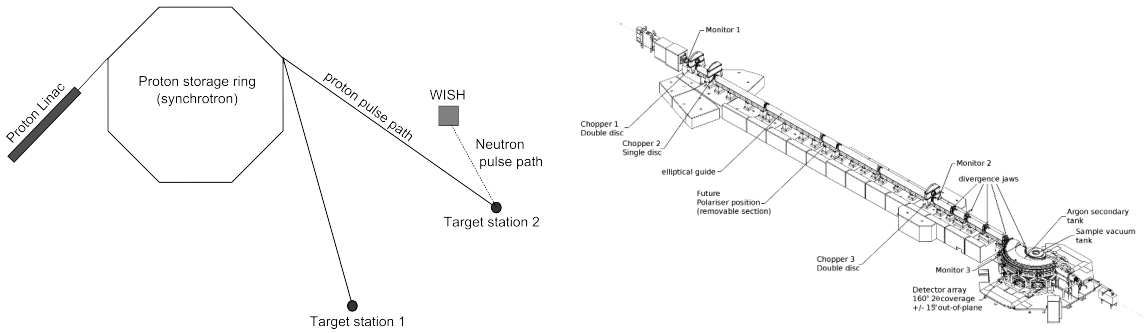

(a) ISIS (b) WISH

Fig. 2.13 Schematics of a) the ISIS facility and b) the WISH beam line (image taken from [113]).

At the ILL the sample was held in a cryofurnace with a He atmosphere for temperatures between 300K and 550K. The sample was mounted so that the *ac* plane was formed a diffraction plane between the detector and incident beam [114]. At ISIS the sample was held in vacuum, for a similar temperature range. The sample was mounted with either the c or a plane vertical so that the scattering plane was sensitive to (h,k,0) or (0,k,l) respectively.

2.3 Magneto Measurements

2.3.1 SQUID

SQUID magnetometers use a superconducting ring with Josephson junctions to measure minute changes in magnetic field, that can be sensitive to a single magnetic flux quantam [115]. The Josephson junctions are weak links consisting of insulating or non-superconducting material, which separate the superconducting regions of the SQUID. The superconducting rings in a SQUID may contain either a single or double Josephson junction. Single junctions are found in RF type SQUIDs, while DC SQUIDs use double junctions. In both RF and DC SQUIDs a sample is moved through second order gradiometer (pickup loops) that are inductively coupled to the Josephson junction or junctions as shown in figure 2.14. The sample is moved along the axis of the gradiometer, which is perpendicular to the plane of

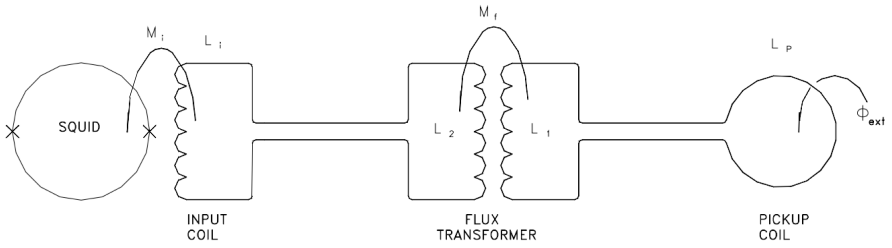

Fig. 2.14 Circuit diagram showing how the pickup coils that the sample moves through are inductively coupled to the Josephson junction. Image taken from [116].

the coils. If an external field is applied then it is also along this axis. The magnetisation measured is sensitive to any magnetisation along this direction and is sometimes called the longitudinal moment. To measure the magnetisation along different crystal directions it is necessary to physically remount the sample with a different orientation.

The total flux in the SQUID ring must be quantised, and in the presence of an external flux, current flows through the loop to ensure that the total flux remains quantised. When the current changes across the loop a voltage signal is detected in the feedback loop (RF coil). The feedback loop acts to change the bias current (feedback coil in figure 2.15) the feedback loop reads the applied voltage and uses calibrated measurements to convert this into the magnetisation of a point dipole. A typical circuit diagram for a RF SQUID is shown in figure 2.15.

When there is no applied field set on the RF SQUID there remains a small magnetic field in the system otherwise it would not be able to detect a signal, as there must be a change in the magnetic flux through the pick up coils to detect a signal. A Quantum Design Magnetic Properties Measurement System was used for all work carried out in this thesis. Samples of 4mm x 5mm were mounted either in plane or out of plane and a standard measurement procedure is outlined in figure 2.16.

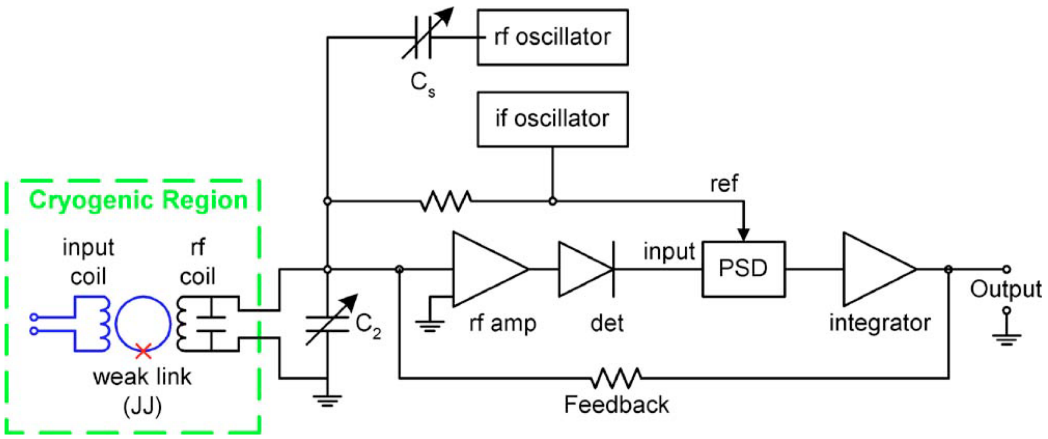

Fig. 2.15 Circuit diagram showing a typical RF squid. The input coil is inductively coupled to the pickup loops. Image taken from [115].

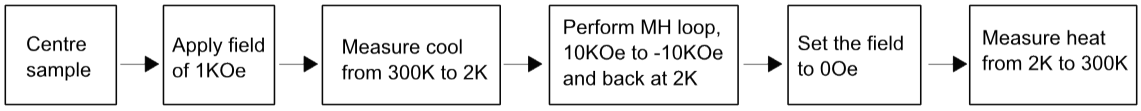

Fig. 2.16 Standard measurement procedure for SQUID measurements performed in this thesis. When the field is set to 0Oe there will remain a small field or measurement would not be possible.

2.3.2 Magneto Transport

Transport measurements of materials are used to measure properties such as carrier concentration, mobility and phase transition temperatures. The conductivity can be described by the free electron model of a metal. By applying an electric field (**E**) to a metal the Fermi distribution of electrons and the occupation probability for an electron are no longer equivalent. By considering the electron movement as that of a wave packet, the classical equation of motion for an electron is 2.7 where m_e is the mass of an electron is:,

$$m_{\mathrm{e}}\frac{d\mathbf{v}}{dt_0} = -e\mathbf{E} - e\mathbf{v}\times\mathbf{B} \tag{2.7}$$

where **v** is the velocity, t_0 is the time, e is the charge of the electron and **B** is the magnetic field. In a DC electric field the velocity of an electron is given by

$$\mathbf{v} = -\mu\mathbf{E} = -\frac{e\tau}{m_e}\mathbf{E} \tag{2.8}$$

where μ is the mobility of the electron, which is the product of the electron charge (e), the time between collision (τ) and the inverse of the electron mass. There are several different sources of collisions that can affect τ. Interactions betweenelectrons and thermal lattice vibrations (phonons) is temperature dependent ($\tau_{\text{ph}}(T)$) and in a perfect crystal would be the dominant source of scattering. In an imperfect crystal non temperature dependent interactions (τ_0) occur from structural defects in the crystal and impurities or vacancies in the structure [11]. The total scattering rate can be defined as

$$\frac{1}{\tau(T)} = \frac{1}{\tau_{\text{ph}}(T)} + \frac{1}{\tau_0} \tag{2.9}$$

The conductivity of a material is related to the mobility by

$$\sigma = ne\mu_{\text{e}} = \frac{ne^2\tau}{m_{\text{e}}} \tag{2.10}$$

where n is the carrier concentration of electrons and μ_{e} is the electron mobility. The electrical resistivity is the inverse of the conductivity and combining equation 2.9 and 2.10 gives the temperature dependent resistivity

$$\rho(T) = \rho_{\text{I}}(T) + \rho_0 = \frac{m_e}{ne^2}\left(\frac{1}{\tau_{\text{ph}}(T)} + \frac{1}{\tau_0}\right) \tag{2.11}$$

This is known as Mattheisen's rule, where ρ_{I} is the ideal resistivity of a perfect crystal and ρ_0 is the residual resistivity from an imperfect crystal. In a semiconductor the equation is more complicated as the mobility of both electrons and holes must be considered. The velocities of

the electron and holes are different so they must be summed together to give the conductivity [12]

$$\sigma = ne\mu_{\mathrm{e}} + pe\mu_{\mathrm{h}} \tag{2.12}$$

where p and n are the respective carrier concentrations of the holes and electrons. The carrier concentration and mobility for a single carrier model can be calculated for a material by the Hall effect. The Hall effect occurs if the current, electric field and applied magnetic field are orthogonal to each other and is defined as

$$\mathbf{E}_{\mathrm{H}} = R_{\mathrm{H}}\mathbf{B} \times \mathbf{j} \tag{2.13}$$

where $\mathrm{R_H}$ is the Hall coefficient. The effect will occur if there are orthogonal components. The orthogonal magnetic field and current (or components of) cause a Lorentz force on the moving charged particles in a magnetic field, which causes the carrier to move to the edge of a material and generates an electric field (E_{H}) tangential to the current (figure 2.17).The forces must balance so the drift velocity perpendicular to the current must be zero so the electric field (E_y) must be equivalent to the Lorentz field generated:

$$\mathbf{E_y} = v_x\mathbf{B_z} = -\frac{1}{ne}j_x\mathbf{B_z} \tag{2.14}$$

The Hall coefficient $\mathrm{R_H}$ is defined as $-\frac{1}{ne}$, which allows the carrier concentration to be calculated. $\mathrm{R_H}$ can then be linked to the conductivity from equation 2.10 by:

$$\sigma = \frac{\mu}{|R_{\mathrm{H}}|} \tag{2.15}$$

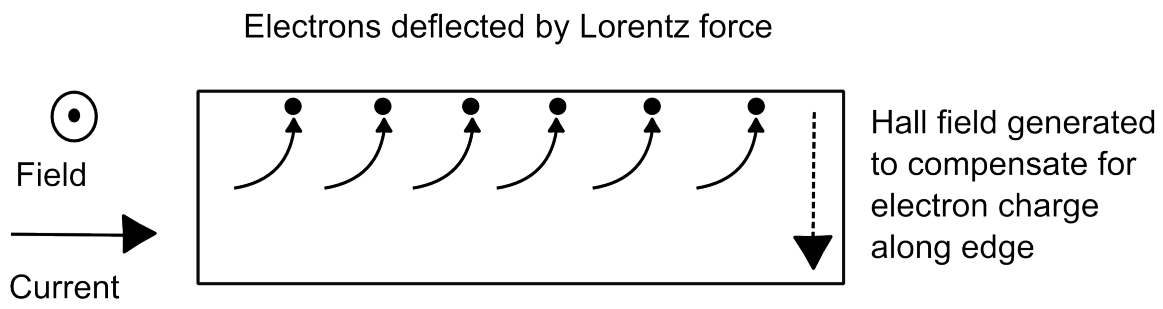

Fig. 2.17 Schematic showing the generation of the hall effect. The charged particles moving in an electric field are deflected to the edge of the material. This causes a build up of charge along one edge and a Hall field is generated to compensate

However in a two carrier model the different concentrations and mobilities of the holes and electrons must be considered and using equation 2.12 the R_H is [11]

$$R_H = \frac{\left(p\mu_h^2 - n\mu_e^2\right)}{e\left(p\mu_h + n\mu_e\right)^2} \tag{2.16}$$

R_H is the Normal Hall Effect (NHE) which will cause a linear gradient between the resistance vs field. However in FM materials an Anomalous Hall Effect (AHE) is also observed, which is also linear but with a steeper gradient at low fields until it reaches a maximum at some higher field, above which it remains at the same value. The AHE is dependent on the magnetization (M_Z) of the sample and has the Anomalous Hall coefficient (R_A). As the strength of the field increases the magnetic domains within the layer align with the magnetic field until a saturation field where all of the domains are aligned with the applied field. The NHE and AHE combine to cause resistance vs field measurements of the kind sketched in figure 2.18, which demonstrate the empirical formula

$$R_{xy} = R_H B_Z + R_A M_Z \tag{2.17}$$

for the $\mathbf{R_{xy}}$ of a ferromagnet [117]. There are many theories about the cause of the AHE with the likely sources being a combination of skew scattering, phonon scattering and side jump

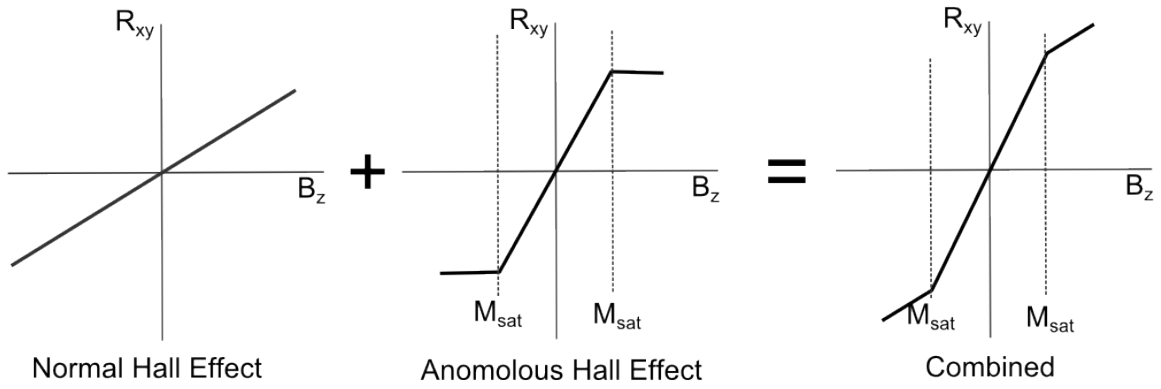

Fig. 2.18 Schematics of the NHE(left) and AHE(middle) with field dependence and the resulting measurement for the two effects (right). Both Hall effects are linear in field. The gradient of the AHE is steeper, and reaches a constant value.

scattering [117, 118]. Skew scattering is where the spin orbit interaction causes the electron to be asymmetrically scattered from an impurity. In side jump scattering the electron path shifts around an impurity and continues on a parallel path, the scattering is caused from spin orbit coupling with impurities. The value of the scattering factor, η, can be indicative of the dominant type of scattering. The η is found from

$$R_{\mathrm{A}} \propto R_{xx}^{\eta} M \tag{2.18}$$

Depending on the dominant scattering mechanism η is predicted to have a value between one and two. If side jump scattering is dominant then there will be a η of two, if skew scattering from impurities is dominant there is a predicted η of one and if phonon scattering is present then η will increase towards two [117].

Vector Magnet

An Oxford Instruments vector magnet system is used in this report to measure the magneto-transport of samples. This system has the capability to measure samples between 4K-350K and is cooled and heated by allowing helium through a needle valve with a heating element attached and a thermocouple located near by. One of thermocouples is located near the needle

valve and the calibration for the PID setting are for this thermocouple and use it's reading for feedback to the heater. The sample rod has a thermocouple located near the sample holder to measure the temperature of the sample. The vector magnets system was able to apply a field of 6T in the out of plane (z direction). It also had the capability of applying a field of up to 2T in any x,y,z direction.

High temperature system

A vacuum system was designed in-house to heat and measure transport samples in high vacuum conditions to avoid degrading materials by oxidation whilst heating them above room temperature. The system has two mounting positions of in plane and out of plane to a 0.4T rotatable electro magnet. The sample space was pumped by a turbo pump and had a background pressure of 1×10^{-6}Torr.

The samples were heated by a halogen lamp encased in copper to allow the heat to transfer both radiatively and conductively to the samples. The heating was controlled by a Eurotherm temperature controller, with a type T thermocouple located adjacent to the out of plane mounting. Type T was chosen due to the appropriate temperature range and non magnetic properties [119]. Samples were mounted on machinable ceramic sample holders using silver paint. A platinum resistance thermometer was mounted onto each sample holder and connected in series with the sample to measure the sample temperature independently of the thermocouple. Aluminium bond wires connected the sample to brass pins in the ceramic holders. The brass pins were secured by friction and silver paint into their mounting holes. The ceramic holders were designed to minimise the out gassing in the vacuum chamber.

Samples were measured in four terminal mode with an applied current of 50-100μA. Four terminal resistivities were measured with a series of measurements being made for opposing currents to eliminate DC offsets, as shown in the flow chart in figure 2.20. The DC offsets were caused by thermal voltages generated by the temperature differences along the

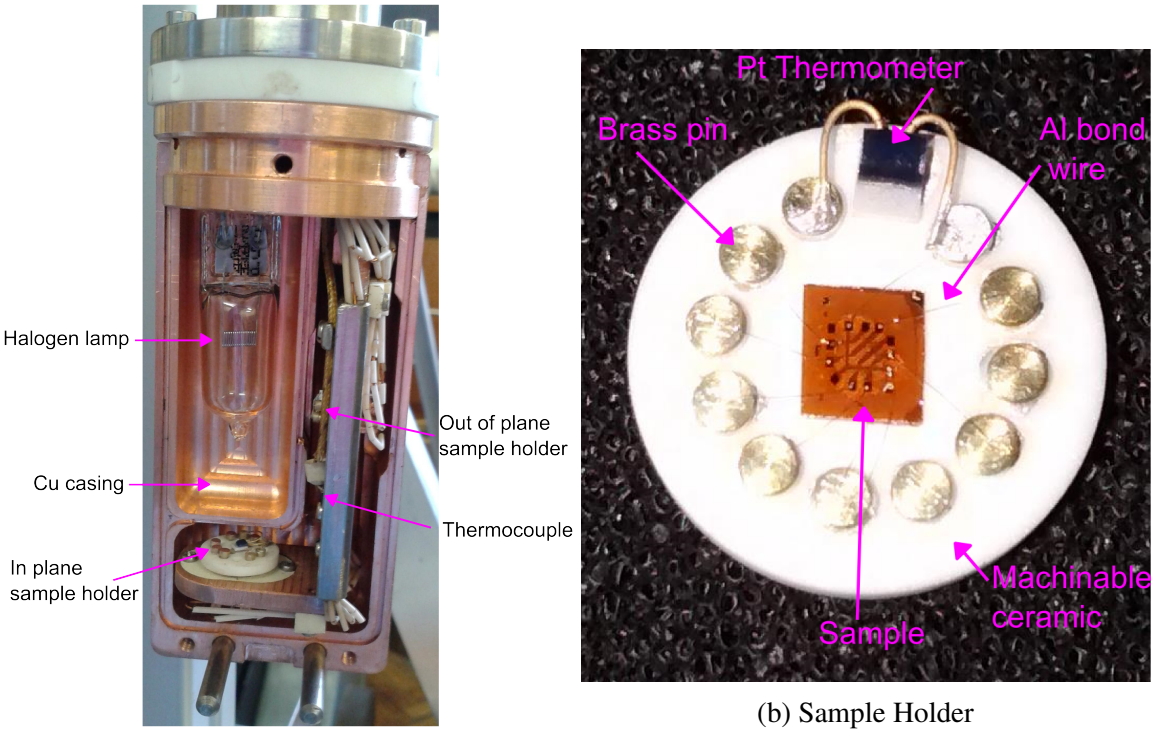

(a) Sample environment

(b) Sample Holder

Fig. 2.19 Pictures of the sample environment and ceramic sample holder for the high temperature system. (a) shows the sample holder with half of the casing removed. (b) shows a sample mounted on a ceramic sample holder.

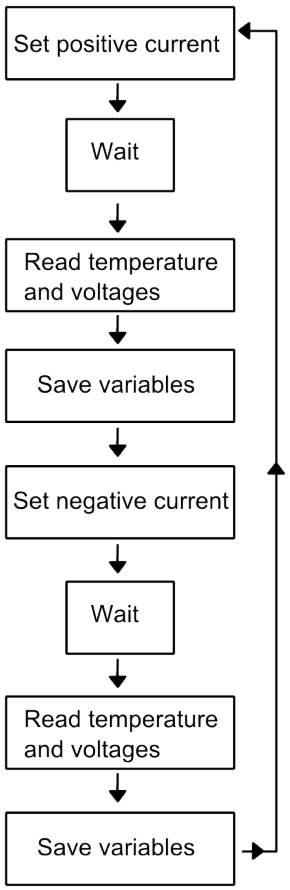

Fig. 2.20 Flow chart showing the measurement procedure for the mock AC measurements in the high temperature system.

length of the cables. The ramp rate for heating the system was typically 0.5K/min to create a steady heating regime. The system was cooled radiatively by rapidly decreasing the set point so that power was turned off to the heat source. This mode of cooling was chosen as in a slow cooling regime heat spikes would appear in the derivative of the temperature as the heater initially struggled to control the rate of cooling.

Due to the large amount of data accumulated in each temperature run it was necessary to perform several data processing steps. The data was first trimmed to exclude the initial and final regions where the temperature had either been static or had been increasing in a non linear manner as the power of the heater varied as the PID settings reacted to the system temperature lagging behind the set point as power was applied. When the system does not

respond quickly enough the PID settings will increase the power to the heater and when the system begins to heat and overshoots the working set point the PID will decrease the power. The data was then sorted into wider temperature bins and the mean value for each bin calculated. A piecemeal interpolation was then applied along with a smoothing function so that the data size was reduced to make features more visible. These parameters for these three techniques could be varied. The temperature derivative of the resistivity was then calculated.

Device fabrication

Devices for transport measurements were patterned on wafers of CuMnAs by photo lithography and wet etching. Samples without a protective capping layer were first exposed to a developer solution of AZ400K:H_2O (1:4) for 10 seconds to remove the top surface as previous attempts at fabrication on this material had found that the material etched unevenly. A positive photo resist was spun on to device chips, typically a resist such as BPRS150 was used, followed by a 70$^{\circ}C$ bake on a hot plate for seven minutes. Exposures were performed on a UV mask aligner using glass and chromium masks. An appropriate exposure time for the photo resist was used (approximately six seconds), based on the manufacturers guidelines. The sample was then developed in the recommended concentration of AZ400K developer, of 1:9 AZ400K: H_2O. This left the layer with the device design covered in resist and the rest of the chip exposed. Samples were wet etched with a solution of orthophosphoric acid, hydrogen peroxide and water H_3PO_4:H_2O_2:H_2O. The reagent ratio of 1:10:800 had a CuMnAs etch rate of 2nm/s. There was a difference between the etch rates of this solution for CuMnAs and GaP. The etch rate on GaP was so small as to be undetectable for the etch times used. The etch rate was determined by using a step profiler. For layers of CuMn($As_{(\mathbf{1-x})}P_{\mathbf{x}}$) it was necessary to alternate the etchant between H_3PO_4:H_2O_2:H_2O and HCl as a dark residue was left behind from the H_3PO_4:H_2O_2:H_2O etch. The resit was removed by soaking in acetone. Where used, contact pads of 20nm Cr and 100nm Au were patterned using the same

Device	Figure	R_{xx} length (μm)	Channel width (μm)
Large Hall bar	2.21c	750	250
Phillips Hall bar	2.21a	310	50
L-bar	2.21b	400	100

Table 2.1 Dimensions of different Hall bars fabricated.

photo-lithographic procedures for coating with a positive photo resit, UV exposure and resit development. After the resist was developed the only area exposed were the regions to be the contact pads, the rest of the chip was covered in resit. The metal was deposited using metal evaporators with a background pressure of 10^{-6}Torr. A selection of devices were used for measurements in this thesis, typically of a Hall bar or L-bar geometry. An L-bar consisted of two orthogonal Hall bars joined together at one end, example pictures are shown in figure 2.21, with example dimensions in table 2.1.

2.4 Surface Measurement Techniques

2.4.1 Atomic Force Microscopy

AFM is a widely applicable technique for non destructively measuring the topography of a surface [120]. The technique is sensitive to sub nanometre scale changes in the height of a surface. A schematic of a typical AFM is shown in figure 2.22 where a cantilever with an atomically sharp tip is moved across a surface to form an image. The tip will trace a path back and forth along one line before advancing to the next line. The image is formed from a combination of the forwards and backwards lines. Piezoelectric actuators are used to control the position of the sample and the tip height. A feedback loop between the tip height and the control program is used to adjust the height. If the shape of the tip is wider than the feature that is being imaged the image of that feature will become blurred as the tip width smears the feature, which is why atomically sharp tips are used.

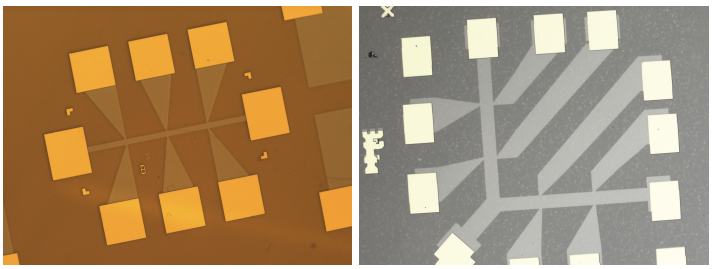

(a) Phillips Hall bar (b) L-bar

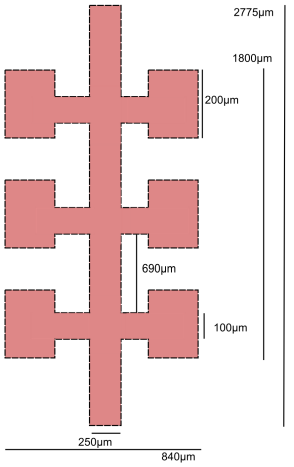

(c) Large Hall bar

Fig. 2.21 Photographs or schematics of the different designs of Hall bar used in this thesis.

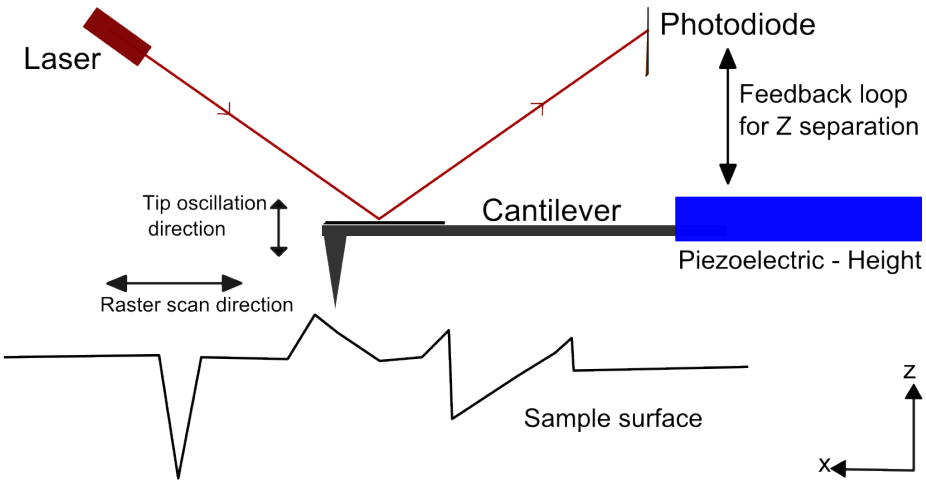

Fig. 2.22 A simplified schematic showing the set-up for AFM imaging in tapping mode. The laser path is shown in red as it reflects of the cantilever.

There are a variety of modes that the cantilever tip can be controlled in to form the image and these utilise different tip - sample interactions. This thesis will only discuss amplitude modulated (tapping mode) AFM [120] for measurements performed in air on solid surfaces.

In amplitude modulated AFM the tip is oscillated just off the resonant frequency of the cantilever. The frequency of oscillation is chosen as just off resonance so that the effect of any changes in the oscillating frequency cause the maximum change in the amplitude. As the tip approaches the surface it is initially weakly attracted to the surface by van der Waals before being repelled by short range Pauli forces [121]. When the height of the surface changes, the tip-surface distance will change along with the force experienced by the tip. The change in the force alters the amplitude of oscillation will change and the feedback loop will adjust the height of the sample to achieve the same amplitude and tip-sample separation.

AFM Image Processing Protocols

In some work in this thesis it is necessary to determine the proportion of material that has been lost forming a crevice or has risen above the surface as inclusions. Images were flattened and the colour scale limited in Gwyddion [122] before being further analysed using Matlab.

For this process there were two different protocols depending on the area covered by the material that are shown in figure 2.23. A threshold to define the surface is either calculated from the mode value of the gray scale or chosen manually. Figure 2.24 shows the effect of changing the threshold bounds on the percentage. The higher the threshold value used the more of the surface is deemed to be a hole. Having a threshold of the mode value and 30% below the mode value the percentage of missing material changes from 47.5% to 14.1%. From comparing by eye the image with the original the most accurate selection of the hole area appears in figure 2.24e. This threshold can then be used as the standard for all the other images. In some cases a human judgement call was used and a different threshold (eg 20%

below the mode value) will be set if it provides a better representation of the data. For each sample a range of image sizes were analysed from random locations on the sample.

2.4.2 Magnetic Force Microscopy

MFM uses an experimental set-up similar to AFM. The main difference between the techniques is in the tip and operation. The tip of a MFM cantilever is covered in a FM material [123] and a measurement is made by performing a standard AFM topography scan before increasing the tip - sample separation ($\sim$ 50nm) and re-scanning the tip. A magnetic image is built up by the magnetic forces on the tip far away from the range of the Van Der Waals interactions.

The MFM tips used in this thesis were designed to only be sensitive to stray magnetic fields that are in the direction of out of plane of the sample. Depending on the direction of the magnetic forces, either attractive or repulsive to the tip, the area will appear as either light or dark. Areas with no magnetic field will appear as gray.

2.5 Conclusion

This chapter has described the different growth and characterisation methods that have been used in this thesis. Chapter 3 and chapter 4 will use MBE to grow the samples described and several techniques to characterise the layer including XRD, neutron diffraction, SQUID magnetometry, AFM and MFM. In chapter 5 and 6 magneto transport measurements will be made for a a variety of samples.

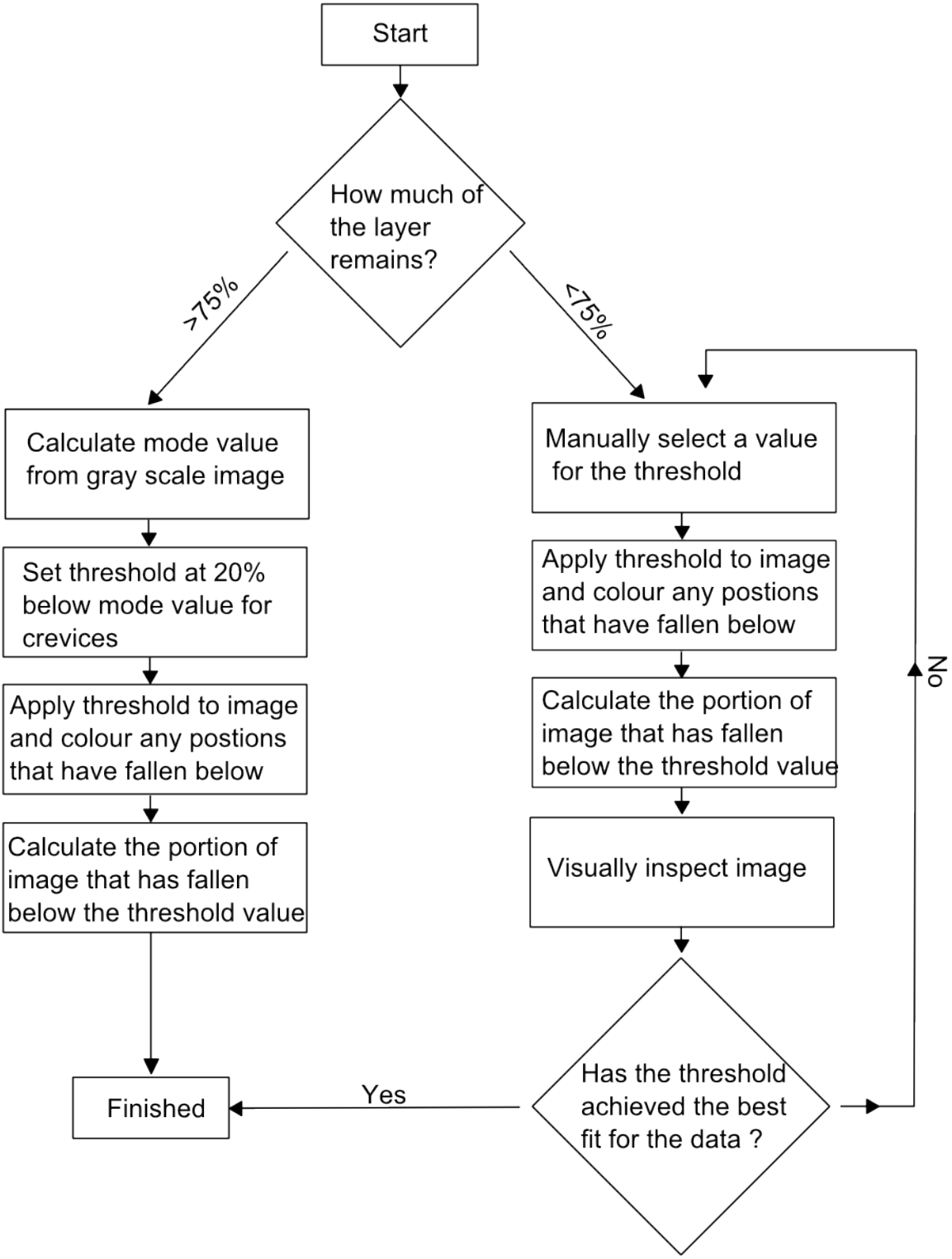

Fig. 2.23 Flow chart showing the steps for processing a grey scale AFM image. The software was designed to remove any borders from the image analysis software which could have skewed results.

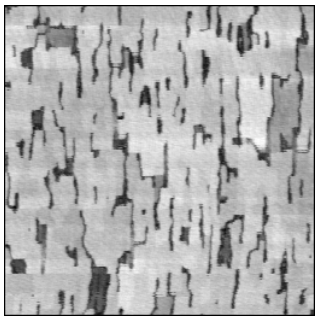

(a) Unprocessed image

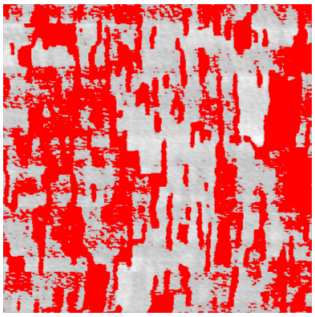

(b) Threshold set at the mode value. 47.5% of the surface is missing.

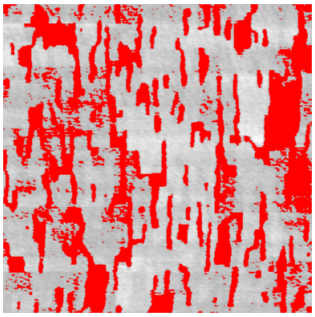

(c) Threshold set at 5% below the mode value. 33.0% of the surface is missing.

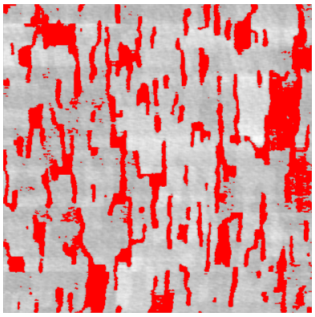

(d) Threshold set at 10% below the mode value. 25.34% of the surface is missing.

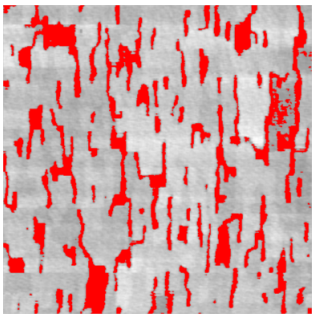

(e) Threshold set at 20% below the mode. 18.23% of the surface is missing.

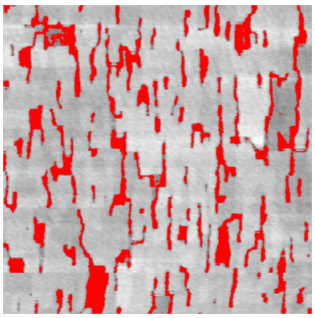

(f) Threshold set at 30% below the mode value. 14.09% of the surface is missing.

Fig. 2.24 An example of the difference in the percentage of a layer that is holes by changing the threshold value used on a single image. The image used is of a 4nm CuMnAs film with 2nm Al cap. The image has the lateral dimensions of $1.5\mu\text{m}\times1.5\mu\text{m}$.

Chapter 3

Characterisation and Growth of Copper Manganese Arsenide

3.1 Introduction

The growth of epitaxial CuMnAs grown by MBE and investigations into the structural, magnetic and surface properties of thin film CuMnAs will be covered in this chapter. There will be a discussion of the growth conditions needed to grow high quality stoichiometric tetragonal CuMnAs on GaAs and GaP substrates and the differences in growth conditions used to grow non-stoichiometric CuMnAs. Then we will look at the properties of stoichiometric CuMnAs on both substrates, by studying the crystal structure by XRD, the magnetic structure by neutron diffraction, the external magnetic properties by SQUID, and the surface characteristics by AFM and MFM.

Non-stoichiometric CuMnAs will then be investigated by similar techniques to study the effects of a secondary FM phase that is observed in the layer and the possible percentage of the FM phase will be estimated using three different methods.

Finally we will look at growing ultra thin (sub 10nm) films of CuMnAs on GaP. There will be a discussion of the technical problems with growing these layers and into different

growth and nucleation methods to improve the layer quality. The surfaces of the ultra thin films will be mainly characterised by AFM, but will also look at the structural and external magnetic properties in some samples by XRD and SQUID.

3.2 MBE growth of CuMnAs

This section will detail the growth conditions for CuMnAs on the III-V semiconductors GaAs and GaP. A discussion of the previous work and theory on CuMnAs is detailed in section 1.2. Initial work by R.P. Campion, V. Novàk and XRD by P.Wadley, established the stoichiometric conditions for CuMnAs [39]. The samples discussed in this section are listed in Table 1 and Table 2.

3.2.1 Growth of stoichiometric CuMnAs

Stoichiometric samples of CuMnAs were grown with a flux ratio of 1:1:1.2 for Cu:Mn:As, which resulted in an incorporation ratio of 1:1:1. For either III-V substrate (GaAs or GaP) a high temperature buffer layer of undoped GaAs or GaP was grown to improve the quality of the substrate surface after oxide removal had been observed on the RHEED. For both substrates RHEED and LAOS was used to establish the quality of the surface. The growth conditions and expected observations for GaAs and GaP are well established [87]. The CuMnAs layer was grown at a T_{sub} of $280^{\circ}C$. The T_{sub} was ideally measured using band edge temperature measurements, which was possible for all GaAs samples and some GaP samples, otherwise the thermocouple temperature was used as the T_{sub}. As the film grew the temperature of the sample would increase due to the increased free carrier absorption of the CuMnAs compared to the substrate. The CuMnAs is also strongly absorbent of the incident light and as the layer becomes thicker the band edge signal tends to decrease until it is no longer possible to measure. An example of this is shown in figure 3.1 where the intensity of

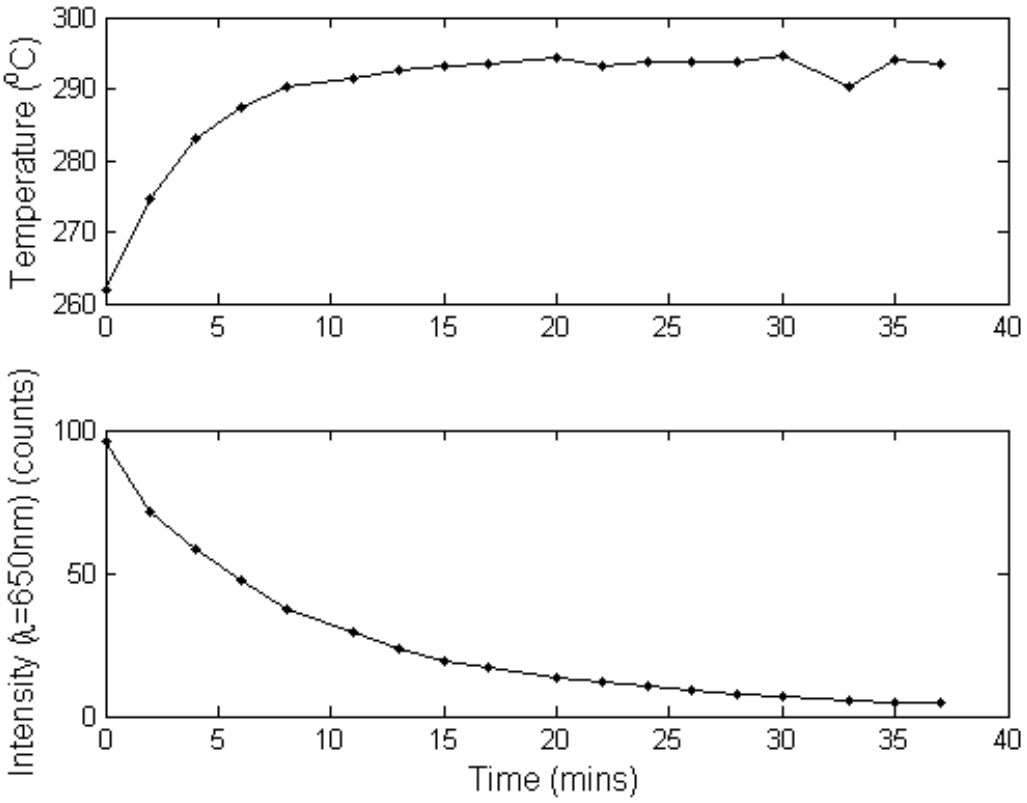

Fig. 3.1 Band edge measurements of a layer of CuMnAs grown on semi-insulating GaP (100) (Sample:1-5). The top figure shows the temperature measured against time and the bottom figure shows the intensity of the signal, at a wavelength of 650nm, against time.

the signal continually decreases with time. The loss of signal also means that the temperature measurement has a larger inaccuracy.

All of the CuMnAs samples were grown at 46nm/hr, which was the calibrated growth rate from a previous sample measured by X-ray reflectivity.

When CuMnAs is grown on GaAs it is necessary for the lattice to relax as it grows. The transition from strained to relaxed growth could possibly be visible in the RHEED, as soon after the growth begins the RHEED pattern will become very disperse before sharpening up as the growth progresses. On GaP the layer remains fully strained, as the difference in the lattice parameters is less, as shown in table 3.1. On GaP a 2x2 RHEED pattern is seen during the growth of CuMnAs that becomes stronger throughout the growth.

Material	Unit cell	a(Å)	b(Å)	c(Å)
GaAs	Zinc blende	5.6533	5.6533	5.6533
GaP	Zinc blende	5.4505	5.4505	5.4505
CuMnAs (relaxed)	tetragonal	3.820	3.820	6.318

Table 3.1 The lattice parameters for GaAs, GaP and relaxed CuMnAs. Values from [39, 124]

	Copper (Torr)	Manganese(Torr)
Stoichiometric	4.9×10^{-9}	7.4×10^{-9}
Non-stoichiometric	3.3×10^{-9}	7.4×10^{-9}

Table 3.2 BEP used in MBE growth of CuMnAs for stoichiometric and non-stoichiometric samples.

3.2.2 Growth of non-stoichiometric CuMnAs

Whilst establishing the stoichiometric ratio for CuMnAs R. Campion and V. Novâk grew a series of samples with different growth ratios. The sample to be discussed was part of that series (Sample:2-1) and was grown with different BEP ratio to a stoichiometric sample, with the fluxes listed in table 3.2. This corresponds to a growth ratio of 1:1.48 for the Cu:Mn. The arsenic is not listed as it was applied with an overpressure so it does not limit growth.

Sample:2-1 was grown on a GaAs substrate at the assumed growth rate of 46nm/hour for a thickness of 337nm. The growth was started with a T_{sub} of 300°C, which then varied by $\pm$10°C during the growth. The growth rate is for stoichiometric CuMnAs but the volume of CuMnAs is expected to be similar.

3.3 Characterisation of stoichiometric CuMnAs

In this section a range of different stoichiometric samples will be examined using several different techniques. The samples are listed in table 1 in the list of samples used in this thesis.

Shape	Lateral dimension	Vertical dimension	RMS misalignment
Elipsoid	50nm	20nm	1.5°

Table 3.3 Parameters of mosaic block model fitted to CuMnAs/GaAs [39]

3.3.1 Characterisation of the layer structure

Determination of crystal structure by XRD

XRD measurements were performed by P.Wadley on the system described in section 2.2.1. XRD established that epitaxial CuMnAs formed a tetragonal rather than orthorhombic unit cell with the relaxed lattice parameters of $a = b = 3.820$Å and $c = 6.318$Å.

As detailed in P.Wadley et al. [39] and shown in figure 3.2, which compares the CuMnAs(003) diffraction peak for layers grown on GaAs and GaP it is clearly visible that the sample on GaAs has a markedly broader peak with a larger reciprocal space map. The larger Full Width Half Maximum (FWHM) of this peak signifies that there are smaller crystallites of CuMnAs in the layer. These can be fitted to a mosaic block model with the parameters listed in table 3.3. However for CuMnAs/GaP there is a significantly sharper diffraction peak in the $2\Theta/\omega$, which represents an improved crystal quality due to the smaller lattice mismatch with the substrate and layer.

Determination of the magnetic structure from neutron diffraction

Neutron diffraction is a key method for probing the magnetic structure in AF materials as discussed in section 2.2.2. Two different experiments were used to determine the magnetic structure of CuMnAs at two different facilities. At the ILL (section 2.2.2) a 500nm film of CuMnAs on GaP (Sample:1-2) was studied in a cryofurnace with a He atmosphere. A cryofurnace uses a flow of helium through a needle valve to heat the chamber inside above room temperature in a controlled manner. The work was performed by P. Wadley,

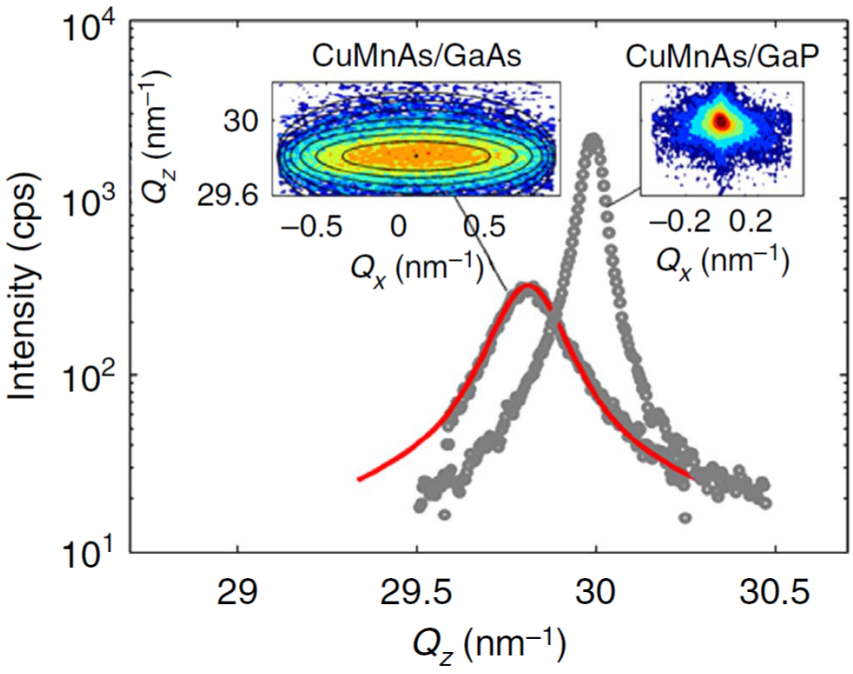

Fig. 3.2 $2\Theta/\omega$ scans of CuMnAs/GaAs and CuMnAs/GaP showing the difference in the crystallite size for the (003) diffraction peak. The CuMnAs/GaAs has a red line denoting the fit of a mosaic block model. The insets show the (003) reciprocal space maps. Image taken from P.Wadley et al. [39].

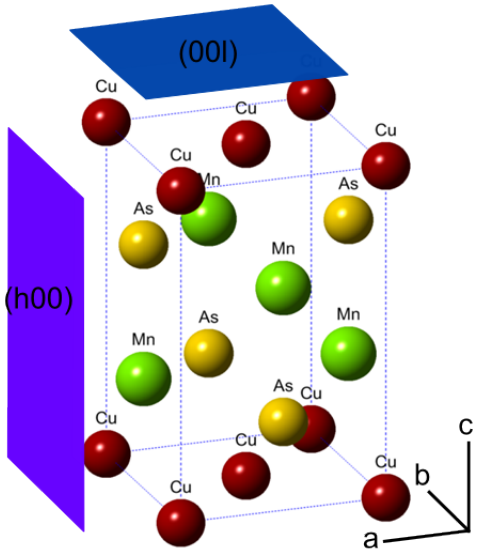

Fig. 3.3 Diagram of how the (h00) reflection, lilac, and the (00l) reflection, blue, relate to the unit cell of CuMnAs.

B. Ouladdiaf and the author. At ISIS Sample:1-3 was studied in vacuum and the work was carried out by S. Langridge, D. Khakyavin, P.Wadley and the author.

For tetragonal CuMnAs grown on GaP(001) two peaks were studied using neutron diffraction, the (100) diffraction peak, which is a purely magnetic signal as the nuclear component is structurally forbidden for the *P4/nmm* space group and the (001) peak, which contains both a nuclear and magnetic component. These two peaks are part of the (h00) and (00l) families respectively and figure 3.3 visualises how these planes relate to the unit cell of CuMnAs. For either direction the intensity of the diffraction peak from the magnetic components is sensitive to the magnetic moments that are aligned perpendicular to the scattering vector. The (h00) family is sensitive to magnetic projections aligned out of plane to the CuMnAs(100) and perpendicular in plane, which is also the *bc* plane. The (00l) family is sensitive to magnetic projections that are aligned in either in-plane direction, to the CuMnAs(100) which is the *ab* plane.

Figure 3.4 shows examples of the raw data from each diffraction peak. It is clear that a peak forms in each direction and that this is temperature dependent. The horizontal axis

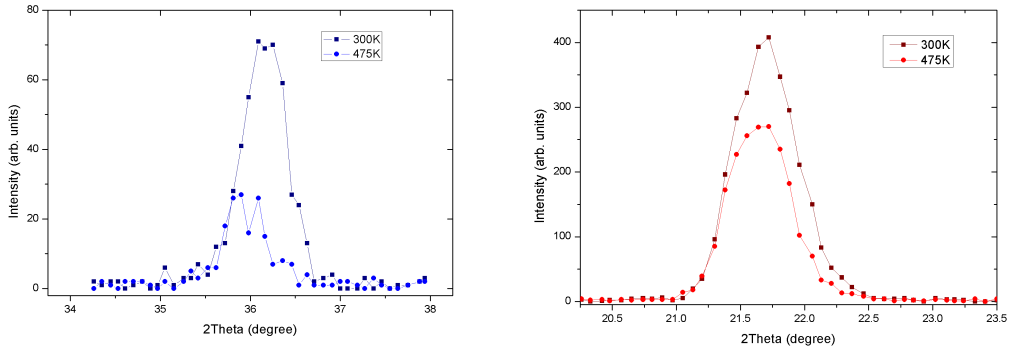

(a) (100) (b) (001)

Fig. 3.4 Unprocessed neutron diffraction data showing the difference between the diffraction peak measured at 300K and 475K. Measurements performed on 500nm stoichiometric CuMnAs (Sample:1-2).

for figure 3.4 is the 2θ angle between the incident and scattered beam. The vertical axis corresponds to the number of neutrons incident at the detector. The low interaction rate between neutrons and the sample means it was necessary for one million neutrons to be incident on the sample for every point on the figure.

The (100) diffraction peak is entirely magnetic so at higher temperatures the peak has significantly decreased, figure 3.4a, due to the temperature dependence of the magnetic ordering. The remnant peak is from $\lambda/2$ contamination. The monochromator allows through some wavelengths of a higher order which causes extra diffraction peaks to contribute to the signal.

For the (001) reflection, figure 3.4b, the peak has a nuclear and magnetic contribution, at the higher temperature the magnetic contribution disappears. The nuclear peak has a very weak temperature dependence and is neglected in the analysis described below. The nuclear component is from the CuMnAs (220) diffraction peak.

Figure 3.5 shows a wider range of temperatures and a slow decrease in the intensity with temperature for both peaks. The larger overall intensity of the (001) peak means that there is a smoother shape to the diffraction peaks as it has a large signal to noise ratio where as the (100) peaks have a smaller signal to noise ratio.

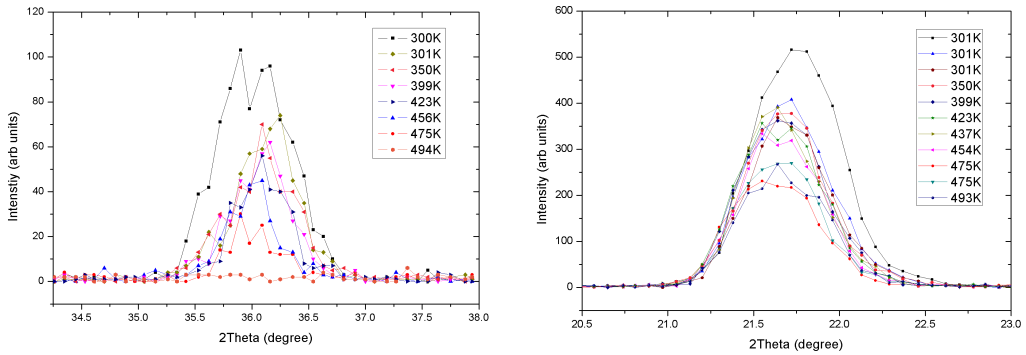

(a) (100) (b) (001)

Fig. 3.5 Unprocessed neutron diffraction data showing the results for several different temperatures overlaid. The legend is arranged in temperature order and not chronological order. Measurements performed on 500nm stoichiometric CuMnAs (Sample:1-2).

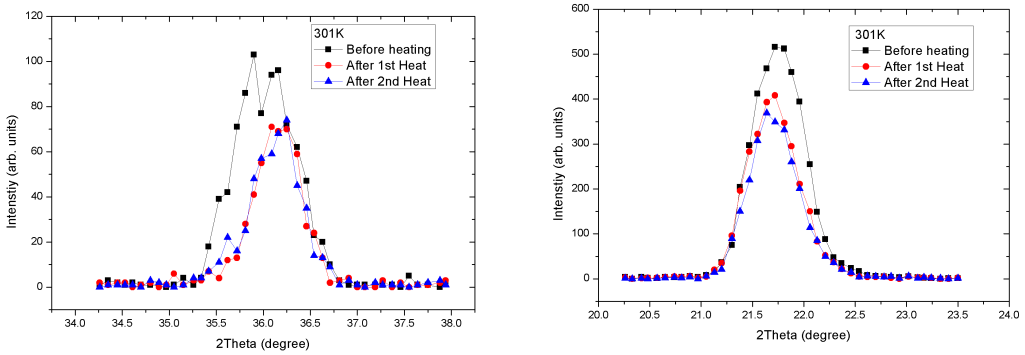

(a) (100) (b) (001)

Fig. 3.6 Unprocessed neutron diffraction data showing the effect of heating cycles on the (001) and (100) diffraction peaks when remeasured at 300K. Measurements performed on 500nm stoichiometric CuMnAs (Sample:1-2).

Another significant feature that is highlighted in figure 3.6 is that there is a change in the size and shape of the diffraction peak after the sample has been heated. The change in shape, which is clearest in the (100) (figure 3.6a).

The intensity was analysed by fitting a Gaussian curve to the intensity against 2θ and calculating the area underneath the curve. A typical fitting is shown in figure 3.7. The area for a specific temperature is then calculated as a percentage of the area for the initial 300K temperature measurement for each reflection, so the change in magnitude of the diffraction peak can be compared between temperatures. The reflections were measured sequentially and the temperature remained stable throughout each measurement. There was a minor (3K) temperature offset between the two measured reflections, which does not affect the results significantly.

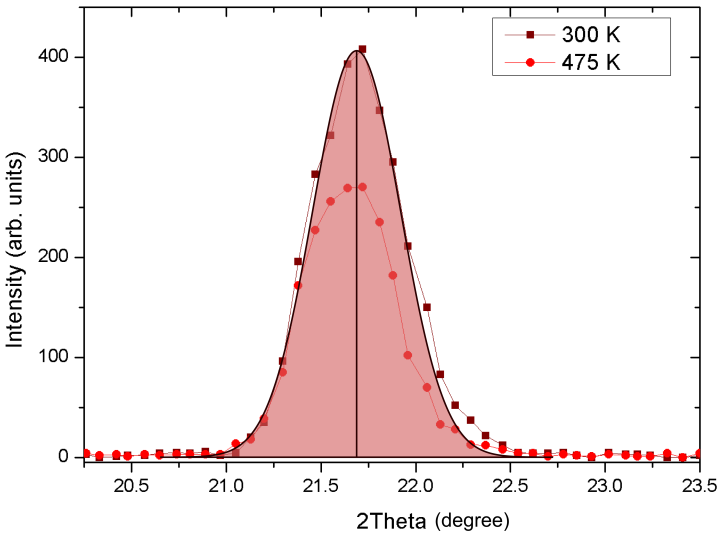

Fig. 3.7 A representative demonstration of fitting a curve to the data (300K data set fitted to) to calculate the area underneath. Light pink fill denotes the area.

The sample was grown at around 550K and the magnetic ordering was shown to be absent above 500K in a single prior neutron measurement [39], which implies that the layer has undergone a phase transition, probably into a paramagnetic state. The sample was first heated

to 480K where the magnetic peak disappeared however on cooling to 300K the magnetic signal was only partially recovered, figure 3.8a & figure 3.9a.

From the raw data (figure 3.6) the largest peak represents the first measurement at 300K and the other measurements around 300K were performed after heating, it is clear that the post heating measurements have a smaller overall intensity, which is reflected in the integrated percentage intensities (figures 3.8 & 3.9). For the (100) reflection only 55% of the signal was recovered on returning to 300K. The material may have degraded in the contaminated helium atmosphere as it was heated causing a change in the magnetic signal. For the (100) reflection only 20% of the signal was recorded at 480K. Whereas the (001) follows a similar pattern but due to the nuclear contribution reduces to 50% and recovers to 75%.

When the temperature was pushed to 500K the (001) intensity remains constant implying that the T_N had been surpassed. At this temperature the (100) reflection shows a slight decrease which could be due to sample degradation. The sample was held in a helium environment, but when removed from the system, it was apparent that a physical change had occurred in the sample as it had a reddish tint, supported by a huge loss in the nuclear peak. When the sample was heated above 500K the magnetic signal became irrecoverable on cooling down, indicating that there was a loss or change of behaviour in the magnetic order.

After the sample was heated once it remained structurally stable without further degradation during subsequent heating and cooling measurements, which also demonstrates the repeatability of the magnetic transition and that the transition was consistent for both heating and cooling, as demonstrated in figure 3.8a & figure 3.9a. In figure 3.9b the apparent decrease in the intensity between 300K-400K could be due to a reordering of the moments into an undetected direction as the scattering vector is insensitive to moments that are aligned parallel to it.

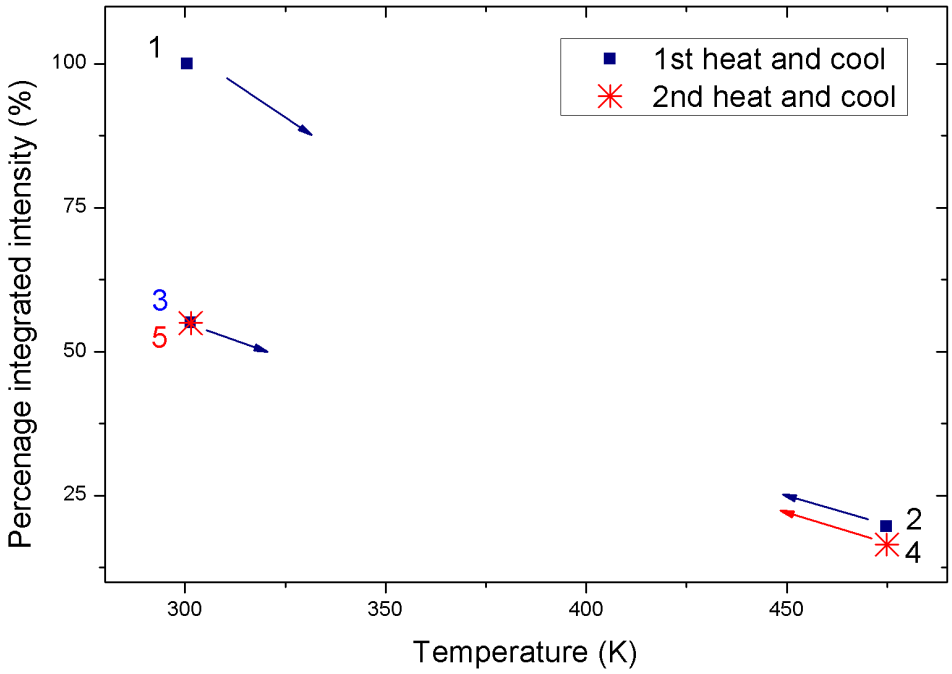

(a) Path of heat cycling

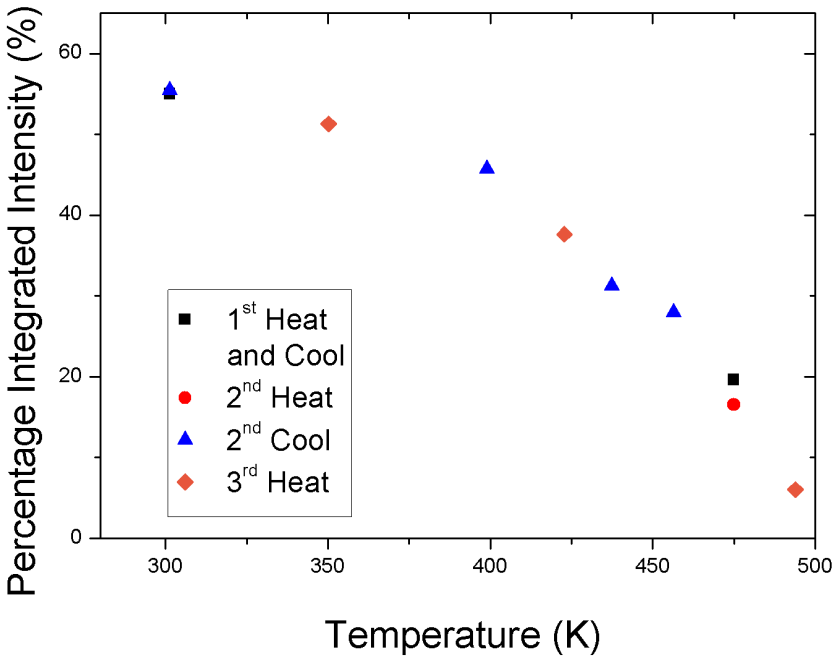

(b) All temperatures

Fig. 3.8 The top figure shows the path of the heating cycles and effect on the percentage integrated intensity for the (100) peak in neutron diffraction. The bottom figure shows all the measured points for the heat cycles together. Measurements performed on 500nm stoichiometric CuMnAs (Sample:1-2).

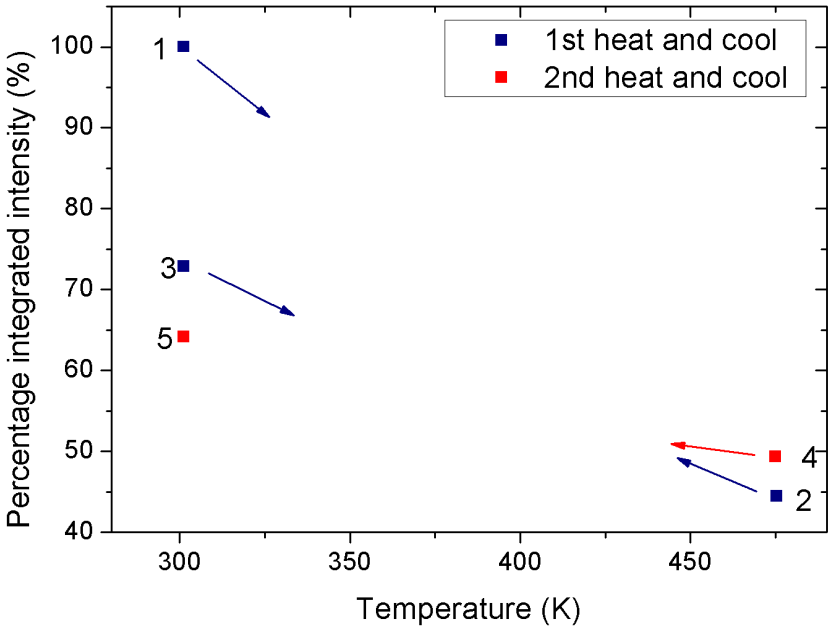

(a) Path of heat cycling

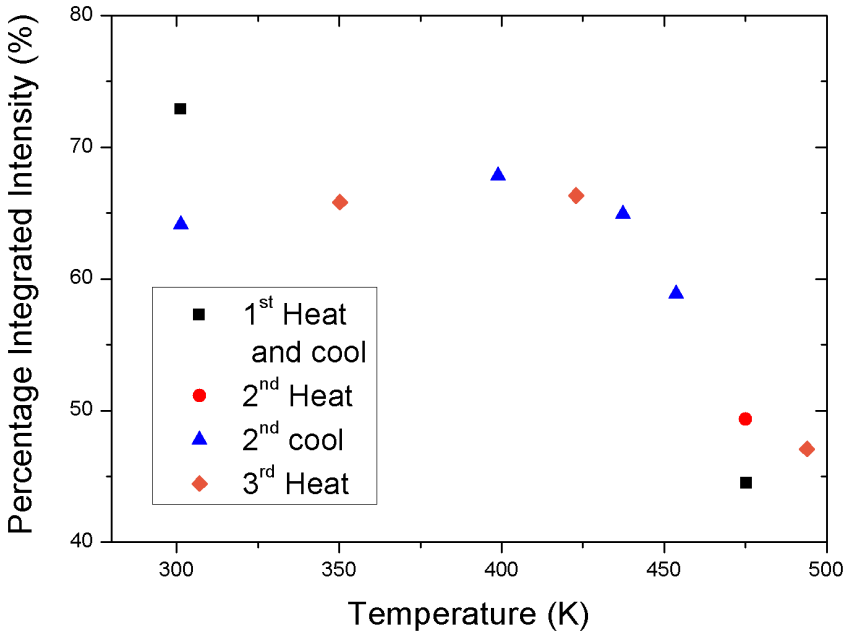

(b) All temperatures

Fig. 3.9 The top figure shows the path of the heating cycles and effect on the percentage integrated intensity for the (001) peak in neutron diffraction. The bottom figure shows all the measured points for the heat cycles together. Measurements performed on 500nm stoichiometric CuMnAs (Sample:1-2).

By fitting a function of the form

$$I = \alpha(T_{\mathrm{N}} - T)^{\beta} + c \tag{3.1}$$

where α, β and c are constants, to the different reflections it is possible to extract a T_N. This function is only valid in the range $T < T_N$. Above the value of T_N the value was fixed as the value c in any plots. This function is chosen as it describes the signal decreasing as it approaches the critical temperature until there is no signal at the phase transition. β was extracted from measuring the (100) direction with a value of 0.4037 and used as a constant in calculating the T_N in the other measurements for the (001) reflection and $CuMn(As_{(1-x)}P_x)$ measurements. β is a critical exponent and can be compared to predicted values for the universality class of the material. Materials where second order phase transitions are observed belong to a small number of universality classes, even when the underlying systems are very different [125]. The Heisenberg universality class describes ferromagnetic or antiferromagnetic isotropic magnets [126]. In a Heisenberg system β is predicted to be 0.3689 [126] but values have been observed from 0.34 to 0.44 [126]. The value of β=0.4037 determined from fits to data in figure 3.10 is within that range, suggesting that CuMnAs fits the Heisenberg universality class.

This fit is shown in figure 3.10 which gives a T_N of (480 ± 5)K, where the percentage integrated intensity has been rescaled after the initial heating of the sample.

A 140nm layer (Sample:1-3) of CuMnAs was studied in vacuum at ISIS. This sample showed a similar temperature dependence as the previous sample, measured at ILL. Using the fit expressed in equation 3.1 and a β value from the previous fitting a T_N of (480 ± 10)K can be measured for the (100) direction. The data in figure 3.11 shows the loss of intensity with temperature as the sample was heated. This sample showed some loss of signal after being initially heated but remained repeatable after. There is good agreement between the two

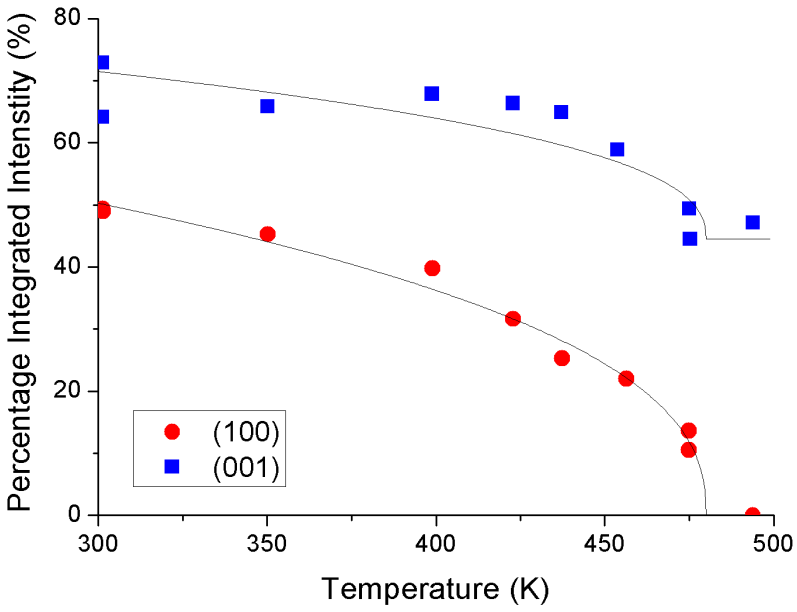

Fig. 3.10 Percentage integrated intensity against temperature for CuMnAs in neutron diffraction. The blue dots represent the (001) reflection and the red dots represent the (100) reflection. Both lines have been fitted to show the calculated T_N. Measurements performed on 500nm stoichiometric CuMnAs (Sample:1-2).

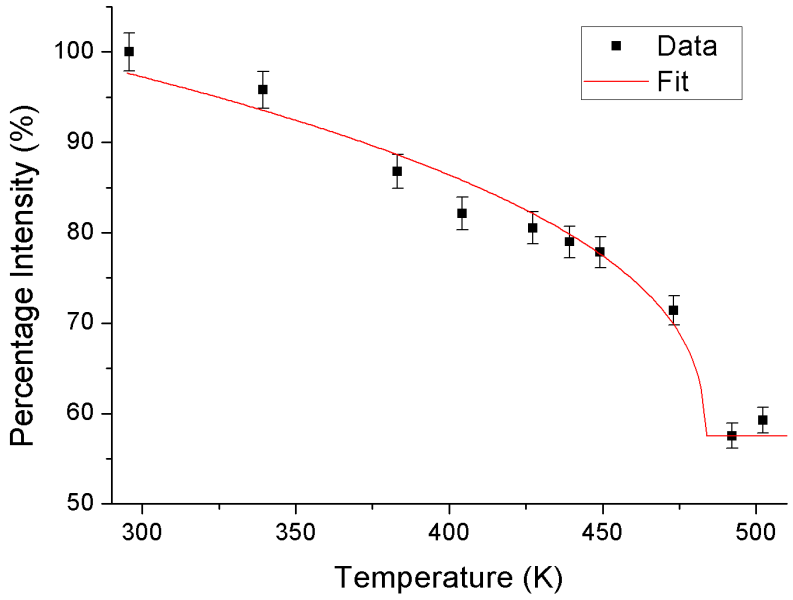

Fig. 3.11 Intensity decrease for neutron diffraction data taken at ISIS on stoichiometric CuMnAs (Sample:1-3) for the (100) reflection. The black dots represent the measured intensities and the red line is the fit to calculate the T_N.

samples measured by neutron diffraction for the T_N and the values lie within experimental error of each other.

3.3.2 Magnetic characterisation by SQUID

Magnetometry measurements were carried out using SQUID on CuMnAs to investigate if there was any ferromagnetic or paramagnetic secondary phases. Figure 3.12 shows the in plane magnetometry measurements for Sample:1-1 with a field cool, with an applied field of 1T, and remanence heat, with no applied field. There are no marked signs of a prominent FM second phase in the SQUID measurements but there is a small diamagnetic signal from the film. There is a small increase in the magnetic moment in the field cool at very low temperatures. In the two hysteresis loops there is no significant gap in the paths at low fields.

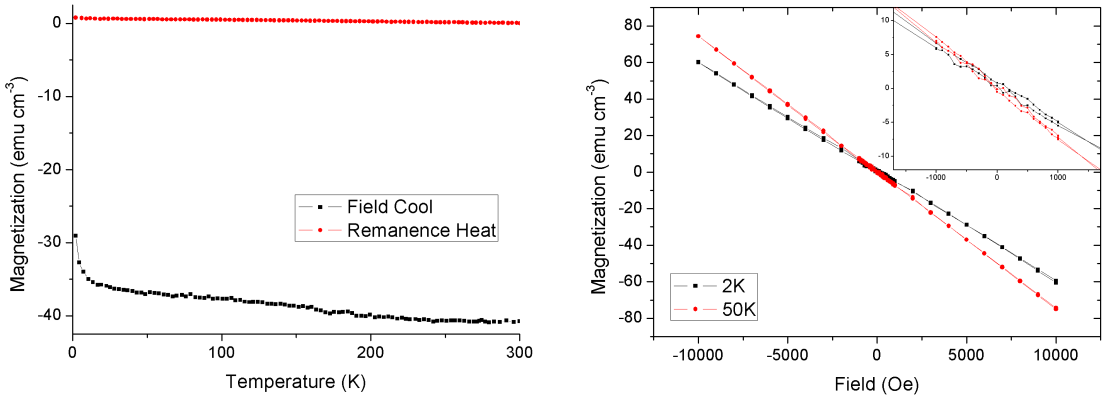

(a) Temperature dependent measurements (b) Magnetic hysteresis loops at 2K and 50K

Fig. 3.12 The projection of the magnetization along an in plane axes from SQUID, results for stoichiometric CuMnAs (Sample:1-1).

The diamagnetic background of the substrate has not been removed which is the large linear trend on the data.

Any paramagnetic phase within the measurement can be estimated by considering the magnetisation of the paramagnetic moment. The magnetisation can be calculated using Hunds rules', which dictate how electrons will fill the atomic orbitals of an atom, and a Brillouin function for the magnetisation (M) it is possible to show that,

$$M = Ng\mu_{\mathrm{B}} J B_{\mathrm{J}}(x) \tag{3.2}$$

where N is the number of Bohe magnetons per unit volume, J is the total angular momentum (5/2) for Mn2+, g is the g-factor that has a value of 2 in this case, and $B_{\mathrm{J}}(x)$ is a Brillouin function defined as [11],

$$B_{\mathrm{J}}(x) = \frac{2J+1}{2J}\coth\left(\frac{2J+1}{2J}x\right) - \frac{1}{2J}\coth\left(\frac{x}{2J}\right) \tag{3.3}$$

where x is a ratio of several constants and the applied field (B) and temperature (T) given as

$$x = \frac{g\mu_B BJ}{k_B T} \tag{3.4}$$

Using figure 3.12b the difference between the 2K loop and the 5K loop are a measure of the paramagnetic moment if it is assumed that the diamagnetic contribution is temperature independent and that at 50K the paramagnetic contribution is negligible, which means the difference (shown in figure 3.13) is the paramagnetic signal at 2K.

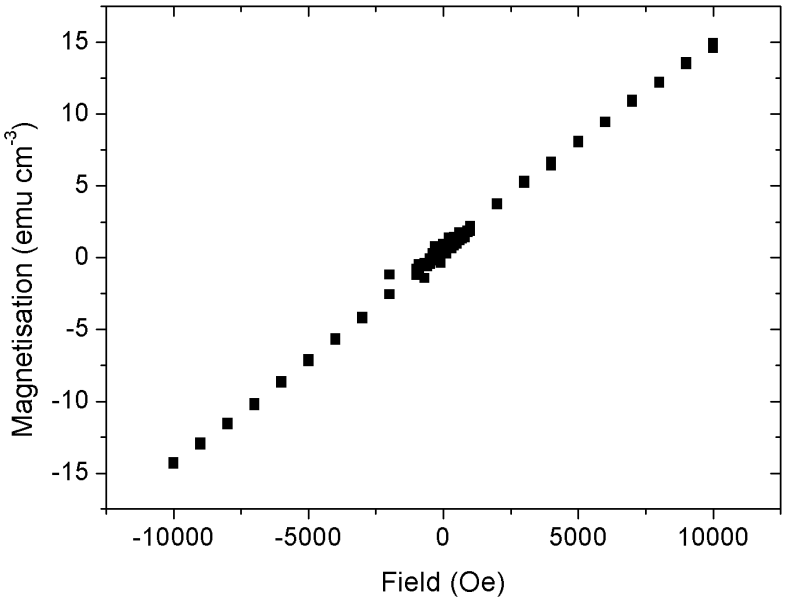

Fig. 3.13 The difference in magnetisation between the 2K and 50K loop in figure 3.12b. The difference in magnetisation is the paramagnetic signal.

Using the value of the magnetisation at the maximum applied field of 1T and the magnetisation relationship with a Brillouin function in equations 3.3 and 3.4 the number of Bohr magnetons per unit volume (N_{Para}) is $5\times10^{20}\mu_B cm^{-3}$. The number of Bohr magnetons per unit volume of AF Mn in CuMnAs can be calculated as the product of the number of Bohr magnetons per Mn and the number of Mn per unit cell by the volume of the unit cell of

CuMnAs. CuMnAs has $3.6\mu_B/Mn$ and two Mn per unit cell. The unit cell has a volume of $9.22\times10^{29}m^3$, which gives N_{AF} as $7.8\times10^{22}\mu_B$ cm^{-3}. The fraction of N_{Para}/N_{AF} is 0.6% of the AF moment, which is markedly smaller. If there is interstitial (or substitutional) Mn then it could be strongly coupled to the AF Mn, so it may not display simple paramagnetic behaviour.

3.3.3 Surface characterisation

Atomic Force Microscopy

The surfaces of CuMnAs layers grown on both GaAs and GaP were studied using AFM, section 2.4.1. Examples of typical surfaces for layers on each substrate will be presented but this behaviour was shown in multiple samples.

Images of the surface of CuMnAs on GaAs, for Sample:1-4, are shown in figure 3.14. The surface is characterised by a short cross hatching pattern that runs along the [100] and [010] directions of the GaAs crystal lattice. As the CuMnAs crystal lattice rotates by 45° to the GaAs crystal lattice, the cross hatching pattern runs along the CuMnAs [110] and [$\bar{1}$10]. This hatching pattern is observed in layers of CuMnAs that are 40nm or thicker. Figure 3.14a has an Root Mean Square (RMS) roughness value of 2nm.

Example images of the surface of CuMnAs on GaP, for Sample:1-5, are shown in figures 3.15 and 3.16, the surface is markedly covered in sharp lines that run parallel and perpendicular to each other. These lines run along the [100] and [010] directions of the GaP crystal lattice, which is the equivalent of the [110] and [$\bar{1}$10] directions for the CuMnAs crystal lattice. The height profiles (figure 3.16b) from this surface show that there is a distinct repeating step at these edges. However within a tile it is possible to see almost monolayer flatness in the height variation.

There are clear differences between the CuMnAs on GaAs and GaP surfaces; Difference in the sharpness and length of the lines, density of cross hatching and size of the unaffected

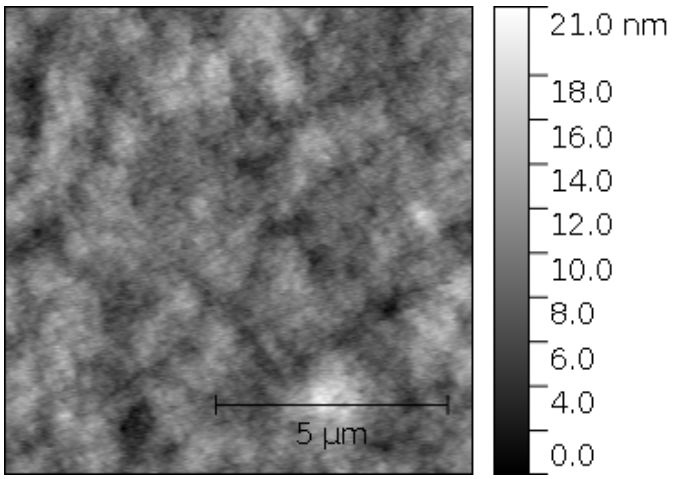

(a) 10μm×10μm image

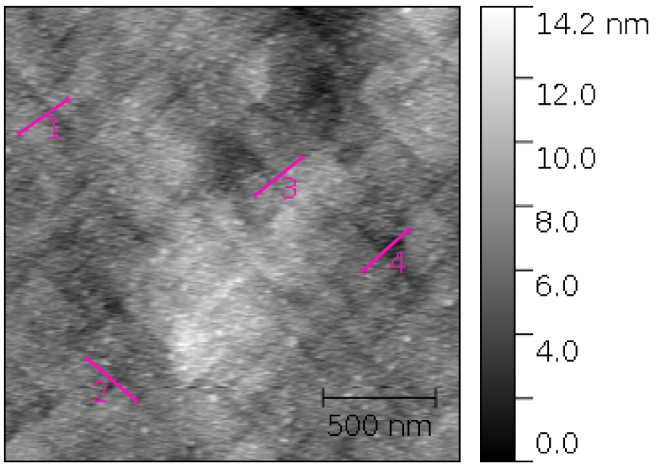

(b) 2μm×2μm image

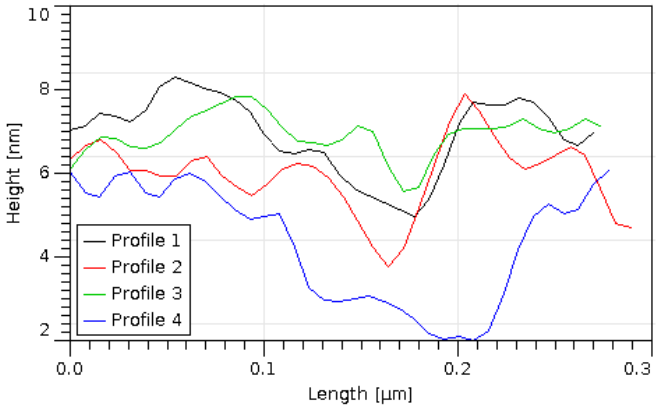

(c) Height profiles

Fig. 3.14 AFM images of the surface of stoichiometric CuMnAs on GaAs (Sample:1-4) at two different scan sizes with corresponding height profiles (numbered pink lines) for the smaller area scan. The scan line are across the cross hatching pattern seen on the surface.

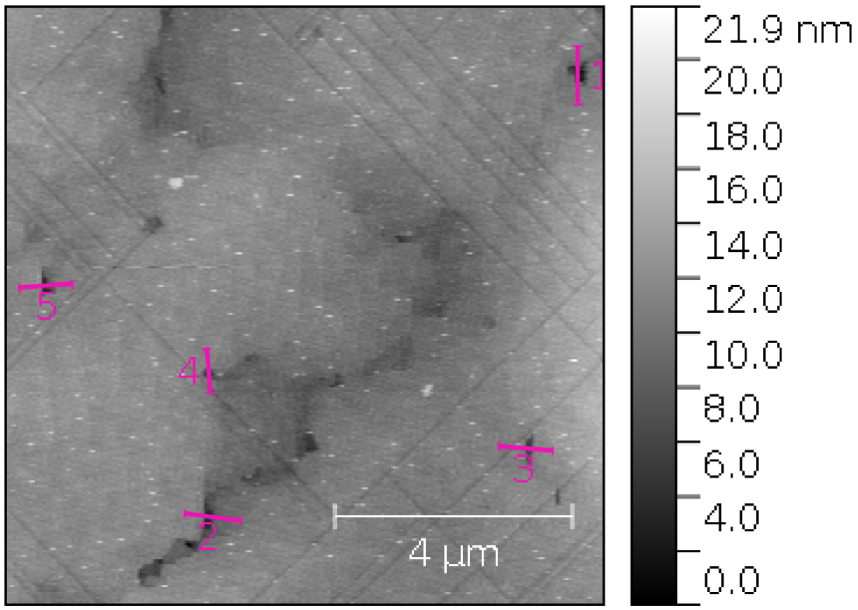

(a) 10μm$\times 10\mu$m

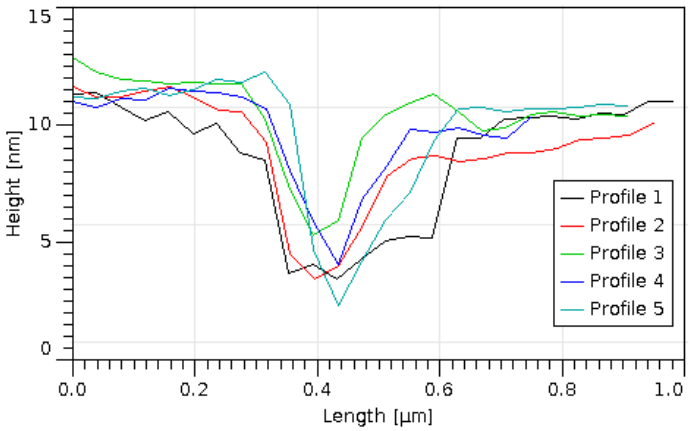

(b) Height profiles

Fig. 3.15 10μm$\times 10\mu$m AFM image of the surface of stoichiometric CuMnAs on GaP, Sample:1-5 with corresponding height profiles (numbered pink lines). The height profiles are selected on hole defects in the material.

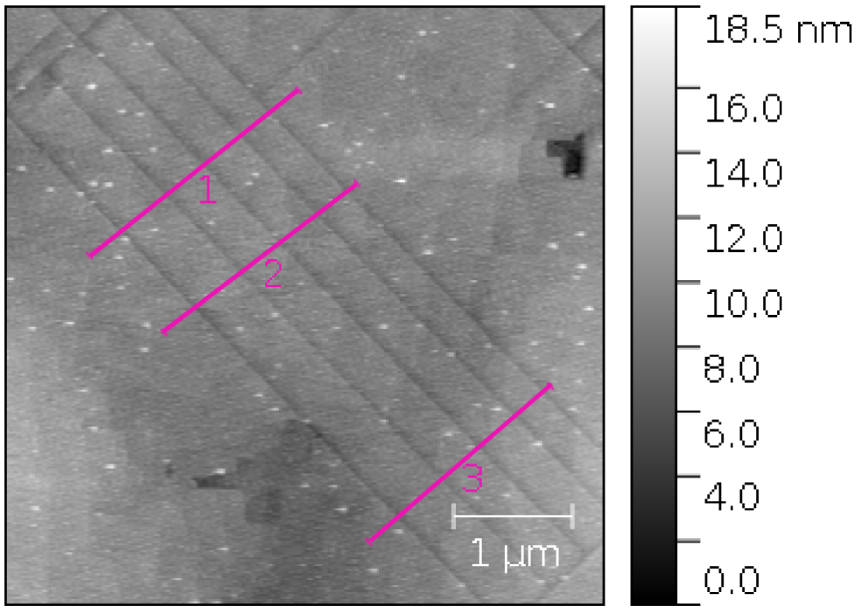

(a) 5μm$\times 5\mu$m

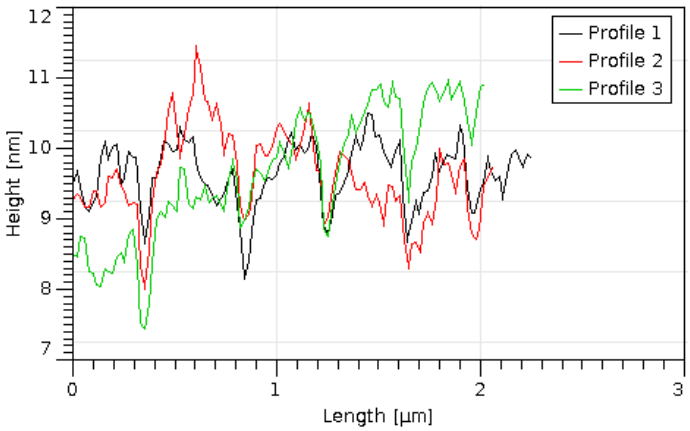

(b) Height profiles

Fig. 3.16 5μm$\times 5\mu$m AFM image of the surface of CuMnAs on GaP, Sample:1-5 with corresponding height profiles (numbered pink lines). The height profiles are aligned across the edges of the cross hatching pattern.

tiles. The lines on CuMnAs on GaP, which can be longer than 5μm, are an order of magnitude longer than those on GaAs, which are less than 500nm. For both substrates the hatching patterns are only seen in layers with a thickness greater than 40nm, which means that there could be a connection between the cross hatching and the mechanism for lattice mismatch or relaxation with the CuMnAs and substrate. On layers less than 40nm the hatching pattern is not present and in some samples it is possible to see monolayer steps on the surface.

Magnetic Force Microscopy

MFM, described in section 2.4.2, was performed on stoichiometric CuMnAs, for layers grown on both GaAs and GaP. The images showed no discernible features for the effective lateral resolution of these scans, where the lift height was 50nm, it was not possible to detect any features. This implies that at this resolution there were no stray fields detectable, which is consistent with the SQUID measurements.

3.4 Characterisation of non-stoichiometric CuMnAs

Several different techniques will be used in this section to study the non-stoichiometric Sample:2-1 and comparisons will be made between this sample and stoichiometric CuMnAs.

3.4.1 Determination of the crystal structure by XRD

Sample:2-1 has diffraction peaks from XRD, using a 2θ scan, from the CuMnAs (00L) family, which are shown in figure 3.17. The CuMnAs diffraction peaks imply that the lattice constants have not changed due to the incorporation of the excess Mn throughout the crystal lattice. In a glancing angle scan performed by P. Wadley there was also no sign of polycrystalline material in the layer, showing that the excess Mn is not dispersed throughout the layer and has a crystallographic orientation.

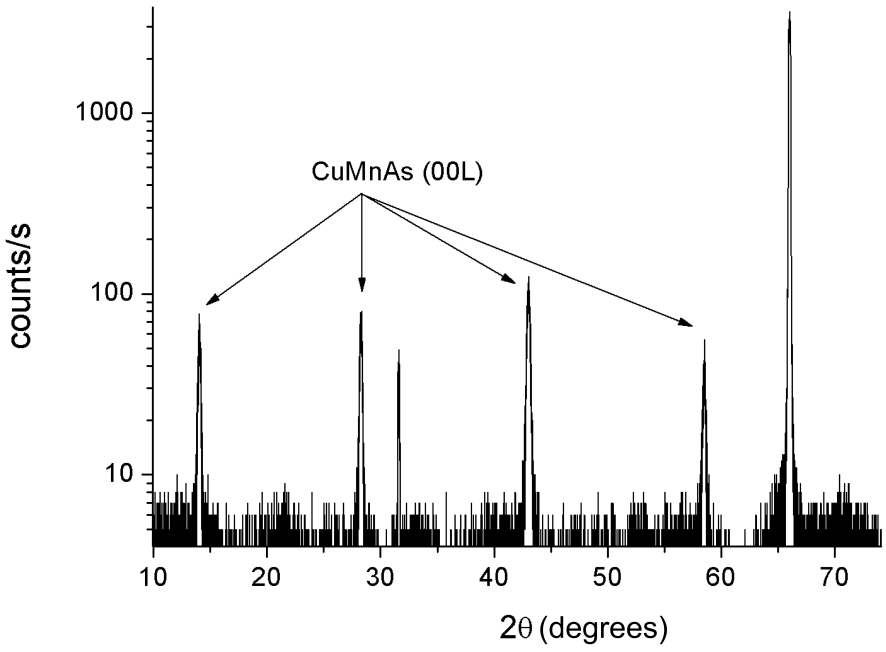

Fig. 3.17 A 2θ XRD scan for non-stoichiometric CuMnAs with an excess of Mn (Sample:2-1). The CuMnAs (00L) peaks are highlighted. Measurements were performed by P. Wadley.

3.4.2 Magnetic characterisation by SQUID

SQUID magnetometry was used to perform hysteresis loops in the temperature range of 4K-300K to see the effect of temperature on the magnetisation of Sample:2-1. The results in figure 3.18 show the hysteresis loops for each of the temperatures listed. At the maximum field of (10kOe or 1T) projection of the magnetization along the direction of the applied is beginning to saturate. The maximum measured projected magnetization is decreasing with increasing temperature.

Figure 3.19 shows the results of cooling the sample with an applied field of 10kOe for the sample mounted in plane and out of plane. There is a clear FM component with a temperature dependence and a T_C that is above the maximum applied temperature of 300K, which is consistent with inclusions of FM MnAs, where the T_C can be between 320K [127] and 340K [128]. There is little difference in the remnant moment between the measurements in plane and perpendicular to plane implying that there is little anisotropy.

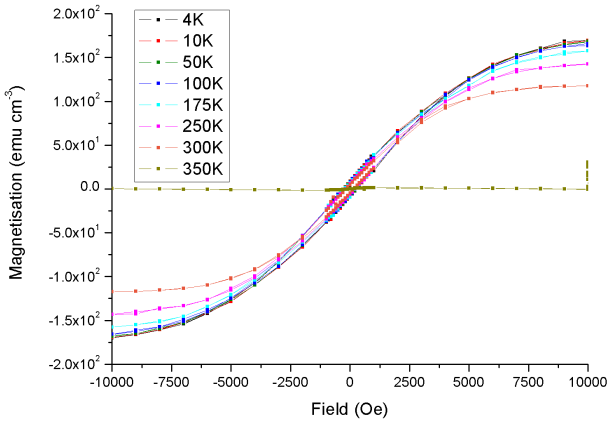

Fig. 3.18 The projection of the magnetization along the direction of the applied field against applied magnetic field between 4K and 350K for Sample:2-1 mounted out of plane.

The magnetometry results shown here for non-stoichiometric CuMnAs are markedly different from the results of stoichiometric CuMnAs, section 3.3.2

3.4.3 Surface characterisation

Atomic Force Microscopy

AFM images were taken at a range of lateral dimensions for the surface of Sample:2-1. At the shorter length scales, as seen in figure 3.20, there is a tiling pattern similar to that seen on stoichiometric CuMnAs with lines running along the principal axis of the CuMnAs, [110] and [$\bar{1}$10]. These lines are sharper and longer than those seen on the stoichiometric CuMnAs grown on GaAs, figure 3.14, which could be due to several factors as there is a significant difference in the layer thickness and the growth conditions. The line length varies from 500nm to several micrometers. The non-stoichiometric CuMnAs layer has a large RMS roughness of 6nm.

However on wider dimension images there are large inclusions, figure 3.20c, which have average dimensions that are listed in table 3.4. These inclusions are aligned along the

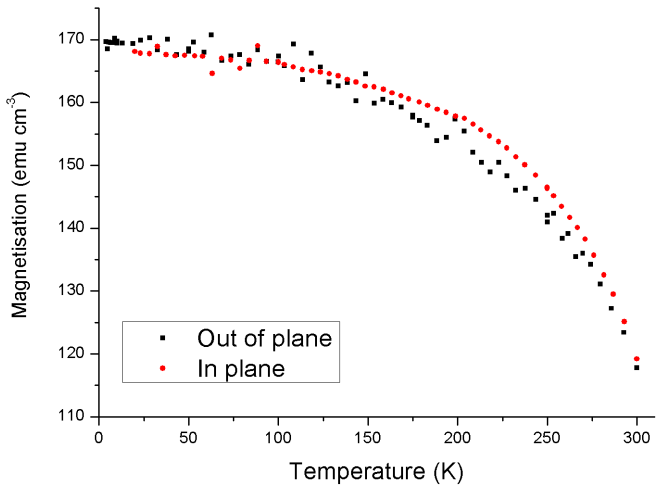

Fig. 3.19 The projection of the magnetization against temperature for non-stoichiometric CuMnAs (Sample:2-1) cooled under an applied magnetic field, mounted in different orientations.

Profile	Width (μm)	Length (μm)	Height (nm)
1	1.3	0.8	110
2	0.92	0.49	90
3	1.4	0.87	100
4	1.4	0.42	50
5	2.3	1.2	120
6	1.1	0.83	160

Table 3.4 Dimensions of inclusions highlighted in 3.20c. Dimensions listed are based on the observed maximum of each inclusion

principle axes of the GaAs substrate, the [100] and [010], which means that the inclusions are aligned at 45^o to the principle axis of the CuMnAs. There are a large number of tiling lines that begin or terminate at the inclusions, though there are also cases where lines continue on either side. There are square micron sized areas that do not have any inclusions.

Examining the dimensions of these inclusions (table 3.4) they are raised from the surface. However it is unknown how far they extend into the matrix. Raised inclusions have previously been observed in GaMnAs:MnAs systems [129] however these were much more uniform in

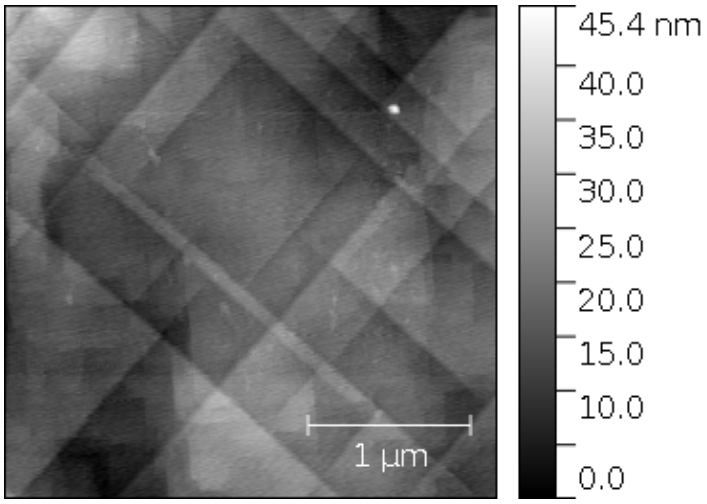

(a) 3μm$\times 3\mu$m

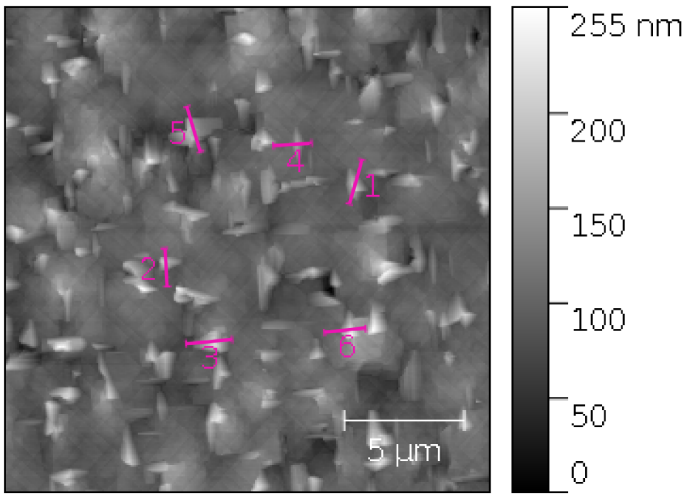

(b) 20μm$\times 20\mu$m

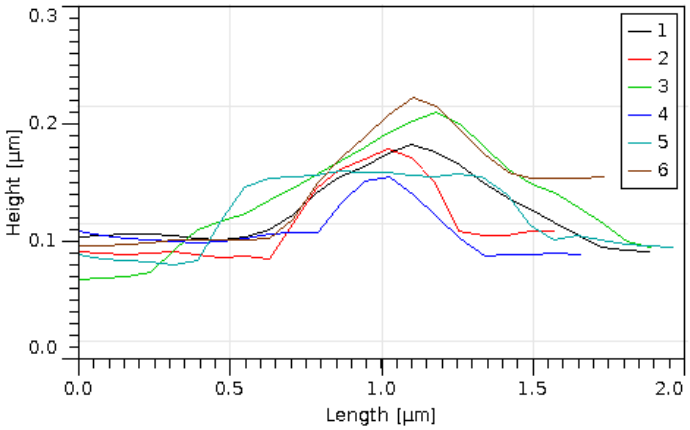

(c) Corresponding profiles

Fig. 3.20 AFM images of non-stoichiometric CuMnAs, Sample:2-1. The top image shows the tiling pattern, typically seen in stoichiometric CuMnAs, in a small area. The bottom image is over a larger area and shows the inclusions that appear on the surface which have corresponding numbered height profiles.

shape (ovals), smaller and shorter (only 20nm in height to a variation of 50nm-160nm) and there are growth theories for inclusions on the surface or just below it [128].

Magnetic Force Microscopy

MFM images were taken of the surface of Sample:2-1 with a tip surface separation of 50nm. The results are seen in figure 3.21b and there are clear domains on the surface. These domains have areas of white and black which corresponds to magnetic field lines in opposite directions, as detailed in section 2.4.2. When comparing the AFM and MFM images it is apparent that the inclusions in the AFM image overlap with the areas of FM behaviour in the MFM image as shown in figure 3.21.

MnAs inclusions have been seen in other hybrid systems to form ferromagnetic inclusions with T_Cs between 340K [128] and 313K [130]. From the known growth conditions of an excess of Mn and As and the XRD results showing a dominant CuMnAs crystal the inclusions are believed to be clusters of MnAs embedded in a CuMnAs crystal, which means that the CuMnAs has grown at stoichiometry and any excess material has been rejected from the crystal lattice. For the growth to form such large inclusions on the surface, which are located micrometers apart, implies a large surface migration of the Mn or MnAs to form these clusters, which is an unusual growth model for the stoichiometric growth to be so energetically favourable that excess material forms on the surface and then may diffuse over a micron to form peaks rising from the surface up to 100nm.

3.4.4 Comparing percentage of MnAs

From the above selections of results it is possible to estimate the amount of MnAs in Sample:2-1. Three different percentages can be calculated from the MBE growth parameters (section 3.2.2), the SQUID magnetisation (section 3.4.2) and AFM (section 3.4.3).

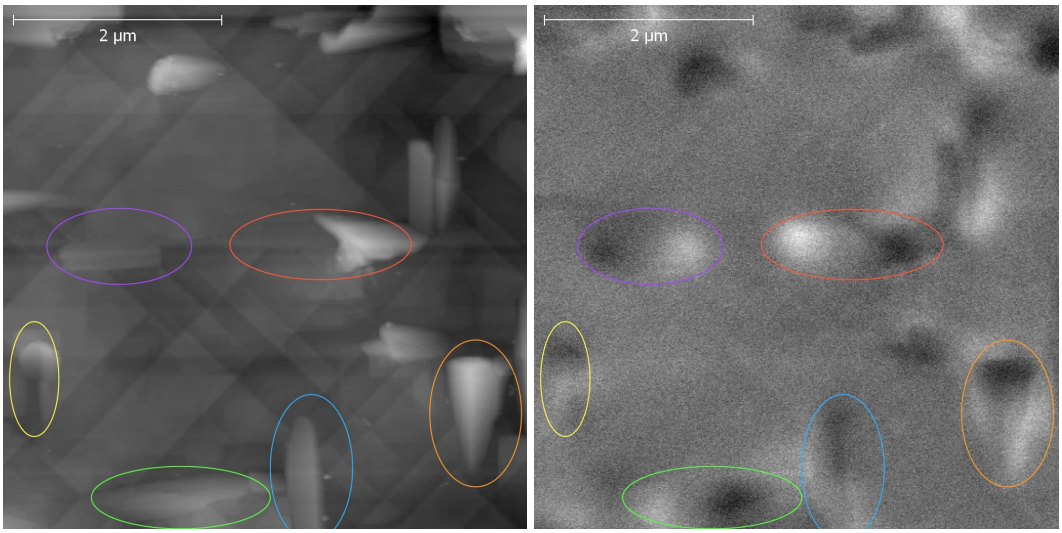

(a) AFM (b) MFM

Fig. 3.21 AFM and MFM of the same 5μm$\times 5\mu$m area, showing the inclusions and highlighting the same areas on the two images, with coloured circles, for non-stoichiometric Sample:2-1.

For several of these methods it is necessary to calculate some properties of CuMnAs and MnAs such as the volume of each unit cell V_{UC} and the volume of Mn per unit cell$V_{UC/Mn}$. Table 3.5 details calculations of the volume of each unit cell (V_{UC}) and the volume of each unit cell that is taken up by manganese ($V_{MnAs/Mn}$ and $V_{CuMnAs/Mn}$). This assumes that the MnAs inclusions have the same lattice parameters as bulk material. The ratio of these two values can then be calculated as:

$$\frac{V_{\mathrm{MnAs/Mn}}}{V_{\mathrm{CuMnAs/Mn}}} = 0.748 \tag{3.5}$$

Method 1: Growth Parameters

Using the fluxes for Cu and Mn it is possible to calculate the percentage of excess Mn that could have formed MnAs during the growth. The arsenic is applied in an overpressure so it is not a limiting factor on the growth and it is assumed that all excess As will re-evaporate. It is

necessary to assume that all the Cu formed CuMnAs and that any excess Mn formed MnAs. From previous growths it is known that CuMnAs grows in a 1:1:1 stoichiometric ratio [39]. This ratio was achieved with the Beam Equivalent Pressures (BEP) these are detailed in Table 3.2. Comparing the ratios of these flux the non-stoichiometric ratio is 1:1.48 of Cu:Mn

Using the assumption that all the copper has been used to make CuMnAs in a 1:1 ratio with manganese then there is 0.48 moles of MnAs formed per mole of CuMnAs. This gives a molar fraction of 0.324, which is the number of moles of Mn formed into MnAs over the total amount on Mn (1.48).

With the ratio of the molar volume pre manganese (0.748) and the molar fraction (0.324) it is then possible to work out the maximum possible amount of MnAs as the product of these values. This gives a percentage of 24.2% of the total volume of the film occupied by MnAs.

Method 2: Magnetisation

For this method it is necessary to have a value of the saturation magnetisation for a pure film of MnAs. Throughout the literature there is a variety of reported values for the magnetisation. A selection of these for samples grown by MBE on GaAs(001) are listed in table 3.6. A magnetisation of $4\mu_B/Mn$ will be used throughout, which corresponds to 1008emu/cm^{-3} through:

$$M_R = \frac{M_{\mu_B/Mn}\mu_B}{V_{MnAs/Mn}} \tag{3.6}$$

	Unit Cell (uc)	Lattice Constants (Å)	V_{UC}	No. of Mn/uc	$V_{UC/Mn}$ (10^{-30}m^3)
MnAs	Hexagonal	a=3.72, c=5.76	$\frac{3\sqrt{3}a^2c}{2}$	6	$V_{MnAs/Mn}$=34.5
CuMnAs	Tetragonal	a=3.82, c=6.318	ca^2	2	$V_{CuMnAs/Mn}$=46.1

Table 3.5 Calculating Volume per Manganese for MnAs [131] and CuMnAs [39].

Author	Year	Film Thickness (nm)	M (μ_B/Mn)
Berry et al. [127]	2001	41	4.46
Wikberg et al. [1]	2010		4.1
Satapathy [131]	2005	20	2.61
Schippin et al. [132]	2000	100	2.58

Table 3.6 Difference in Magnetisation for MnAs from literature for Material grown by MBE.

To work out the magnetisation of our sample we used a sample with the dimensions of 5mm x 5mm x 340nm , which has a volume of 8.5×10^{-6}cm^3. From SQUID measurements the Saturation Magnetisation (M_{sat}) is around 1.12×10^{-3}emu.

The volume of MnAs in the entire sample is then:

$$V_{\mathrm{MnAs}} = \frac{M_{\mathrm{sat}}\mu_{\mathrm{B}}}{M_{\mathrm{R}}} = 1.11 \times 10^{-6}\mathrm{m}^{-3} \tag{3.7}$$

From the total volume of the sample this gives a percentage of 13.1%. This percentage only considers FM (α phase) MnAs however there may also be some β MnAs in the inclusions, which it is not possible to consider with this method.

Method 3: AFM image analysis

Using the image processing protocols described in section 2.4.1, it is possible to calculate the percentage of the surface in the AFM images that are covered in inclusions. After calculating the number of inclusions for all possible areas the mean percentage of inclusions is (22$\pm$1)%. To analyse the images thresholds of 20-30% above the mode gray scale value were used. A technical issue with the method is that the background image has large variation in height, which means that extra areas can be selected as part of the inclusions. A problem with this method is that it assumes that the surface area covered by the MnAs is representative of the distribution of MnAs in the rest of the sample. The percentage could be an over

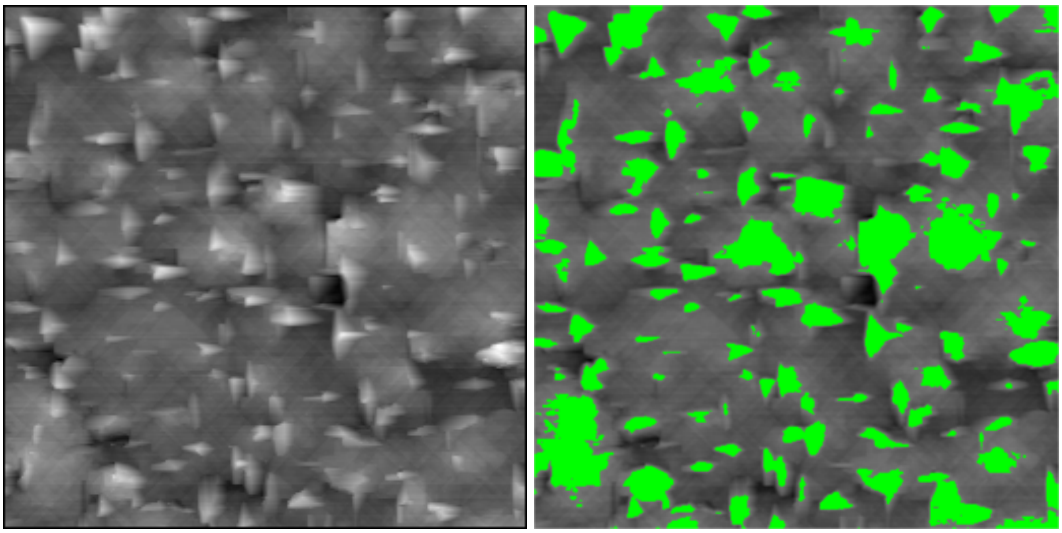

(a) Unprocessed (b) Processed, threshold 20%

Fig. 3.22 Original and processed AFM image to determine the percentage of area covered with inclusions in non-stoichiometric CuMnAs (Sample:2-1) using a threshold to select areas that were 20% above the mode gray scale value.

	Method	Percentage
1	Growth	24.2%
2	Magnetisation	13.1%
3	AFM	(22±1)%

Table 3.7 Percentages of the amount of MnAs in Sample:2-1 calculated by different methods.

representation of the MnAs if all the MnAs has diffused to the surface and there is none in the matrix itself.

In conclusion the percentages yielded by the three different methods are listed in table 3.7. The figure of 13% can be considered as a lower bound since it assumes a near maximum magnetisation for the inclusions, while the figure of 24% can be considered as an upper bound since it assumes 100% incorporation of the excess Mn as MnAs inclusions. However the third estimate of the percentage of MnAs from AFM lies within these two bounds, which gives a good agreement between the three methods. These figures are used in discussing the transport properties of this material in Chapter 6.

3.5 Optimising the growth conditions for ultra thin films of CuMnAs

This section will detail investigations into the surface qualities of sub 10nm films of CuMnAs, it will start by looking at the effect of different capping layers, then move on to describe the variation of surface quality with thickness and finally describe the effects of different growth mechanisms.

All the samples to be discussed (Tables:3, 4 & 5) were grown on wafers from the same batch of semi insulating GaP and in each case with a nominal growth rate of 46nm/hr and incorporation stoichiometry of 1:1:1. For all the samples a high temperature GaP buffer was grown at T_{TC} of 660°C. The buffer was a minimum of 30nm and produced a strong 2x4 RHEED reconstruction. During these growths, the band edge technique for direct measurement of the temperature on GaP, which was discussed in 2.1.2, was developed and where possible will be mentioned. RHEED was used to monitor all growths. During the CuMnAs growth the 2x2 RHEED reconstruction typically seen in CuMnAs growths was observed [39]. The 10nm layers (Sample:3-1 / Sample:4-1) and 5nm layer (Sample:4-2) were cooled at a maximum rate of 30K/min prior to the deposition of an aluminium cap. In later samples the decision was made to reduce the cooling rate to 5K/min to exclude the possibilities of effects from rapid cooling. All of the samples in this series were capped with either 2nm aluminium (grown at a T_{TC} of 0°C), 2nm of GaAs or 30nm of GaP (both grown at the CuMnAs growth temperature).

3.5.1 Growth and surface characterisation of ultra thin films with different capping layers

This section will start by looking at the effect of different capping layers on the surface of 10nm films of CuMnAs, the samples are listed in table 3. The schematics of these samples

are shown in figure 3.23. The surfaces of the samples were analysed using AFM (described in section 2.4.1).

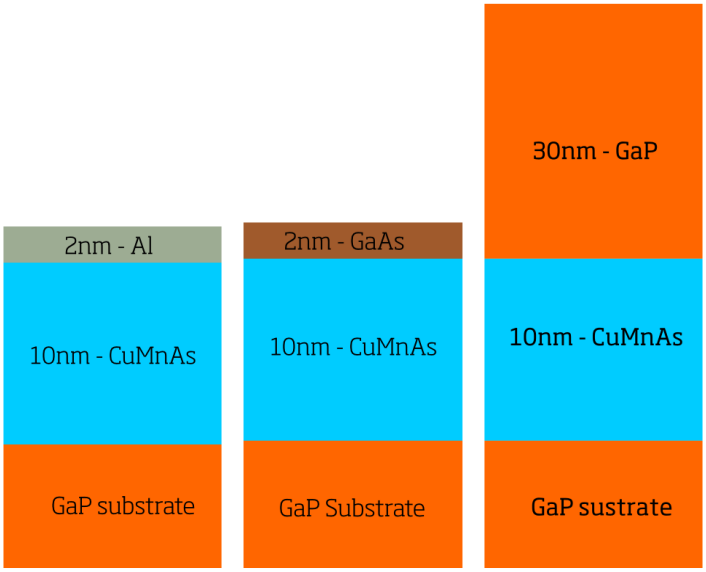

(a) Sample:3-1 (b) Sample:3-2 (c) Sample:3-3

Fig. 3.23 The layer structure of the samples in Table 3, which looks at the difference in capping layer for ultra thin films of CuMnAs.

Aluminium Capping

Sample:3-1 is a 10nm CuMnAs sample film with a 2nm Al cap (shown in figure 3.24). The AFM image shown in figure 3.24a indicates that there are holes visible over a wide area, spread randomly across the surface. Line profiles taken across these holes, shown in figures 3.24b & 3.24c reveal that these holes can be up to 10nm deep, which is the full depth of the CuMnAs film. The holes with larger x-y spatial extent are flat-bottomed.

There is no indication of extra material around the edges, which would be seen if the material was being displaced and migrating away from a point defect during the growth. It is therefore supposed that this material is falling out after the growth of the CuMnAs; probably whilst the layer is cooling in vacuum before the Al cap is applied.

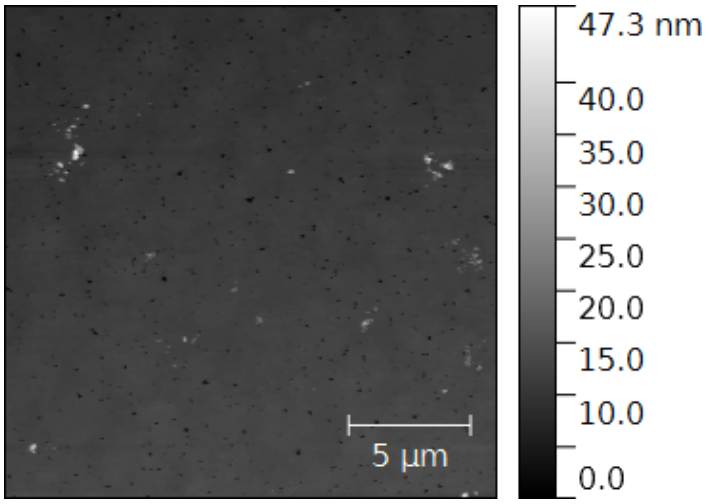

(a) 20μm×20μm

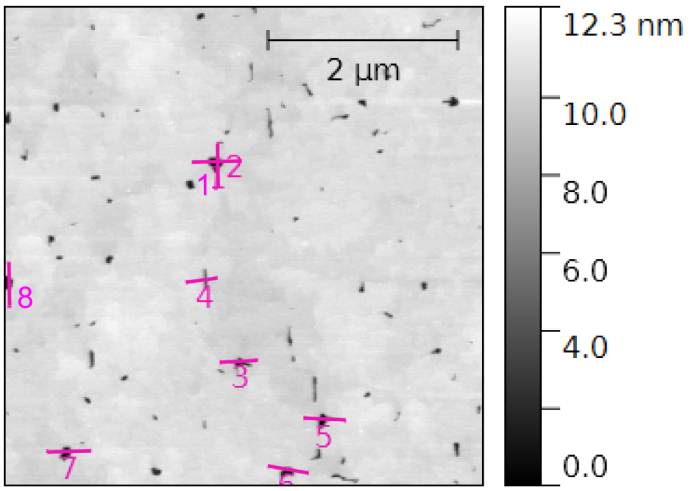

(b) 5μm×5μm

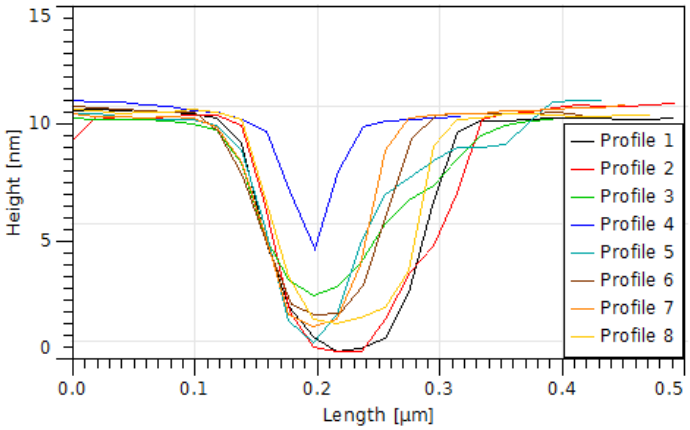

(c) Height profiles corresponding with numbered marks in figure 3.24b.

Fig. 3.24 AFM images of 10nm CuMnAs with 2nm Al cap (Sample:3-1). The top image shows a large area than the middle image. Both of the images show small dark patches (holes) across the surface.

Gallium Arsenide Capping

Sample:3-2 was capped with a 2.7nm layer of GaAs. The AFM image shown in figure 3.25 indicates that the surface of this sample is markedly different to that for the Al-capped Sample:3-1 (see figure 3.24 for the corresponding AFM image). Small lateral dimension AFM scans reveal three distinct levels in z-contrast. These steps (labelled in figure 3.25c) are ascribed to (a) the complete structure with GaAs cap, (b) a CuMnAs layer with no cap, and (c) a hole through to the GaAs substrate. These three steps in the AFM profiles are readily seen in the AFM images and have been observed on multiple GaAs capped samples.

Using the image analysis technique described in 2.4.1, the percentage of missing CuMnAs and amount of GaAs remaining in Sample:3-2, have both been estimated which and these values are shown in figure 3.26. Using a threshold of 5% above the mean value, the amount of GaAs remaining is 34.5%, whereas there is 1.7% of the CuMnAs missing with a threshold of 30% below the mean value.

When CuMnAs is grown on GaAs there is a large lattice mismatch of 1.5% compared with a lattice mismatch of 0.3% when grown on GaP [39]. The low angle optical observations during growths suggest that the material surface of CuMnAs on GaAs is rougher than on GaP and XRD peaks have a greater FWHM implying greater mosaicity or smaller crystallite size. This difference in roughness could suggest that the greater lattice mismatch is having a detrimental effect on the interface adhesion between CuMnAs/GaAs. We observed that there is a wider area of GaAs cap missing around the holes than occurs when the CuMnAs layer has remained intact.

Gallium Phosphide Capping

Given the smaller lattice mismatch between CuMnAs and GaP, a thick (30nm) GaP cap was grown (Sample:3-3). The GaP cap was grown immediately after the CuMnAs growth. During the growth of the GaP cap, the RHEED appeared to show a rougher surface and

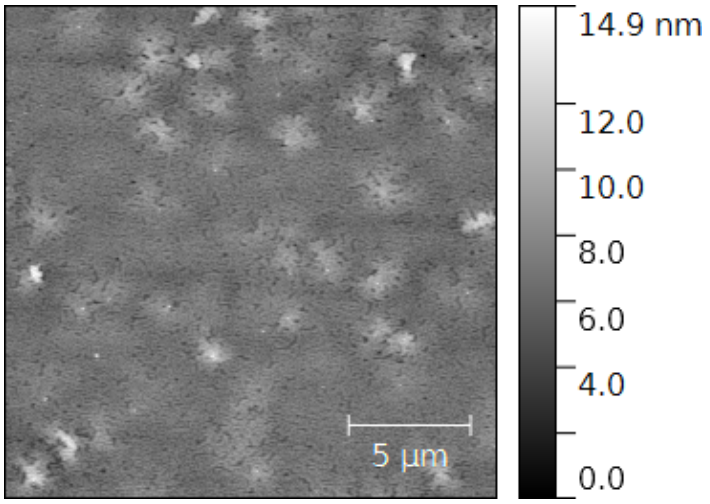

(a) 20μm×20μm

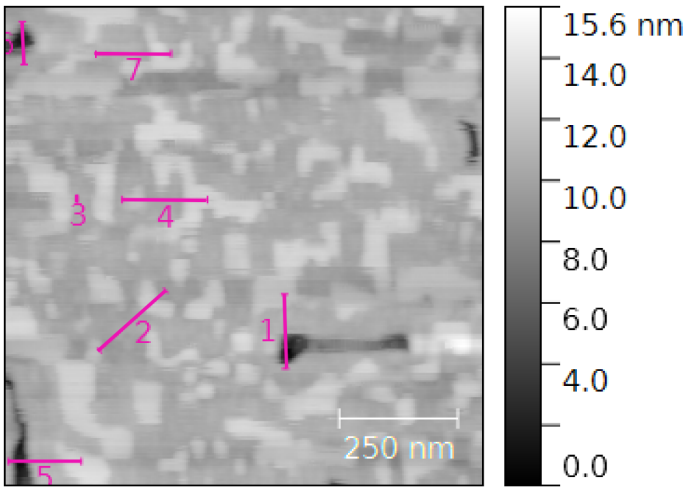

(b) 1μm×1μm

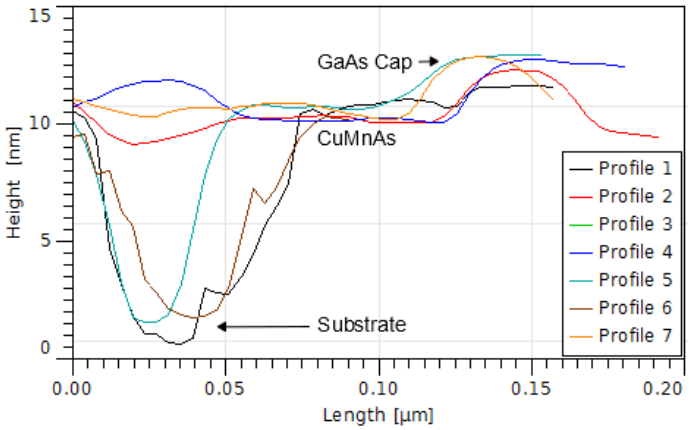

(c) Height profiles corresponding with numbered marks in 3.25b.

Fig. 3.25 AFM images of 10nm CuMnAs with a 2.7nm GaAs cap (Sample:3-2). The top image shows a larger area than the middle image. In the middle image three distinct layers (colours on the grey scale). These different layers are labelled in the bottom figure as part of the height profiles.

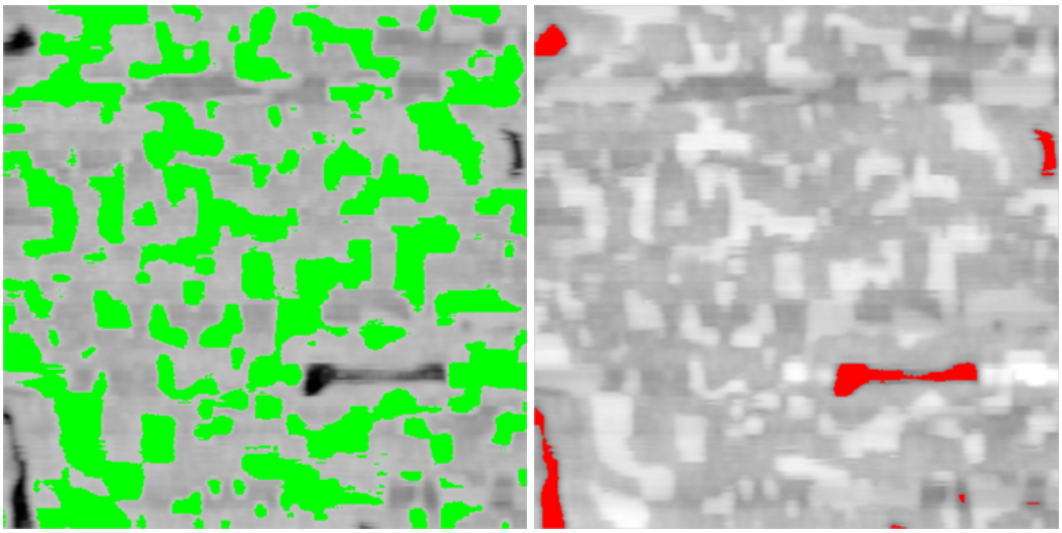

(a) GaAs cap highlighted in green (b) Visible substrate highlighted in red

Fig. 3.26 Processed versions of figure 3.25b. The colours areas are selected as above or below a threshold that is set as the CuMnAs layer.

possibly twinning or other crystallographic defects (section 1.4). The sample temperature was measured independently from the T_{TC}, using the band edge measurement, to observe the evolution of the temperature in growth, as shown in figure 3.27. From this we can see that the starting growth temperature was 260°C, and that even though the thermocouple temperature remained constant the sample temperature rose by nearly 50°C during the growth, this is typical behaviour that we have seen to occur in other CuMnAs/GaP growths and in other material systems [133, 134]. During the growth of the GaP buffer, the temperature remained constant with the measured T_{sub} being 10°C higher than the thermocouple was set to.

The AFM images for Sample:3-3 can be seen in figure 3.28. In figure 3.28a there are large inclusions on the surface, which are up to 300nm in length and 140nm high, but we do not observe the 10nm holes that we observed in the other layers. These features do not markedly change as the scan area is decreased (figure 3.28b). At the 5μm lateral resolution a few holes are visible in the GaP layer but these have a different profile to the holes seen in the previous samples. The holes are more rectangular, with inclusions inside and a depth profile throughout the GaP capping layer. The lack of 10nm holes suggests that the CuMnAs layer

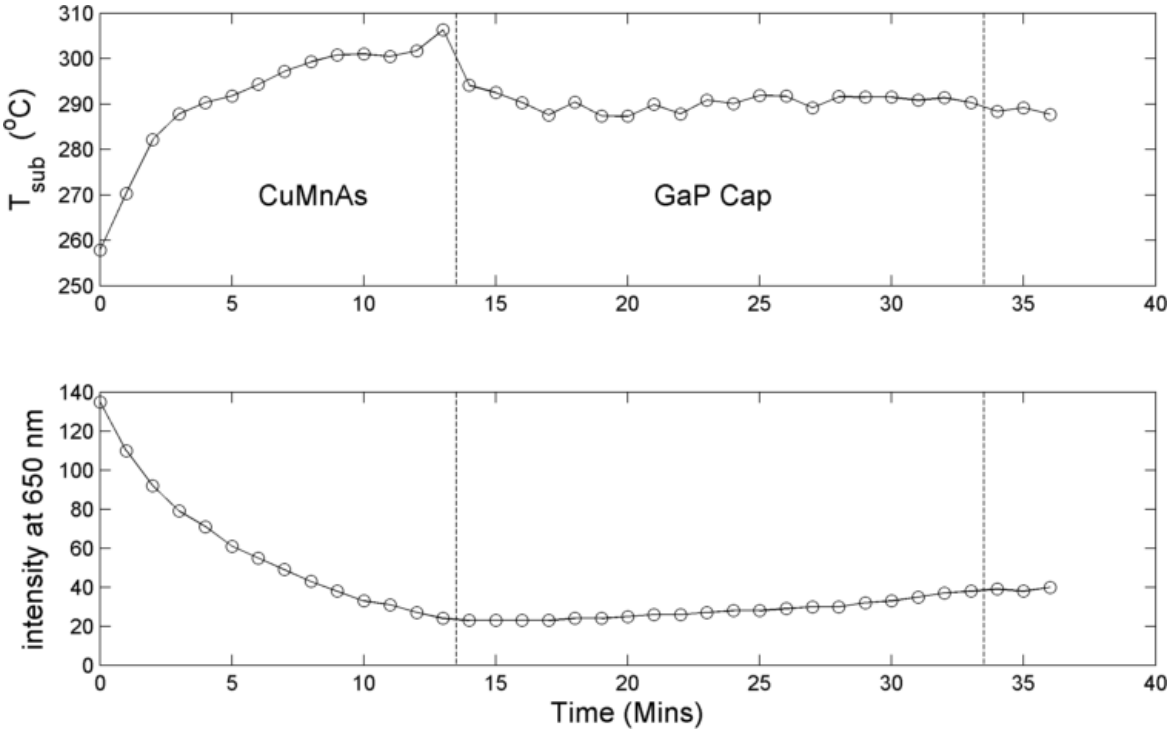

Fig. 3.27 Temperature of the substrate measured using the band edge of GaP for CuMnAs on GaP with a GaP cap (Sample:3-3).

has stayed intact due to the complete capping layer over it. If the CuMnAs had been falling out during the growth then we would have expected to see these holes cause inflections through to the GaP capping layer.

In conclusion, from this series of samples (Table:3) it is possible to make the observation that parts of the CuMnAs ultra thin films are being lost; the material is probably being lost post layer growth as the majority of the holes have a profile of the layer thickness, instead of a wide distribution of hole depths, which would be seen if material was being lost during growth. When a substantial capping layer has been grown these holes are not observed. When the capping layer is unable to adhere to the CuMnAs surface post growth then a complicated situation arises where the CuMnAs material is able to fall out where the capping layer is incomplete and it can be observed than a larger area of the capping layer is vacant around the holes in the layer.

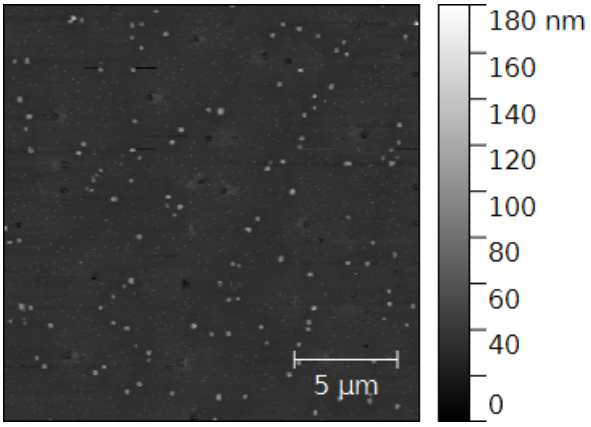

(a) 20μm×20μm

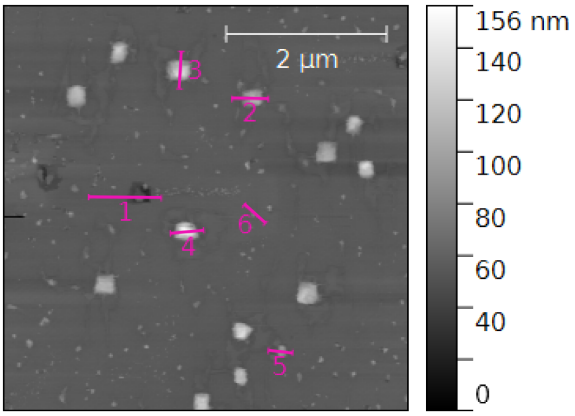

(b) 5μm×5μm

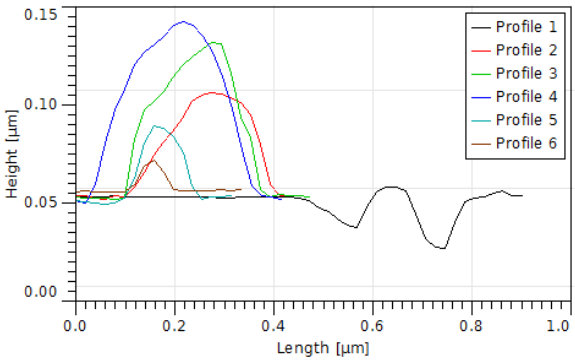

(c) Height profiles corresponding with numbered marks in figure 3.28b.

Fig. 3.28 AFM images of 10nm CuMnAs with a 30nm GaP cap (Sample:3-3). On the AFM images square inclusions can be seen as well as holes on the larger area top image.

The holes observed in this series of samples could be attributed to a number of different factors. One is that there could be a large differential thermal expansion between the CuMnAs and GaP crystal lattices. At this time we do not have a value for the thermal expansion of tetragonal CuMnAs to compare them. Secondly there could be poor adhesion at the interface; this scenario is supported by the apparent poor adhesion at the CuMnAs/$GaAs_{cap}$ interface. We do not observe layer thick holes in thicker samples of CuMnAs as the material is probably self supporting.

3.5.2 Analysis of surface film quality with different film thickness

To study the effect of thickness on the CuMnAs layer quality the next series of samples (Table 4) were grown with thickness ranging from 10nm-2nm. The samples were capped with 2nm aluminium so that the material was uncovered during the cool down to to create the simplest system to study. For each layer AFM was performed in several arbitrary locations at different scan sizes. The percentage of missing material was calculated using the image processing protocols described in section 2.4.1.

Figure 3.29 shows a representative selection of images for the four different layers considered in this series. In the unprocessed images (figure 3.29a, c, e & g) we can see an increasing amount of dark areas in the image which correspond to missing material in the layer; as the layers become thinner the density and shape of the holes changes from small pin prick holes (figures 3.29a & 3.29c) to highly directional lines (figure 3.29e) and then isolated islands of material (figure 3.29g). The diagonal striped patterns on some of the images are due to electrical noise interfering with the AFM. In figures 3.29b, d, f & h we can see the processed images, the red regions correspond to the areas that have been determined to be missing material. In figure 3.29h we can see that with the level of electrical noise it is difficult to define the border between layer and substrate. The percentage of missing material for all these images can then be plotted to show a clear trend which is shown in figure 3.30.

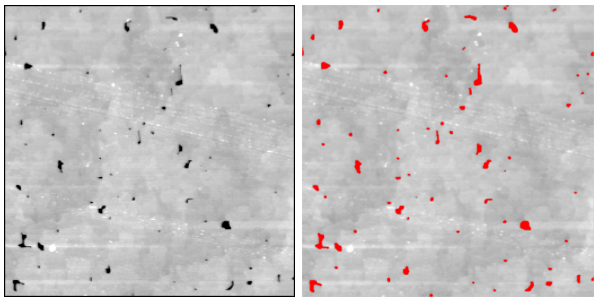

(a) Thickness:10nm (b) Thickness:10nm
Size:5μm$\times$5μm

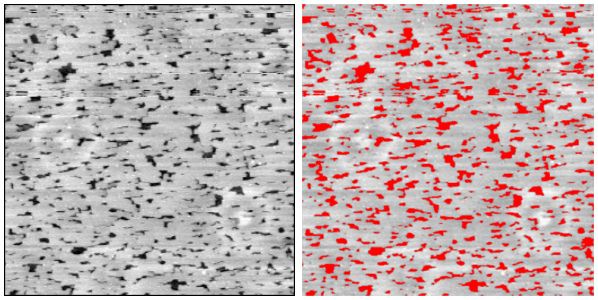

(c) Thickness:5nm (d) Thickness:5nm
Size:5μm$\times$5μm

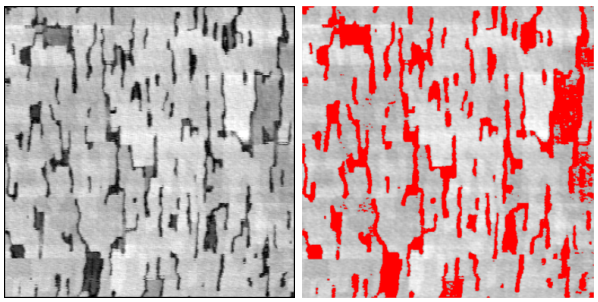

(e) Thickness:4nm (f) Thickness:4nm
Size:1.5μm$\times$1.5μm

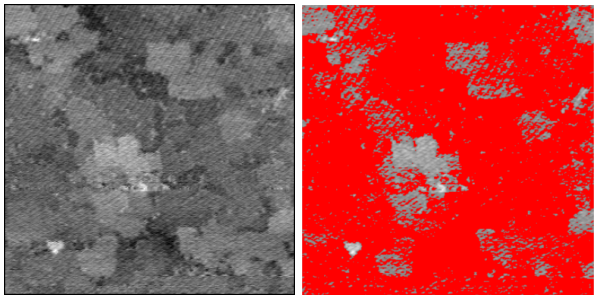

(g) Thickness:2nm (h) Thickness:2nm
Size:1μm$\times$1μm

Fig. 3.29 Example AFM images for the different layer thickness of CuMnAs with Al cap showing the original (left) and processed (right) images. The red colour in the processed images is the areas determined by the processing tool to be an area where CuMnAs is missing. The samples in descending order are Sample:4-1, Sample:4-2, Sample:4-3 and Sample:4-4.

This graph shows a rapid increase in the percentage of missing material as the layer thins. A rough functional form has been added to demonstrate this but there are too few points for a meaningful functional relationship.

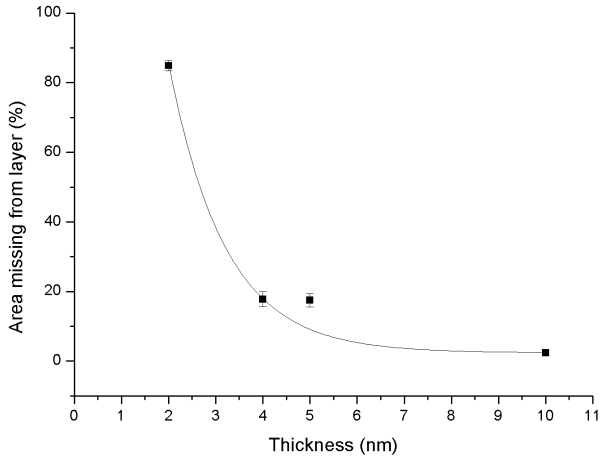

Fig. 3.30 Graph showing the effect of layer thickness on the percentage of an AFM image that is defined by image processing as a hole. Each data point represents the mean percentage for a range of images for that wafer. The samples used are Sample:4-1, Sample:4-2, Sample:4-3 and Sample:4-4.

3.5.3 Improving the surface quality of ultra thin film CuMnAs with different growth methods

The inability to grow a continuous ultra thin film of CuMnAs means that it is impossible to grow tunnelling structures to measure TAMR etc. For that reason this section will detail the effects of different nucleation and growth methods to reduce or eliminate the holes in these films. The surface quality and magnetisation results of five different approaches, which are detailed in figure 3.31, will be discussed. Four different nucleation layers were grown on quarters of the same semi-insulating GaP wafer and the final layer was grown on a quarter of a wafer from the same boule. The growth conditions from the other ultra thin film layers were used (section 3.5).

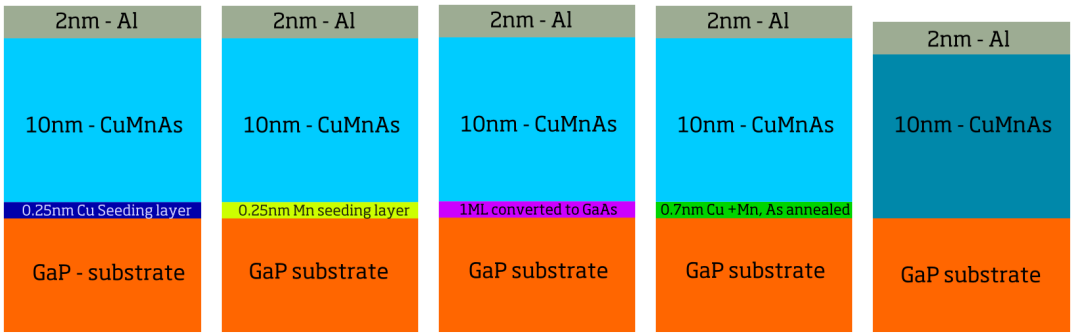

(a) Sample:5-1 (b) Sample:5-2 (c) Sample:5-3 (d) Sample:5-4 (e) Sample:5-5

Fig. 3.31 Schematics of the different growth mechanisms for ultra thin film.

The four seeding layers (figures 3.31a - 3.31d) were grown with an initial growth temperature in the region of 265°C-290°C, measured by the band edge, which then rose during the growth to 300°C-310°C. Figure 3.31e was grown at a growth temperature of 209°C, which rose to 263°C during the growth. The band edge measurements for these samples are shown in figure 3.32 The thermocouple set point remained steady throughout so the increase was due to radiant heating from the sources and increased thermal absorption due to the increasing free carrier absorption.

For the Cu seeding layer (figure 3.31a, Sample:5-1) extra crystalline features became visible on the RHEED as the seeding layer was deposited, as demonstrated in figure 3.33c, when the normal growth was commenced these disappeared halfway through the CuMnAs layer growth and the expected 2 by (figure 3.33b) and 1 by (figure 3.33a) were observed. The one by direction is at 45°. For both the Mn seeding layer (figure 3.31b, Sample:5-2) and the As converted mono layer (figure 3.31c, Sample:5-3), when all three fluxes were applied the expected RHEED reconstruction was observed within twenty seconds of the growth commencing. For the dual element seeding layer (figure 3.31d, Sample:5-4) the Cu and Mn seeding layer was deposited and then the fluxes were shuttered off. The sample was then exposed to As for several minutes. During this time the RHEED pattern recovered from a spotty pattern (figure 3.33d) with just the Cu and Mn to the expected CuMnAs reconstruction

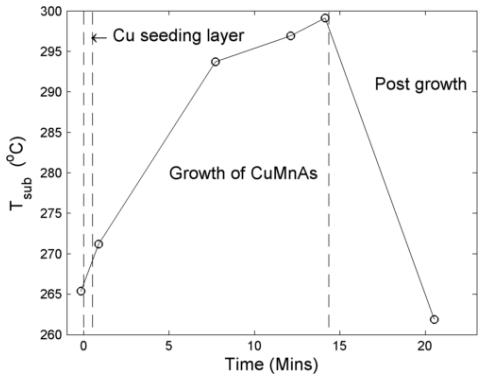

(a) Cu seeding layer (Sample:5-1)

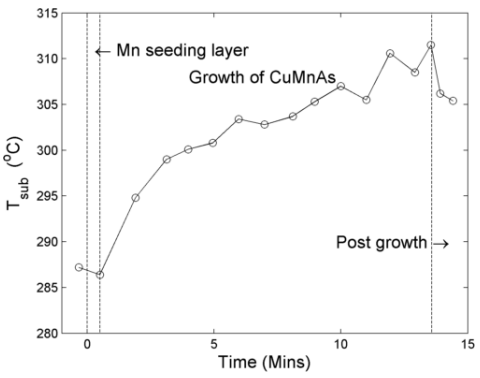

(b) Mn Seeding layer (Sample:5-2)

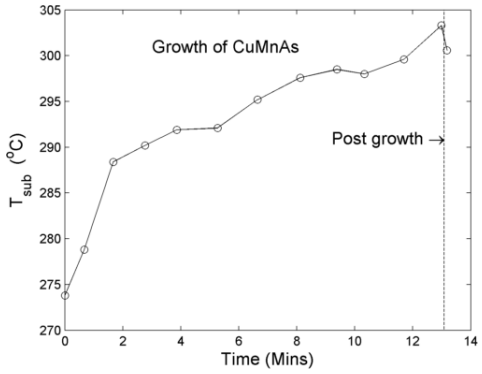

(c) As converted layer (Sample:5-3)

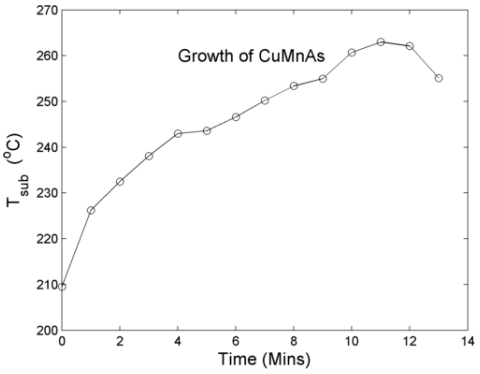

(d) Colder Substrate temperature (Sample:5-5)

Fig. 3.32 Temperature measured by the band edge for different growth methods of ultra thin films of stoichiometric CuMnAs.

with some extra spots along the streaks (figure 3.33c). When the growth was resumed these disappeared and towards the end of the growth second order spots were visible along the one by direction. During the lower temperature growth (figure 3.31e) the expected RHEED pattern emerged quickly and halfway through the growth the second order dots were again visible along the one by direction.

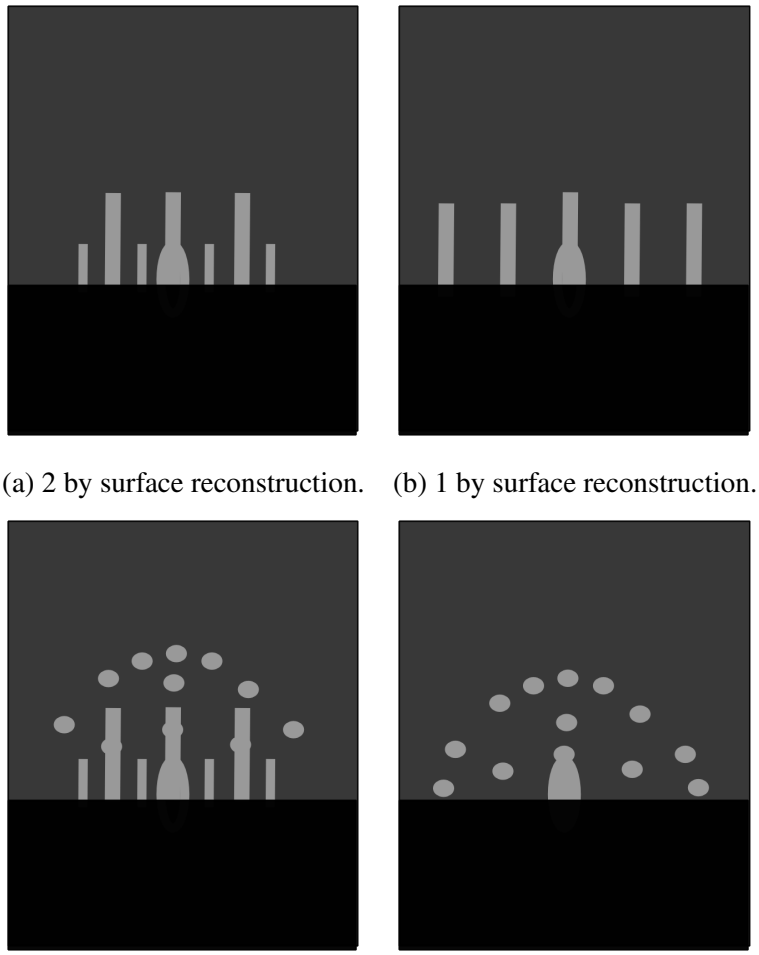

(a) 2 by surface reconstruction.

(b) 1 by surface reconstruction.

(c) 2 by surface reconstruction with the emergence of an aligned secondary phase imposed.

(d) Spotty surface reconstruction observed by RHEED for a Cu and Mn seeding layer.

Fig. 3.33 Schematic images of the different surface reconstruction observed by RHEED whilst growing CuMnAs.

Analysis by surface characterisation

AFM was performed on all the layers in several arbitrary locations and at different scan sizes. The images were analysed using the image processing protocols described in 2.4.1.

For the single element seeding layers we see similar surfaces in the AFM with a comparable percentage of holes which is shown in figure 3.34. In these images we see the profile of several holes in the material that are of nearly the same depth as the film and flat along the bottom with a width of up to 100nm. It should also be noted that in figure 3.34a thin inclusions that can be seen along the edges are from distortions in the layer caused by defects in the buffer layer.

For the dual element seeding layer Sample:5-4 the AFM images, see figure 3.36, reveal that there is a substantial improvement in the surface quality of the CuMnAs. The cooler substrate growth temperature (figure 3.35) also shows a clear improvement in the surface quality but still contains some holes. However these are different in shape having an angled edge and only being the thickness of the layer at a sharp point.

Using the image analysis protocol (section 2.4.1) the percentage of holes in each of the seeding layers can be compared and the values are listed in table 3.8. This table clearly shows that the three single element seeding layers have caused an increase in the number of holes from the plain layer by a factor of around 4 and a significant increase in the RMS. However for the joint seeding layer and the cold growth temperature the percentage of holes has reduced to approximately the experimental error, and the RMS has more than halved. For both of these two layers especially the Cu and Mn seeding layer the calculated holes are partly caused by artefacts from the AFM. Both of these layers were then further investigated by SQUID, XRD (which will be discussed presently) and transport measurements will be discussed in 5.4.2.

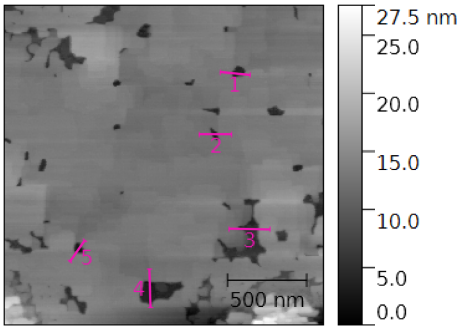

(a) Cu seeding layer Sample:5-1

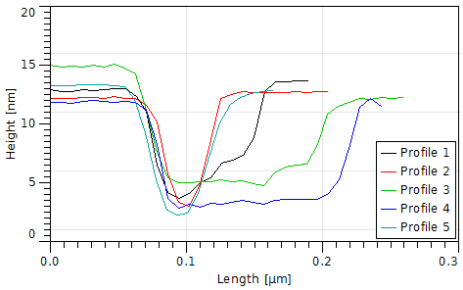

(b) Profiles

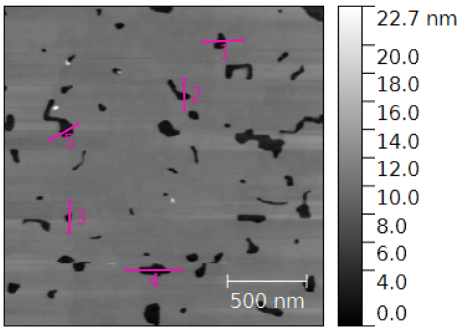

(c) Mn seeding layer Sample:5-2

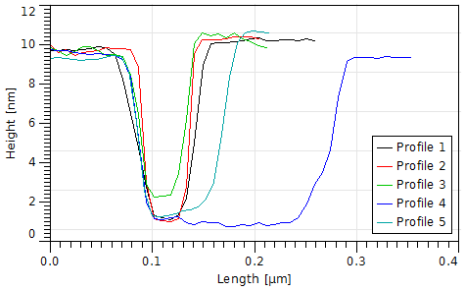

(d) Profiles

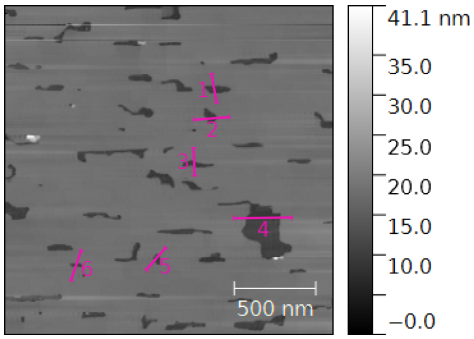

(e) Converted GaAs surface Sample:5-3

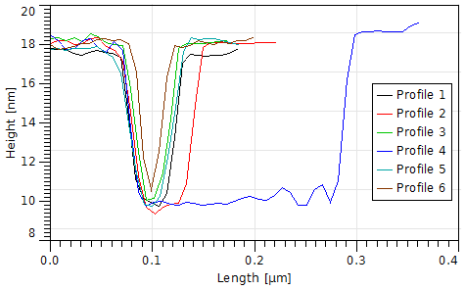

(f) Profiles

Fig. 3.34 2μm×2μm AFM images for three different single element seeding layers paired with the selected profiles from the image. All of the images show holes in the layers (darker areas).

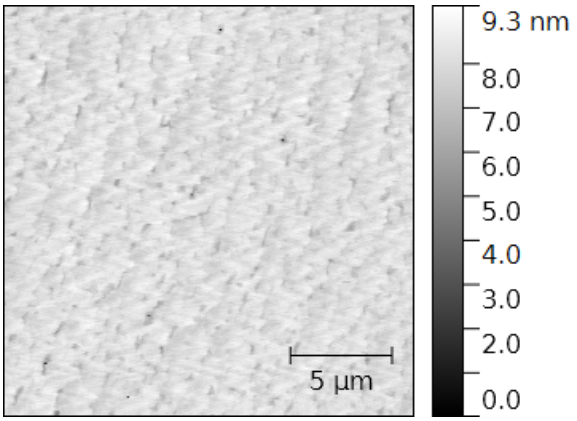

(a) 20μm×20μm

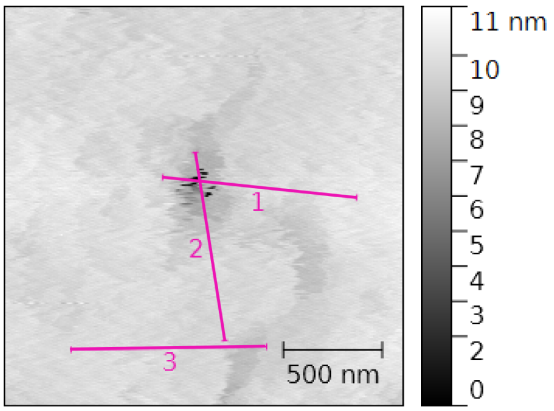

(b) 2μm×2μm

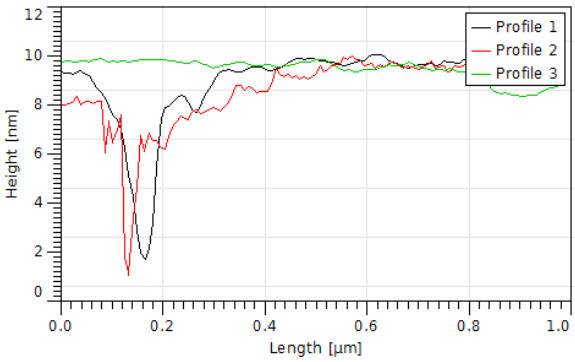

(c) Profiles

Fig. 3.35 AFM images for the lower substrate temperature growth of 10nm CuMnAs (Sample:5-5) with corresponding height profiles of the layer. The zigzag pattern over the AFM images is due to electrical noise.

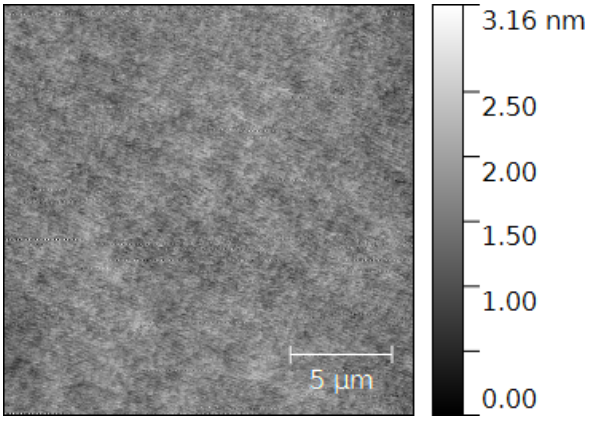

(a) 20μm×20μm

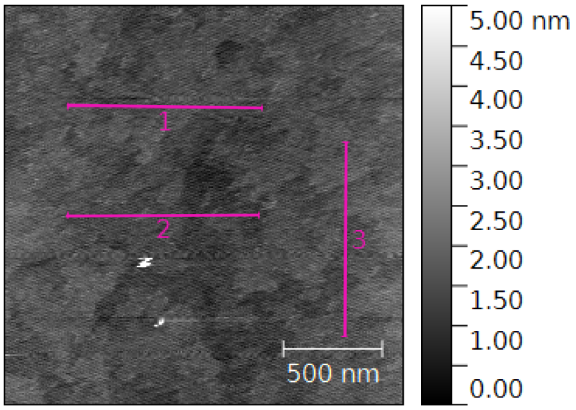

(b) 2μm×2μm. The colour scale of the image has been altered so that the surface is visible.

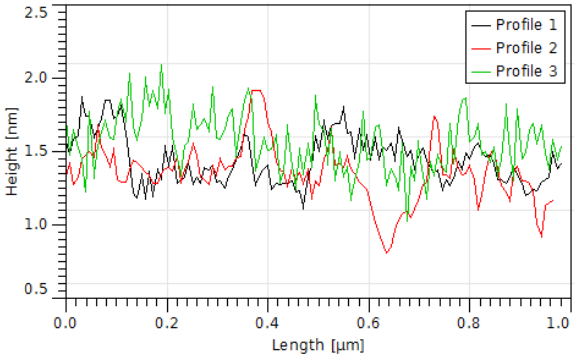

(c) Profiles corresponding to the numbered lines on 3.36b.

Fig. 3.36 AFM images for the Cu and Mn seeding layer of 10nm CuMnAs (Sample:5-4). Electrical noise is visible on the AFM images.

Sample	Growth Method	Percentage of Holes	RMS (nm)
Sample:3-1	Standard	$(2.4 \pm 0.4)\%$	(1.1 ± 0.2)
Sample:5-1	Cu seeding layer	7.8%	2.24
Sample:5-2	Mn seeding layer	$(9.3 \pm 0.6)\%$	(1.86 ± 0.09)
Sample:5-3	As mono layer	$(8.4 \pm 0.3)\%$	(1.85 ± 0.04)
Sample:5-4	Cu & Mn seeding layer	$(0.09 \pm 0.07)\%$	(0.36 ± 0.03)
Sample:5-5	Cold T_{sub}	$(0.10 \pm 0.07)\%$	(0.46 ± 0.04)

Table 3.8 The percentage of missing material and RMS values for layers with different growth methods. The copper layer has no listed error as due to problems with the growth of the buffer layer there were other features, that made the measurement of holes implausible.

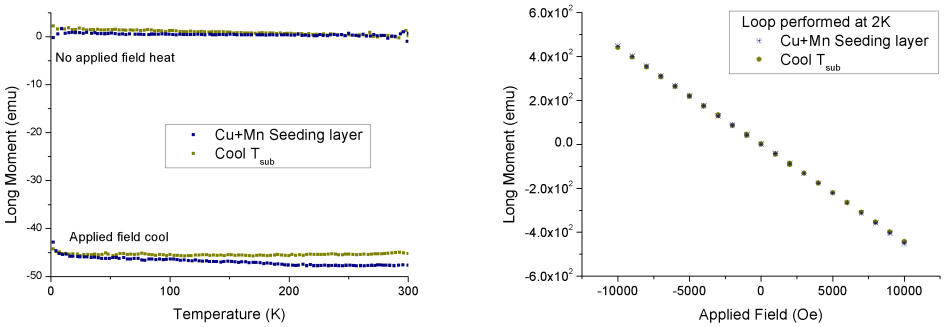

(a) Field cool and remnance heat

(b) Hysteresis loops performed at 2K

Fig. 3.37 The projected magnetization of layers along an in plane axes from SQUID results, for 10nm CuMnAs with a Cu and Mn seeding layer Sample:5-4 (orange) and for 10nm CuMnAs with a cooler substrate temperature Sample:5-5 (navy).

Analysis by Magnetic characterisation

Following on from the AFM results the two most successful growth methods were measured using SQUID. For both samples the standard SQUID measurements were taken. In both samples there was no sign of any ferromagnetic behaviour (figure 3.37) so it could be concluded that no secondary FM phases have formed. From the applied field cool data there is a small temperature dependence at low temperature, which could be indicative of PM behaviour. From section 3.3.2 the number of Bohr magnetons per unit volume would be very small compared to the number of Bohr magnetons per unit volume for antiferromagnetic Mn.

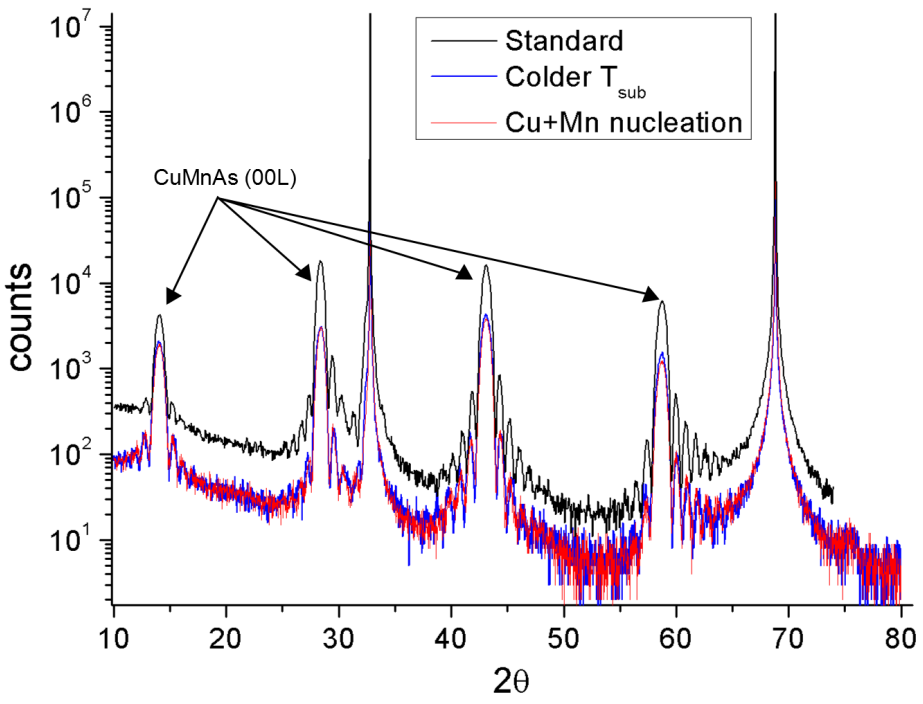

Fig. 3.38 2θ XRD scans for 10nm layers of CuMnAs. The black line is for standard growth conditions (Sample:3-1). The blue line, obscured by the red line, is for a sample grown with a cooler T_{sub}(Sample:5-5) and the red line is for a nucleation layer of Cu and Mn (Sample:5-4). The two unlabelled peaks are the GaP (004) and (002).

Analysis of crystal quality by XRD

The diffraction peaks for the two successful growth techniques for ultra thin films of CuMnAs are compared to a standard layer (Sample:3-1) in figure 3.38. The scans show that the three layers have an excellent and comparable crystal quality. The difference in the standard layer scan are caused by differences in the set up of the line scan as it was performed at a separate time. The CuMnAs (00L) peaks are labelled in the figure and there are fringes around these peaks, but not the GaP peaks. These fringes are called finite size fringes and using fitting software an accurate layer thickness can be calculated from them, discussed in section 2.2.1.

3.6 Conclusion

This chapter started by discussing the MBE growth conditions needed to grow stoichiometric and non-stoichiometric CuMnAs. XRD was used to demonstrate the tetragonal crystal lattice of CuMnAs. We can also use XRD to show the varying crystal quality for different substrates. Neutron diffraction was used to establish that the spin axis is confined to the *ab* plane so that the spins couple FM in plane and AF out of plane. Neutron diffraction also demonstrated a T_N of (480±5)K [114]. When stoichiometric samples of CuMnAs are studied with magnetometry there is no sign of FM behaviour from any secondary phases. When the surfaces of CuMnAs on GaAs and GaP are studied with AFM there are variations in the surface though both display a cross hatching pattern that lies along the principal axis of the CuMnAs.

In the non-stoichiometric CuMnAs, which was grown with a Mn and As excess, the magnetometry data shows the presence of a strong ferromagnetic element from a secondary phase, which has a T_C above room temperature, that could be MnAs. The results of AFM and MFM show large ferromagnetic inclusions on the surface of this sample which implies a growth model where the CuMnAs has grown preferentially and the excess material has migrated significant distances to form large clusters.

Three different methods have been used to calculate the possible percentage of MnAs in the non-stoichiometric sample using the growth fluxes, magnetometry information, and the percentage of inclusions on the AFM. These different techniques have given estimates of the percentage of MnAs between 13% to 24%.

Finally this chapter discussed the surface and crystal quality of ultra thin films of CuMnAs on GaP and found that there is a thickness dependent element to the CuMnAs layers ability to remain on the substrate during cooling. Several different nucleation and growth methods were tried to improve this problem and it was found that the most effective solution was to deposit a thin layer of Cu and Mn and then anneal As into this before commencing

with the layer growth. The second most effective method was to significantly lower the growth temperature. Both the dual nucleation and reduced growth temperature have produced excellent quality crystals when measured by XRD and show no signs of secondary phases in SQUID measurements.

Chapter 4

Growth and Characterisation of $CuMn(As_{(1-x)}P_x)$

4.1 Introduction

$CuMn(As_{(1-x)}P_x)$ is an alloy of CuMnAs where phosphorus is incorporated substitutionally on to As lattice sites in the CuMnAs tetragonal lattice. The motivation for growing $CuMn(As_{(1-x)}P_x)$ is to increase the band gap of tetragonal CuMnAs towards the theoretical band gap predicted for CuMnP [38]. R. Campion and V. Novàk previously attempted to grow CuMnP by MBE at Nottingham, but found that it strongly phase separated into Manganese phosphide (MnP) and other compounds of Cu and As, the MnP was detected due to it's prominent magnetic signal in SQUID. Phosphorus is a smaller group V element and will compete with the As for the sites. If the phosphorus incorporates it will reduce the lattice parameters causing the Mn atoms to lie closer together. This would possibly cause the T_N of the material to increase. The competition between the group V elements can be very temperature dependent as they compete for the same lattice sites. The arsenic dimer bond is weaker than the phosphorus dimer bond and phosphorus will also re-evaporate at a higher rate than As.

This chapter will discuss the MBE growth conditions used for three different growth series of epitaxial CuMn($As_{(\mathbf{1-x})}P_{\mathbf{x}}$). Then the samples will be characterised by several techniques. XRD will be used to establish the crystal structure and compare the lattice constants with CuMnAs and the proportion of phosphorus. Neutron diffraction will be used to establish and compare the spin axis of CuMn($As_{(\mathbf{1-x})}P_{\mathbf{x}}$) with that of CuMnAs. The magnetometry of the samples will be studied with SQUID to detect the presence of any secondary phases. Finally the surfaces of the samples will be characterised by AFM.

4.2 Growth of CuMn($As_{(1-x)}P_x$)

All the samples in this section were grown in a Veeco Gen III MBE machine, described in section 2.1.1. The phosphorus flux was produced from the thermal decomposition of GaP and the arsenic beam was set-up as As_4.

4.2.1 First growth run

A sulphur doped GaP (001) wafer was used to grow the two samples in growth series 6. High temperature GaP buffer layers of 100nm were grown on the day proceeding each layer growth. The samples were grown with the same ratio of Cu:Mn as stochiometric CuMnAs (1:1) and the As overpressure was reduced to compensate for the P. The As flux was set at the same value for every CuMn($As_{(\mathbf{1-x})}P_{\mathbf{x}}$) growth regardless of the P flux. The T_{TC} was set to 280°C, which from later work with band edge temperature measurements could correspond to a temperature as low as T_{sub}=230°C.

During the growth of Sample:6-1 at the commencement of the growth there was an immediate change in the RHEED. A streaky 2x2 reconstruction formed along the [110] and [1$\bar{1}$0] directions with a 1x construction at 45°. The 2x2 reconstruction was well defined and streaky and is shown in figure 4.1; The streaky nature of the 2x2 reconstruction implies that

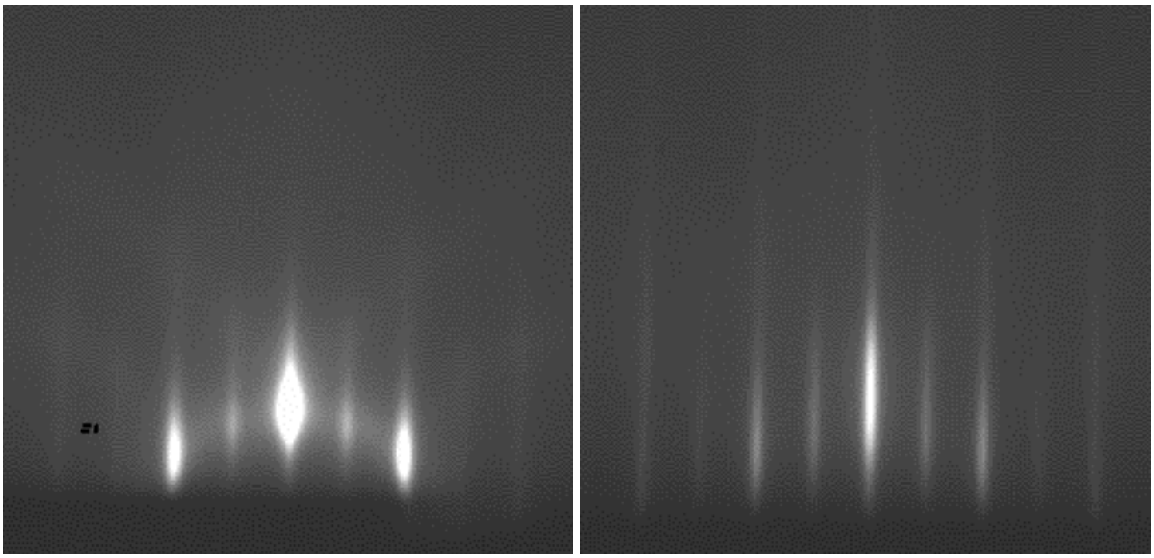

(a) [110] (b) [$1\bar{1}0$]

Fig. 4.1 RHEED images aligned along the noted axis for the first growth of CuMn($As_{(\mathbf{1-x})}P_{\mathbf{x}}$) with a P flux of 1×10^{-8}Torr Sample:6-1.

2D single crystal growth was occurring. Arcing occasionally occurred on the RHEED during the growth due to the build up of charge on the sample holder.

A thick layer of CuMn($As_{(\mathbf{1-x})}P_{\mathbf{x}}$) was grown over several hours at an assumed growth rate of 46nm/hr from the calibrated CuMnAs growth rate, which gives a layer thickness of 214nm, using a reduced As over pressure and a phosphorus flux of 1×10^{-8}Torr. However the thickness is likely to be smaller due to the change in lattice size from the alloying of phosphorus.

Sample:6-2 was grown with the same As flux but an increased phosphorus flux of 2×10^{-8}Torr. The layer initially grew with a streaky 2x2 RHEED with a wide gap at 45°, however during the growth the surface became rougher and the RHEED showed that non 2D growth was developing. The growth was stopped before it fully phase separated and the layer thickness is believed to be 200nm using the growth rate for CuMnAs.

4.2.2 Second growth run

Sample:7-1 is the only sample in series 7. Sample:7-1 was grown on undoped GaP (001) with a high temperature buffer of GaP the preceding day and then coated with a cap of P and then As_4 to protect the surface. The cap was evaporated off the surface at T_{TC}=300°C immediately before the layer growth. The CuMn($As_{(\mathbf{1-x})}P_{\mathbf{x}}$) layer was grown at a T_{TC} =280°C for an estimated thickness of 50nm based on the growth rate of CuMnAs. From later band edge measurements of similar undoped GaP (001) wafers the substrate temperature could be 280°C. The layer was grown with the same As and P fluxes as Sample:6-1.

During the growth the RHEED image formed a streaky 2x2 reconstruction. By halfway through the growth there was some indication of an alternative reconstruction or a second phase developing that stabilised as the growth developed. The LAOS showed no change in the surface roughness during the growth.

4.2.3 Third growth run

This growth series, series 8, was grown sequentially on quarters of the same wafer of undoped GaP (001). The wafer was single side polished, unlike the preceeding layers grown on double polished wafers. After oxide removal a high temperature buffer layer of GaP was grown before cooling to the CuMn($As_{(\mathbf{1-x})}P_{\mathbf{x}}$) growth temperature. The elemental fluxes were matched to those used in the first growth run of CuMn($As_{(\mathbf{1-x})}P_{\mathbf{x}}$). The substrate temperature was measured by band edge measurements, described in section 2.1.2, and a starting T_{sub} between 260-270°C. By having a non static heater temperature the T_{sub} was kept below 275°C during the growth.

The first three samples in the series were grown for the same time, which was estimated to be 40nm/hour from the calibrated CuMnAs growth rate. All of the samples were grown with a seeding layer of CuMnAs, where 0.7nm of Cu and Mn were co-deposited before the surface was then exposed to solely an As_4 flux for several minutes during which time the RHEED

developed into the start of a 2x2 reconstruction along the [110] and [1$\bar{1}$0] directions. RHEED observations were made throughout all the growths and in the two lower P flux samples strong RHEED reconstructions were observed similar to those in Sample:6-1. Sample:8-4 showed strong signs of a second phase appearing on the RHEED after 10nm of growth. The second phase appeared on the RHEED as a series of small aligned dots in a series of semi circles.

The phosphorus fluxes are listed in the initial section of samples used in this thesis in tables 6, 7 and 8.

4.3 Characterisation of CuMn($\mathbf{As_{(1-x)}P_x}$)

The samples were characterised by several different methods. The crystal structure was analysed by XRD. This demonstrated if the phosphorus had incorporated into the crystal structure and caused changes to the lattice constants, which allowed for the comparison of the different concentrations of phosphorus and the study of the effect of different growth conditions on the incorporation of phosphorus into the CuMn($\mathbf{As_{(1-x)}P_x}$). The magnetic structure of Sample:6-1 was determined by neutron diffraction and compared to that of CuMnAs and the temperature dependence was able to give an indication of the T_N for this sample. Magnetometry measurements were taken for samples from the different growth runs. The magnetometry information demonstrated if there were any secondary magnetic phases. The surfaces were characterised by AFM to study the surface quality.

4.3.1 Bulk

Determination of the crystal structure by XRD

Figure 4.2 shows the CuMnAs $(00l)$ peaks (and GaP (004) and (002) substrate peaks). From the measurements it is clear that CuMn($\mathbf{As_{(1-x)}P_x}$) shares the same structure and diffraction peaks as CuMnAs. From the inset in the figure there is a marked shift in the peak position,

which shifts monotonically with the increasing phosphorus flux. The peaks also become broader with the increasing phosphorus flux and decrease in intensity. The lattice parameter is calculated from fitting to the (003) peak. Figure 4.3 shows the change in the value of the lattice parameter with increasing phosphorous flux. The change in the lattice parameter from CuMnAs/GaP ($\Delta\mathbf{c}$) increases with the applied phosphorus flux. This is because the lattice is under tensile strain to match the diagonal of the GaP substrate. This causes the *ab* plane to stretch to match and the *c* axis to compress. At the maximum phosphorus flux the change in the lattice constant is comparable to the lattice mismatch between CuMnAs/GaAs.

For a significantly thicker layer of CuMn($As_{(\mathbf{1-x})}P_{\mathbf{x}}$) (Sample:6-1) there is a marked difference in the lattice peak position for the comparable applied phosphorus flux, as shown in figure 4.4. The thicker layer has a shifted diffraction peak that coincides closely with the peak for the lower applied phosphorus flux in the other growth series (Sample:8-1). The intensity of the peak is markedly lower and broader than the other diffraction peak though, which is highlighted in figure 4.5. The difference between the *c* axis parameters for the layers with $F_P = 1.0 \times 10^{-8}$Torr could be due to the thicker layer surpassing a critical thickness and relaxing. Alternatively it could be due to different T_{sub} during the growth causing a change in the competition between the arsenic and phosphorus so that a lower proportion of phosphorus has incorporated into the layer.

Determination of the magnetic structure by neutron diffraction

Sample:6-1 was studied at the WISH [135] beamline at ISIS with P. Wadley, D. Khalyavin and myself. The direction of the spin axis was first compared to that of CuMnAs, which results are described in 3.3.1, and then the temperature dependence of the CuMn($As_{(\mathbf{1-x})}P_{\mathbf{x}}$) was studied. Two magnetic peaks were again studied for CuMn($As_{(\mathbf{1-x})}P_{\mathbf{x}}$), the (100) purely magnetic peak and the (001) magnetic and structural peak, which are shown in figure 4.6.

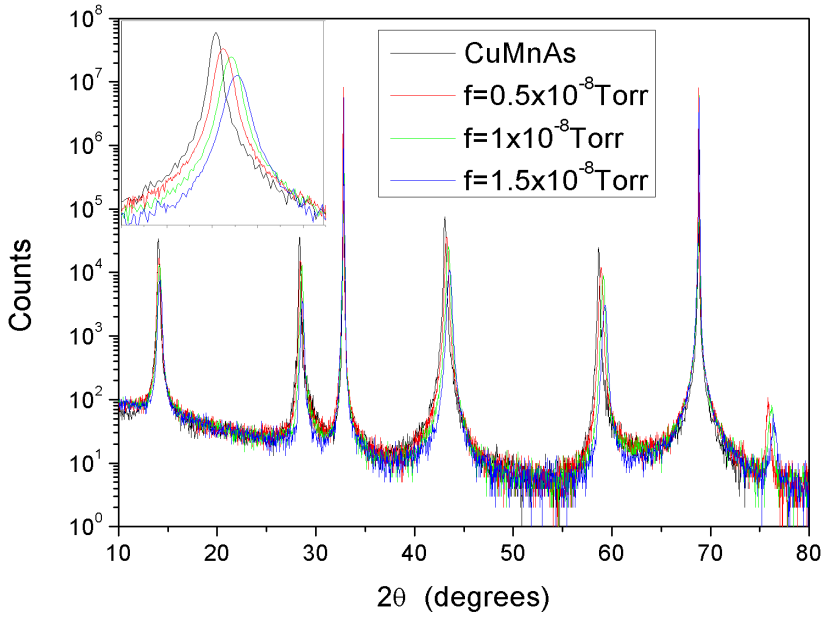

Fig. 4.2 2θ scans in XRD for the series of samples 8. The black line is a 50nm film of CuMnAs/GaP, red is an applied phosphorus flux of 0.5×10^{-8}Torr (Sample:8-1), green is an applied phosphorus flux of 1.0×10^{-8}Torr (Sample:8-2) and blue is an applied phosphorus flux of 1.5×10^{-8}Torr (Sample:8-3). The inset shows an enlarged area of the diffraction peak around 45°.

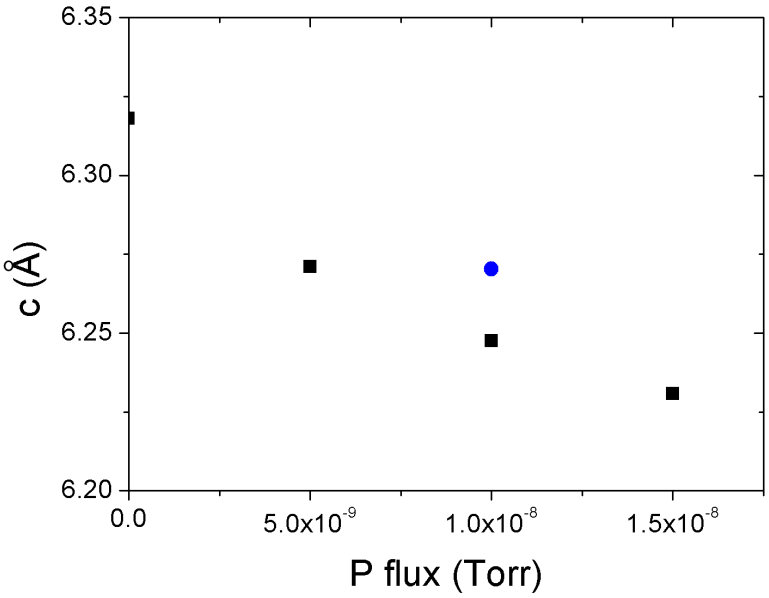

(a) c lattice constant

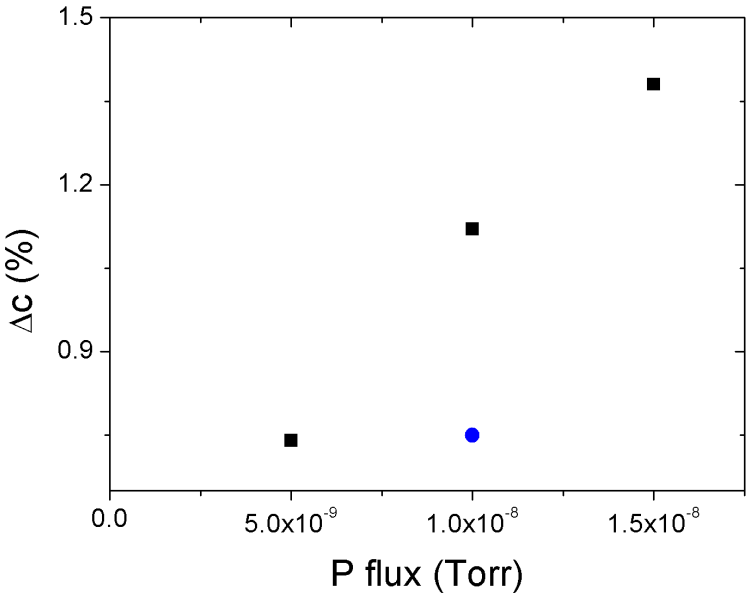

(b) Percentage change in c from CuMnAs

Fig. 4.3 Comparing the lattice constant against the P flux. The black dots are the following samples in increasing P flux: Sample:1-3, Sample:8-1, Sample:8-2 and Sample:8-3. The blue dot is Sample:6-1, which is significantly thicker that the other samples.

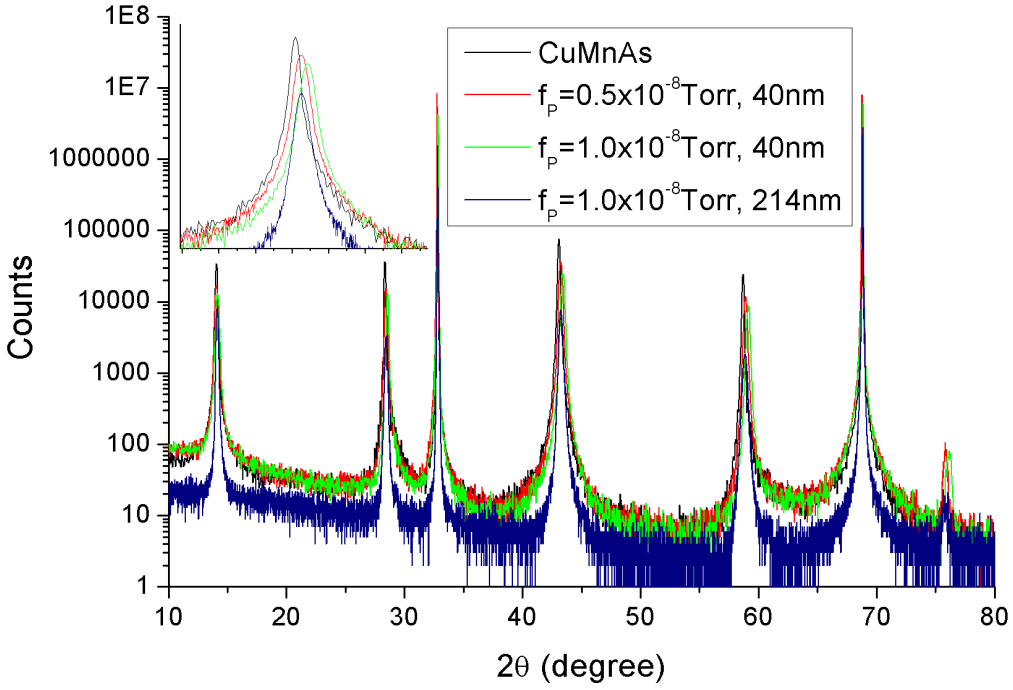

Fig. 4.4 2θ XRD scans of CuMn($As_{(\mathbf{1-x})}P_{\mathbf{x}}$) showing the difference in peak position and height for a thick layer of CuMn($As_{(\mathbf{1-x})}P_{\mathbf{x}}$) with a P flux of 1.0×10^{-8}Torr (Sample:6-1), in navy, compared to the thinner layers (Sample:8-1 with 0.5×10^{-8}Torr (red), Sample:8-2 with 1.0×10^{-8}Torr (green)). The black line is a reference sample of 50nm CuMnAs/GaP. The inset shows an enlarged area of the diffraction peak around 45°.

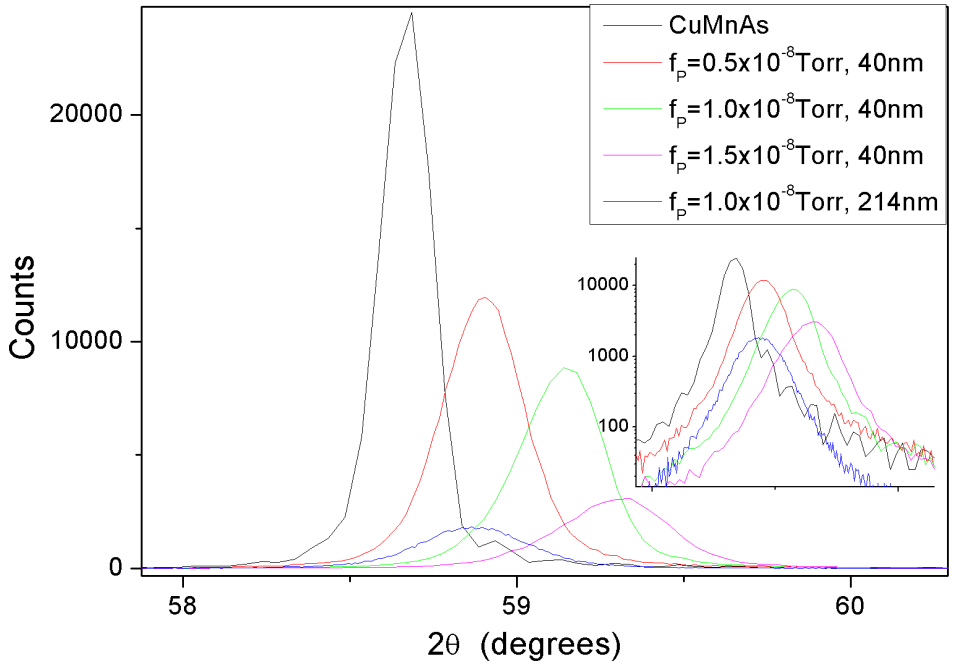

Fig. 4.5 The difference in intensity for the diffraction peaks for CuMn($As_{(1-x)}P_x$) layers on a linear scale. The inset shows the same peak on a logarithmic scale. The coloured lines are black - CuMnAs, Red - Sample:8-1, green - Sample:8-2, pink - Sample:8-3 and blue - Sample:6-1.

The presence of these peaks demonstrates that the magnetic spins are confined to the *ab* plane and have the same spin structure as CuMnAs.

The temperature dependence was measured in the (100) reflection, as shown in figure 4.7. It is apparent that at 550K the purely magnetic (100) reflection has disappeared, as the sample has transitioned to an unaligned magnetic phase. If the intensity of the (100) reflection is plotted at several different temperatures the intensity of the diffraction peak as the strength of the magnetic ordering decrease with the increasing temperature until a T_N of (500.0 ± 0.1)K. The T_N was calculated using the same functional form as the (001) reflection of CuMnAs shown in

$$f(T) = \alpha(T_N - T)^{0.4037} + d \tag{4.1}$$

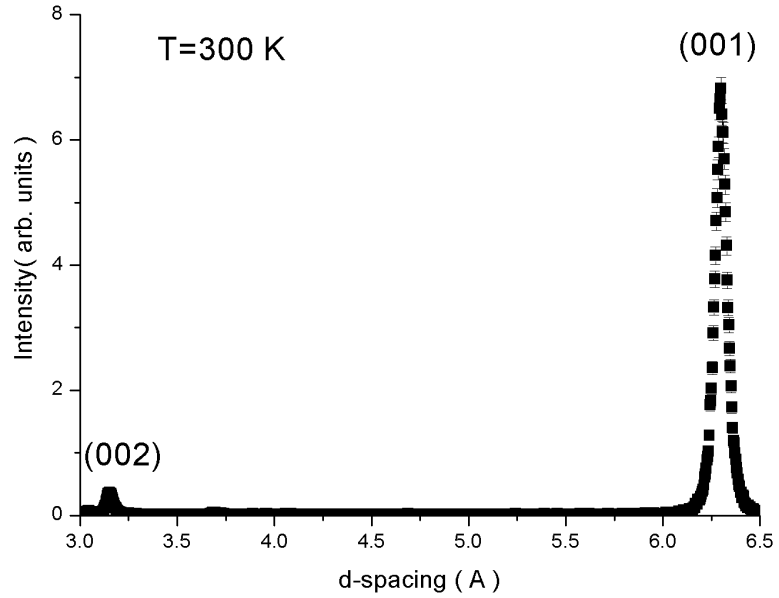

(a) (001) peak

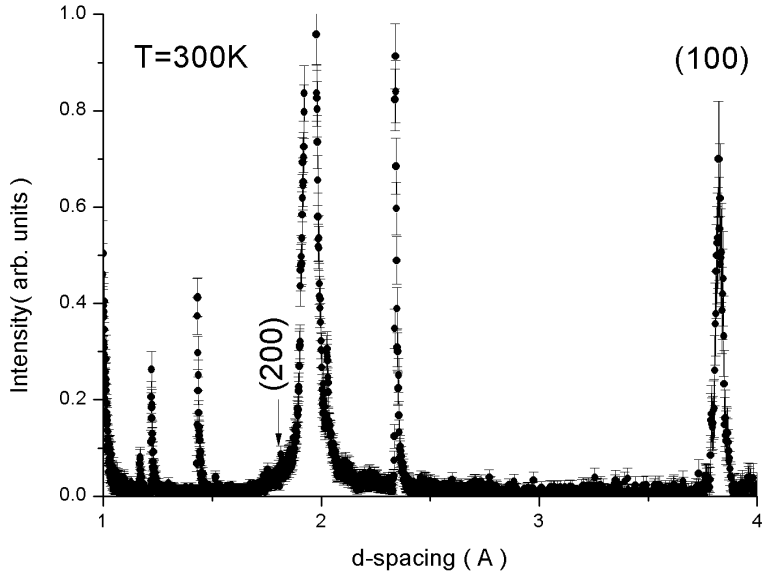

(b) (100) peak

Fig. 4.6 Neutron diffraction peaks for CuMn($As_{(1-x)}P_x$) (P flux of 1.0×10^{-8}Torr, Sample:6-1) at room temperature. The unlabelled peaks are from the substrate.

Due to the limited data for this sample the power component was fixed at the value of 0.4037 from fitting CuMnAs (001). The intercept (d) was set as the percentage integrated intensity at 550K, the gradient, α value was calculated as $(6 \pm 1)\mathrm{K}^{-1}$ for the blue fit in figure 4.8. The calculated value of the T_N from the fitting has an unexpectedly small error considering the error that could have arisen from the temperature measurement and the limited number of data points. If the data point at 500K is excluded from the fitting (purple line in figure 4.8) then a different T_N is predicted, with a very large error. From figure 4.8 the region between these two fits could be taken to be the likely value of T_N for Sample:6-1. A more accurate reading could be achieved if more data points were available. The temperature of the sample was measured by a thermocouple which was not directly mounted on to the sample so there is likely to be a temperature offset between the two. The limited number of data points is due to technical issues during the beam time limiting the number of measurements that could be made.

4.3.2 Magnetometry by SQUID

Figure 4.9 shows the temperature dependence of the magnetic response for several different CuMn($As_{(\mathbf{1-x})}P_{\mathbf{x}}$) samples that were mounted in plane to the applied field. Figure 4.9a shows the response for the sample being cooled in a field of 1kOe and figure 4.9b shows the response for the sample when heated without an applied field. The diamagnetic background has not been removed in these measurements. Sample:6-1 demonstrates the smallest magnitude of magnetisation in the field cool. Both Sample:8-1 and Sample:8-2 show little temperature dependence in the field cool. Sample:8-3 shows some temperature dependence in the magnetisation in response to the external field. The temperature dependence could indicate the presence of some paramagnetic Mn in the layer. When there is no applied field on the samples there is a very small magnetic response, which implies that there is negligible magnetic secondary phase. Apart from Sample:8-3 which has a temperature dependence

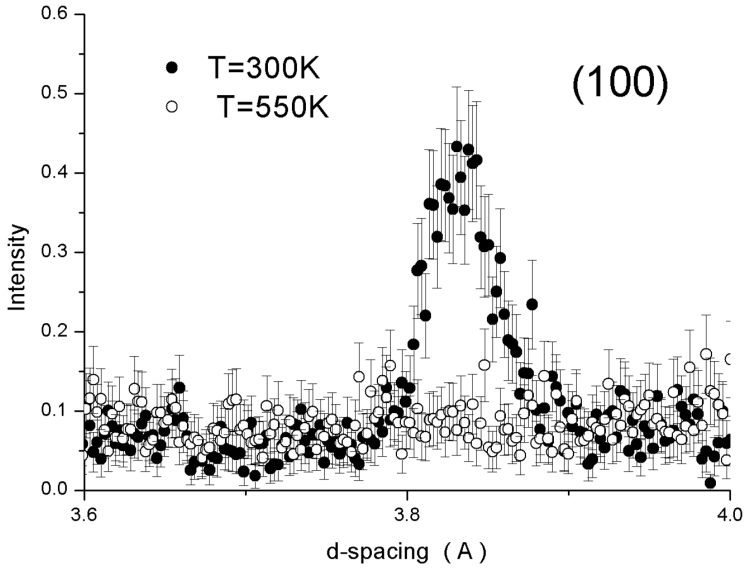

Fig. 4.7 Difference in intensity for (100) reflection at 300K and 500K for CuMn($As_{(\mathbf{1-x})}P_{\mathbf{x}}$), for Sample:6-1 with a P flux of 1.0×10^{-8}Torr.

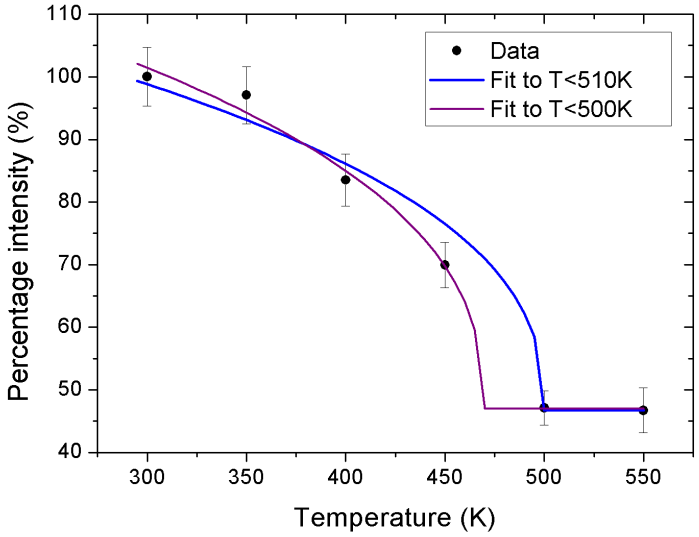

Fig. 4.8 Temperature dependence of (001) reflection between 300K to 550K for CuMn($As_{(\mathbf{1-x})}P_{\mathbf{x}}$), with a P flux of 1.0×10^{-8}Torr (Sample:6-1). The black dots are the measured data, the blue line is a fit to the data including all the data points below 510K and the purple line is a fit to the data including all the data points below 500K.

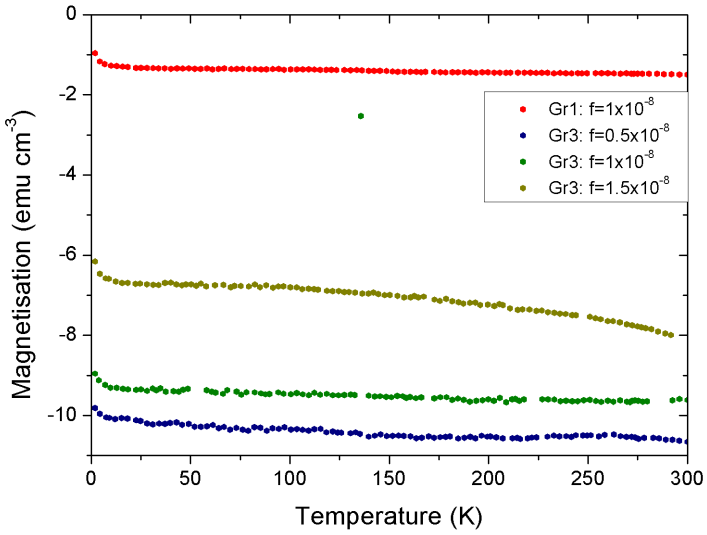

(a) Field Cool (F=1KOe)

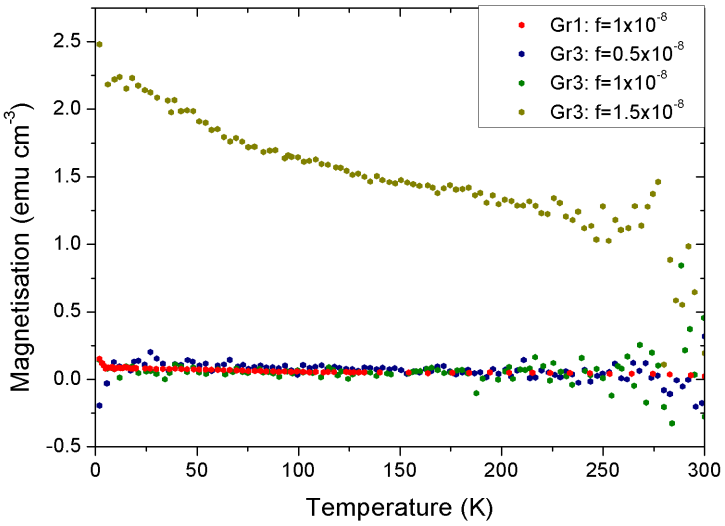

(b) Remnant Heat (F=0Oe)

Fig. 4.9 SQUID magnetometry measurements for different CuMn($As_{(1-x)}P_x$) samples. Showing the projection of the magnetization along one of the in plane axes. Red is Sample:6-1with a P flux of 1.0×10^{-8}Torr, blue is Sample:8-1 with a P flux of 0.5×10^{-8}Torr, green is Sample:8-2 with a P flux of 1.0×10^{-8}Torr and yellow is Sample:8-3with a P flux of 1.5×10^{-8}Torr.

and a larger signal. The noise increases in the long moment with no applied field due to a physical problem with the SQUID system.

Sample:6-1 and Sample:8-2 have nominally the same applied phosphorus flux but are significantly different in thickness and it is unclear as to the difference in the substrate growth temperature, which could affect the amount of phosphorus included in the layer. The phosphorus and arsenic compete for the group V site and arsenic has the lower dissociation energy, which gives it the advantage, thus the incorporation of P will tend to be lower than the ratio of the fluxes would suggest where there is an overpressure of total group V fluxes. Another possible cause is any differences in the substrate quality. These reasons could therefore lead to the difference in the SQUID response for Sample:6-1 and Sample:8-2.

Sample:8-3 has the strongest temperature dependence in the magnetic response with and without an applied field. There are clear signs of a decreasing magnetic signal with temperature when there is an applied field where there may be a phase transition above the range measured. Due to the increasing noise signal in the measurement without an applied field it is difficult to make a fair conclusion about whether the material is about to undergo a phase transition. However it is clear that there is a markedly stronger magnetic response of an order of magnitude compared to Sample:8-1 and Sample:8-2. The strength of the magnetic response also decrease by 60% between 10K and 200K.

Sample:6-2 has complicated magnetometry data that is a clear indication of multiple competing phases occurring during the growth, which is not shown.

4.3.3 Surface topology by atomic force microscopy

AFM was used to characterise the surfaces of the different CuMn($As_{(\mathbf{1-x})}P_{\mathbf{x}}$) layers and compare them to CuMnAs. In this section images will be used to demonstrate and discuss the changes in features for different layers. The first comparison to be made is with the distinctive cross hatching pattern seen on CuMnAs. Figure 4.10 shows the changes in the

length and density of the cross hatching for a sample of CuMnAs (Sample:1-5) compared to the increasing P flux for series 8. It is possible to observe that the direction of the orientated lines remains the same throughout all the layers. The average length of the lines appears to decrease with the increase in the applied phosphorus flux. It is also possible to see a change in the behaviour of the lines. In figures 4.10a & 4.10b the lines tend to begin and end at intersections, whereas in figures 4.10c & 4.10d there are many lines that begin or terminate on their own and not at intersections. Figure 4.11 shows higher resolution images of the samples in series 8. Profiles of the surface have been taken across the edges of the cross hatching lines. The edges have a distinct shape of a sharp drop of 1nm followed by a shallower increase. When line profiles are taken across different steps in each image the same shape is measured. The images also faintly show a block pattern across the image that varies in height by a maximum of 0.5nm between blocks. The steps between these blocks are less than the size of the unit cell of the CuMn($As_{(\mathbf{1-x})}P_{\mathbf{x}}$) and could represent the growth edges of the layer or they could be due to the Al capping layer on the samples.

In some of the samples it is possible to see a range of extra irregular features to the cross hatching, these will be discussed in two paragraphs as holes and aligned scars or trenches. Figure 4.12 shows a range of unaligned holes seen on the samples in series 8. Sample:8-1 (figure 4.12a) shows one large hole which has a depth of 18nm and square lateral dimensions just under 1μm. There are also signs of very small holes over the surface at this image resolution. If a 20μm$\times$20μm image is examined then there are up to four of these large holes in the given area. In Sample:8-2 (figure 4.12d) there are small holes with a depth of up to 3nm across the film. The depth of these holes is less than 1% of the total film thickness. There is one hole with wider lateral dimensions and a peak in the middle, which could be due to a contaminant impinging on the surface during growth.

In the final figure (4.12e) for Sample:8-3 there is the presence of holes at least 20nm deep, which is $\geq$ 50% of the total film thickness. The holes have a square or rectangular

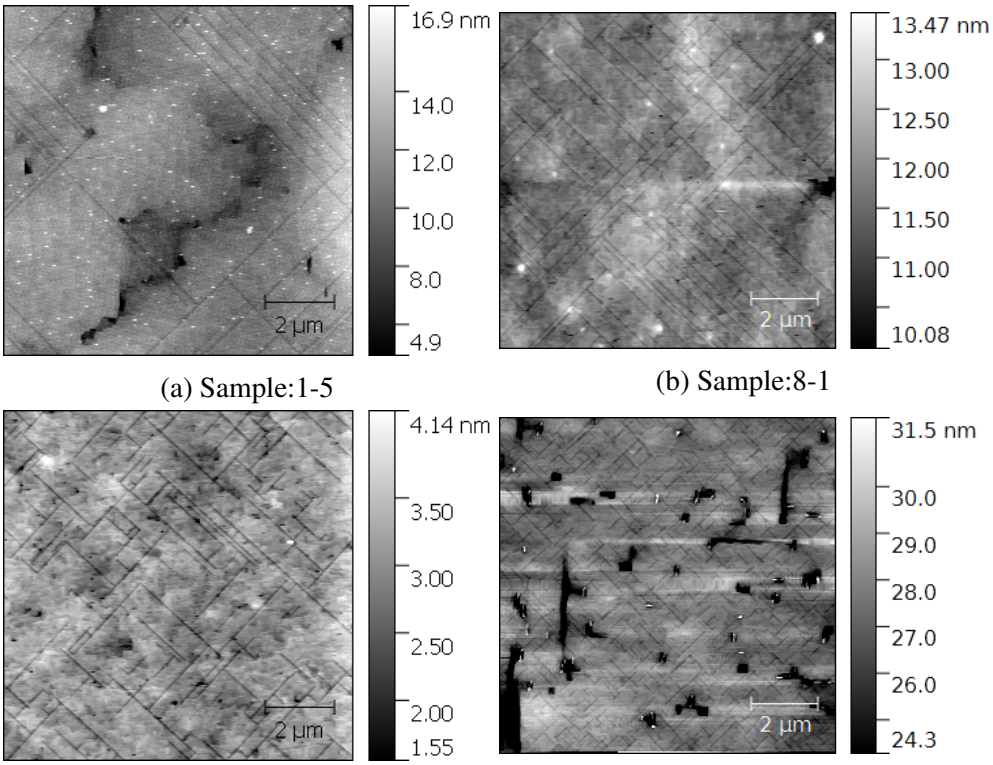

(a) Sample:1-5

(b) Sample:8-1

(c) Sample:8-2

(d) Sample:8-3

Fig. 4.10 10μm$\times$10μm AFM images of layers of CuMn($As_{(\mathbf{1-x})}P_{\mathbf{x}}$) samples from series 8, with increasing P flux of 0.5×10^{-8}Torr, 1.0×10^{-8}Torr and 1.5×10^{-8}Torr compared to a layer of stoichiometric CuMnAs (Sample:1-5). The colour scales have been restricted in all of the images to highlight the features.

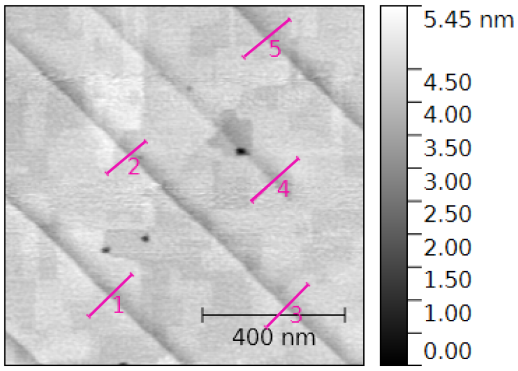

(a) Sample:8-1

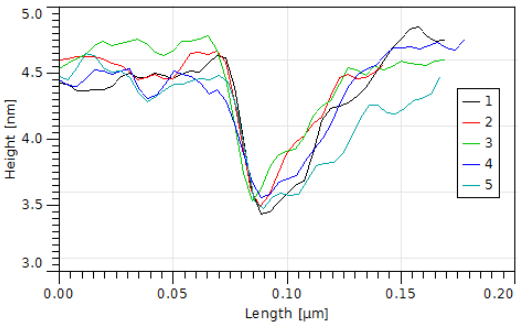

(b) Profiles

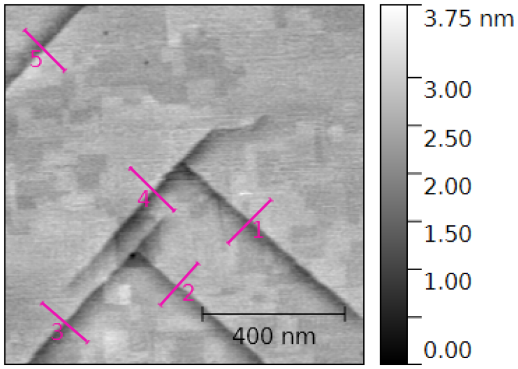

(c) Sample:8-2

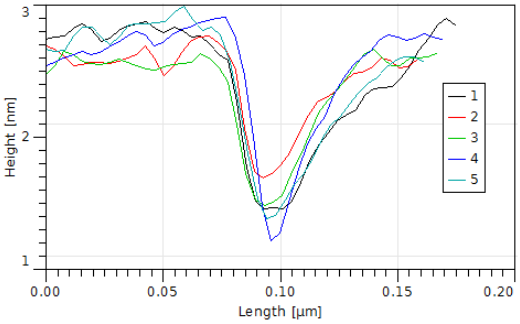

(d) Profiles

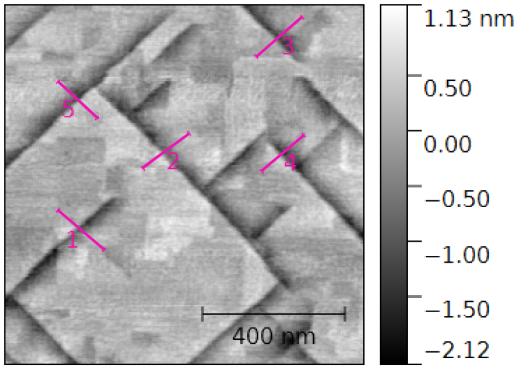

(e) Sample:8-3

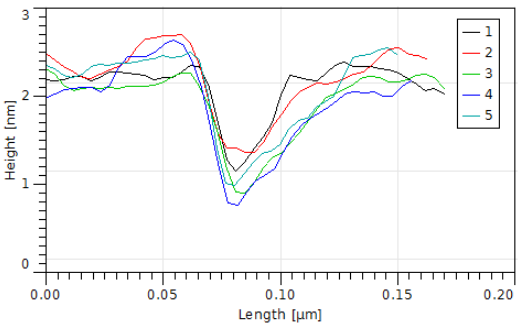

(f) Profiles

Fig. 4.11 1μm×1μm AFM images of series 8 highlighting the step edge profiles at the cross hatching lines. The P flux increases with the descending images of 0.5×10^{-8}Torr, 1.0×10^{-8}Torr and 1.5×10^{-8}Torr.

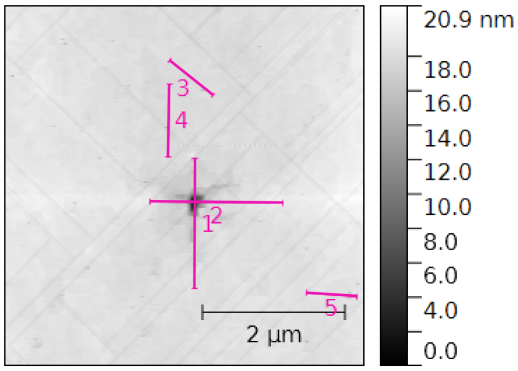

(a) Sample:8-1

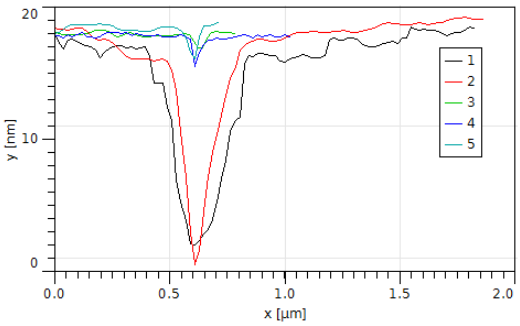

(b) Profiles

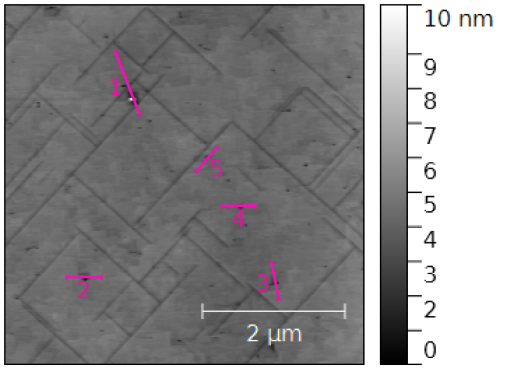

(c) Sample:8-2

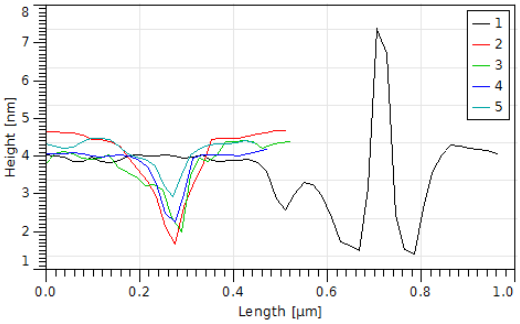

(d) Profiles

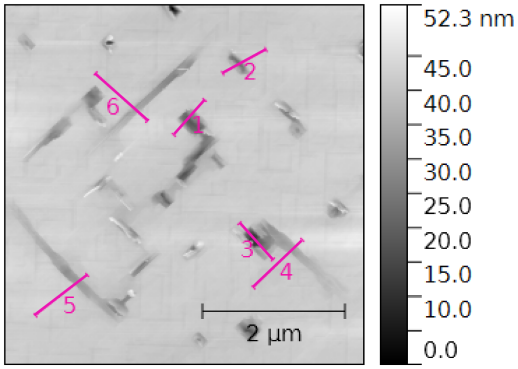

(e) Sample:8-3- Scan rotated by 45^o

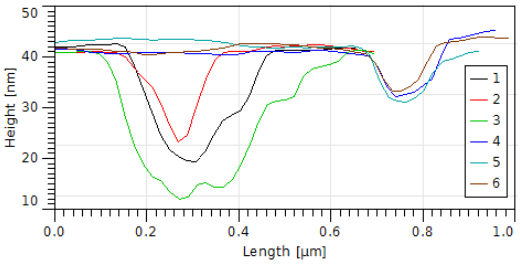

(f) Profiles

Fig. 4.12 5μm×5μm AFM images of series 8 profiling the size of holes in the layer. The P flux increases with the descending images of 0.5×10^{-8}Torr, 1.0×10^{-8}Torr and 1.5×10^{-8}Torr.

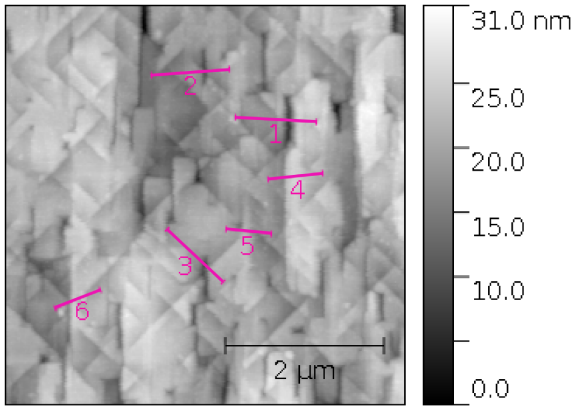

(a) Sample:6-1- 5μm×5μm

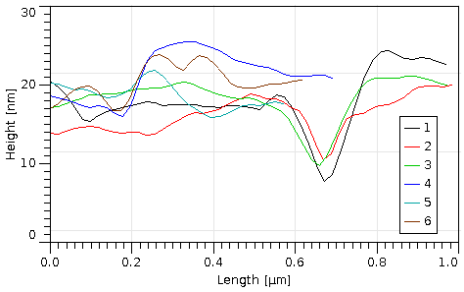

(b) Profiles

Fig. 4.13 AFM images and corresponding height profiles of the aligned trenches and scars in the thickest layer of CuMn($As_{(1-x)}P_x$) with a P flux of 1.0×10^{-8}Torr.

shape but cause artefacts to form when imaging them so they appear blurred, but do appear to be similarly shaped when the scanning direction is rotated by 45°.

Sample:8-3 also shows another feature of trenches aligned along the [110] as shown in figure 4.13 and $[1\bar{1}0]$ directions of the GaP substrate, which represents the [010] and [100] directions of the CuMn($As_{(1-x)}P_x$). The trenches have a depth of $\sim$ 10nm, which corresponds to 25% of the film thickness. These trenches are big enough to represent a significant change in the path of an applied current and could cause anisotropic resistances in the different directions. Sample:6-1 demonstrates scars and trenches aligned along only one of the [110] and $[1\bar{1}0]$. There are significantly more scars and trenches on the layer compared to Sample:8-3. The two samples are from different growth series, with different thickness and with different applied phosphorus fluxes. The changes in conditions between the samples could mean that the aligned scars and trenches are due to an increasing incorporation of the P flux. The same marks are not seen across samples of the same applied P flux as shown in figure 4.14.

For Sample:6-2 where the material had competing phases the surface of the material, shown in figure 4.15, shows a 3D growth structure where towers of material are forming.

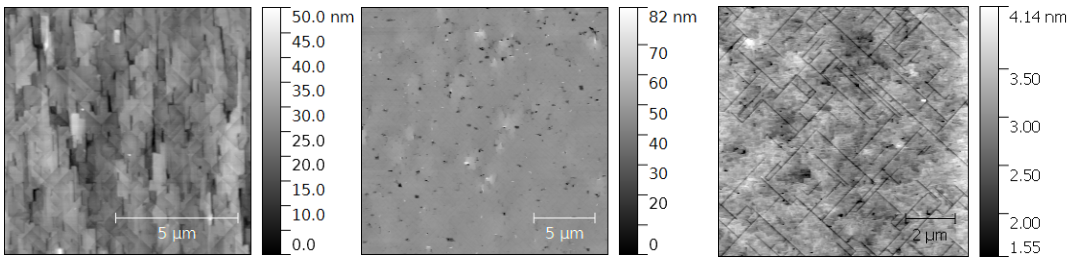

(a) Sample:6-1 (b) Sample:7-1 (c) Sample:8-2

Fig. 4.14 Comparing the surfaces of the three different samples grown with an applied P flux of 1×10^{-8}Torr. Images taken with AFM with an image size of 10μm$\times 10\mu$m (left and right images) or 20μm$\times 20\mu$m (center). Figure 4.14c has a restricted colour scale.

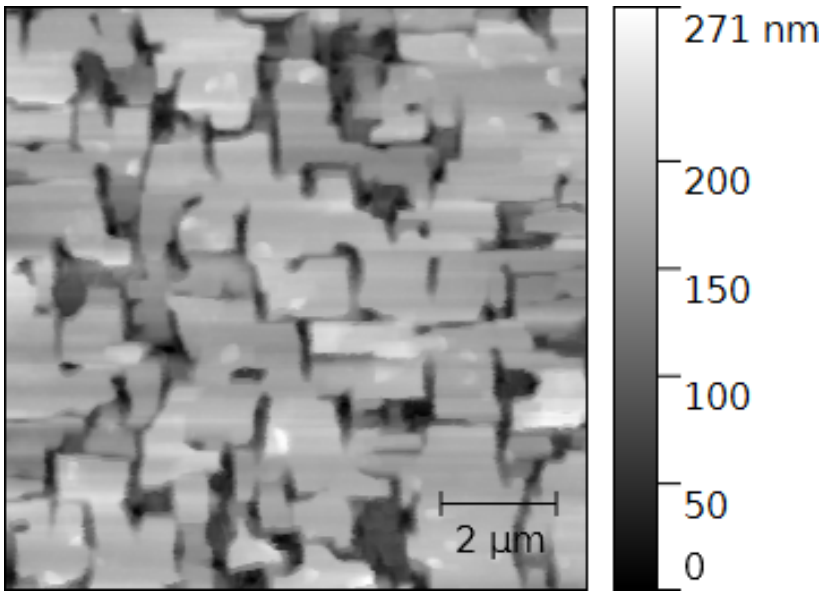

Fig. 4.15 10μm$\times 10\mu$m AFM image of CuMn($As_{(\mathbf{1-x})}P_{\mathbf{x}}$) with a P flux of 2.0×10^{-8}Torr (Sample:6-2).

4.4 Conclusion

In conclusion epitaxial samples of tetragonal CuMn($As_{(1-x)}P_x$) have been grown by MBE and at different growth conditions the phosphorus has incorporated into the crystal lattice and caused a change in the lattice constants, which is dependent on the phosphorus flux. CuMn($As_{(1-x)}P_x$) has been shown to have the same antiferromagnetic structure using neutron diffraction as CuMnAs with the spins coupled FM in plane (*ab*) and coupled AF out of plane (*c* direction). Neutron diffraction has also shown that CuMn($As_{(1-x)}P_x$) loses its AF ordering by 550K and the temperature dependent measurements predict a T_N of (500 ± 5) K. Though a stronger prediction could be made if there were more measurements at other temperatures.

XRD has shown that there is a systematic change in the *c* parameter with the increasing phosphorus flux for the third growth series. The layers also come under greater strain as the phosphorus content increases and the lattice mismatch increases to be comparable to CuMnAs/GaAs. In the thick sample of CuMn($As_{(1-x)}P_x$) (Sample:6-1) the layer may have relaxed as the *c* value has decreased to that of the lowest phosphorus flux in growth series three (Sample:8-1), which had a flux of 0.5×10^{-8} Torr.

The AFM images for the different samples of CuMn($As_{(1-x)}P_x$) show a range of interesting behaviours. The most prominent feature is the cross hatching pattern that is also observed in CuMnAs. The length of the lines begins to shorten as the phosphorus flux begins to increase. On several of the samples it is also possible to observe small and large holes on the surface of the material, which could be related to the problems of poor surface adhesion that were observed in films of CuMnAs.In two samples there are scars or trenches aligned with the cleaving lines of the GaP.

For phosphorus fluxes $\geq 1.5 \times 10^{-8}$ Torr the material begins to phase separate as seen in magnetometry measurements and AFM images. The magnetometry of several samples with low phosphorus fluxes showed some paramagnetic signal from the material.

Chapter 5

Determination of the Magnetic Phase Transition from Longitudinal Resistivity

5.1 Introduction

Measuring the phase transition temperature from the resistivity of an itinerant material was discussed in section 1.3. The system described in section 2.3.2 was used to measure the temperature dependence of the resistivity, in high vacuum, for CuMnAs. It was necessary for the sample to be heated under high vacuum due to oxidation effects causing structural changes in the material, which had been observed in previous experiments.

This chapter will detail the results of investigations into the ρ_{xx} and $d\rho_{xx}/dT$ of CuMnAs. The temperature obtained for the magnetic phase transition will be compared to the neutron diffraction data discussed in section 3.3.1 to analyse the accuracy of obtaining the T_N from resistivity. The chapter will compare the results for several different layers of CuMnAs. There will be a study of the effect of film thickness on the T_N of CuMnAs, the effect of using different growth methods, the difference in measurements with a GaAs or GaP substrate, the effect of oxidation, how alloying with phosphorus effects the T_N and finally the non-

stoichiometric CuMnAs with MnAs inclusions system will be studied to observe the two different phase transitions.

5.2 Obtaining the T_N of CuMnAs from the dρ_{xx}/dT

This section will detail the procedure for extracting the T_N of CuMnAs by measuring the resistivity against temperature. The ρ_{xx} will principally be discussed including the effects of heat cycling the sample. There will be a brief discussion of the $\rho_{\mathbf{xy}}$. The experimental set-up and data processing procedures for the measurement system that will be used for this section are detailed in section 2.3.2.

5.2.1 Longitudinal resistivity

The ρ_{xx} against temperature for stoichiometric CuMnAs was measured at cryogenic temperatures with helium gas flow and high temperatures under vacuum (section 2.3.2). Figure 5.1 shows the combination of the resistivity measurements for these two systems. Starting at the lowest temperature around 4K it is clear that there has been no apparent freezing out of carriers, which would have been indicative of an intrinsic semiconductor and the resistivity is too low for a highly doped semiconductors [136]. As discussed in section 1.2.1, CuMnAs is probably a semi-metallic material, but there have been some contradictory results indicating it could be a narrow gap semiconductor (section 1.2.1). The resistivity of CuMnAs increases with temperature due to the increasing phonon scattering. The temperature increases with a T^2 dependence which has been observed in semimetal systems [137, 138]. The resistivity deviates from T^2 dependence at higher temperatures near the T_N, in the critical fluctuation regime. The resistance increase faster than the T^2 relationship due to critical fluctuations, which are large thermodynamic fluctuations[139] of the spins from their average value. In the data break between the two systems there is a small difference in the data trends. This

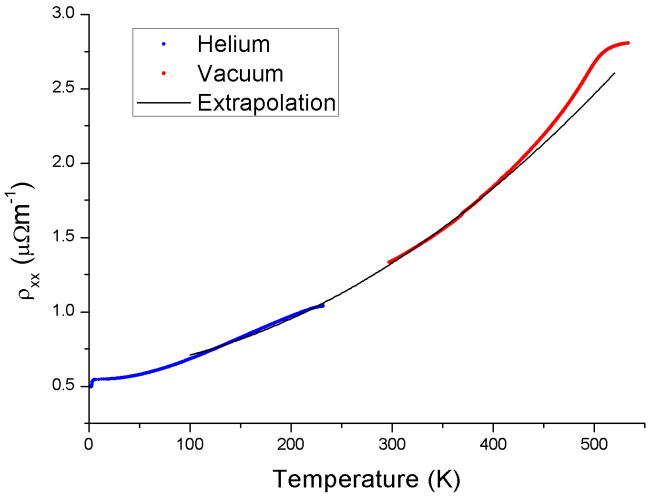

Fig. 5.1 Longitudinal resistivity against temperature for Sample:1-3. The blue data shows the ρ_{xx} vs T is a steady cooling regime in a helium gas cooled cryogenic system. The red data shows the steady heating (ramp $\sim 1K/min$) in the high temperature vacuum system. The black line represents a square power extrapolation from the 100-200K and 300-400K regions.

could be due to one of the systems not being in a steady heating or cooling state when the measurement was made causing there to be a changing offset between the sample and the thermocouple measuring the temperature. At the highest recorded temperature it is possible to see a distinct deflection in the resistivity which is caused by the magnetic phase transition of the CuMnAs. This deflection increases the resistivity from the square fit to the extrapolated data

In figure 5.2 the resistivity shows a clear deflection around 480K. In the temperature derivative of the resistivity there is a large cusp in the $d\rho_{xx}/dT$ at 480K, which is indicative of the system undergoing a phase transition as it passes through the T_N and has been observed in similar ferromagnetic systems [48] and is detailed in section 1.3. There is also a smaller peak around 330K, which is consistent with a small amount of MnAs as a secondary phase material, implying that the layer was grown slightly off stoichiometry, and will be discussed in more detail in section 5.6.

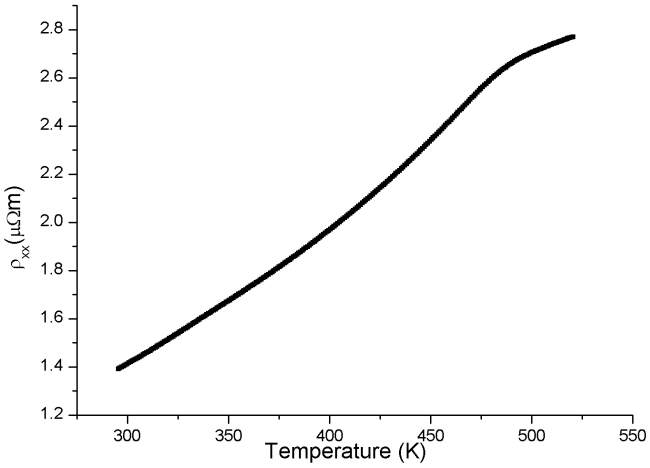

(a) ρ_{xx} vs T

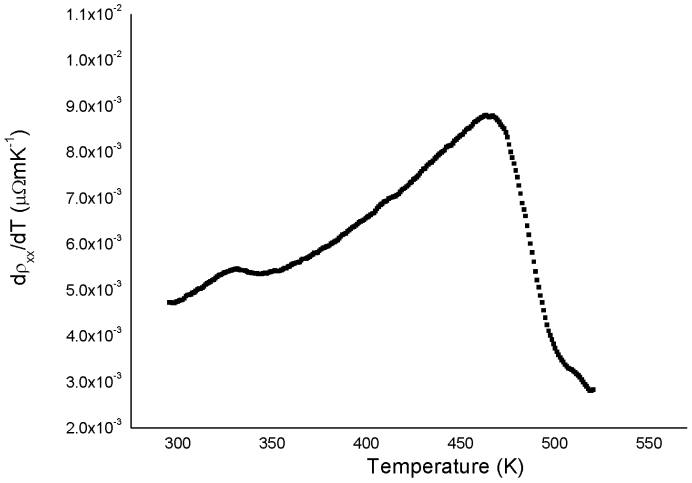

(b) $d\rho_{xx}/dT$ vs T

Fig. 5.2 Resistivity measurements in a vacuum environment for stoichiometric CuMnAs (Sample:1-3) showing the temperature dependence which exhibits a change in $d\rho_{xx}/dT$ around the T_N. The measurement shown are after the material has been heated through the T_N once. The smaller cusp in the $d\rho_{xx}/dT$ could be due to the presence of MnAs in the material as detailed in section 5.6.

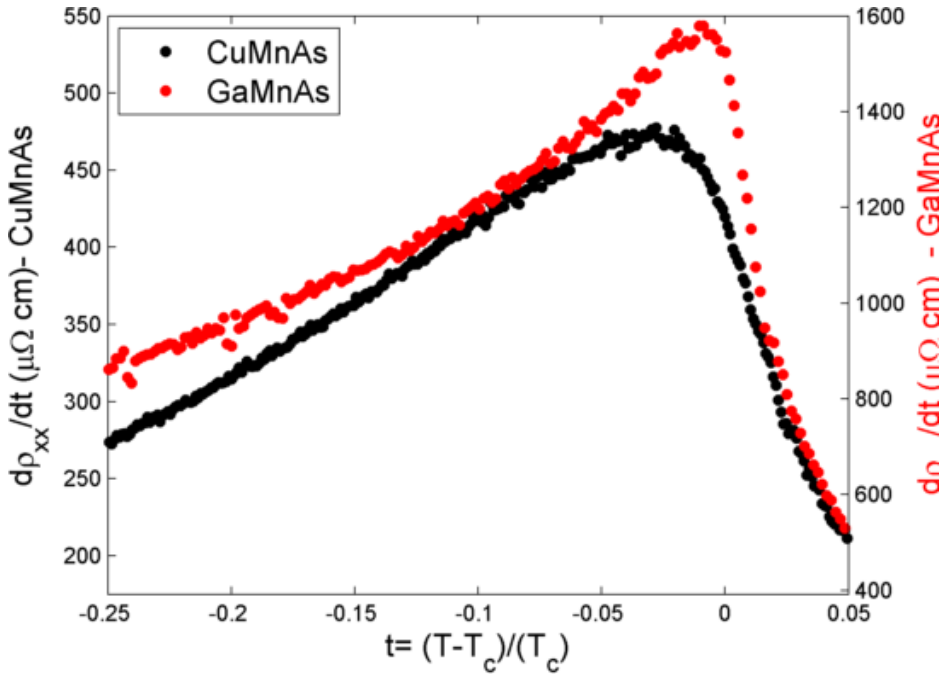

Fig. 5.3 A comparison of the functional form of the $d\rho_{xx}/dT$ for CuMnAs (black) and GaMnAs (red). GaMnAs data comes from [49] with a T_C of 179K.

The functional form of the derivative can be compared to measurements made on GaMnAs [48] as shown in figure 5.3. The temperature has been scaled by the magnetic transition temperature of each layer as described in section 1.3. The peak for CuMnAs is broader than the peak of GaMnAs. The peak could be broader due to the increased thermal fluctuations and phonon scattering from the higher temperature that the CuMnAs measurement is taken.

5.2.2 The effects of multiple heat cycles on the resistivity measurements

The procedure for measuring the resistivity of samples to determine the T_N was to heat and cool the sample at least twice to ensure that the observed behaviour was repeatable. This allowed information to be obtained about any changes in the sample resistivity with time, if there were any systematic differences between the resistivity measured for the heating and cooling modes and the repeatability of a sample.

Figure 5.4 shows two heating cycles for Sample:1-3. After the first heating of the sample there was an irreversible change in the resistivity (figure 5.4a). Above 480K the resistivity has decreased and then follows a shallower gradient so that at room temperature the resistivity has increased from the beginning of the first heat cycle. The sample then remains in a similar resistivity vs temperature state for second heat cycle to the first cool. The change in the resistivity behaviour is reflected in the $d\rho_{xx}/dT$ (figure 5.4b). In the first heat data there is a large feature, which does not have the expected functional form and is caused by a combination of several different factors including a non reversible time dependent element caused by heating the sample. The later measurements have the expected functional form. There is a small offset between the second heat and the cool measurements, which could be caused by differences in the heating rates.

Antiferromagnets have a T_N and a Blocking Temperature (T_B). T_B is the temperature at which an AF does not exhibit exchange bias with a FM[10]. The relationship between T_N and T_B varies in single crystal materials $T_N \approx T_B$ or in materials with small grains or domains $T_N > T_B$. To establish that the transition being observed in the resistivity measurement is the T_N and not T_B a comparison is made of the domain size and the mean free path of carriers. If the domain size is greater than the mean free path then the T_N is being measured as the electrons would only experience the magnetic effects within single domains. From magnetic linear dichroism measurements performed on the material (work led by Dr K. Edmonds and P. Wadley without the author's involvement) the average domain size is around 100nm. The mean free path (l) of a carrier is defined as,

$$l = \frac{m_e v_f}{\rho_{xx} n e^2} \tag{5.1}$$

where m_e is the mass of an electron, v_f is the Fermi velocity, which has values of 1.57×10^8cm/s (Cu) [12], 1.58×10^8cm/s (Mn) [12] and 2.73×10^7cm/s (GaAs) [140], n is the carrier concentration and e is the electron charge. For CuMnAs measurements of the carrier concentration,

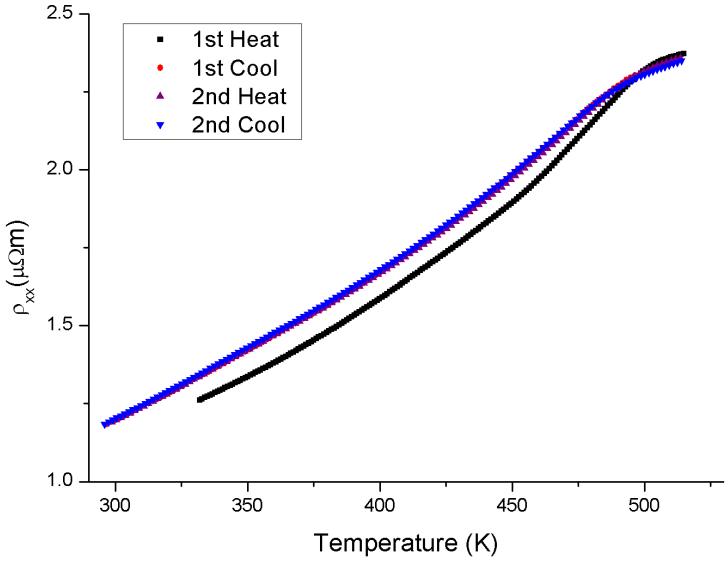

(a) Longitudinal Resistance vs Temperature

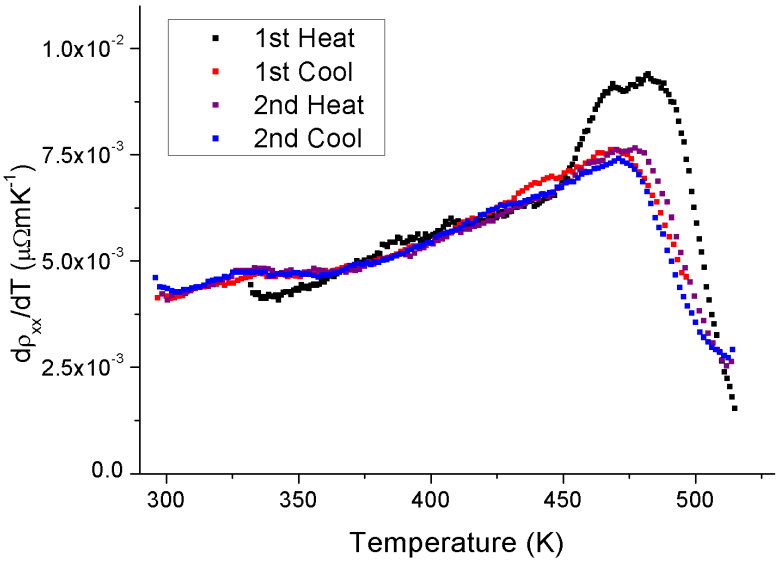

(b) Derivative of longitudinal Resistance against T

Fig. 5.4 The effects of two heating and cooling cycles on a sample of stoichiometric CuMnAs (Sample:1-3). Black is the first heat, red is the first cool, purple is the second heat and blue is the second cool.

from the hall effect using a single carrier model, are $1.1\times10^{22}\text{cm}^{-3}$ [39] . Using this value [of n] and a v_f of 10^8cm/s and 10^7cm/s gives a mean free path of 1.2nm or 0.12nm, which is at least around two orders of magnitude below the domain size observed in CuMnAs. This suggests that the resistivity is measuring the T_N rather than T_B,However the carriers in CuMnAs are expected to follow a two carrier model, rather than a single carrier. Even with any changes this could cause to the carrier concentration due to the large resistivity measured at the transition, it is expected that $l << $ domain size and the measurement is of the T_N and not T_B.

5.3 Comparing T_N obtained from resistivity and neutron diffraction measurements

The Néel temperature for CuMnAs has previously been measured as (480±5)K from neutron diffraction [114] as discussed in section 3.3.1. There is a good agreement between the two methods for measuring the T_N as seen in figure 5.5. It is expected that the maximum in the cusp of the $d\rho_{xx}/dT$ will be shifted below T_N due to long length scale inhomogeneities in the sample causing a range of T_c [125] and the cusp is found to be shifted by about 20K from the T_N given by neutron diffraction for CuMnAs.

Neutron diffraction is a well established method of measuring the T_N of AF materials. However it requires access to neutron sources and each measurement is very time consuming, so it is difficult to measure a series of samples. By being able to measure the T_N in a lab based experiment it is possible to analyse the properties of a series of samples much quicker.

For stoichiometric CuMnAs there was good agreement between the neutron diffraction T_N and the value from the transport measurement. In figure 5.6 the same relationship is shown for CuMn($As_{(\mathbf{1-x})}P_{\mathbf{x}}$) (Sample:6-1), which also shows a marked similarity between the two results.

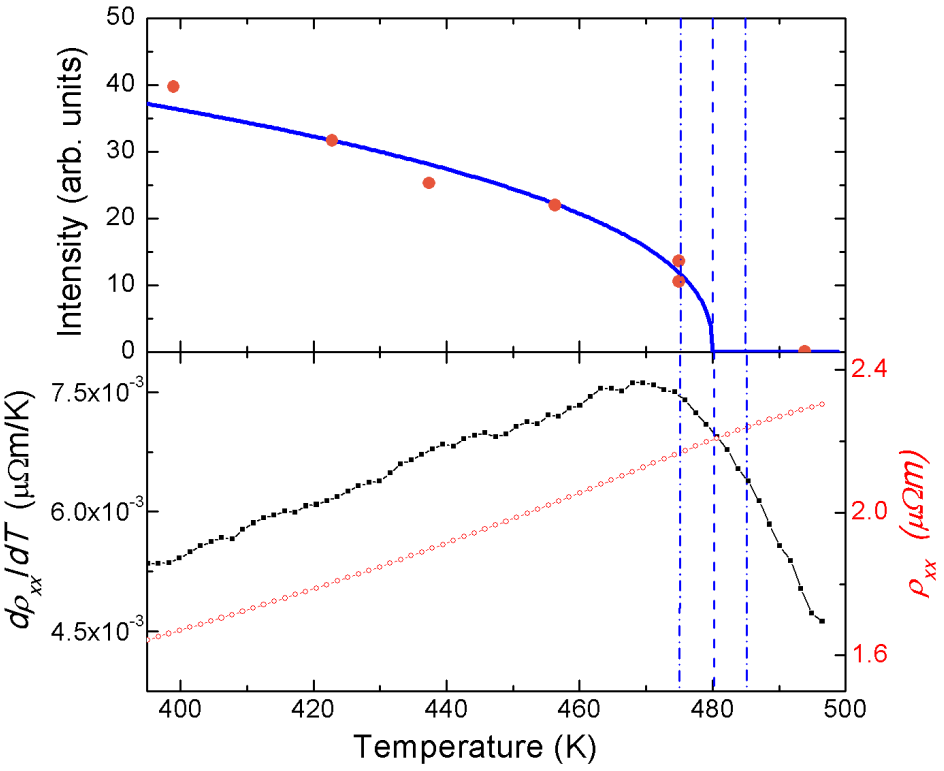

Fig. 5.5 Comparison of the T_N measured by neutron diffraction (top panel) and longitudinal resistivity (bottom panel). The red line is the resistivity and the black curve is $d\rho_{xx}/dT$, for stoichiometric CuMnAs (Sample:1-3). The dashed blue lines across the two figures represent the calculated value and error of the T_N from neutron diffraction.

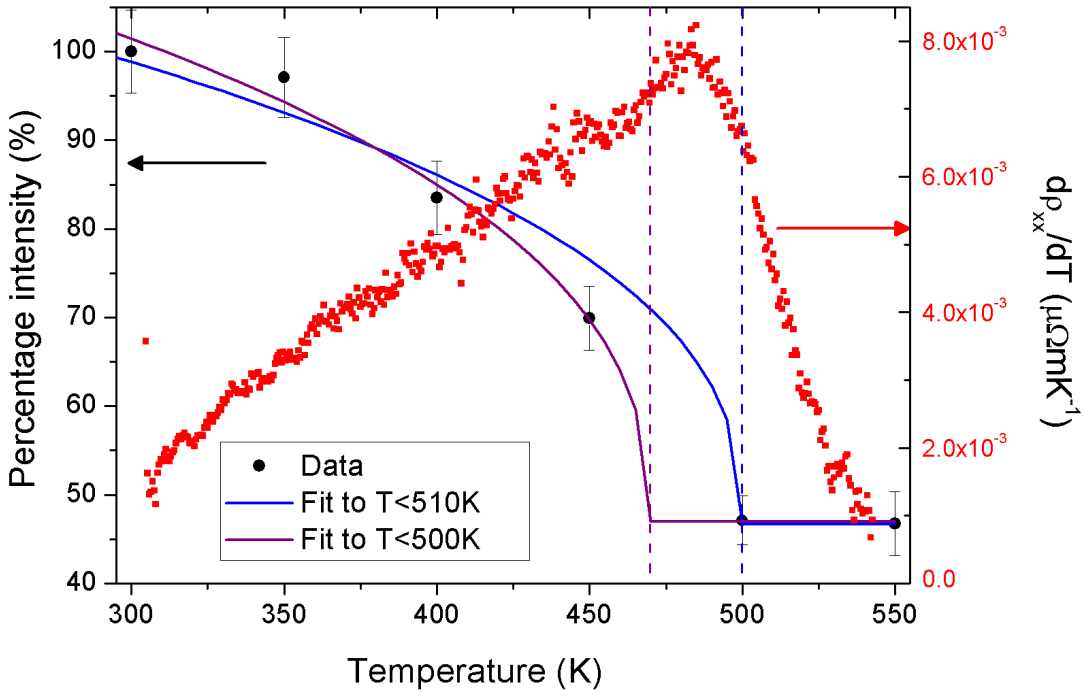

Fig. 5.6 Comparing the T_N from neutron diffraction (black dots, blue andpurple fits) and the temperature derivative of the resistivity (Red) for 214nm of CuMn($As_{(1-x)}P_x$) with a P flux of 1×10^{-8} Torr (Sample:6-1). The dashed blue and purple lines represents the calculated value of the T_N for the two different fits to the neutron data.

5.4 Studying the T_N of stoichiometric CuMnAs

The following section will detail the results of investigations into the T_N of several different samples of epitaxial CuMnAs. It will look at the dependence of T_N on layer thickness, the effects of the different growth and nucleation methods for ultra thin films, the difference in measuring on GaAs and GaP as substrates and the effect of oxidation on ultra thin films.

5.4.1 Investigating the thickness dependence of the T_N

It has been observed in other magnetic materials that for ultra thin layers there is a suppression of the magnetic transition temperature [141].

In this study the results will be shown for a series of samples of different thickness (Sample:1-3, Sample:1-8, Sample:3-1 & Sample:1-6). The resistivity against temperature and its derivative are shown in figure 5.7. In the ρ_{xx} measurement, figure 5.7a there are some clear differences between the samples. The 20nm and 140nm thick layers have very similar temperature dependent resistivities and $d\rho_{xx}/dT$. The resistivity of the 10nm thick layer follows a similar trend but is larger and increases more with temperature. The 5nm thick layer has similar behaviour but shifted to a lower temperature. The difference in the magnitude of the change of the resistivity is also clear in the $d\rho_{xx}/dT$, which is shown in figure 5.7b. All of the derivatives have the same basic cusp shape with the 10, 20 and 140nm thick layers having similar T_N. In the 5nm layer $d\rho_{xx}/dT$ has a sharper peak, which is significantly shifted to a lower T_N. Figure 5.7c shows the normalised $d\rho_{xx}/dT$ for the different layers. The three thicker layers show a marked similarity in their T_N and broadness. The 5nm layer clearly has a T_N suppressed to $\sim 400K$.

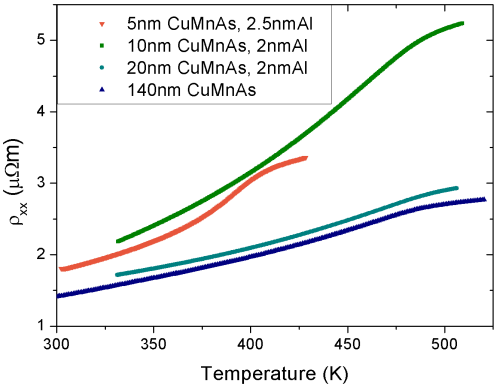

(a) ρ_{xx} vs T

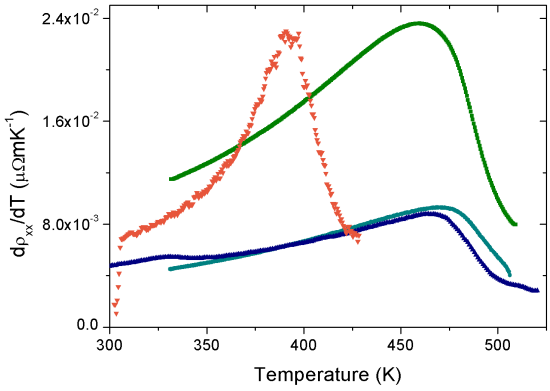

(b) $d\rho_{xx}/dT$ vs T

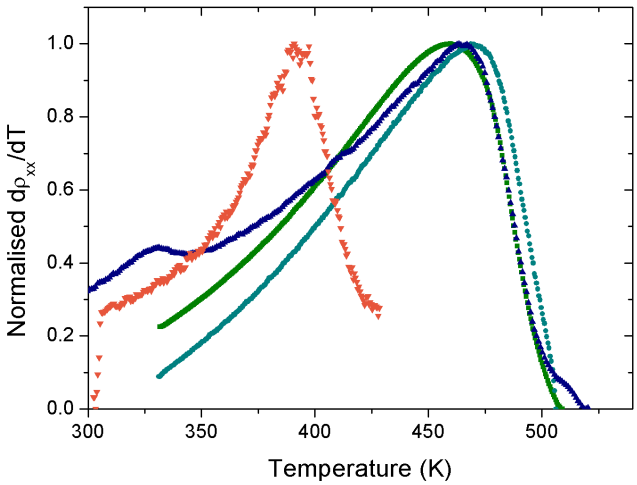

(c) Normalised $d\rho_{xx}/dT$ vs T

Fig. 5.7 Transport measurements for different thickness films of stoichiometry CuMnAs. Orange - 5nm CuMnAs (Sample:1-6), green - 10nm CuMnAs (Sample:3-1), teal - 20nm CuMnAs (Sample:1-8) and blue - 140nm CuMnAs (Sample:1-3).

5.4.2 Analysing the effect of seeding layer growth conditions of the transport measurements

The two different growth methods for Sample:5-4 and Sample:5-5 have been characterised in several different ways in section 3.5.3, which have shown that the layers have excellent crystal and surface qualities and that Sample:5-5 has a significantly larger magnetic uni-axial component. The resistivity behaviour for the two layers is shown in figure 5.8, where it is also compared to Sample:3-1 as a reference.

The resistivities of Sample:5-4 and Sample:5-5 are comparable and they correspondingly have very close transitions in the derivative. The resistivity of Sample:3-1 is slightly larger than that of the other two layers and it also has a T_N that is slightly higher. The shape of the derivative for the three samples is comparable and there does not appear to be a marked difference in the broadness of the transition.

Sample:5-4 and Sample:5-5 also have distinct heat cycle patterns to those observed in other stoichiometric layers of CuMnAs, which are shown in figure 5.9. The samples increase in resistivity after the first heat cycle, however during the first heat cycle they both show the same behaviour where the gradient of the resistivity deflects downwards around 360K. This creates a double cusp in the $d\rho_{xx}/dT$. The cool and subsequent heating behaviour displays the expected cusp in the $d\rho_{xx}/dT$. As the double cusp is not repeatable after the first heat it is not believed to have the same origin as the non-stoichiometric material. The extra sharp features in figure 5.9b are due to the temperature measurement being taken from the thermocouple rather than a resistance thermometer for this sample. The features are caused by the offset between the thermocouple and the actual temperature in the sample changing sign.

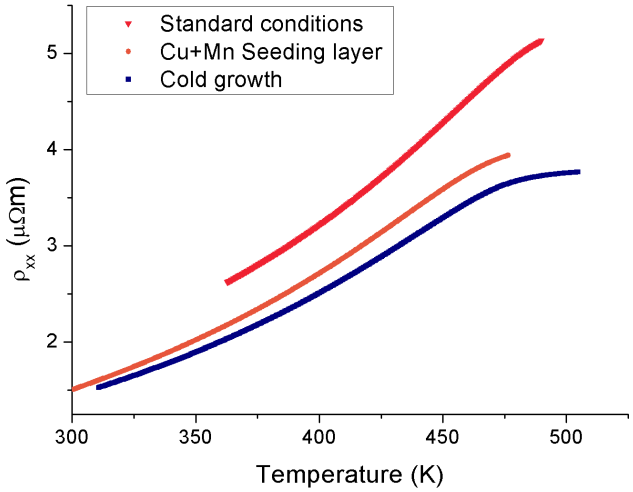

(a) ρ vs T

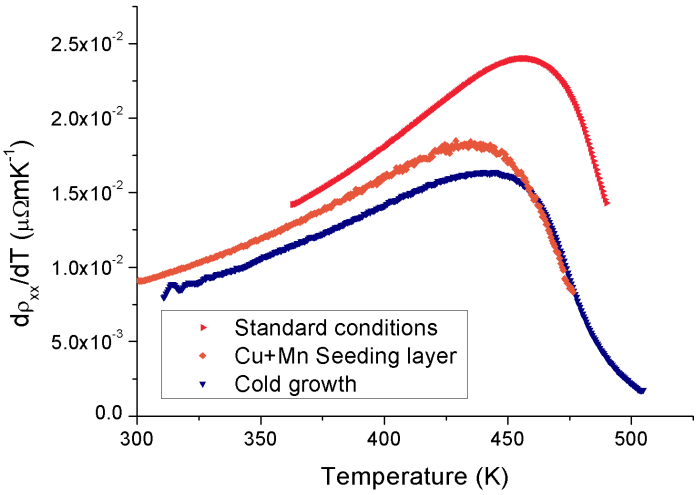

(b) $d\rho_{xx}/dT$ vs T

Fig. 5.8 Longitudinal resistivity for 10nm layers of CuMnAs with different growth methods. Red is Sample:3-1 grown with standard conditions, orange is Sample:5-4 grown with a copper and manganese nucleation layer and blue is Sample:5-5, which was grown with a reduced T_{sub}.

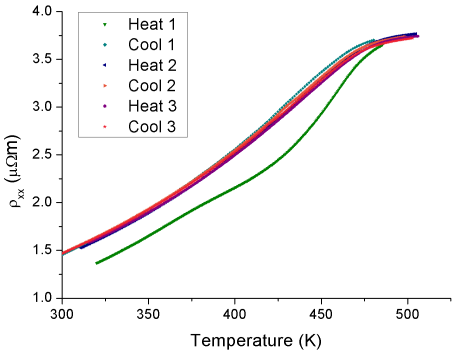

(a) Sample:5-4

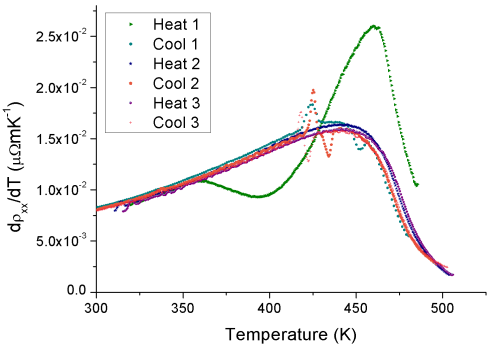

(b) Sample:5-4

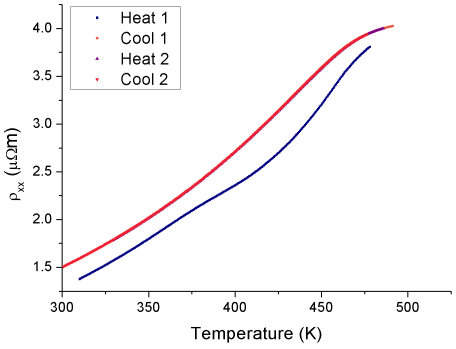

(c) Sample:5-5

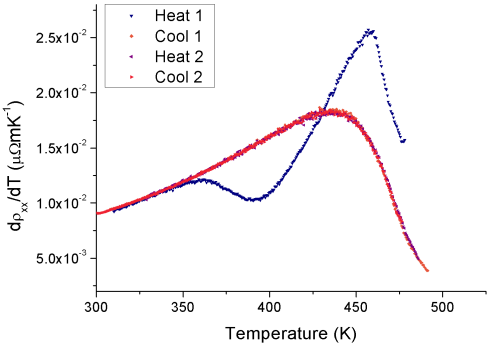

(d) Sample:5-5

Fig. 5.9 Heat cycle for Sample:5-4 and Sample:5-5. Samples were measured with a heating ramp rate of 0.5K/min and a free cooling regime. The small extra features in (b) are from a technical issue with the measurement so the thermocouple temperature is used rather than a resistance thermometer.

5.4.3 Investigating the difference in the resistivity measurements for CuMnAs on GaAs and GaP substrates

There are clear differences in the behaviour of the longitudinal resistivity of CuMnAs layers on GaAs and GaP, as shown in figure 5.10. After the magnetic transition the resistivity of CuMnAs/GaP continues to rise at a decreased linear gradient, whereas for CuMnAs/GaAs the resistivity begins to decrease. The $d\rho_{xx}/dT$ (figure 5.10b) of both the layers display a phase transition at similar temperatures. However after the transition the CuMnAs/GaP $d\rho_{xx}/dT$ falls and levels out without turning negative. For the CuMnAs/GaAs layer after the magnetic transition the $d\rho_{xx}/dT$ continues to decrease linearly and becomes negative. A feature in both the ρ_{xx} and the $d\rho_{xx}/dT$ of CuMnAs/GaAs is that there is no change in the resistivity between the first heat and any subsequent measurements. A possible reason for this is that the crystal lattice relaxes during the growth on GaAs, but remains strained when grown on GaP [39] and possibly undergoes a partial relaxation during heating. A possible reason for the behaviour of ρ_{xx} for CuMnAs/GaAs could be a secondary conduction channel opening in the GaAs substrate at the higher temperatures. GaAs has a smaller E_g than GaP, which means that it has a higher intrinsic carrier concentration, n_i, that scales exponentially with temperature [12] as

$$n_i = p_i = 2\left(\frac{k_B T}{2\pi\hbar^2}\right)^{\frac{3}{2}} (m_e m_h)^{\frac{3}{4}} exp\left(-\frac{E_g}{2k_B T}\right) \tag{5.2}$$

where n_i and p_i are the intrinsic carrier concentration, m_e and m_h are the effective mass of electrons and holes, k_B is the Boltzmann constant, E_g is the band gap, which is temperature dependent, and T is the temperature. The parameters for GaAs and GaP are listed in table 5.1

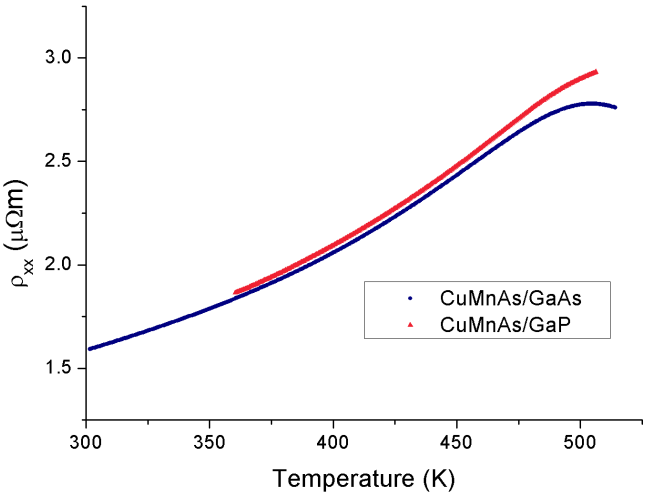

(a) ρ_{xx} vs T

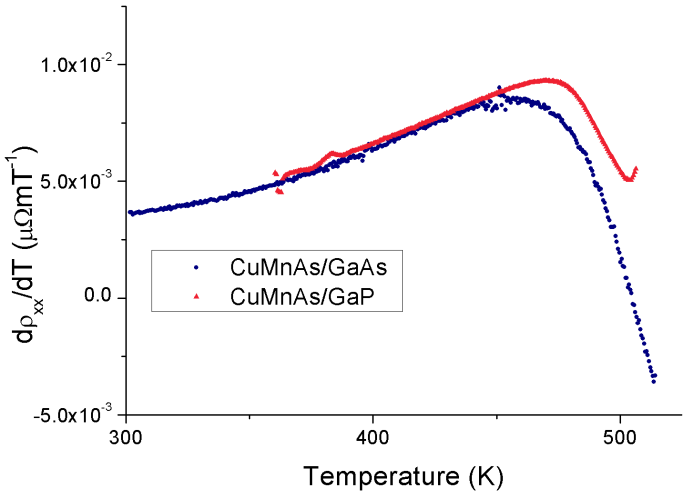

(b) $d\rho_{xx}/dT$ vs T

Fig. 5.10 The resistivity measurements for CuMnAs/GaAs(Sample:1-4) in blue and CuMnAs/GaP(Sample:1-8) in red. At the higher temperatures there is a difference in the behaviour.

Parameter	GaAs	GaP
m_e (m_e/m)	0.066	1.12
m_h(m_h/m)	0.5	0.79
μ_e(cm^{2}V^{-1}s^{-1})	$8000 \times \frac{300}{T}^{\frac{2}{3}}$	250
μ_h(cm^{2}V^{-1}s^{-1})	$400 \times \frac{300}{T}^{2.3}$	150

Table 5.1 Parameters and temperature dependences for GaAs and GaP. E_g is the band gap, the effective masses (m_e & m_h) are given as a fraction of the mass of an electron at rest. The mobilities (μ_e & μ_h) are in (cm^{2}V^{-1}s^{-1}). Parameters are from [124]

with the temperature dependences for the E_g is

$$E_{g,GaAs} = 1.519 - \left(5.405 \times 10^{-4} \frac{T^2}{T+204}\right) (eV) \tag{5.3a}$$

$$E_{g,GaP} = 2.34 - \left(6.2 \times 10^{-4} \frac{T^2}{T+460}\right) (eV) \tag{5.3b}$$

Figure 5.11 shows how the n_i for the two substrates varies with temperature. The n_i is several orders of magnitude higher than GaP. At 480K the respective n_i of GaAs and GaP are 3.74×10^{11}cm^{-3} and 1.50×10^{8}cm^{-3}. The carrier concentration of CuMnAs has not been accurately calculated as the single carrier model yields a concentration of 1.1×10^{22}cm^{-3} [39], which is belived to be a significant overestimate. The carrier concentration would be expected to be in the typical range for a semi-metal, which is between $10^{18} - 10^{21}$cm^{-3} [12].

The mobility of holes and electrons in semiconductors can be calculated so that it is possible to determine the conductivity (σ) of the material. In GaAs the electron mobility is significantly greater than the hole mobility, so the latter will be ignored in further calculations. The conductivity is calculated as

$$\sigma(T) = e n_i(T) \mu_e(T) \tag{5.4}$$

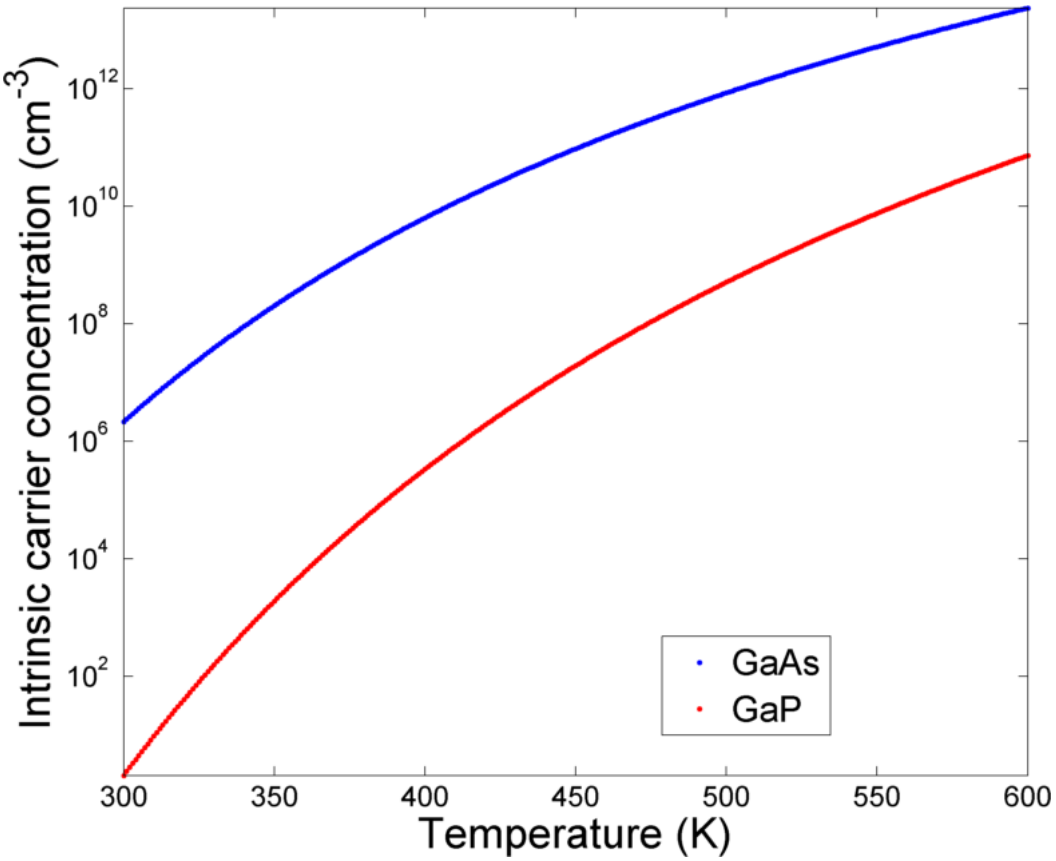

Fig. 5.11 Expected temperature dependence of the intrinsic carrier concentration for GaAs(blue) and GaP(red). Predictions are made from equation 5.2.

where μ is the mobility of the holes or electrons. The temperature dependence of the mobility scales as a power law [12], which contributes significantly less than the exponential change of the carrier concentration. The resistivity is defined as the inverse of the conductivity. Figure 5.12 shows the changing resistivity with temperature for GaAs.

Having worked out the temperature dependence of the resistivity for GaAs a system can be set up to compare the resistance of CuMnAs on GaAs and CuMnAs. First a simplified parallel resistor model is constructed (figure 5.13a), where the total resistance of the system is defined as,

$$\frac{1}{R_{\mathrm{CuMnAs/GaAs}}} = \frac{1}{R_{\mathrm{GaAs}}} + \frac{1}{R_{\mathrm{CuMnAs}}} \tag{5.5}$$

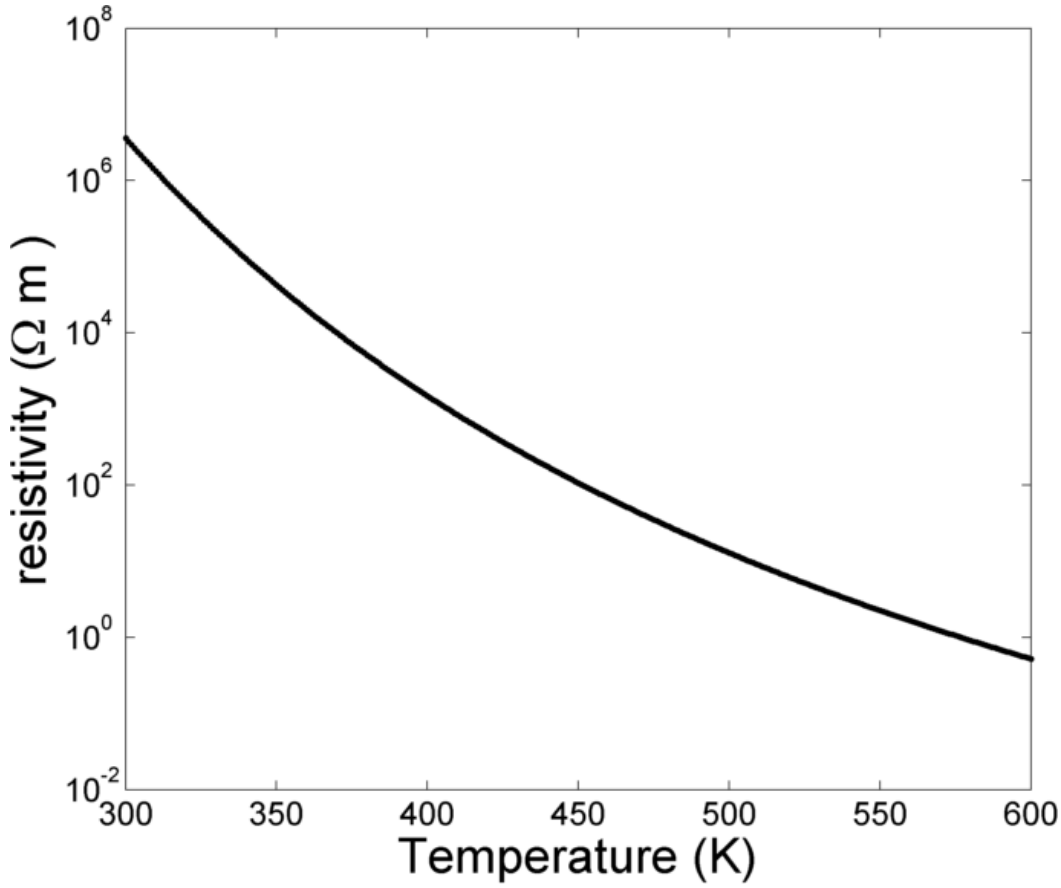

Fig. 5.12 Expected dependence of the resistivity of GaAs with temperature.

While this model is valid to describe the cross sectional representation of the CuMnAs/GaAs (figure 5.13b), the model does not consider the differences in the current paths through the different materials.

Figure 5.14 shows the difference between the minimum length current paths between the current source and drain for the CuMnAs and GaAs. The measurements for the CuMnAs were made in four terminal mode so it is necessary to scale the resistance of the CuMnAs and GaAs by the two terminal resistance to compensate for the different paths, which gives the total resistance for the system as

$$R_{\mathrm{CuMnAs/GaAs}} = \frac{R_{\mathrm{GaAs}}}{R_{\mathrm{GaAs}} + R_{\mathrm{CuMnAs,2T}}} R_{\mathrm{CuMnAs,4T}} \tag{5.6}$$

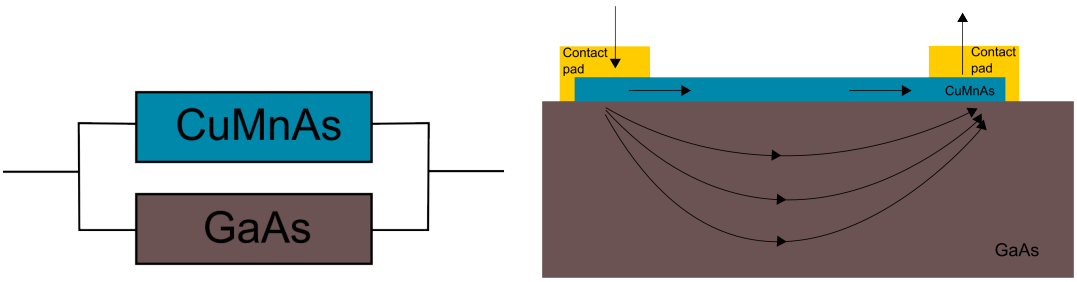

(a) CuMnAs/GaAs as a parallel resistor system (b) Schematic showing a the possible current paths through a cross section of the CuMnAs/GaAs system.

Fig. 5.13 Schematics showing the modelled resistor system and a cross section of the current path for a layer of CuMnAs on GaAs at temperatures where the GaAs has a carrier concentration high enough to open a secondary conduction path.

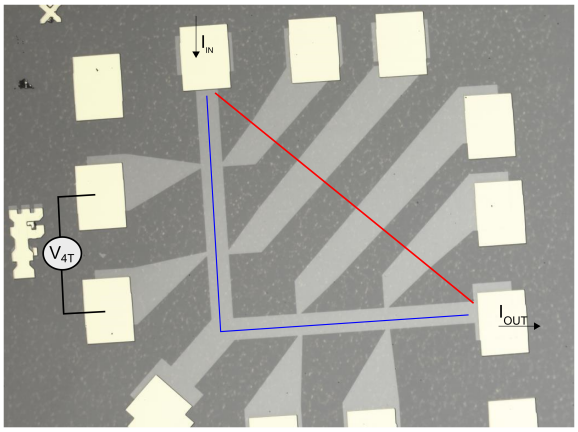

Fig. 5.14 An annotated photo showing the different minimum path lengths that can be taken between the current in and out terminals. The blue line represents the minimum path length of the CuMnAs and the red line represents the minimum path length for the GaAs (the GaAs can take a range of paths).

To calculate the resistances the resistivities were converted back to the resistance using the following definitions. The dimensions of the GaAs wafer are assumed to have a width of 5mm a substrate thickness of 0.4mm and a path length of the shortest difference from source to drain. In a Lbar device this is assumed to be the hypotenuse of the right angled triangle.

Device	CuMnAs (001)	GaP (001)
D1	[110] or [1$\bar{1}$0]	[100] or [010]
D2	[100] or [010]	[110] or [1$\bar{1}$0]
D3	[010] or [100]	[1$\bar{1}$0] or [110]

Table 5.2 Possible orientations of Hall bar devices on Sample:3-1with the cleavage plains of CuMnAs or GaP. The alignment of the device is based on the long axis of the current carrying channel in the device.

Figure 5.15 shows several different comparisons for the effect of a secondary conduction channel from the GaAs on resistance and resistivity of the CuMnAs. The figures show that the change in resistance from the secondary channel begins to compensate for the changed behaviour correctly. However it does not cause changes in the behaviour strong enough for the effect seen. This could be due to several different reasons, the current path of the GaAs could be over simplified or there could be charges travelling through the GaAs to the conductive silver paint used to adhere the chip to the holder. This effect would be more pronounced on thinner layers of CuMnAs on GaAs.

5.4.4 Investigating the age effects of 10nm films of stoichiometric CuMnAs

Capping layers are deposited on thin films to protect layers, typically from oxidation. During this work there have been several interesting results due to time dependent changes of 10nm samples that will now be detailed. Sample:3-1 is a stoichiometric 10nm layer of CuMnAs on GaP with a 2nm Al capping layer and from AFM measurements $(2.4 \pm 0.4)\%$ of the layer is missing, detailed in section 3.5. The layer has been the most extensively studied for the effects of time dependent changes and figure 5.16 shows the results of 3 different devices. The devices (D1, D2, and D3) were fabricated simultaneously on the same chip and are all orientated in different directions, listed in table 5.2. After processing the chip was divided up into individual devices, which could be mounted on different sample holders.

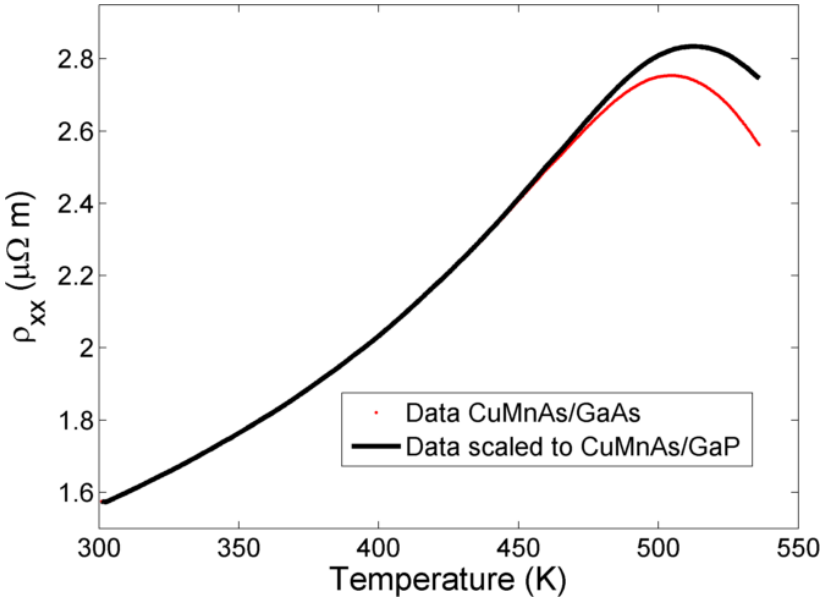

(a) Adjusting from CuMnAs/GaAs to CuMnAs/GaP, which increases the resistivity at higher temperatures.

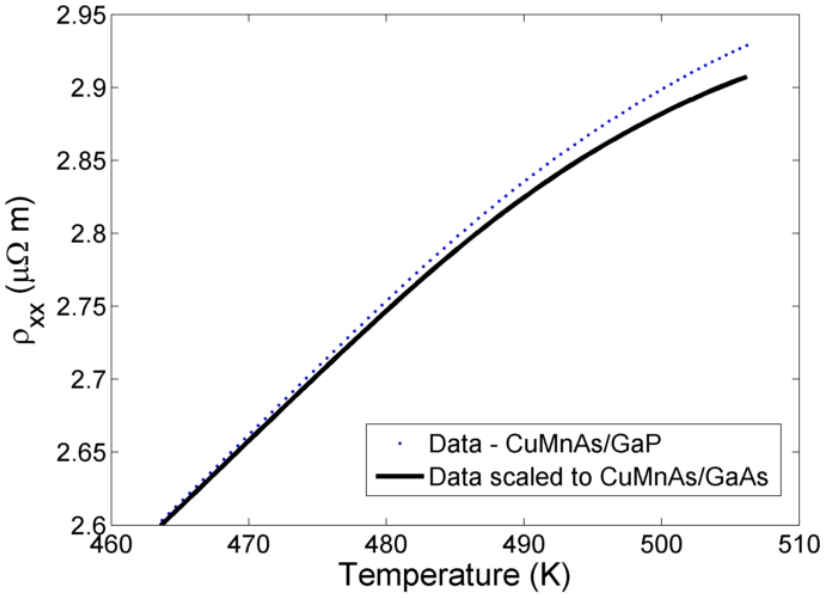

(b) Adjusting from CuMnAs/GaP to CuMnAs/GaAs, which reduces the resistivity at higher temperatures. Zoomed in on higher temperatures.

Fig. 5.15 Using equation 5.6 to calculate the resistivity of pure CuMnAs from a CuMnAs/GaAs sysyem and to calculate the resistivity of CuMnAs/GaAs from a measurement of CuMnAs/GaP (assumed to be a measurement of solely CuMnAs).

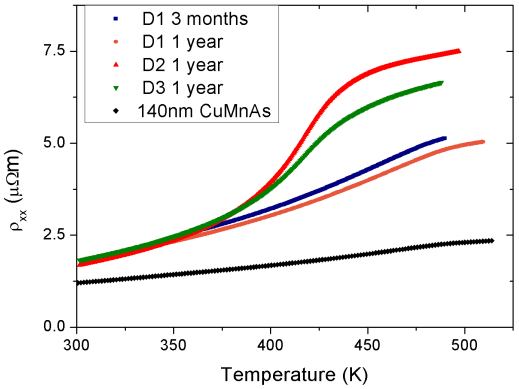

(a) ρ_{xx} vs T

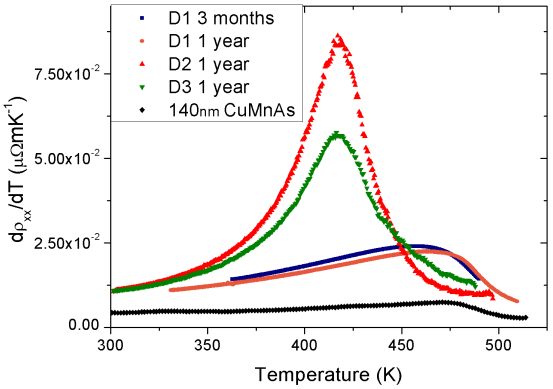

(b) $d\rho_{xx}/dT$ vs T

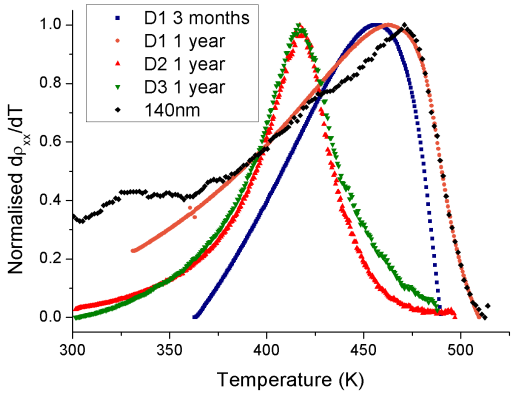

(c) normalised $d\rho_{xx}/dT$ vs T

Fig. 5.16 ρ_{xx} vs T and $d\rho_{xx}/dT$ for three devices made from 10nm stoichiometric CuMnAs (Sample:3-1). The first device (D1) was measured twice, initially at 3 months after growth (dark blue) and measured again at 1 year after growth (orange). D1 is orientated along the CuMnAs [110] or [1$\bar{1}$0] directions. The second (D2 - red) and third (D3 - green) devices were measured one year after the layer growth without any prior heating.They are two orthogonal devices aligned along the CuMnAs [010] or [100] directions. All three devices were patterned at the same time as a single chip. The black line is a 140nm layer of CuMnAs (Sample:1-3).

D1 was measured by heat cycling at 3 months and the same device was measured again 1 year after the layer was grown. There is a very slight change between the resistivity for both measurements, the resistivity has decreased slightly at the higher temperatures, there is not a significant change in the shape of the cusp of the derivative, but there is a marginal increase in the temperature of the peak, which could be due to experimental error.

D2 and D3 were measured simultaneously a year after growth having not been heat cycled before this point. At 300K they have a comparable resistivity to D1 but after 350K their resistivity increases sharply. At the higher temperatures the bars have different resistivities that are above those of D1. The difference in the resistivity in the two orthogonal direction could be due to a crystalline anisotropy of the resistance. The $d\rho_{xx}/dT$ of the different devices (figure 5.16b) show a significantly larger $d\rho_{xx}/dT$ in D2 and D3 compared to D1 where the cusp is more symmetric and also decreased by up to 50K.

Another layer that showed significant suppression the T_N due to time dependent changes was Sample:1-7, which had an incomplete GaAs capping layer. Figure 5.17 compares the resistivity and normalised $d\rho_{xx}/dT$ for this layer against those of Sample:3-1. The GaAs capped layer has a marginally decreased resistivity at room temperature, the difference in the magnitude of the decrease in resistivity increases with temperature. The T_N of the GaAs capped sample has also decreased significantly compared to all the Al capped devices.

The GaAs capped layer as discussed in section 3.5 has a significantly larger exposed surface area and was also measured later after growth.

5.5 The effect on the Néel temperature by alloying with Phosphorus

The method of incorporating phosphorus into CuMnAs to make $CuMn(As_{(\mathbf{1-x})}P_{\mathbf{x}})$ was discussed in the previous chapter. The different lattice parameters for nominally matching

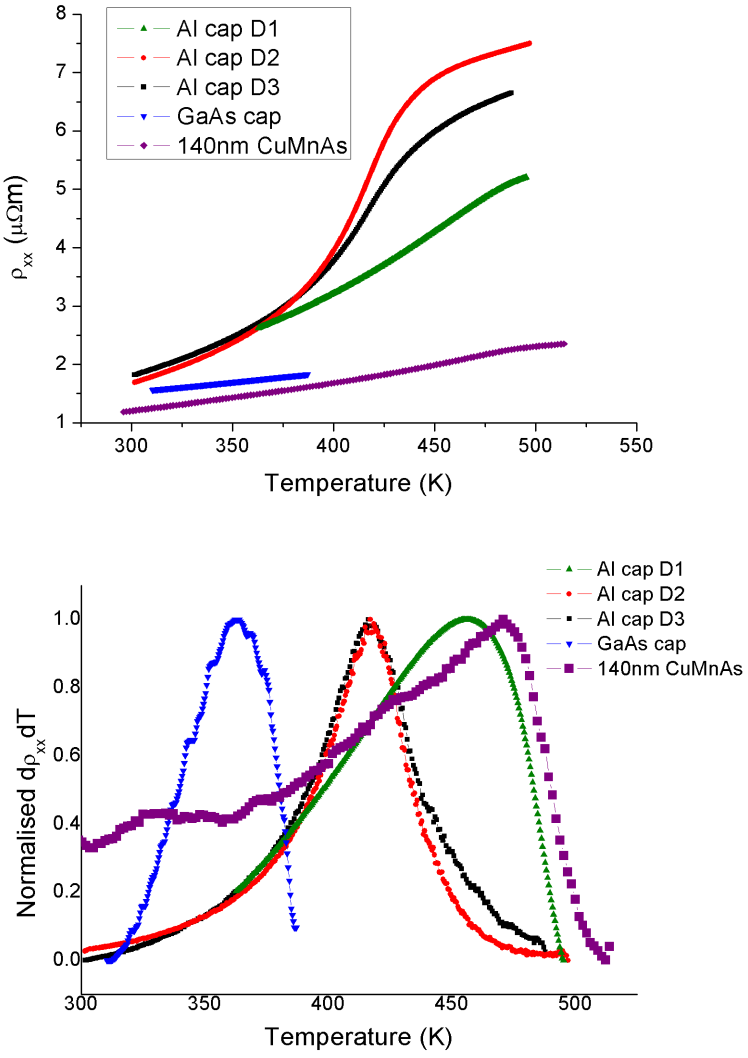

Fig. 5.17 Longitudinal resistivity for 10nm layers that have suffered varying degrees of time dependent changes in the T_N. The green, red and black lines are the different devices from Sample:3-1 (discussed in figure 5.16) and the blue line is Sample:1-7. The purple line is a thicker layer of stoichiometric CuMnAs (Sample:1-3).

phosphorus fluxes is possibly due to differences between strained and relaxed layers. This section will look at the effect of phosphorus doping on the T_N. A study will be made of the effect of the phosphorus flux for series 8. Also a comparison will be made for three layers grown with the same applied phosphrous flux but with differences in the layer thicknesses, lattice parameters, and T_{sub} (Sample:6-1, Sample:7-1 & Sample:8-2). The CuMn($As_{(\mathbf{1-x})}P_{\mathbf{x}}$) layers will also be compared to a stoichiometric layer of CuMnAs (Sample:1-3).

5.5.1 The effect of phosphorus flux on the T_N of CuMnAsP

Figure 5.18 shows the resistivity and its temperature derivative for the growth series 8. As discussed in the previous chapter the growth conditions were maintained to minimise the differences from uncertainties in the flux and the incorporation of phosphorus. Figure 5.18a shows the room temperature resistivity increasing with the phosphorus flux from 0.5×10^{-8}-1.5×10^{-8} Torr. This could be due to a decrease in the mobility or in carrier concentration. The latter is expected on the basis of band structure calculations [38], which indicate a lower electron and hole concentration for CuMnP than for CuMnAs. The magnitude of the resistivity change varies significantly between the samples and is listed in table 5.3; there is no distinct pattern on how the percentage change varies with phosphorus flux. In figures 5.18b & 5.18c the derivative for the different sample shows a decreasing T_N. The cusp has a similar shape for all the samples with a slightly larger change in magnitude for the phosphorus doped samples, as discussed in section 4.3.1. The decrease in the T_N could be due to the possibly increasing strain in the layers as the phosphorus flux was increased. As the lattice mismatch increases in the different samples the *ab* plane will be stretched apart increasing the distance between the layers of FM coupled Mn atoms. The *c* axis will also compress with the strain, bringing the AFM coupling between the opposing FM planes closer together. The distortions in the coupling between the Mn atoms will alter the energy of the

	CuMnAs	CuMn($As_{(1-x)}P_x$) $f = 0.5 \times 10^{-8}$Torr	CuMn($As_{(1-x)}P_x$) $f = 1.0 \times 10^{-8}$Torr	CuMn($As_{(1-x)}P_x$) $f = 1.5 \times 10^{-8}$Torr
$\Delta(\rho_{xx})$	84.9%	123.2%	52.6%	58.9%

Table 5.3 Percentage change in the ρ_{xx} from 310K to 500K

exchange interaction. If the distorted lattice is less energetically favourable then smaller thermal perturbations will be able to disrupt it causing the T_N to decrease.

5.5.2 The effect of growth conditions on the T_N of CuMn($As_(1-x)P_x$)

Figure 5.19 shows a comparison of the three different layers of CuMn($As_{(1-x)}P_x$). The layers were grown with nominally the same applied arsenic and phosphorus fluxes but different layer thickness, GaP substrates and T_{sub} as discussed in the previous chapter. The following is a comparison of the ρ_{xx} in figure 5.19a. The first layer (Sample:6-1) closely matches the resistivity of the stoichiometric CuMnAs (Sample:1-3) other than the deflection in the gradient occurs at a higher temperature. The second layer (Sample:7-1) has a significantly higher resistivity than all the other samples. The third layer (Sample:8-2) has a resistivity that is constantly displaced higher than that of the CuMnAs and the deflection occurs at a slightly lower temperature. The derivatives of the resistivity shown in figures 5.19b & 5.19c show that the three different layers have three different transition temperatures. The first layer has an T_N increased by $\sim 20K$ from that of CuMnAs, the second layer has a T_N similar to that of CuMnAs and the third layer has a T_N that has decreased by $\sim 20K$ from that of CuMnAs. The second layer also demonstrates a second smaller transition around 375K, which could be due to a secondary phase in the material.

There are two key possible sources for the differences in the T_N between the three samples; the differences in the material remaining strained or relaxed could cause the T_N to decrease and increase respectively, which could be dependant on the thickness of the layer as it will relax past a critical thickness. Alternatively the sensitivity to the T_{sub} of the

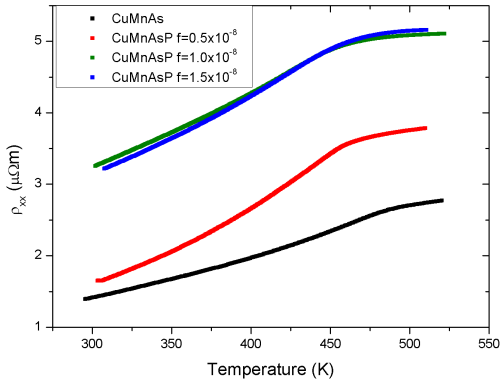

(a) ρ_{xx} vs T

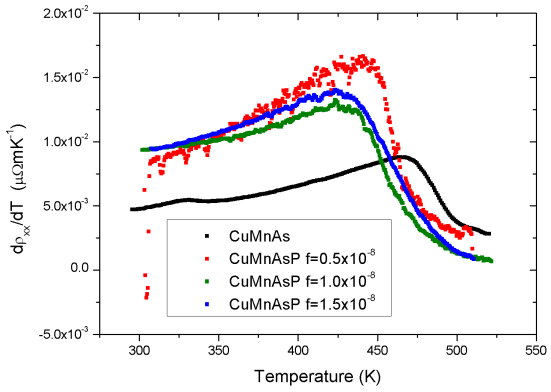

(b) $d\rho_{xx}/dT$ vs T

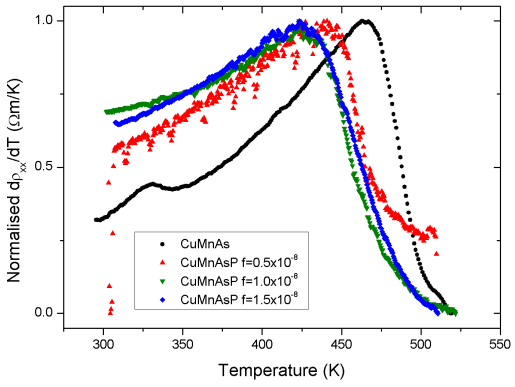

(c) Normalised $d\rho_{xx}/dT$ vs T

Fig. 5.18 Comparing the transport measurements for samples with varying levels of P flux applied during growth. Black is stoichiometric CuMnAs (Sample:1-3), red is Sample:8-1, green is Sample:8-2 and blue is Sample:8-3.

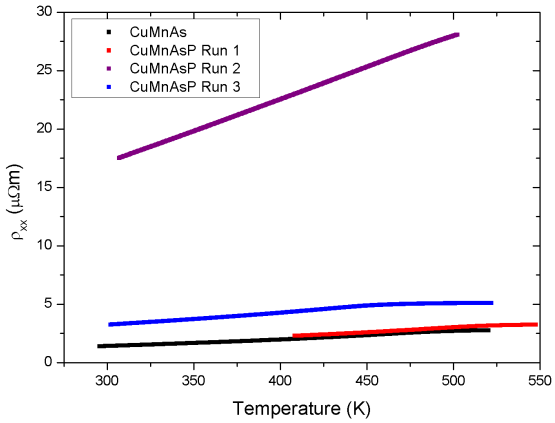

(a) ρ_{xx} vs T

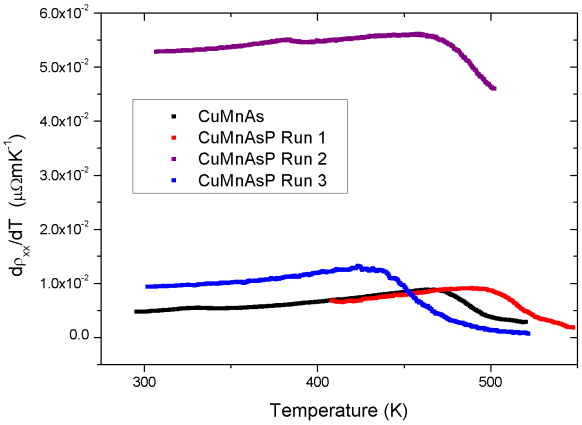

(b) $d\rho_{xx}/dT$ vs T

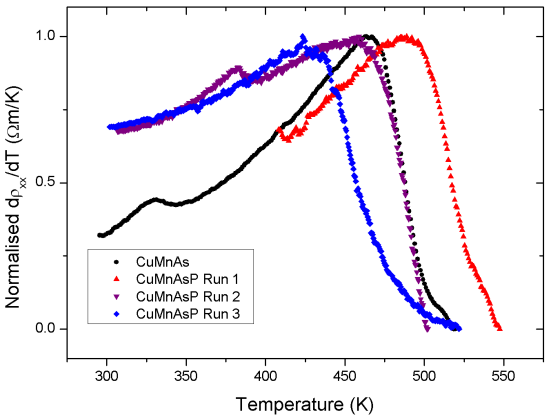

(c) Normalised $d\rho_{xx}/dT$ vs T

Fig. 5.19 The effects of different growth conditions on CuMn($As_{(1-x)}P_x$) with a flux of 1×10^{-8}Torr. Red is Sample:6-1, purple is Sample:7-1 blue is Sample:8-2 and black is CuMnAs (Sample:1-3).

competition for the group V sites between arsenic and phosphorus could cause different percentages of phosphorus to be incorporated.

The expectation is that as the group V element becomes lighter and smaller there is an increase in the temperature of magnetic transitions or other behaviours. The heavier group V element Sb forms CuMnSb with a T_N of 55K [142], which is significantly reduced from that seen in CuMnAs.

5.6 Measuring multiple phase transition temperatures in non-stoichiometric CuMnAs

The non-stoichiometric sample of CuMnAs (Sample:2-1) that was described in section 3.2.2 has a secondary FM phase. Figure 5.20 shows the ρ_{xx} measurements for this layer. There are two clear turning points in the resistivity. The first around 350K and the second at 500K. These form two clear cusps in the $d\rho_{xx}/dT$ (figure 5.20b), these peaks correspond to the two critical transitions of FM MnAs around 335K and AF CuMnAs around 480K. The CuMnAs peak appears to be slightly increased by 10K on other measurements of stoichiometric CuMnAs

From figure 5.20 there are several observations to note, the sharp peak for the MnAs implies that any particulates that have formed are crystalline, the width of the peak implies that there is a small range of T_C for the MnAs particulates and is confirmation that a portion of the current runs through the inclusions.

By calculating the reduced temperature (t) defined in 1.3, it is possible to compare the two transitions in the sample equally (figure 5.21). The CuMnAs peak is significantly larger when rescaled than the MnAs transition. There is only a small difference in the peak width, which could mean that there is a similar crystal quality for both materials.

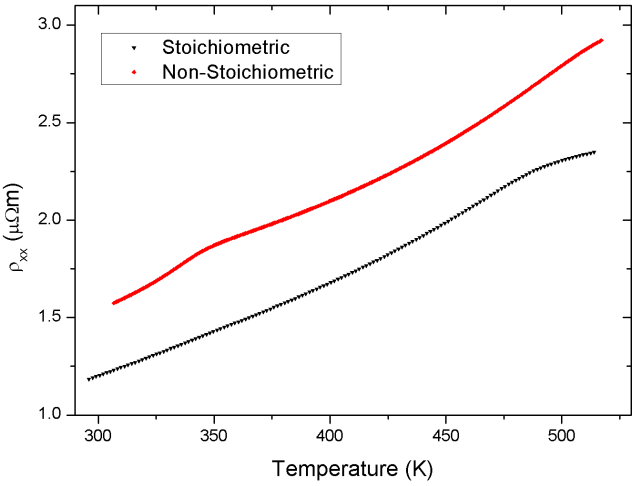

(a) ρ_{xx} vs T

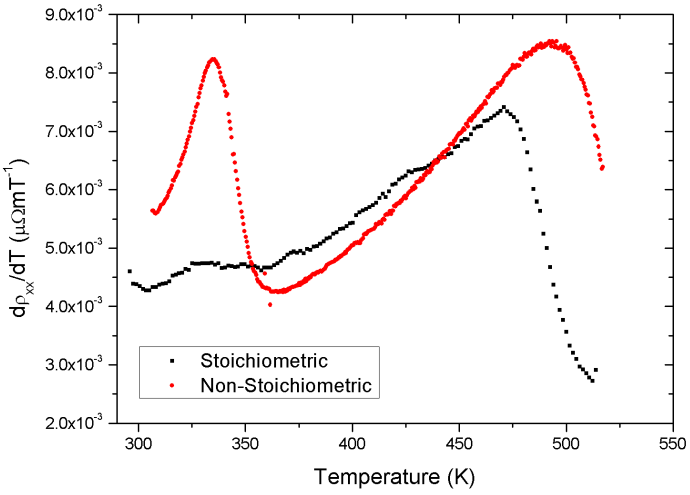

(b) $d\rho_{xx}/dT$ vs T

Fig. 5.20 Longitudinal transport measurements for non-stoichiometric CuMnAs (Sample:2-1) in red, compared to stoichiometric CuMnAs (Sample:1-3) in black.

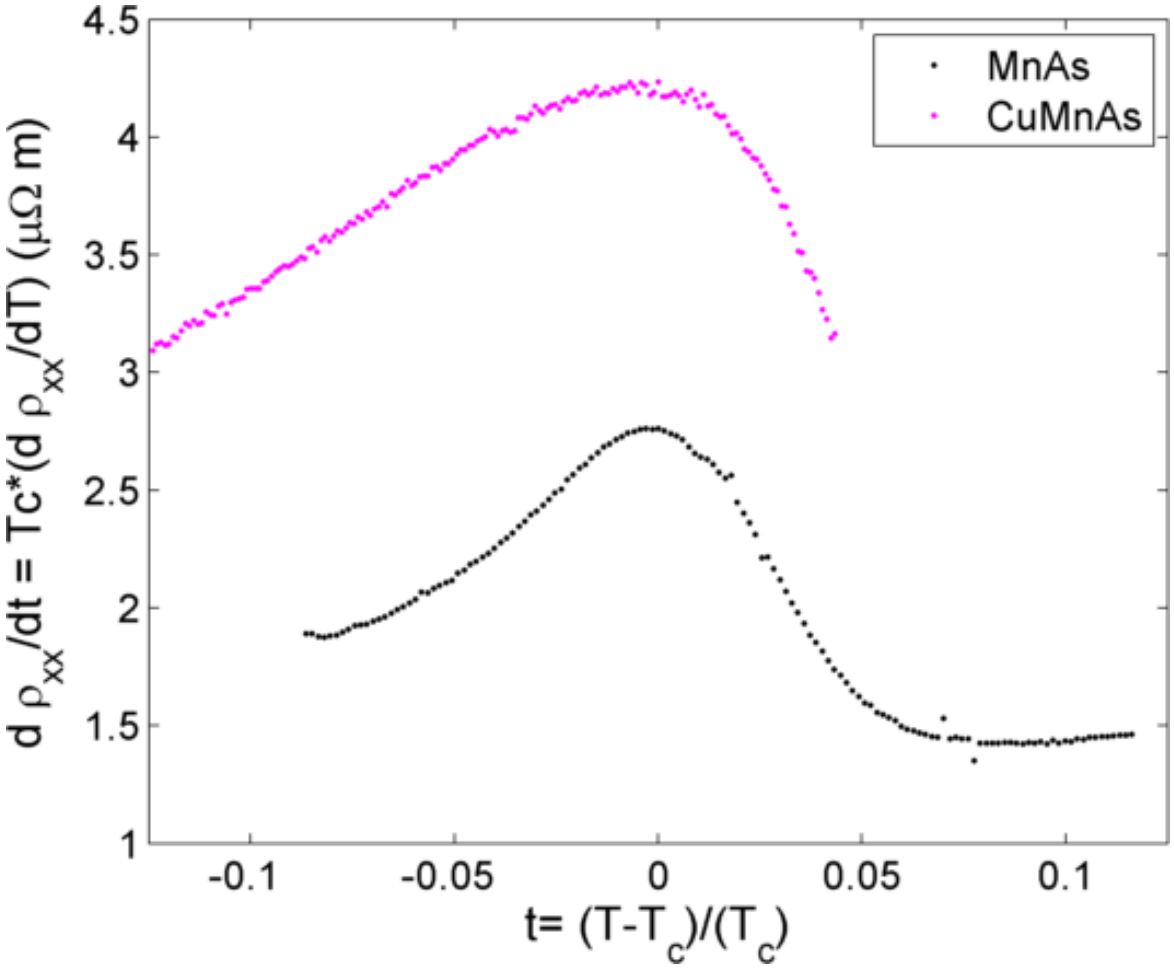

Fig. 5.21 Comparing the T_c for CuMnAs and MnAs in non-stoichiometric grown CuMnAs (Sample:2-1), with the reduced temperature t. Black is from the MnAs and pink is from the CuMnAs transition.

5.7 Conclusion

This chapter has discussed a variety of results. The key results is that from measuring the resistivity against temperature, in no applied field, it is possible to determine the T_N of a layer of CuMnAs. There is a clear cusp in the $d\rho_{xx}/dT$ against the temperature, which corresponds well to the T_N calculated from neutron diffraction for both CuMnAs and CuMn($As_{(\mathbf{1-x})}P_{\mathbf{x}}$). These results mean that the method of measuring the T_N from the resistivity can be used as a lab based tool to provide information quickly on the T_N.

A common feature on first heating a device is a non-reversible change in the resistivity. The change in the resistivity could be due to some form of annealing effect on the sample. In some more resistive samples when held at high temperatures past their T_N there is a larger time dependent element to the resistivity change.

The measurements have been used to show that below 10nm there is a suppression of the T_N. It has also been demonstrated that for the different growth and nucleation methods there is no significant change in the T_N. In thin films there has been shown to be a time dependent change in a layer, with a depression in the T_N without a significant change in the room temperature resistivity.

The T_N of CuMn($As_{(\mathbf{1-x})}P_{\mathbf{x}}$) measured for different samples and growth runs creates a complicated picture of the behaviour of the T_N that is very dependent on the individual growth conditions of each layer. For three different sample with the same nominal applied As and P fluxes but with different possible growth temperatures. The T_N for the three different samples is above, below and the same as CuMnAs. The significant differences in the T_N for these samples could be due to the difference with the lattice mismatch of the layer, depending on if the layer is strained or relaxed or that the incorporation of phosphorus into the crystal lattice during growth is very sensitive to the substrate growth conditions. For the growth series 8 the T_N appears to decrease with the increasing phosphorus flux.

The final result of this chapter was simultaneously measuring the T_C of MnAs and T_N of CuMnAs in the two phase system of non-stoichiometric CuMnAs (Sample:2-1). The cusp in the resistivity for the MnAs transition appears to be very sensitive and can be observed in some nominally stoichiometric samples (Sample:1-3, Sample:7-1). This measurement technique can therefore be used in future to establish the presence of secondary phases in layers.

Chapter 6

Comparing transport measurements for non-stoichiometric CuMnAs to simulations of mixed conductivity systems

6.1 Introduction

The following chapter will detail investigations into the magneto-transport for longitudinal and transverse resistivity of Mn rich non-stoichiometric CuMnAs, Sample:2-1. The transverse resistance will be separated out into the NHE and AHE to observe the effects of the FM MnAs inclusions on the measurements of the bulk material. The longitudinal resistivity will be used to describe the Isotropic Magnetoresistance (IMR) of the material.

The chapter then goes on to discuss simulations of a 2D simplified model of the situation seen in this sample where FM inclusions of MnAs are incorporated in a matrix of CuMnAs and both contribute to the transport measurements (section 5.6). In the calculations the

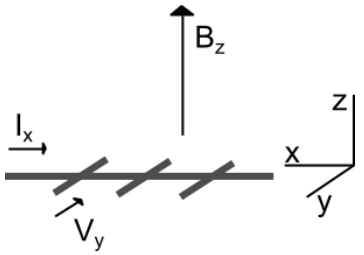

Fig. 6.1 Schematic showing the axis orientation of the current, voltage and field for measuring the out of plane magneto-transport.

longitudinal and transverse conductivity is varied, for systems with a uniform conductivity and with inclusions of different conductivity, to see the effects on the longitudinal and transverse resistivity.

Finally the chapter will conclude by comparing the predictions of the conductivities model with the resistivities discussed earlier in section 6.2 for non-stoichiometric CuMnAs.

6.2 Magneto-transport for non-stoichiometric CuMnAs

Resistivity measurements for non-stoichiometric CuMnAs were performed on the vector magnet system, described in section 2.3.2. The measurements were carried out on large Hall bars of 1mm by 3mm with the procedure outlined in 2.3.2. The geometry of the system is shown in figure 6.1 where the applied current, measured voltage and applied field are all orthogonal to each other.

Figure 6.2 shows the ρ_{xx} between 4K-500K. This temperature range includes the results displayed in section 5.6. The ρ_{xx} increases with increasing temperature and there is strong agreement between the measurement made in cryogenic conditions and the sample measured in vacuum at higher temperatures. The increase in the resistivity is due to increased phonon and moment disorder scattering (section 1.3). In some semi-metals intrinsic carrier concentration is independent of temperature when below room temperature. Sample:2-1 was

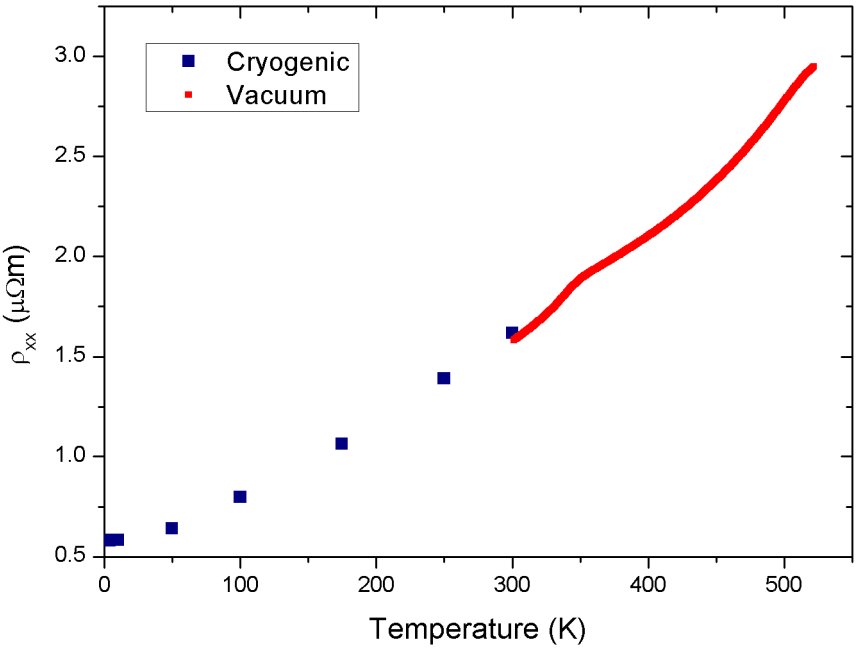

Fig. 6.2 ρ_{xx} against temperature for Sample:2-1. The data in red represents the measurements made in the high temperature system and the blue points represents the resistivity at zero field for field sweeps at each temperature.

grown on GaAs so at higher temperatures, as discussed in section 5.4.3, the intrinsic carrier concentration of the GaAs substrate can become significant.

The Magneto Resistance (MR) of the CuMnAs layer was calculated as

$$MR = \frac{\rho_{xx}(B) - \rho_{xx}(0)}{\rho_{xx}(0)} \tag{6.1}$$

where $\rho_{xx}(B)$ is the longitudinal resistivity at a certain applied field, $\rho_{xx}(0)$ is the longitudinal resistivity at zero field, the value is calculated as the mean of all data points at zero field (some of which are not shown on figure 6.3 for clarity). Stoichiometric CuMnAs has been shown to have a very small MR, in figure 6.3 the MR is $(0.003 \pm 0.003)\%$ at 296K, with a corresponding small normal Hall coefficient which gives exaggerated predictions of the carrier density in the single band model [39].

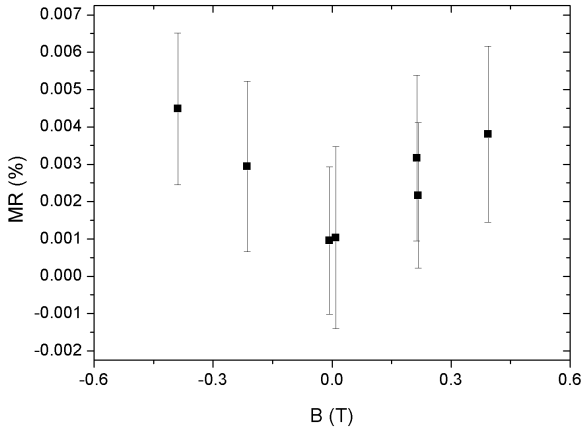

Fig. 6.3 The mean MR at different applied fields for CuMnAs (Sample:1-8) at 296K. The black dots represent the mean value for the data measured at the field strength. The error bars are the standard error for the measured data.

For non-stoichiometric CuMnAs individual magnetic field sweeps were performed at a series of temperatures in the range of 4K-300K and the ρ_{xx}, figure 6.4, and transverse resistivity, figure 6.6 were measured. Between 4K and 50K the longitudinal resistivity increases with the magnitude of the applied magnetic field.

The size of the change in the MR is shown in figure 6.5. The MR changes from positive to negative with the temperature above 100K. The magnitude of the MR is up to 1%. As the measured sample temperature increases, the drift present in the measurements is due to instability in the temperature control of the system which increases the error on the MR.

Figure 6.6 shows the transverse resistance against applied out of plane magnetic field for several different temperatures. At the lowest temperatures between 4K and 50K there is a linear relationship between the applied field and the $\mathbf{R_{xy}}$, as the temperature increases two different gradients are observed, a steeper gradient when the field is less than about 1T and a shallower gradient for fields above 1T. The magnitude of the gradient when there are small applied fields increases with temperature. The $\mathbf{R_{xy}}$ curves can be split into two components, the linear NHE, figure 6.7a, and the AHE. The NHE is calculated as the gradient of resistivity against field after the material has become fully saturated, described in section 2.3.2. The

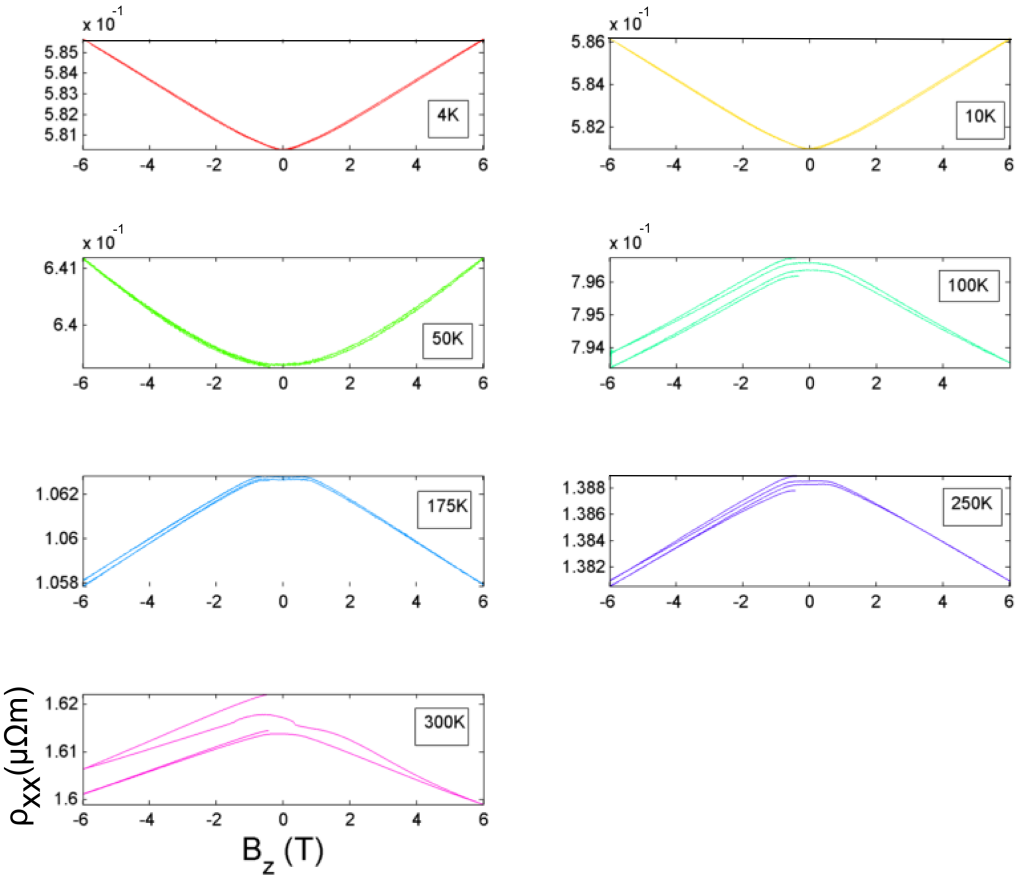

Fig. 6.4 ρ_{xx} as a function of applied magnetic field for a series of temperatures between 4K and 300K for non-stoichiometric CuMnAs (Sample:2-1). As the temperature increases from 50K the temperature controller becomes unstable leading to artefacts in the results.

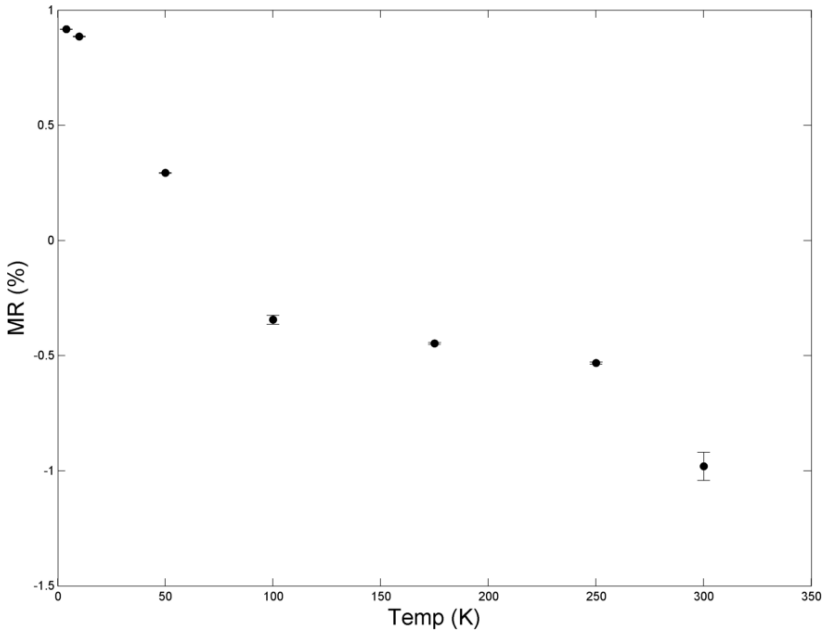

Fig. 6.5 Change in the magneto resistance for the ρ_{xx} for non-stoichiometric CuMnAs (Sample:2-1) at different temperatures.

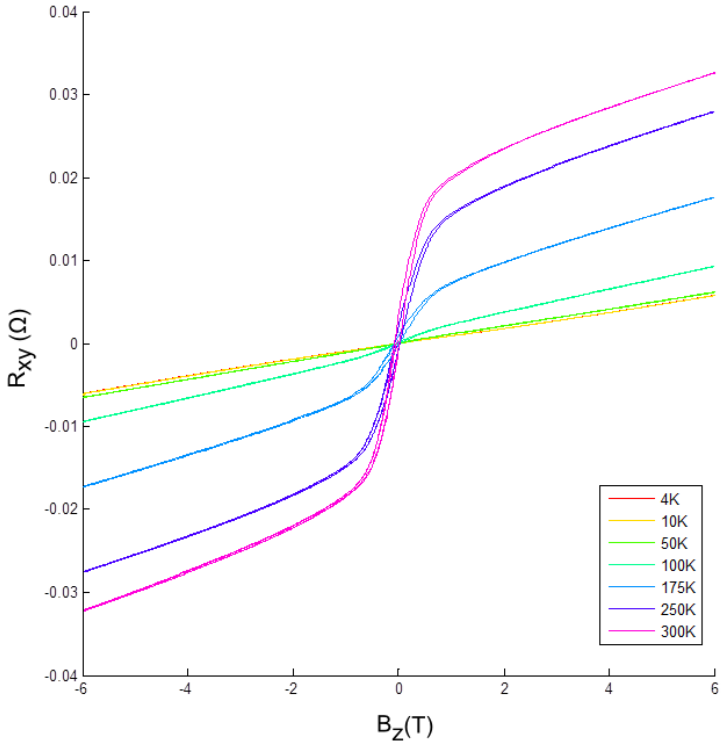

Fig. 6.6 R_{xy} against applied magnetic field at a series of temperatures for non-stoichiometric CuMnAs (Sample:2-1) . Each temperature corresponds to a different line colour.

gradient increases with temperature as can be seen in figure 6.7b, below 50K the gradient remains constant before increasing non linearly with temperature.

The other component of the resistance is from the AHE, figure 6.8, which is calculated from the raw data by removing the NHE. The presence of an AHE is indicative that a material contains a FM material (see section 2.3.2), which is MnAs from previous results on Sample:2-1, discussed in chapter 3. Another feature to note from figure 6.8 is that the magnitude of the AHE increases with temperature. Above 100K the the magnitude of the AHE increases markedly. MnAs has been shown to have an increasing $\rho_{\mathbf{xy}}$ with a change in the sign of the MR for the longitudinal resistivity [127], that is attributed to a two carrier system where electrons are dominant at low temperatures and an increasing hole carriers with increasing temperature. GaAs(MnAs) systems have been studied where MnAs clusters have dominated the magneto-transport and had an enhanced T_C up to 340K [128].

The R_A, the value of the AHE at magnetic saturation can be used to quantify the AHE. The predicted relationship between R_{xx} and R_A has the form [143],

$$R_A \propto R_{xx}^{\eta} M \tag{6.2}$$

where M is the magnetisation and η is a scaling factor that is predicted to be 1 or 2 depending on the dominant mechanism of the scattering as discussed in section 2.3.2. The measured M for the non-stoichiometric (figure 3.18) sample is weakly temperature dependent over the temperature range of figure 6.8 and so equation 2.18 can be checked for the non-stoichiometric CuMnAs by plotting vs R_{xx} on a log-log plot as is done in figure 6.9. This plot should be linear for the predicted power law behaviour, with gradient η. However for Sample:2-1 a linear trend is not present and the apparent n value at low temperatures is very large.

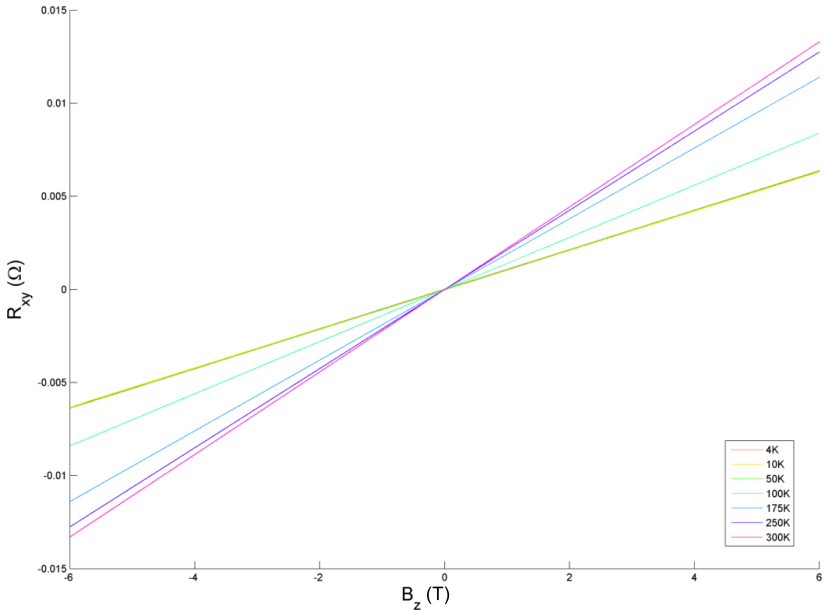

(a) Gradient against field

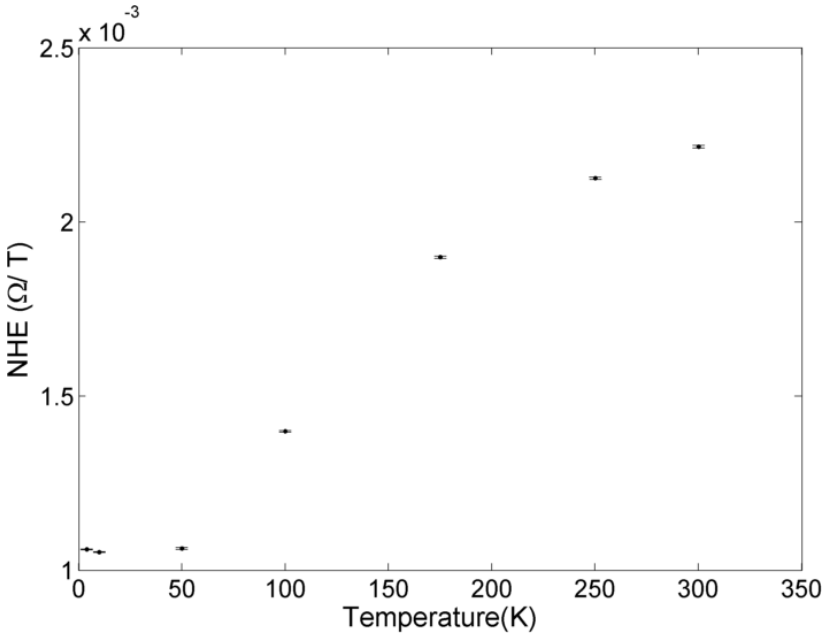

(b) Gradient against temperature

Fig. 6.7 The fitted linear gradient of the transverse resistance against applied field for non-stoiochiometric CuMnAs (Sample:2-1). The gradient is calculated when the sample is fully saturated.

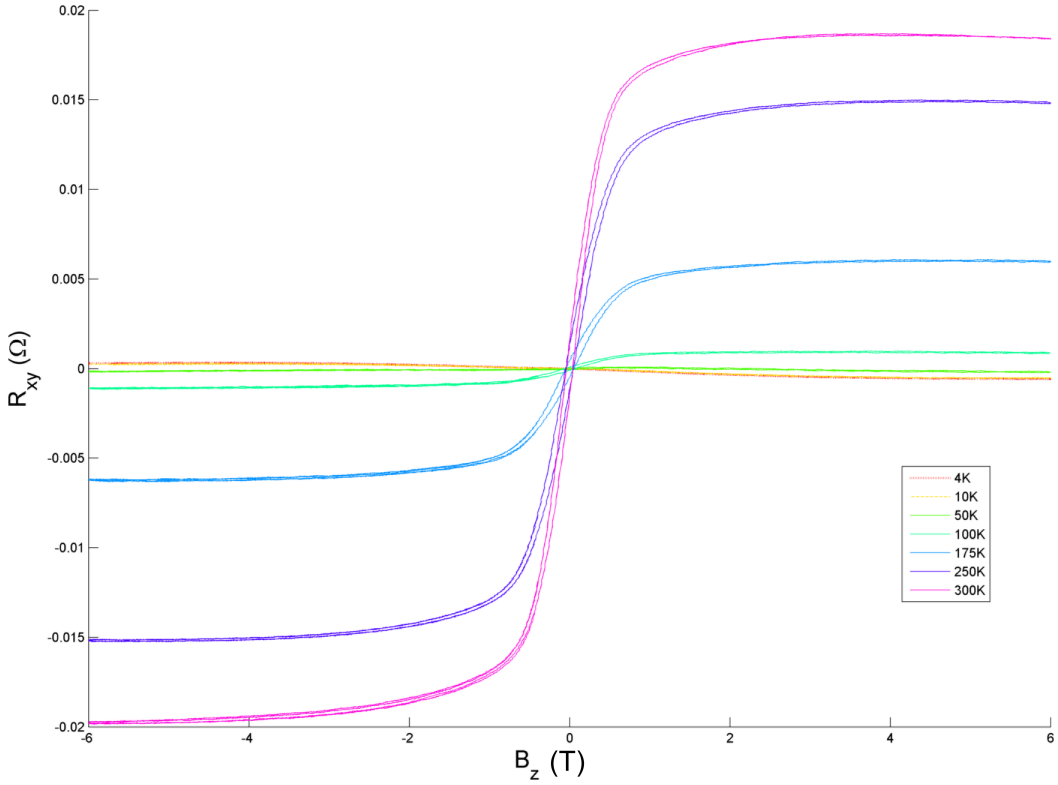

Fig. 6.8 AHE contribution of the R_{xy} against applied magnetic field at temperatures from 4K-300K for non-stoichiometric CuMnAs (Sample:2-1). Each line colour represents a different temperature.

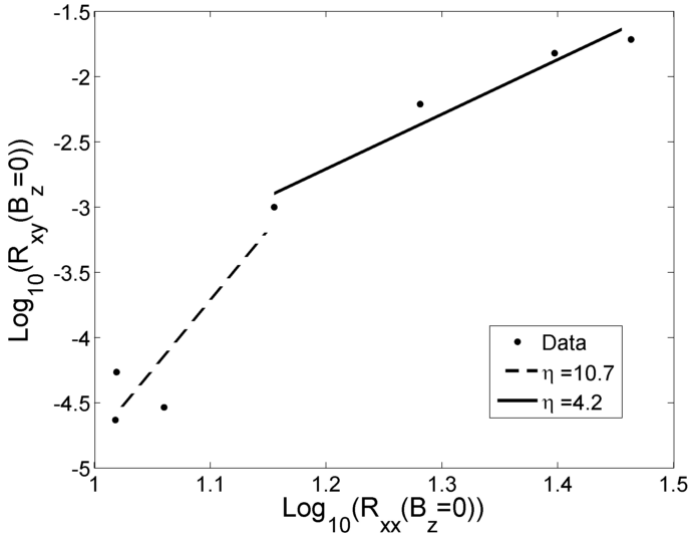

Fig. 6.9 A log-log plot of the Hall coefficient against the R_{xx} to determine the scattering factor, η, from equation 2.18. The temperature regions are split into two different scaling factors.

6.3 Simulating higher conductivity inclusions in a uniform background

The non-stoichiometric Sample:2-1 has been shown to be a two phase system with a matrix of CuMnAs and a percentage of ferromagnetic MnAs (section 3.4 and 5.6). The ferromagnetic contribution has been shown to dominate the magneto transport. A 2D model of this system was made to determine the effect of different conductivities for the matrix and inclusions. The model will be used to study the current paths, resistivities and Hall resistivities of a 2D system and to compare the results with the measured data. The model uses Matlab's Partial Differential Equations (PDE) tool box to solve the situation using finite element analysis, which is described next.

6.3.1 Modelling the resistivities of inhomogeneous conductors using PDE modelling

In this thesis the effect of an inhomogeneous conductivity on systems on the current density and voltage will be simulated by solving PDE for the Maxwell equations [144]. The system is set up with the boundary conditions as shown in figure 6.10. The system is defined as a electric conductor, with perfect contacts, to give the following equations for the boundary conditions (equations 6.3 & 6.4). The D boundaries are Dirichelet boundaries that must satisfy the condition

$$\widehat{\nu} \times \mathbf{E} = 0 \tag{6.3}$$

where $\widehat{\nu}$ is the outward unit vector and $\mathbf{E}$ is the electric field. Physically the Dirichelet boundaries represent that the current can enter and leave from these boundaries and that there must be a specified change in potential between them. The N boundaries are Neumann

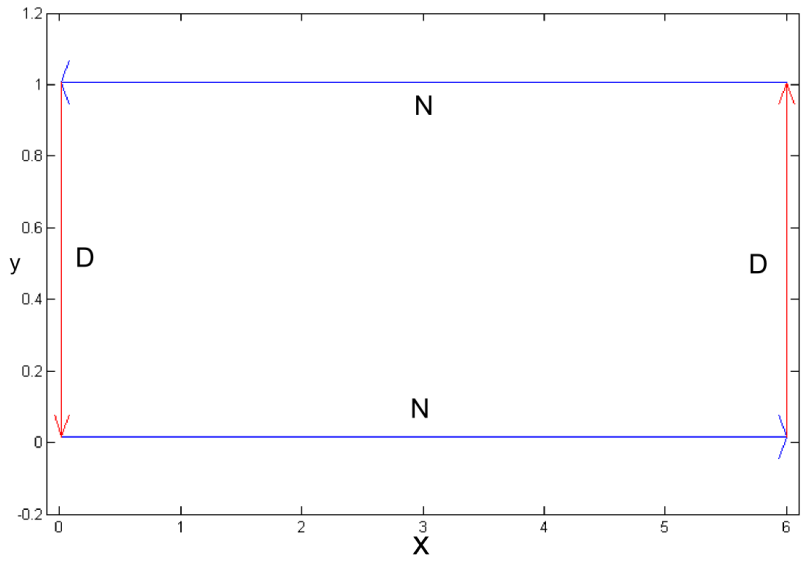

Fig. 6.10 Example of boundary conditions used for simulations in this thesis. D (red) is a Dirichelet type boundary and N (blue) is a Neumann type boundary.

boundaries that must satisfy the condition

$$\widehat{\nu} \times \nabla \times \mathbf{H} = 0 \tag{6.4}$$

which specifies the value that the gradient must take on the boundary. Physically this represents that current can not be lost through these edges. of the sample

The PDE equations are solved using FEA [145], which divides a 2D system into a series of triangular shapes. The triangles are joined together by nodes. These triangles create a mesh across the system which can be made finer to increase the accuracy of the result. Figure 6.11 shows the mesh generated for boxes with uniform and non uniform conductivity. In the uniform boxes it is possible to see a near even distribution of triangles across the image with an increased density of triangles around the x=0 and x=6 edges. In the non uniform system it is possible to see a significant difference in the mesh layout where there are a higher density of triangles (with smaller area) around the inclusions. The next section will describe the equations for the conductivity and how the current density, voltage and resistivity are calculated.

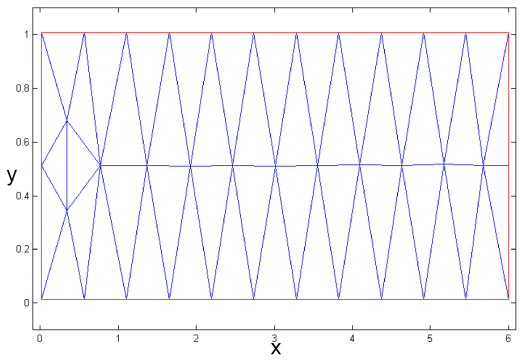

(a) Uniform medium with a coarse mesh.

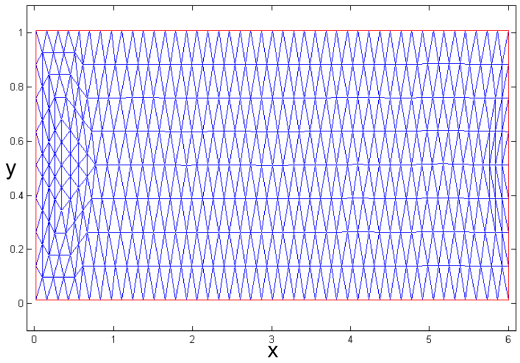

(b) Uniform medium with a finer mesh.

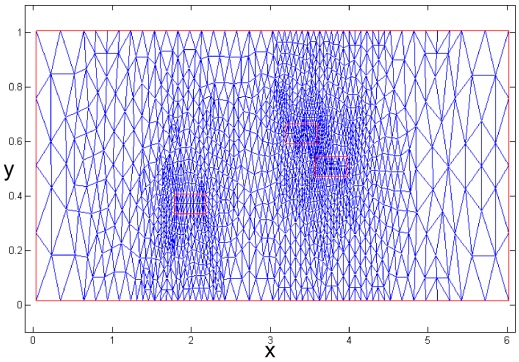

(c) Non uniform system with a mesh.

Fig. 6.11 Examples of the FEA mesh. The mesh is made up of triangles formed between nodes. At more complex computational areas there will be a higher density of nodes and smaller triangles.

6.3.2 Simulating a uniform conducting medium

Initially the model was set up as a uniform conducting medium to compare the results with predictions of the relationship between transverse and longitudinal components of conductivity and resistivity.

The conductivities (σ) of the matrix and the inclusions in the model have the form of

$$\sigma = \begin{pmatrix} \sigma_{xx} & \sigma_{xy} \\ \sigma_{yx} & \sigma_{yy} \end{pmatrix} \tag{6.5}$$

and the following conditions are applied throughout the model $\sigma_{xx}= \sigma_{yy}$ and that -$\sigma_{xy}= \sigma_{yx}$. The conductivity tensor simplifies to

$$\sigma = \begin{pmatrix} \sigma_{xx} & \sigma_{xy} \\ -\sigma_{xy} & \sigma_{xx} \end{pmatrix} \tag{6.6}$$

Throughout the model a negative value of σ_{xy} will be used so the conductivity tensor can be written as

$$\sigma = \begin{pmatrix} \sigma_{xx} & -\sigma_{xy} \\ \sigma_{xy} & \sigma_{xx} \end{pmatrix} \tag{6.7}$$

where σ_{xy} is always a positive number. The resistivity and conductivity are the inverse of each other and the transverse and longitudinal resistivities are linked to each other as

$$\rho_{xx} = \frac{\sigma_{xx}}{(\sigma_{xx}^2 + \sigma_{xy}^2)} \tag{6.8a}$$

$$\rho_{xy} = \frac{\sigma_{xy}}{(\sigma_{xx}^2 + \sigma_{xy}^2)} \tag{6.8b}$$

To compare the model to predictions it is necessary to convert the model outputs into resistivities. To calculate the resistivity requires the voltage (V) and current density (**j**). The voltage is output as a variable at every point on a triangular mesh . **j** varies with each position and requires several steps to calculate, which are detailed below. The first step calculating the electric field (E), which is

$$\mathbf{E} = -\nabla.V \tag{6.9}$$

where V is the voltage and s is the direction. The gradient is calculated for both the x and y directions. The current density (**j**) is

$$\mathbf{j} = \sigma.\mathbf{E} \tag{6.10}$$

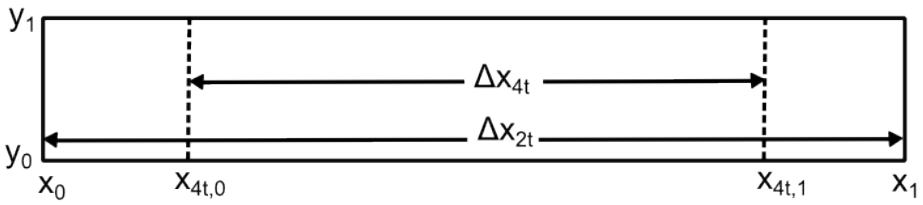

Fig. 6.12 Dimensions of the model.

For the 2D system it can also be described as the current per unit length. Conductivities for every position on the electric field matrix are calculated from the original model and the current components for every component are calculated as

$$j_x = \sigma_{xx}E_x + \sigma_{xy}E_y \tag{6.11a}$$

$$j_y = \sigma_{xx}E_y - \sigma_{xy}E_x \tag{6.11b}$$

The resistivity (ρ) is defined as the:

$$\rho = \frac{V}{j\Delta x_{\mathrm{V}}} \tag{6.12}$$

where Δx_{V} is the distance along the x axis that the voltage is measured from. In two terminal mode this is Δx_{V}=x_1-x_0 and in four terminal mode Δx_{V}=$x_{4t,1}$-$x_{4t,0}$, which is demonstrated in figure 6.12. j is the mean value across the sample.

Set-up of the model

For the simplest model of a rectangle with uniform σ_{xx} and σ_{xy}=0 the results are shown in figure 6.13. The current flow is uniform and the equipotential lines are equally spaced and run parallel to the y dimension. For the case of σ_{xy}=0 the current is the same throughout the bar, which is demonstrated in figures 6.13b & 6.13c.

Figure 6.14a has a non zero σ_{xy}, acting as if a magnetic field was applied, which causes the equipotential lines to rotate. In the bulk of the sample the equipotentials are linear and

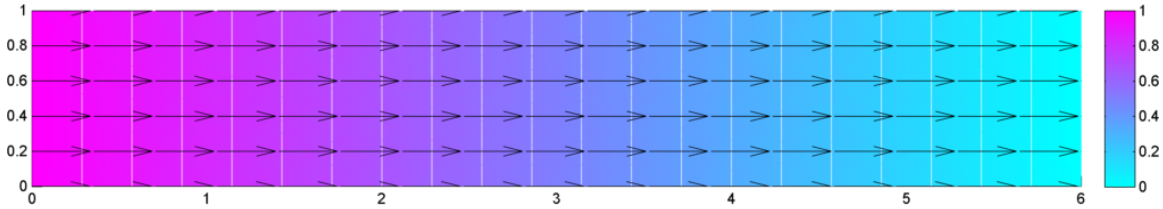

(a) $\sigma_{xx} = 200$ and $\sigma_{xy} = 0$

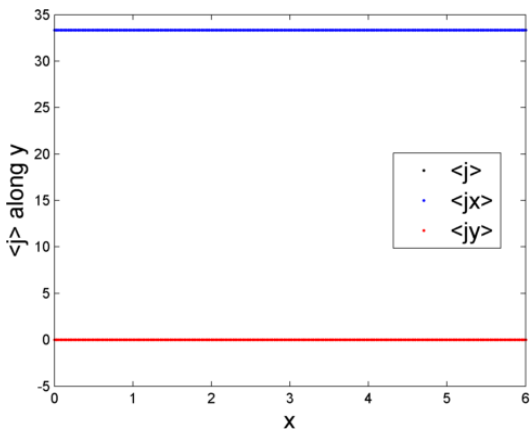

(b) mean j value when summed along the width of the bar

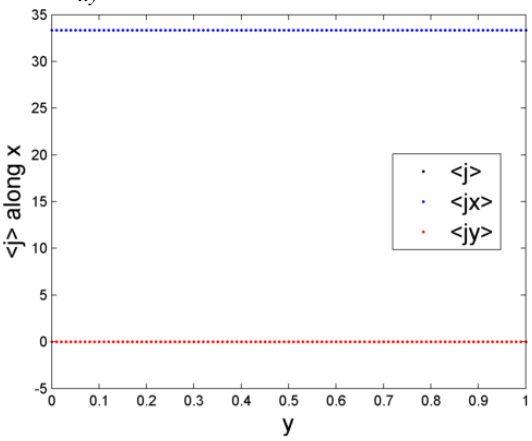

(c) mean j value when summed along the length of the bar

Fig. 6.13 Model for a uniform conductivity medium without a σ_{xy} component. In the top figure the colour map shows the solution equipotential lines are shown in white and the black arrows depict the current density. The bottom figures show the mean values of the current density along different directions. The current density is split into the directional components.

evenly spaced. Where the current enters and leaves the model at the edges of the x directions the equipotential lines are constrained to be parallel to the y direction, this requires the lines to distort. By taking the voltage measurement in the four terminal mode the measured values are taken in the region where there is little distortion of the equipotential lines. Figures 6.20d & 6.20c demonstrate how the current density varies in value with position. The current density value to be taken in calculations is taken from the midpoint to achieve a steady value.

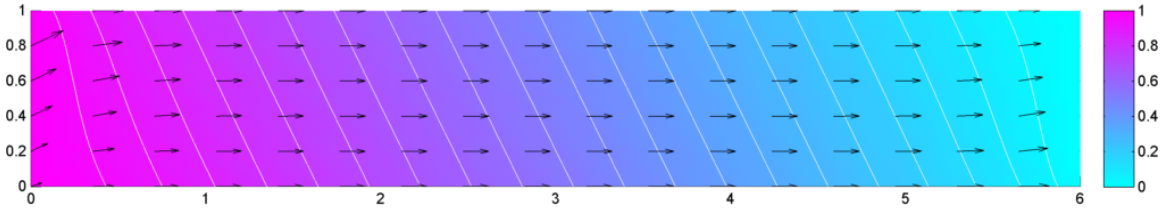

(a) $\sigma_{xx} = 200$ and $\sigma_{xy} = -99$

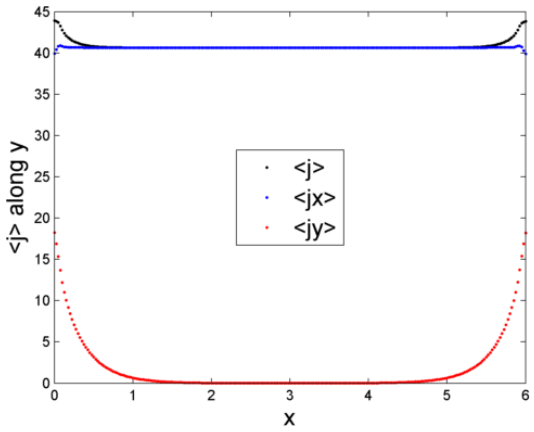

(b) mean j value when summed along the width of the bar

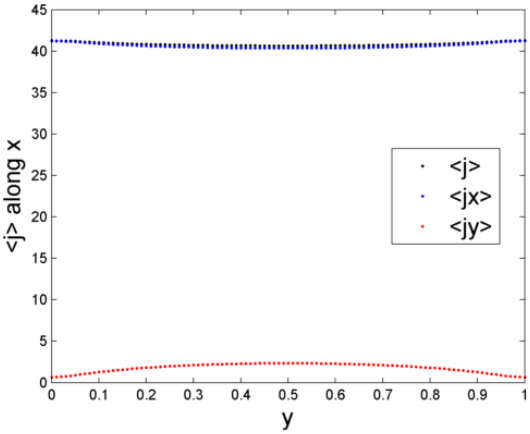

(c) mean j value when summed along the length of the bar

Fig. 6.14 Model for a uniform conductivity medium with a σ_{xy} component. In the top figure the colour map shows the solution equipotential lines are shown in white and the black arrows depict the current density. The bottom figures show the mean values of the current density along different directions. The current density is split into the directional components.

Another consideration is measuring the voltage. If the voltage is measured at the ends it simulates a two terminal measurement, whereas if the voltage is measured away form the ends it represents a four terminal measurement, which is illustrated in figure 6.15. The two and four terminal results will be compared for the longitudinal resistivity of a uniform conducting box as a further test of the calculations and after that only the four terminal results

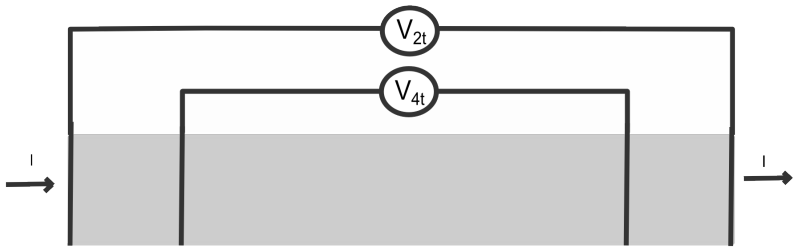

Fig. 6.15 Schematic showing the voltage measurement for two terminal and four terminal measurements. The light grey area is the conductive medium.

will be discussed. The four terminal measurement is taken in a range where the equipotentials are parallel to one another and not being rotated to fit the constraints of the model.

Longitudinal resistivity results

To verify that the model is giving realistic results the following section will compare the results to several predictions. The first comparison will be between the effect of varying the σ_{xy} while the σ_{xx} remains constant at a value greater than σ_{xy}. There are two theoretical predictions to compare the numerical model to initially. The first is predicting the resistivity from the conductivity values using a rearrangement of the equation in 6.8a, which is

$$\rho_{xx,\mathrm{p}} = \left(\sigma_{xx} \left(1 + \left(\frac{\sigma_{xy}}{\sigma_{xx}} \right)^2 \right) \right)^{-1} \tag{6.13}$$

where $\rho_{xx,\mathrm{p}}$ is the predicted longitudinal resistivity. An empirical prediction for the two terminal resistivity can also be made by work done by Hereman [146], which compensates the prediction for the resistivity ($\rho_{xx,\mathrm{H}}$) by considering the dimensions of the shape being measured. It is derived from:

$$\rho_{xx,\mathrm{H}} = \rho_{xx,\mathrm{m}}(\sigma_{xy} = 0) \left(1 + \beta \left(\frac{\sigma_{xy}}{\sigma_{xx}} \right)^2 \right) \tag{6.14}$$

where β is a factor depending on the individual model and $\rho_{xx,m}(\sigma_{xy}=0)$ is the measured longitudinal resistivity without a transverse conductivity. Using the criterion that:

$$\frac{\sigma_{xy}}{\sigma_{xx}} = \frac{\rho_{xy}}{\rho_{xx}} = \tan(\theta_{eq}) \tag{6.15}$$

where θ_{eq} is the angle of the equipotential lines. By using the small angle approximation of $\tan(\theta_{eq}) \approx \theta_{eq}$ in the limit of $\theta_{eq} \to 0$ it can simplify the above equation. This then forms,

$$\rho_{xx,H} = \rho_{xx,m}(\sigma_{xy}=0)\left(1+0.5428\left(\frac{W}{L}\right)\theta^2\right) \tag{6.16}$$

where β is an approximate analytical value of $0.5428\frac{W}{L}$ in the case of $\frac{L}{W} \to \infty$, where W and L are the dimensions of the plain rectangle.

Figure 6.16 shows a comparison between the model and the predictions for a fixed σ_{xx} and a σ_{xy} that varies as a percentage of σ_{xx} from 0-50%. Figure 6.16 clearly demonstrates a good agreement between the predicted ρ_{xx} from the conductivity and the four terminal $\rho_{xx,\mathrm{m}}$ measured by the model. There is also a strong agreement with the two terminal $\rho_{xx,\mathrm{m}}$ and the Hereman prediction, which scales the four terminal measurement based on the shape. The Heremans approximation deviates from the predicted resistivity because of the geometric assumption in the the calculation that $\frac{L}{W} \to \infty$ where as our model has a finite limit of $\frac{L}{W} = 6$.

Figure 6.17 shows the magnitude of the difference between the prediction and the measured four terminal resistivity and 2T resistivity. For the 4T results there is an offset of $\sim 0.1\%$, which depends very weakly on σ_{xy}. This offset is due to the small influence of the contact equipotentials. The 2T result is in good agreement with the Hereman expression.

Transverse resistivity results

A transverse resistivity or Hall voltage is measured in a system where the field, current and voltage are orthogonal to each other. When there is a transverse conductivity (σ_{xy}) in the

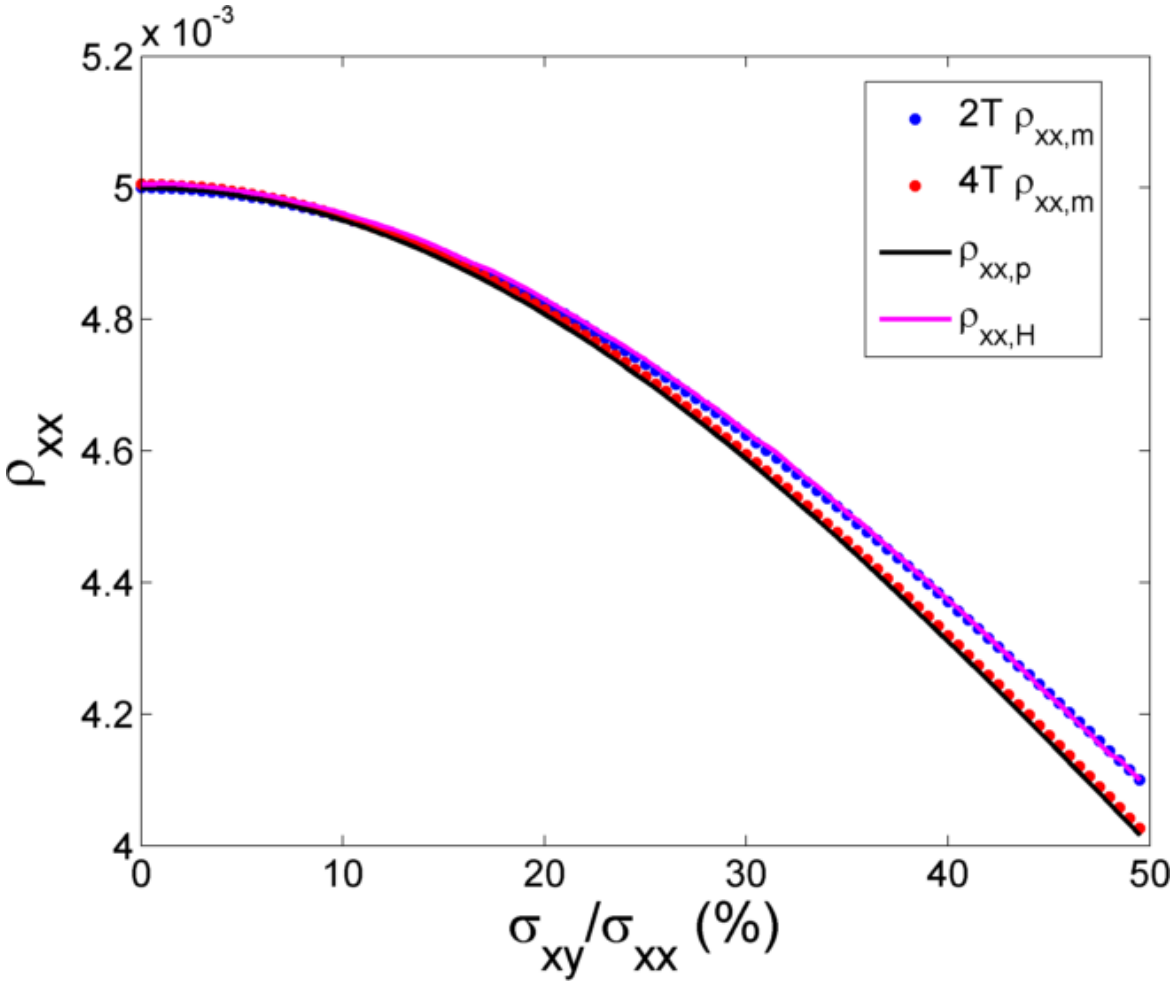

Fig. 6.16 The ρ_{xx} against the ratio of $\frac{\sigma_{xy}}{\sigma_{xx}}$. The blue dots are a two terminal measurement, the red dots are a four terminal measurement, the black line is the predicted values from the conductivity (equation 6.13) and the pink line is the predicted values from the Hereman's prediction (equation 6.16).

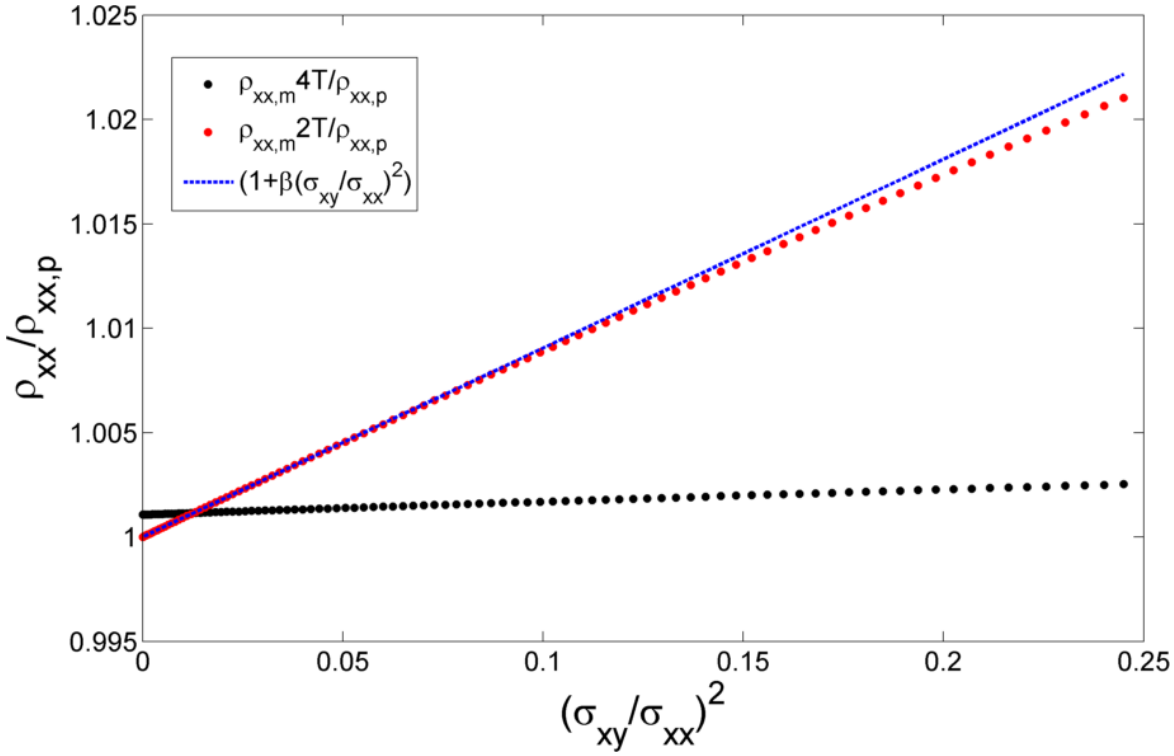

Fig. 6.17 Demonstrating the linear increase in the difference between the predicted (equation 6.13) and measured values for 2T (red) and 4T (black)shown in 6.16. The blue dashed line represents the factor from the Hereman equation (equation 6.16) where $\beta = 0.5428\frac{1}{6}$.

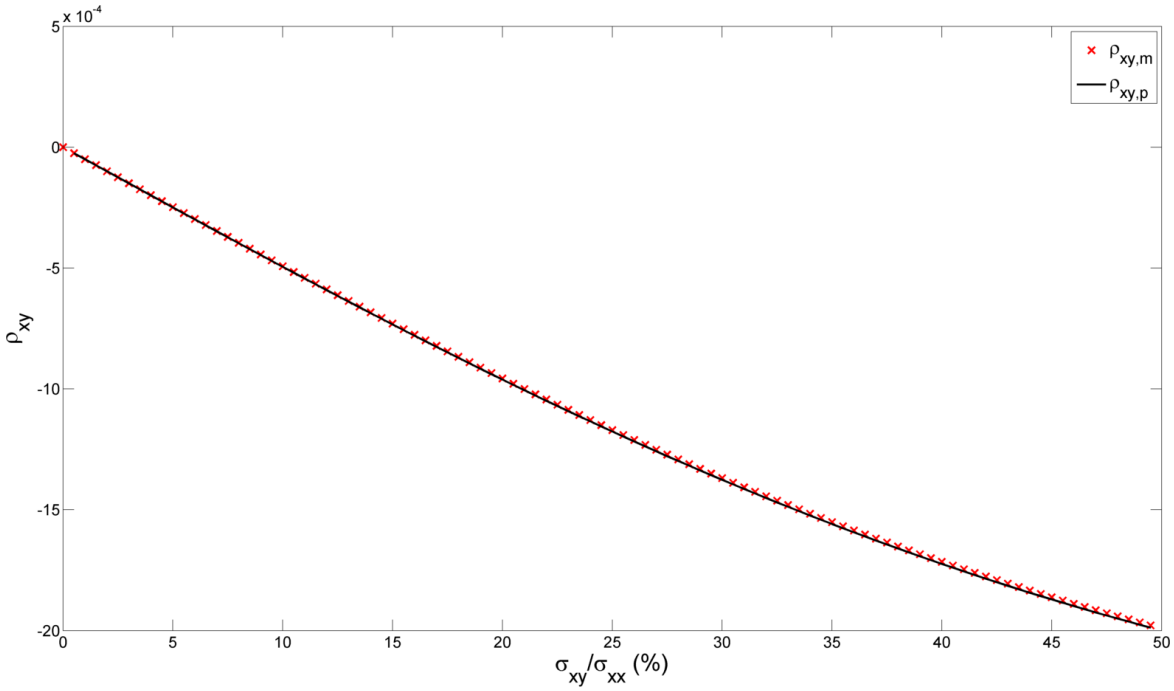

Fig. 6.18 The ρ_{xy} of a uniform medium as a function of $|\sigma_{xy}|$, where $\sigma_{xx} = 200$. The results from the model are shown as red crosses and the black line represents the prediction in equation 6.17.

model this effect is replicated. The transverse resistivity is predicted ($\rho_{xy,\mathrm{p}}$) from equation 6.8b, which can be simplified to

$$\rho_{xy,\mathrm{p}} = \frac{\sigma_{xy}}{\sigma_{xx}^2 + \sigma_{xy}^2} = \left(\sigma_{xy}\left(1 + \left(\frac{\sigma_{xx}}{\sigma_{xy}}\right)^2\right)\right)^{-1} \tag{6.17}$$

The effect of changing σ_{xy} on $\boldsymbol{\rho_{xy}}$ is shown in figure 6.18. The simplest physical result to establish is that when the σ_{xy}=0 that there is no $\boldsymbol{\rho_{xy}}$. Then it is possible to observe that the magnitude of the $\boldsymbol{\rho_{xy}}$ increases with $|\sigma_{xy}|$. The values calculated by the model agree well with the values predicted from the conductivity. All of the results from the uniform case establish that the modelling is accurate.

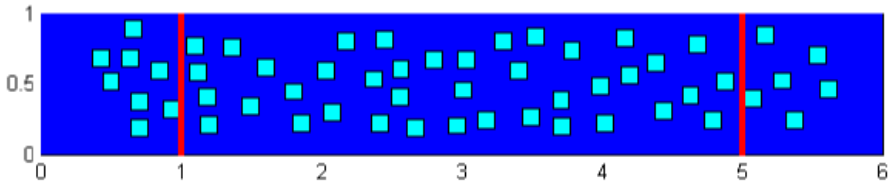

Fig. 6.19 An example of the 2D model showing the background (dark blue) with 13% inclusions (cyan). The red lines superimposed on the image of the model show the point from which the 4 terminal measurement is made.

6.3.3 Simulating a non-uniform conducting medium

Set-up of the model

The model has the capability to simulate a uniform material and a system with randomly placed inclusions, see figure 6.19 for an example of the model used. The inclusions used are square with identical dimensions and conductivity, they are restricted to have a minimum distance between each other and with the edges of the matrix[1]. This is done to ensure the numerical model is stable. The inclusions are allocated to random positions, if an inclusion does not meet the criteria then it is assigned a random new position until it does meet the criteria. For each conductivity scenario the model is performed several times with different randomly placed inclusions. In discussing the result the number of repetitions (reps) will be listed in the figure captions. The background matrix is described with a conductivity tensor where $\sigma_{xy} = 0$ and σ_{xx} is variable. The FM inclusions are described by a conductivity where both σ_{xx} and σ_{xy} may be non zero. An example system is shown in figure 6.19, where there are 13% inclusions. The percentage of inclusions is based upon the percentage of FM MnAs that was calculated in section 3.4.4.

The results for a non uniform model with p_{Incl}=13% inclusions are shown in figure 6.20, where the conductivities are listed in table 6.1. When the inclusions are modelled, the equipotentials rotate and the current density distorts due to the presence of inclusions in their

[1]The length and width of each inclusion is 0.12, the minimum spacing between each inclusion is $\Delta x_{Incl,gap}$=0.07 & $\Delta y_{Incl,gap}$=0.04, the minimum spacing between the edges at x=0 or 6 is 0.25 and the minimum spacing from y=0 or 1 is 0.05

	σ_{xx}	σ_{xy}
background (Ba)	200	0
inclusion (Incl)	200	-99

Table 6.1 Conductivity values for the background and inclusions for figure 6.20

path or nearby. It is worth noting that when an equipotential is examined that crosses between two close inclusions the contour does not progress perpendicularly between the inclusions but appears to rotate backwards slightly as seen in figure 6.20b. The current density also changes in direction when around inclusions and occasionally has a small angle so it points from one inclusion to a nearby inclusion in the x direction. The changes in the calculated current density direction are highlighted in figures 6.20c & 6.20d. The mean value along the calculated current density varies with the presence of inclusions along the line averaged due to limitations in the numerical calculation. This means that measuring the current from the middle of the bar is not an accurate measurement in the non uniform set up. However the current at the edge of the bar is constant as the inclusions are prohibited from being located there. As σ_{xy}=0 for the matrix there is no significant distortion of the current at the edges, so the current will be measured from there.

Longitudinal resistivity results

Figure 6.21 shows the difference in the scale of the change in magnitude of the ρ_{xx} for several different percentage of inclusions p_{Incl}, when compared to the bulk there has been a significant decrease in the size of the change of the resistivity with σ_{xy} but the same trend can be seen. The magnitude of the decrease in resistivity increases with the percentage of inclusions. Table 6.2 compares the magnitude of the change in ρ_{xx}. The change in ρ_{xx} is not the same as the percentage of the inclusions. The change in the resistivity increases linearly with p_{Incl}. The offset between p_{Incl} and the change in the resistivity implies a more complicated changes to the resistivity than simply allowing a portion of material to have a σ_{xy}. The complicated picture that this result implies is shown with the changing direction of the

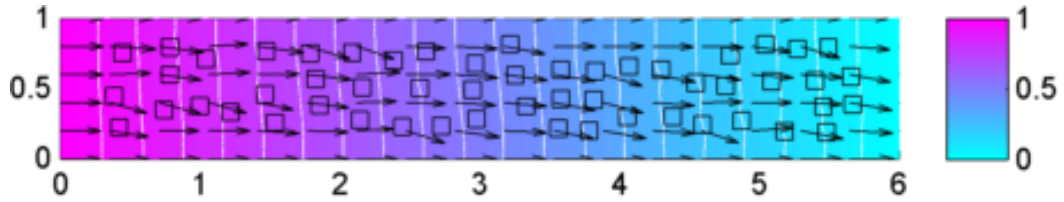

(a) Full image

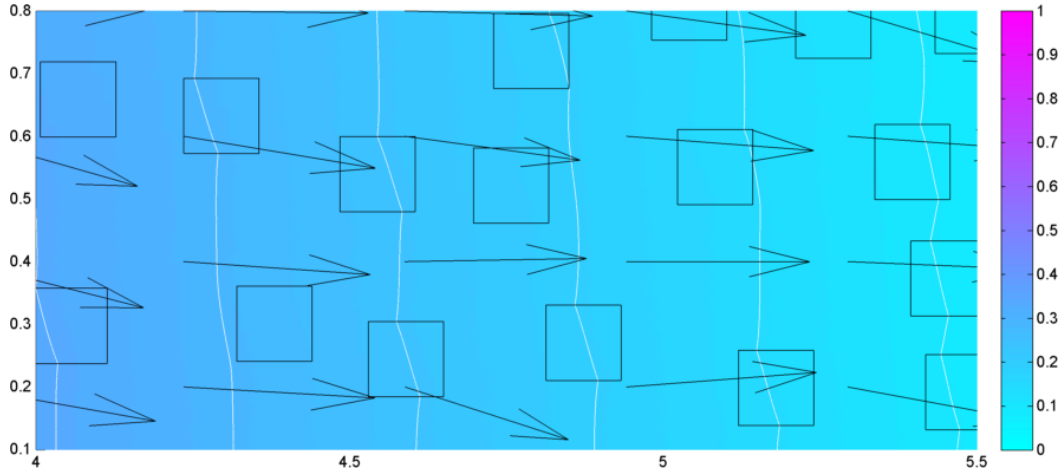

(b) Enlarged view of an area where inclusions lie close together.

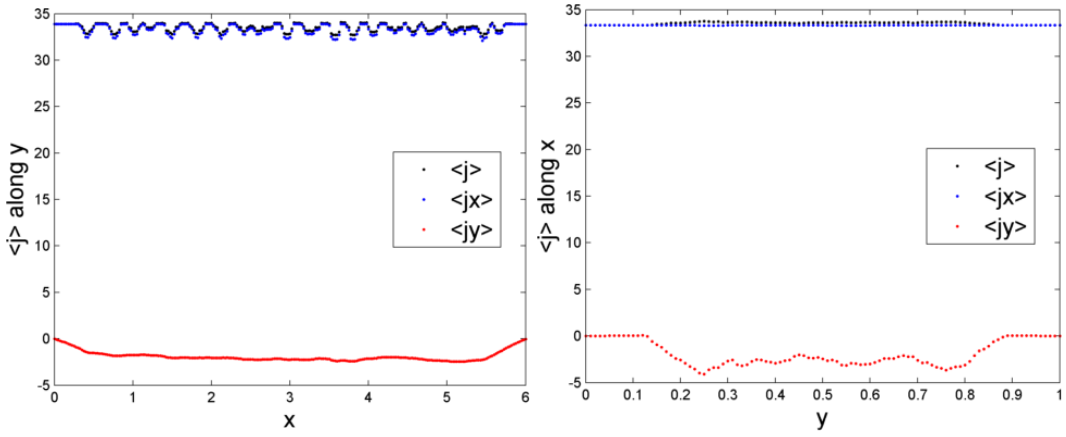

(c) Mean j value when summed along the width of the bar.

(d) Mean j value when summed along the length of the bar.

Fig. 6.20 Results of a 13% inclusion model with conductivity values listed in table 6.1. The colour map is the solution for the model, the blue squares show the boundaries of the inclusions, the white lines are the equipotentials and the black arrows are the current density. The bottom figures show the mean values of the current density along different directions. The current density is split into the directional components.

	$\Delta\rho_{xx} = 1 - \frac{\rho_{xx}(\sigma_{xy}=96)}{\rho_{xx}(\sigma_{xy}=0)}$	$\frac{\Delta\rho_{xx}(NU)}{\Delta\rho_{xx}(U)}$
U (p_{Incl}=100%)	0.1860	-
NU (p_{Incl}=5%)	0.0062	3.3%
NU (p_{Incl}=10%)	0.0136	7.3%
NU (p_{Incl}=13%)	0.0174	9.4%

Table 6.2 Comparison of the magnitude of the change of ρ_{xx} for uniform and non uniform systems

current density in figure 6.20. By scaling the predictions of the longitudinal resistivity that

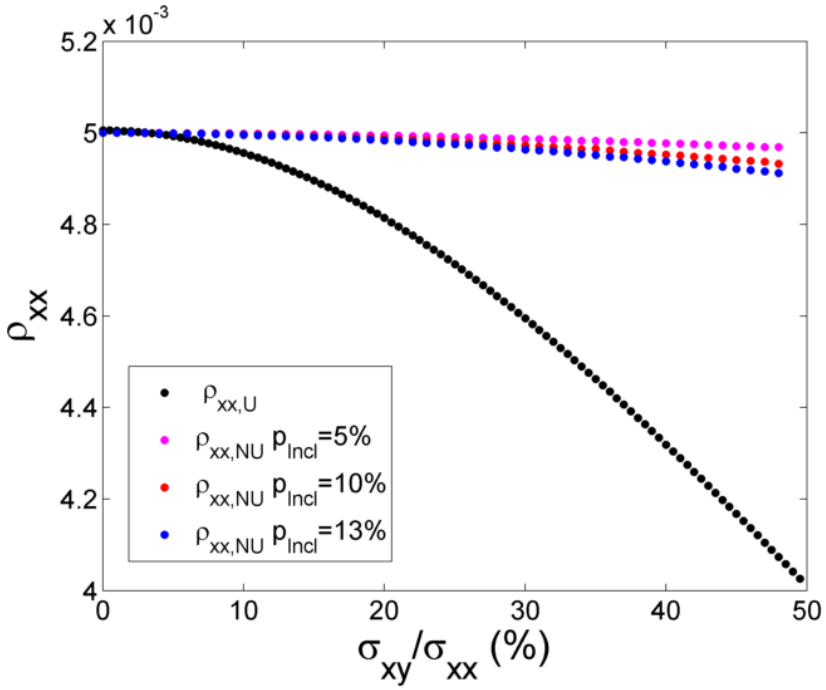

Fig. 6.21 Comparison of the ρ_{xx} as a function of σ_{xy} for a uniform medium (black) and non uniform medium with 5% inclusions (cyan), 10% inclusions (red) and 13% inclusions (blue).

were compared to the uniform conducting medium it is possible to compare the predictions to a non uniform conducting medium. The prediction of the resistivity, equation 6.13, are scaled by p_{Incl}. The ρ_{xx} for a uniform conducting medium is scaled using,

$$\Delta(\sigma_{xy}) = \rho_{U,xx}(\sigma_{xy} = 0) - \rho_{U,xx}(|\sigma_{xy}|) \tag{6.18a}$$

$$\rho_{U,xx,s}(\sigma_{xy}) = \rho_{U,xx}(\sigma_{xy} = 0) - p_{Incl}\Delta(|\sigma_{xy}|) \tag{6.18b}$$

Figure 6.22 shows these different prediction against the calculated results for p_{Incl}=10%. The ρ_{xx} of the non uniform medium lies in the region between the scaled uniform ρ_{xx}, with a difference of 0.36% at the maximum σ_{xy}, and the scaled prediction from equation 6.13, with a difference of 1.1%, implying that the resistivity scales within the bounds that could be expected from the uniform case.

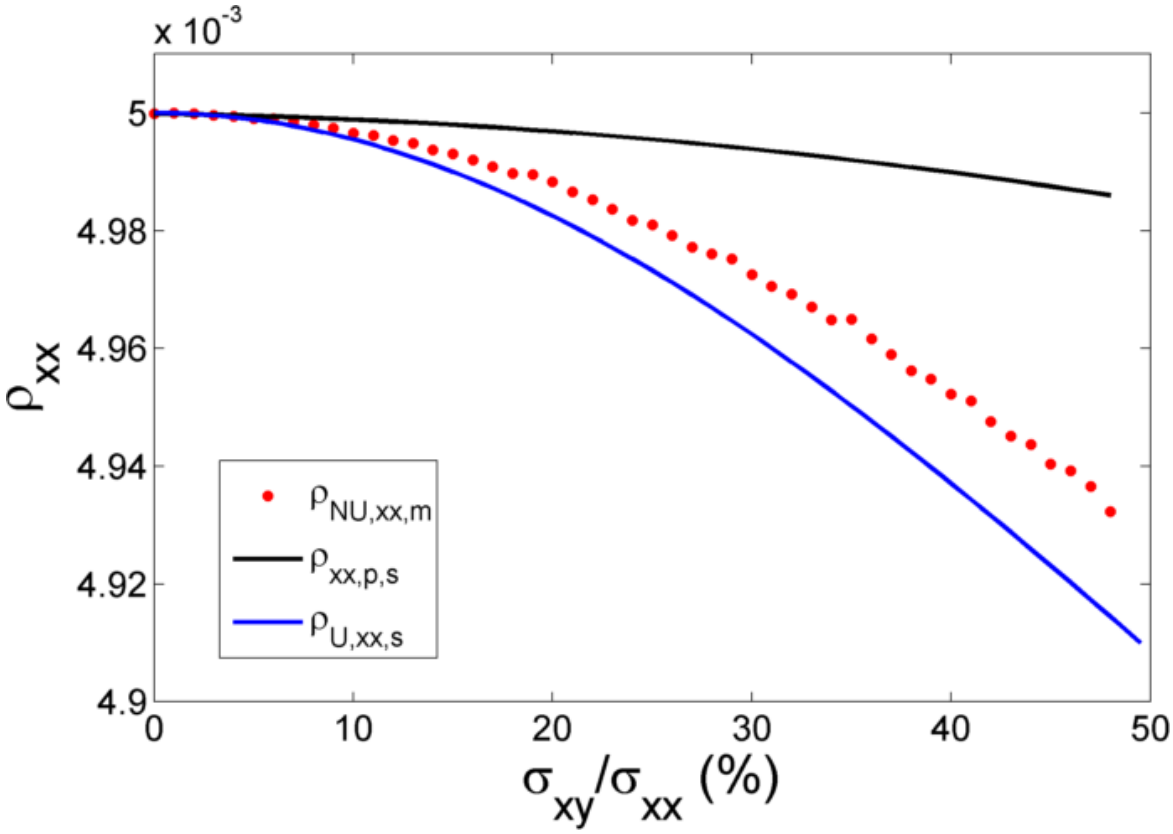

Fig. 6.22 Scaled values of the predictions against the results for 10% inclusions. The red dots show the measured longitudinal resistivity($\rho_{xx,m}$) for a non uniform medium with p_{Incl}=10%. The black line is the scaled predicted longitudinal resistivity$\rho_{xx,p,s}$. The blue line is the scaled longitudinal resistivity of a system with uniform conductivity $\rho_{Uxx,s}$.

When the σ_{xx} of the background and inclusions are plotted as a percentage of $\frac{\sigma_{Uxx}}{\sigma_{Inclxx}}$ then the ratio of $\frac{\rho_{xx4t}}{\rho_{xxU(\sigma_{xy}=0)}}$ demonstrates the effect of changing the percentage of inclusions as shown in figure 6.23. It is clear that as the percentage increases so does the effect of the inclusions on the resistance. It is worth noting that the resistances should be the same in the limit of the resistivity ratio tending to 100%.

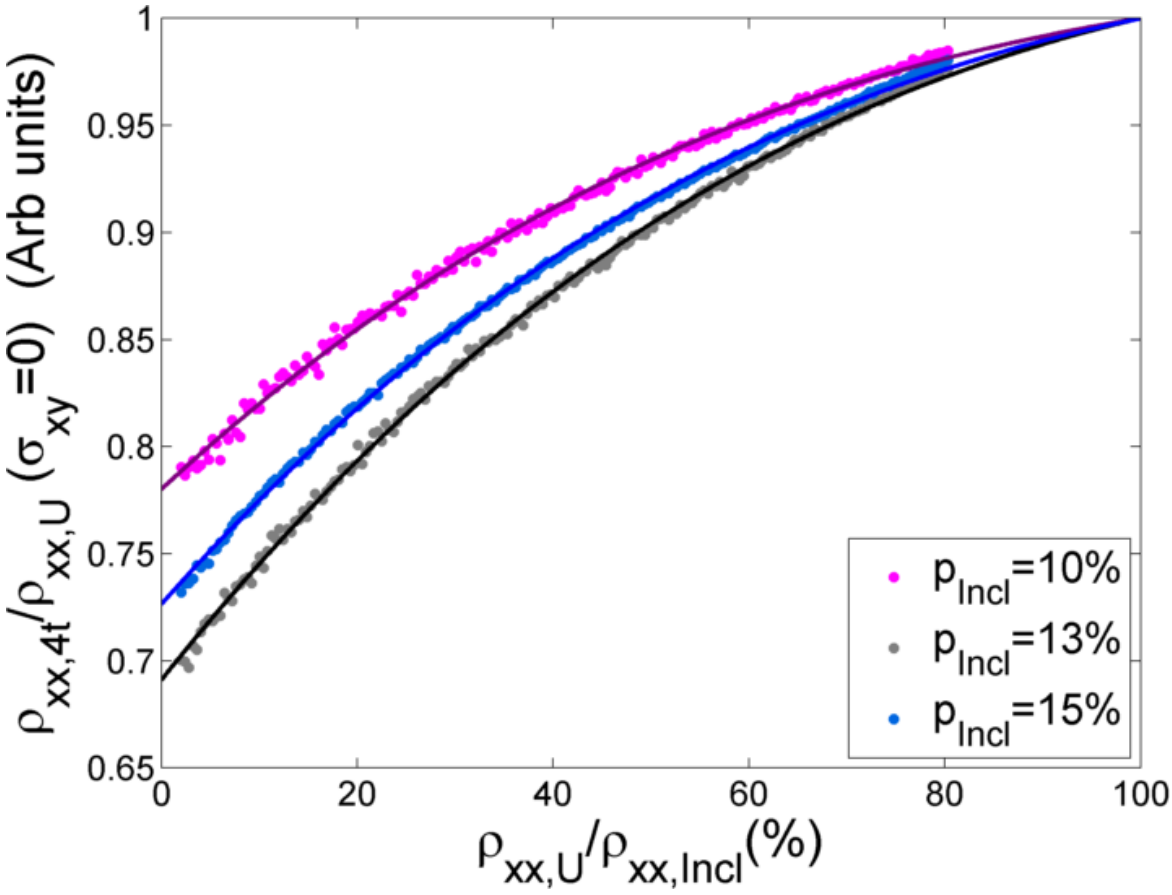

Fig. 6.23 The change in the ratio of resistivities for different percentages of conductivity when measured in 4 terminal mode. The inclusions have a fixed conductivity with $\sigma_{xx} = 200$ and $|\sigma_{xy}| = 99$. The pink data is 10% inclusions with 10 reps, black is 13% with 25 reps, blue is 15% with 10 reps.

p_{Incl}	$\frac{\rho_{NU,xy}(\sigma_{xy}=96)}{\rho_{NU,xy}(\sigma_{xy}=96)}$
5%	6.2%
10%	12.8%
13%	16.1%

Table 6.3 The percentage change in the ρ_{xy} between the uniform system and a non uniform system with different p_{Incl}. Measurements are taken for $\sigma_{xy} = 96$.

The data of figure 6.23 are fitted with a power series function, which will be used later in comparisons with the results on the non-stoichiometric CuMnAs

Transverse resistivity results

The ρ_{xy} in a non uniform medium can be compared to the ρ_{xy} in a uniform medium as a function of the σ_{xy} of the inclusions, which is shown in figure 6.24. Table 6.3 shows the percentage change at the maximum value of σ_{xy} compared with the uniform case. The change in the ρ_{xy} is more than the p_{Incl}, which means that the inclusions have caused a greater change in the transverse resistance than the percentage of the surface covered in inclusions. The change in ρ_{xy} scales linearly with the percentage. The larger change observed is the opposite of the size of the change seen in the longitudinal resistivity.

Another interesting capability of the model to look at is changing the ratio of the longitudinal conductivities between the background and inclusions. Figure 6.25 shows the effect of changing σ_{Uxx} without changing the conductivity of the inclusions. The figure shows that as the background conductivity decreases the change in the transverse resistivity with transverse conductivity of inclusions increases.

It is possible to fix the inclusion conductivity and then vary the longitudinal conductivity of the background. The results of this approach are shown in figure 6.26, where it is possible to see the difference in the resistivity ratio decreases with the increase in σ_{Uxx}. There is a large variation in the spread of the data in figure 6.25, the largest spread is when the

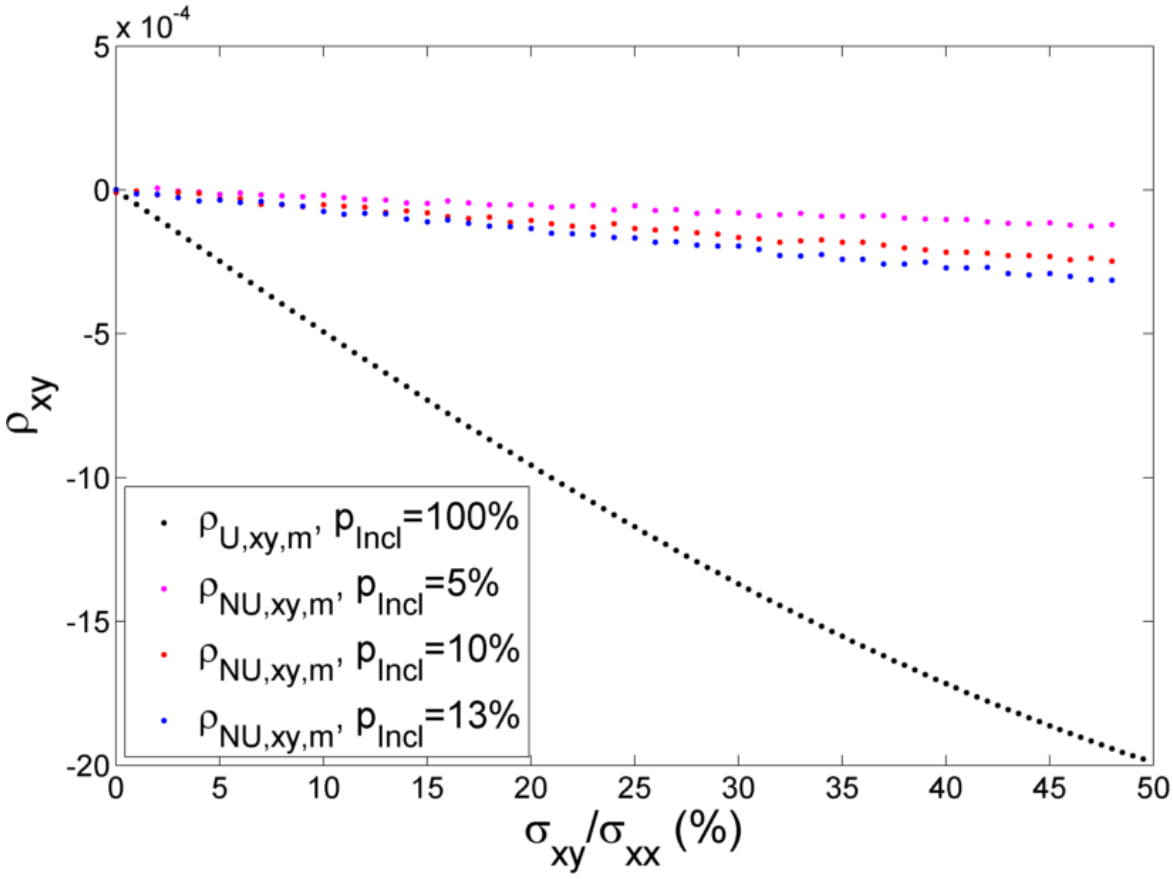

Fig. 6.24 ρ_{xy} as a function of σ_{xy}/σ_{xx}. The uniform medium is in blue and the results for 10% inclusions in red dots. Both models have a σ_{xx}=200. For a model with inclusion each value of σ_{xy} is repeated fifty times and the average taken.

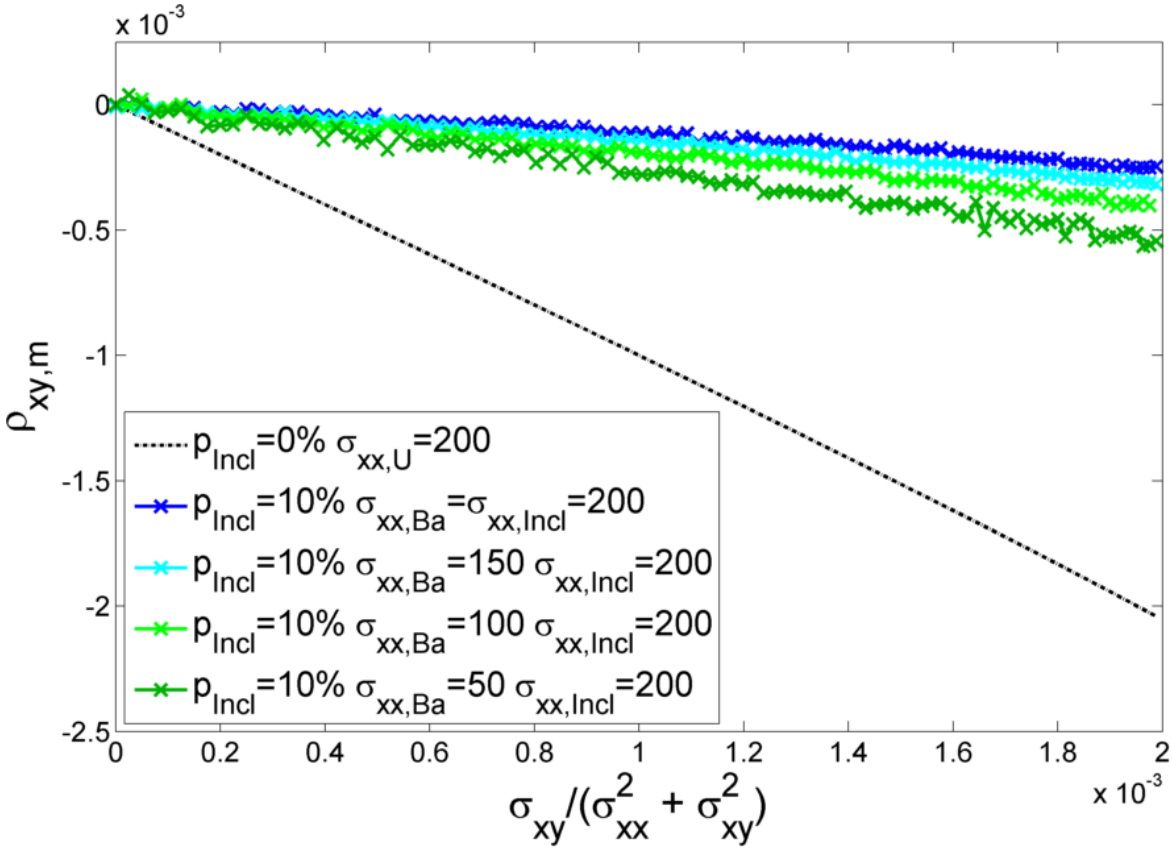

Fig. 6.25 The transverse resistivity against a conductivity ratio that linearise the results and is dependent on the changing transverse conductivity of the inclusions. The $|\sigma_{xy}|$ changes from 0 to 99 for every data set. The black data set shows a uniform medium with an longitudinal conductivity of 200. All the other data sets are for samples with 10% inclusions and $\sigma_{\text{Incl},xx} = 200$. The conductivity of the background medium changes with blue:$\sigma_{\text{Ba},xx} = 200$ (25 repetitions of model), cyan:$\sigma_{\text{Ba},xx} = 150$ (50 repetitions), light green:$\sigma_{\text{Ba},xx} = 100$ (50 repetitions) and dark green:$\sigma_{\text{Ba},xx} = 50$ (50 repetitions)

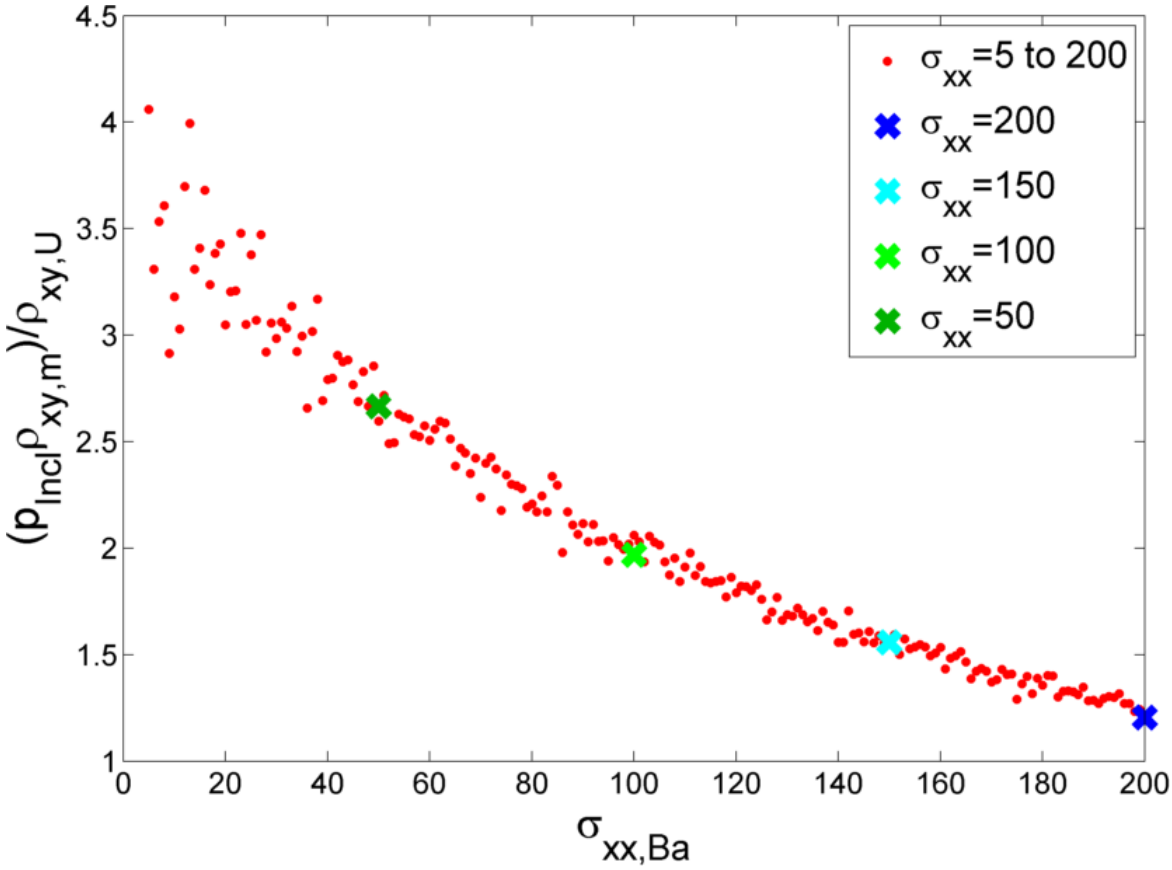

Fig. 6.26 The change in the transverse resistivity for a changing longitudinal background conductivity from 5 to 200. The system has 10% inclusions with a conductivity of $\sigma_{xx} = 200$ & $|\sigma_{xy}| = 99$. For the data in red each data point is the average of 50 repetitions. The crosses represent that values taken from the data seen in figure 6.25 at the set σ_{Incl}.

background has a low conductivity as the conductivity is dominated by the current diverting from inclusion to inclusion.

Figure 6.27 shows the same trend as figure 6.26 but with three different percentages of inclusions. For the maximum longitudinal conductivity of the background both percentages of inclusions have tended to a similar value. Whereas when there is an increase in the $\frac{\rho_{xy}}{\rho_{Uxy}}$ the smaller the percentage of inclusions the steeper the increase as the ratio tends to infinity.

The lines through the data are power series fits, which will be used in comparisons with experimental data.

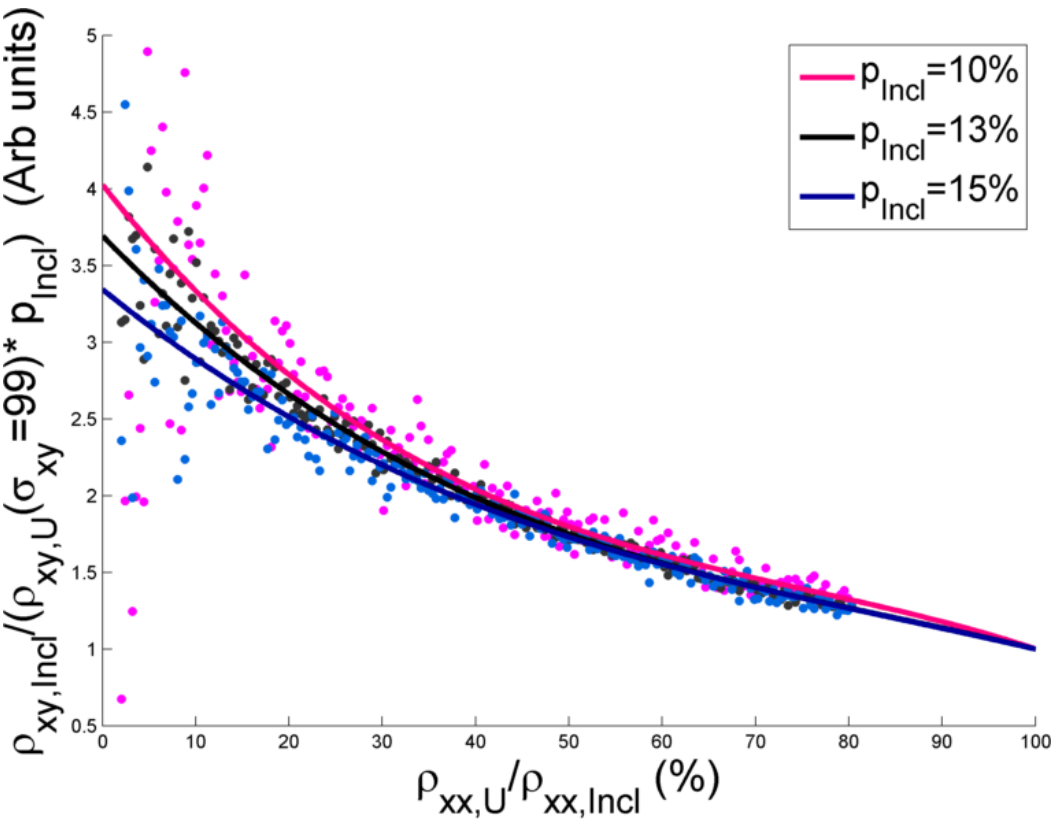

Fig. 6.27 The change in the transverse resistivity measured against the transverse resistivity of the bulk and the percentage of inclusions for a changing longitudinal background conductivity from 5 to 200 against a fixed longitudinal conductivity. The conductivity of the inclusions is $\sigma_{xx} = 200$ & $|\sigma_{xy}| = 99$. Three different percentages of inclusions are shown 10% (pink), 13% (black) and 15% (blue). The data points are fitted for each set with a fit of the form: $1 + a(100-x) + b(100-x)^2 + c(100-x)^3$, where x is the value of $\frac{\rho_{xx,U}}{\rho_{xx,Incl}}$ and a,b and c are constants.

6.4 Comparing the conductivity simulations with experimental measurements

We now compare the results of the model with the measured results for the non-stoichiometric CuMnAs (Sample:2-1). The transport properties of the CuMnAs matrix are taken to be the same as a stoichiometric layer of epitaxial CuMnAs (Sample:1-10), which shows no signs of a secondary phase, and those of the inclusions are taken to be the same as epitaxial MnAs (values will be taken from [127]). The temperature dependent resistivites of the layers are shown in figure 6.28. In the ρ_{xx} there is a clear difference in the three layers. The MnAs has a significantly lower ρ_{xx}, which increases significantly more with temperature than the stoichiometric CuMnAs. The non-stoichiometric CuMnAs has a lower resistivity than the stoichiometric CuMnAs but has a larger temperature dependency. At 300K the resistivities of the CuMnAs layers are similar. As discussed in the introduction to this chapter there is only a very weak MR for stoichiometric CuMnAs, however MnAs has a strong and distinctive MR behaviour. The sign of the MR changes sign between 50K-100K. The non-stoichiometric CuMnAs also shows a distinctive MR with the MR changing sign between 50K-100K, but the magnitude is significantly smaller, which is consistent with the magnetoresistance arising solely from MnAs inclusions. The stoichiometric CuMnAs does not have an anomalous $\boldsymbol{\rho_{xy}}$. The anomalous $\boldsymbol{\rho_{xy}}$ of the non-stoichiometric CuMnAs has a similar temperature dependence to that of MnAs but with a much smaller magnitude.

In the $\boldsymbol{\rho_{xy}}$ the MnAs increases significantly with temperature and the non-stoichiometric CuMnAs shows the same trend but markedly weaker.

Using the ratio of the ρ_{xx} of stoichiometric CuMnAs to MnAs it is possible, using the calculated results in figures 6.23 and 6.27, to calculate the effect of having a certain percentage of MnAs inclusions inside the CuMnAs matrix. The MR and $\boldsymbol{\rho_{xy}}$ for stoichiometric CuMnAs are assumed to be zero. Figure 6.29 compares the resistivities from the model with either

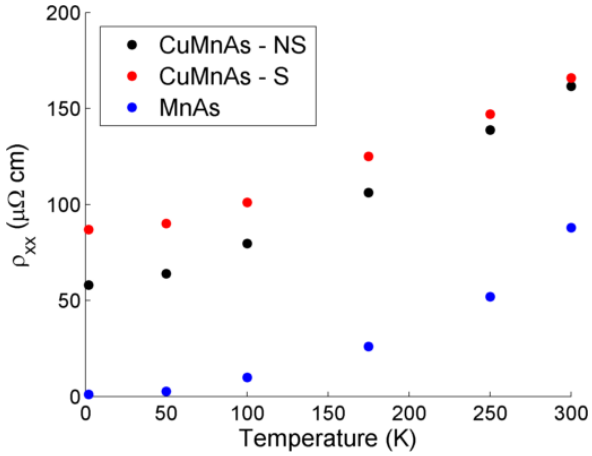

(a) ρ_{xx}

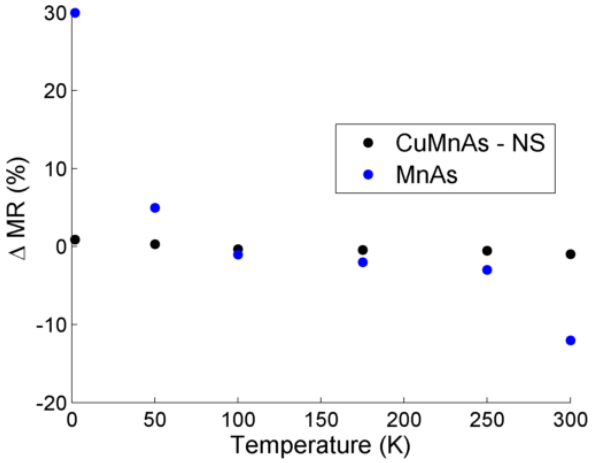

(b) MR

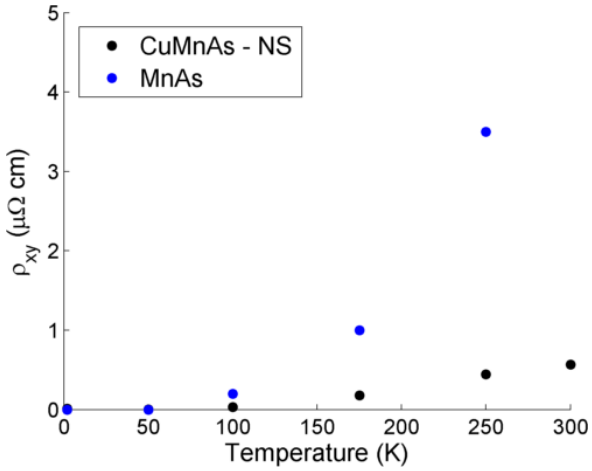

(c) ρ_{xy}

Fig. 6.28 The temperature dependence of the resistivity and MR for layers of stoichiometric (Sample:1-10) (red) and non-stoichiometric (Sample:2-1)(black) CuMnAs and MnAs (blue).

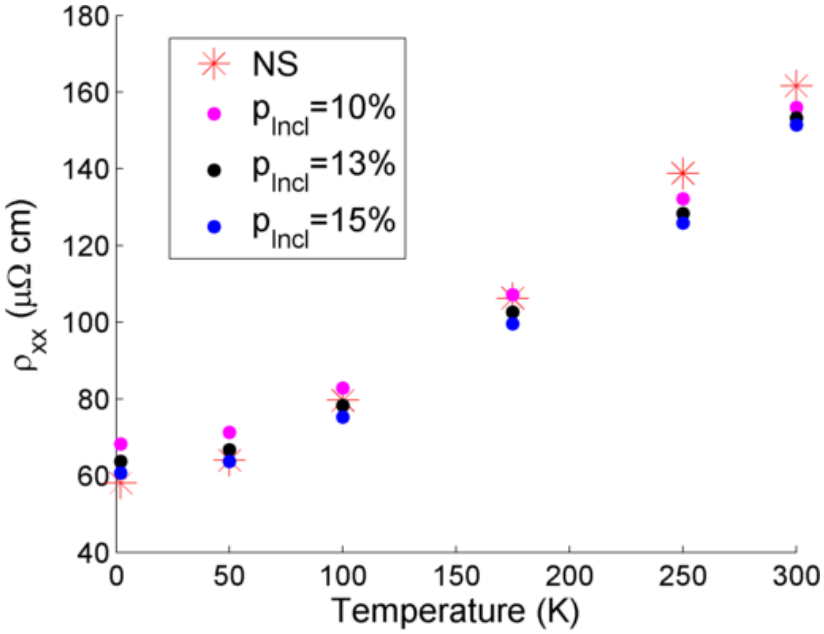

Fig. 6.29 Comparing the ρ_{xx} against T of non-stoichiommetric CuMnAs (Sample:2-1) with modelled values using different percentages of MnAs inclusions.

10%, 13% or 15% inclusions of MnAs. The resistivites of the models are similar to the measured values though the trends differ slightly. At the lowest and highest temperatures there is the weakest agreement between the models and the layer.

The magnetoresistances are compared in figure 6.30. The model manages to mimic the temperature dependence with the change in sign of the MR, but underestimates the effect at low temperatures and overestimates the effect at higher temperatures. This could be due to the MnAs particulates not being of the same quality as the epitaxial layer of MnAs that is being used in the model; Berry et. al [127] found that the T_C and MR at high temperatures was strongly dependent on the quality of the MnAs layer.

Figure 6.31 compares the change in the anomalous resistivity of the modelled non-stoichiometric CuMnAs systems. This figure shows that the model overestimates the effect of the MnAs inclusions on the anomalous resistivity. The over estimation could be due to the difference in the quality of the epitaxial MnAs to the crystallites.

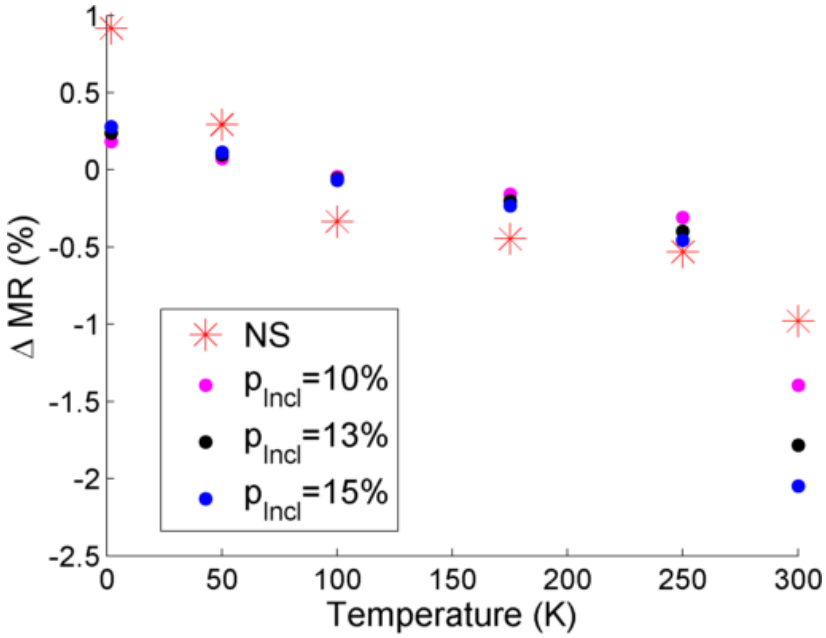

Fig. 6.30 Comparing the change in MR against temperature for non-stoichiometric CuMnAs (Sample:2-1)(red stars) and modelled non-stoichiometric systems with 10% (pink dots), 13% (black dots) or 15% (blue dots) inclusions of MnAs.

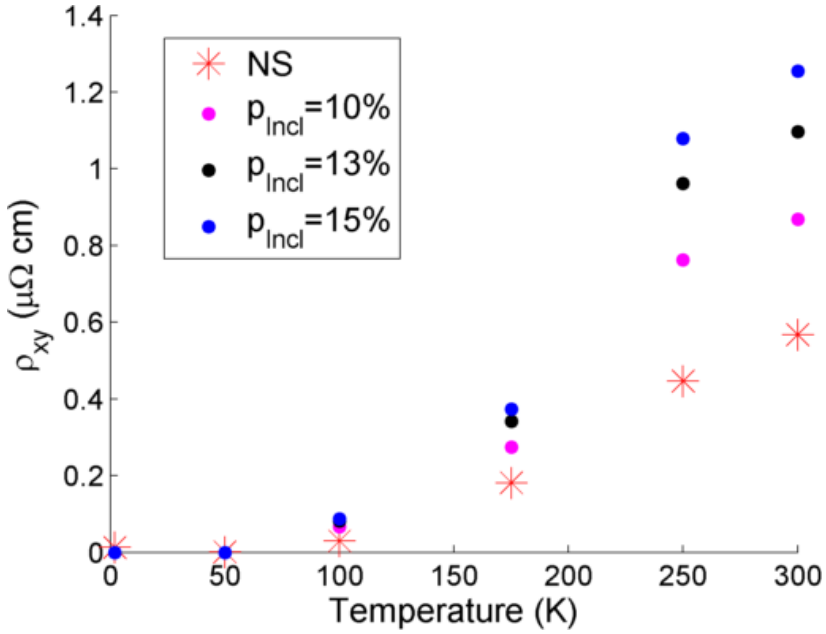

Fig. 6.31 Comparing the ρ_{xy} against temperature for non-stoichiometric CuMnAs (Sample:2-1)(red stars) and modelled non-stoichiometric systems with 10% (pink dots), 13% (black dots) or 15% (blue dots) inclusions of MnAs.

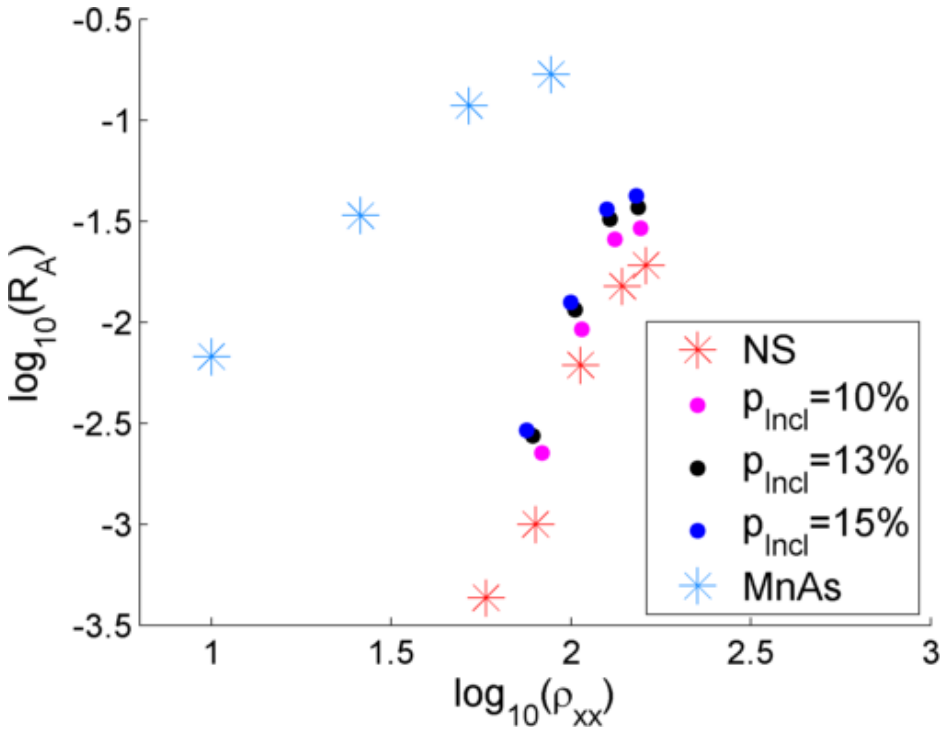

Fig. 6.32 The correction to the R_A from the modelling compared with the anomalous coefficient from MnAs. The data trends are non-stoichiometric CuMnAs (Sample:2-1)(red stars), MnAs (light blue stars) and modelled non-stoichiometric systems with 10% (pink dots), 13% (black dots) or 15% (blue dots) inclusions of MnAs.

The effect on the R_A can be estimated using the values from the conclusion and compared to estimated values for MnAs. Figure 6.32 shows log-log plots of the measured and calculated anomalous Hall coefficient (R_A) for MnAs and non-stoichiometric CuMnAs. With increasing percentage of MnAs the model moves progressively towards the values expected for pure MnAs. MnAs has a shallower gradient than the non-stoichiometric CuMnAs. The shallower gradient would be expected in a simpler system as a gradient of one or two is expected depending on the dominant scattering factor (η). The model values are larger than the measured values for non-stoichiometric CuMnAs but show the same very steep slope at low temperature.

In conclusion our model is able to estimate the changes in the resistivity for a non-stoichiometric sample of CuMnAs. There are some assumptions within the model that could

be improved. The MnAs inclusions in the non-stoichiometric layer have a T_C that is about 20K greater than the T_C of the epitaxial MnAs. If poorer quality MnAs was used in the model then it may address some of the discrepancies seen in the results. There are also variations that could be used in the model by changing the ratio of the transverse and longitudinal conductivities that are entered to see if this changes the behaviour, it is likely to weaken the size of any effects seen.

6.5 Conclusions

In conclusion this chapter has demonstrated how, when present, the FM MnAs dominates the behaviour seen in the longitudinal and transverse magneto-transport. There is a change in the sign of the IMR between 50-100K at which temperature the AHE signal begins to increase significantly in magnitude. The anomalous Hall coefficient R_A does not follow any linear dependencies because $\rho_{\mathbf{xy}}$ comes from MnAs but the ρ_{xx} is a combination of the matrix plus MnAs. When compared to the R_A of MnAs the R_A of CuMnAs is significantly steeper. When the temperature dependence of ρ_{xx}, $\rho_{\mathbf{xy}}$ and MR are compared for stoichiometric CuMnAs, epitaxial MnAs and non-stoichiometric CuMnAs there are some clear similarities in the behaviour of the non-stoichiometric system and the two single phase materials.

A model to simulate the effect of having a background matrix without a transverse conductivity and inclusions that did was developed to provide an estimate to compare with real world systems. The model was used to output the changes in percentages of the longitudinal and transverse resistivity for three different percentages of inclusion (10%, 13% and 15%).

When compared to a real world system by modelling stoichiometric CuMnAs as the bulk and epitaxial MnAs as the inclusions, the model was able to estimate the longitudinal resistivity of the non-stoichiometric CuMnAs and could produce similar trends to the transverse resistivity and MR though there were marked differences in some of these predictions. The

model could be improved by using values for the MnAs that are a closer representation to the quality of the MnAs crystallites. Another improvement in the model may be to alter the ratio of the transverse and longitudinal conductivities of the bulk and inclusions. One further consideration to the results is that the CuMnAs could be causing pinning or exchange bias effects at the interface of the crystallites which could effect the properties.

Chapter 7

Conclusions and Future Work

Our understanding of CuMnAs has developed significantly during the course of the work underlying this thesis. Our understanding has improved in the growth conditions needed to grow high quality epitaxial films of different thickness, the physical characteristics of the material, such as the T_N and the possible device functionality. This chapter summarises the key results discussed in this thesis and suggests some possible directions for future work.

7.1 Stoichiometric CuMnAs

The thesis has investigated the characteristics of stoichiometric CuMnAs using a variety of techniques. The T_N of CuMnAs layers, of thickness > 10nm, was determined to be (480$\pm$5)K [114] from neutron diffraction. This value is in good agreements with results from transport measurements [147]. On layers of CuMnAs grown on a GaP substrate there was a time dependence to the initial resistivity as a function of temperature, not present in layers of CuMnAs grown on GaAs. The absence of this effect on CuMnAs/GaAs could be due to the relaxation of the CuMnAs layer during MBE growth. For CuMnAs layers grown on both III-V substrates the T_N shows a consistent value. For layers of CuMnAs on GaP the T_N does not begin to suppress with thickness until layers thinner than 10nm. In transport

measurement of CuMnAs on GaAs, the resistivity has been shown to decrease around the T_N, possibly due to increasing intrinsic carrier concentration causing a secondary conduction channel to open up.

SQUID measurements of stoichiometric CuMnAs have shown that there is very little remnant magnetisation. In AFM images of stoichiometric CuMnAs on different substrates there are distinct differences and similarities in the topography. Both of the samples show a cross hatching pattern at 45° to the cleavage planes of the substrates. On the GaP substrates the CuMnAs surface has long thin lines, whereas for CuMnAs layers on GaAs the cross hatching lines are markedly shorter and occur with a higher density.

7.1.1 Ultra thin films of stoichiometric CuMnAs

Two promising methods for growing ultra thin films of CuMnAs have been demonstrated. Method one involved decreasing the T_{sub} for the growth and method two involved by depositing a nucleation layer of Cu and Mn that is then exposed to arsenic to form the first monolayer of CuMnAs before commencing the growth.

Layers grown by these two methods showed excellent topographical properties in AFM and crystal properties in XRD. A key issue overcome by these nucleation methods is the improved adhesion of CuMnAs to the substrate and this is thought to be achieved by two separate ways. The Cu and Mn nucleation layer may force a certain layer of the unit cell to be at the interface, which may adhere better to the surface than other layers in the unit cell. In the colder T_{sub} there may be a smaller difference in the lattice constants at the lower temperatures meaning that as the sample cools there is less difference in the lattice contractions and the material is able to adhere better. Future work could be used to optimise the nucleation layer thickness and conditions and using a combination of these methods. The growth methods are expected to also improve the adhesion of thin layers grown on GaAs.

The ability to grow continuous ultra thin layers of CuMnAs will allow the growth of different device structures.

7.2 Non-stoichiometric CuMnAs

This thesis has also looked at the properties of a layer of non-stoichiometric CuMnAs, that was grown with a higher proportion of manganese. The layers has been compared by several different techniques to stoichiometric CuMnAs. The layer was discussed in chapter 3 and chapter 6.

CuMnAs grown with an increased Mn flux has been shown to form a secondary phase with FM MnAs inclusions embedded in a background of CuMnAs. The MnAs inclusions are conducting, leading to two critical temperatures (T_N of the matrix and T_C of the inclusions) in the resistivity results. By modelling the resistivities for non uniform conductivity systems we have been able to estimate the effect of the inclusions on the system and have developed a tool that can be applied to different situations.

These ferromagnetic inclusions could be applied to different device set ups. Using current switching to change the direction of the spin axis in CuMnAs could induce a change in the direction of the magnetisation of the MnAs inclusions. The direction of the magnetisation in FM is detectable and there are many established techniques to observe this.

7.3 Alloying CuMnAs with phosphorous

The growth of CuMn($As_{(\mathbf{1-x})}P_{\mathbf{x}}$) was detailed in chapter 4 along with the characterisations of the layers and in chapter 5 the T_N of different layers was measured, which produced results with contradictory elements. The material growth has been found likely to be highly sensitive to the T_{sub} due to the competition for lattice sites between arsenic and phosphorous. The lattice constants for CuMn($As_{(\mathbf{1-x})}P_{\mathbf{x}}$) are reduced compared to CuMnAs. In some

samples this reduces the lattice mismatch with GaP, but as the applied flux and incorporation of phosphorous increase, the lattice mismatch increases as the unit cell is stretched to align with the substrate. In the thickest layer of CuMn($As_{(1-x)}P_x$) grown there is evidence from the lattice constants that the layer relaxed. For this sample where the lattice has relaxed with smaller lattice constants than CuMnAs then the Mn atoms lie closer together and it could be expected that the T_N would increase. This behaviour is seen in the first sample of CuMn($As_{(1-x)}P_x$) (Sample:6-1), where the T_N has been shown to clearly increase on CuMnAs in both neutron diffraction and resistivity measurements.

In all the other layers that were significantly thinner the lattice constants imply that the layers have remained strained to the substrate. This distorts the unit cell by pulling the FM aligned moments apart and compressing the AF aligned moments. from resistivity measurements these samples have T_N's that are either suppressed or the same as CuMnAs.

There are also several different growth avenues that could be explored. CuMn($As_{(1-x)}P_x$) was investigated as it could have increased the band gap of CuMnAs towards that of CuMnP. However current research into AF functionality does not require a semiconductor, but being technologically compatible with existing devices is a priority. GaAs as an epi-ready substrate is significantly cheaper, more widely available than GaP and used in many existing technologies. This means that tuning the lattice parameters of CuMnAs to lattice match GaAs may prove more technologically useful. The lattice parameters could be expanded by alloying the arsenic with antimony or by alloying the copper with silver or gold. The inclusion of these larger atoms may also increase the spin orbit coupling in the material.

7.4 Future work

This thesis has established some of the characteristic of epitaxial grown CuMnAs. Following the demonstration of current switching in CuMnAs there has been much interest in the material. Several groups are studying the material to observe different features. Groups are

studying the material with XMLD, terahertz techniques and XMLD-Photoemission Electron Microscopy (PEEM) investigations. The current switching should also occur in certain other AF materials, such as Manganese-2 gold (Mn_2Au) and there is work ongoing to explore this.

References

[1] J. Magnus Wikberg, Ronny Knut, Sumanta Bhandary, Igor di Marco, Mikael Ottosson, Janusz Sadowski, Biplab Sanyal, Pål Palmgren, Cheuk W. Tai, Olle Eriksson, Olof Karis, and Peter Svedlindh. Magnetocrystalline anisotropy and uniaxiality of MnAs/GaAs(100) films. *Physical Review B*, 83:024417, 2011.

[2] Claude Chappert, Albert Fert, and Frédéric Nguyen Van Dau. The emergence of spin electronics in data storage. *Nature materials*, 6(11):813–823, 2007.

[3] T. Jungwirth, J. Wunderlich, V. Novák, K. Olejník, B. L. Gallagher, R. P. Campion, K. W. Edmonds, A. W. Rushforth, A. J. Ferguson, and P. Němec. Spin-dependent phenomena and device concepts explored in (Ga,Mn)As. *Reviews of Modern Physics*, 86:855–896, 2014.

[4] Xavier Marti, Ignasi Fina, and Tomas Jungwirth. Prospect for Antiferromagnetic Spintronics. *Magnetics, IEEE Transactions on*, 51(4):1–4, 2015.

[5] T. Jungwirth, X. Marti, P. Wadley, and J. Wunderlich. Antiferromagnetic Spintronics. *Nature Nanotechnology*, 11:231–241, 2016.

[6] Mario Norberto Baibich, Jean Marc Broto, Albert Fert, F Nguyen Van Dau, Frédéric Petroff, P Etienne, G Creuzet, A Friederich, and J Chazelas. Giant magnetoresistance of (001) Fe/(001) Cr magnetic superlattices. *Physical Review Letters*, 61(21):2472, 1988.

[7] Grünberg Binasch, Peter Grünberg, F Saurenbach, and W Zinn. Enhanced magnetoresistance in layered magnetic structures with antiferromagnetic interlayer exchange. *Physical review B*, 39(7):4828, 1989.

[8] FJ Albert, JA Katine, RA Buhrman, and DC Ralph. Spin-polarized current switching of a co thin film nanomagnet. *Applied Physics Letters*, 77(23):3809–3811, 2000.

[9] D. Chiba, Y. Sato, T. Kita, F. Matsukura, and H. Ohno. Current-driven magnetization reversal in a ferromagnetic semiconductor $(\mathrm{Ga},\mathrm{Mn})\mathrm{As}/\mathrm{GaAs}/(\mathrm{Ga},\mathrm{Mn})\mathrm{As}$ tunnel junction. *Physical Review Letters*, 93:216602, 2004.

[10] J Nogués and Ivan K Schuller. Exchange bias. *Journal of Magnetism and Magnetic Materials*, 192(2):203 – 232, 1999.

[11] J.R. Hook and H.E. Hall, editors. *Solid State Physics*. Wiley, second edition, 2013.

[12] Charles Kittel. *Introduction to Solid State Physics*. John Wiley & Sons, Inc., New York, 8th edition, 1986.

[13] Ralph Skomski. *Simple models of magnetism*, volume 41. Oxford University Press Oxford, 2008.

[14] S. Tumanski. *Handbook Magnetic Measurement*. Taylor and Francis, 2011.

[15] Terunobu Miyazaki and Hanmin Jin. *The physics of ferromagnetism*, volume 158. Springer Science & Business Media, 2012.

[16] J. Železný, H. Gao, K. Výborný, J. Zemen, J. Mašek, Aurélien Manchon, J. Wunderlich, Jairo Sinova, and T. Jungwirth. Relativistic Néel-Order Fields Induced by Electrical Current in Antiferromagnets. *Physical Review Letters*, 113:157201, 2014.

[17] P. Wadley, B. Howells, J. Železný, C. Andrews, V. Hills, R. P. Campion, V. Novák, K. Olejník, F. Maccherozzi, S. S. Dhesi, S. Y. Martin, T. Wagner, J. Wunderlich, F. Freimuth, Y. Mokrousov, J. Kuneš, J. S. Chauhan, M. J. Grzybowski, A. W. Rushforth, K. W. Edmonds, B. L. Gallagher, and T. Jungwirth. Electrical switching of an antiferromagnet. *Science*, 351(6273):587–590, 2016.

[18] J. C. S. Kools. Exchange-biased spin-valves for magnetic storage. *IEEE Transactions on Magnetics*, 32(4):3165–3184, 1996.

[19] Tsann Lin, G. L. Gorman, and Ching Tsano. Antiferromagnetic and hard-magnetic stabilization schemes for magnetoresistive sensors. *IEEE Transactions on Magnetics*, 32(5):3443–3445, 1996.

[20] X Marti, I Fina, C Frontera, Jian Liu, P Wadley, Qing He, RJ Paull, JD Clarkson, J Kudrnovskỳ, I Turek, et al. Room-temperature antiferromagnetic memory resistor. *Nature materials*, 13(4):367–374, 2014.

[21] A. Scholl, M. Liberati, E. Arenholz, H. Ohldag, and J. Stöhr. Creation of an Antiferromagnetic Exchange Spring. *Physical Review Letters*, 92:247201, 2004.

[22] X. Martí, B. G. Park, J. Wunderlich, H. Reichlová, Y. Kurosaki, M. Yamada, H. Yamamoto, A. Nishide, J. Hayakawa, H. Takahashi, and T. Jungwirth. Electrical Measurement of Antiferromagnetic Moments in Exchange-Coupled IrMn/NiFe Stacks. *Physical Review Letters*, 108:017201, 2012.

[23] Christopher Marrows. Addressing an antiferromagnetic memory. *Science*, 351(6273):558–559, 2016.

[24] Wei Zhang, Matthias B. Jungfleisch, Wanjun Jiang, John E. Pearson, Axel Hoffmann, Frank Freimuth, and Yuriy Mokrousov. Spin Hall Effects in Metallic Antiferromagnets. *Physics Review Letters*, 113:196602, 2014.

[25] V. Tshitoyan, C. Ciccarelli, A. P. Mihai, M. Ali, A. C. Irvine, T. A. Moore, T. Jungwirth, and A. J. Ferguson. Electrical manipulation of ferromagnetic NiFe by antiferromagnetic IrMn. *Physical Review B*, 92:214406, 2015.

[26] Y Y Wang, C Song, G Y Wang, F Zeng, and F Pan. Evidence for asymmetric rotation of spins in antiferromagnetic exchange-spring. *New Journal of Physics*, 16(12):123032, 2014.

[27] Yeong-Ah Soh and Ravi K Kummamuru. Spintronics in antiferromagnets. *Philosophical Transactions of the Royal Society of London A: Mathematical, Physical and Engineering Sciences*, 369(1951):3646–3657, 2011.

[28] Igor Žutić, Jaroslav Fabian, and S. Das Sarma. Spintronics: Fundamentals and applications. *Review of Modern Physics*, 76:323–410, 2004.

[29] BG Park, J Wunderlich, X Marti, V Holỳ, Y Kurosaki, M Yamada, H Yamamoto, A Nishide, J Hayakawa, H Takahashi, et al. A spin-valve-like magnetoresistance of an antiferromagnet-based tunnel junction. *Nature materials*, 10(5):347–351, 2011.

[30] Y. Y. Wang, C. Song, B. Cui, G. Y. Wang, F. Zeng, and F. Pan. Room-Temperature Perpendicular Exchange Coupling and Tunneling Anisotropic Magnetoresistance in an Antiferromagnet-Based Tunnel Junction. *Physical Review Letters*, 109:137201, 2012.

[31] Y. Y. Wang, C. Song, B. Cui, G. Y. Wang, F. Zeng, and F. Pan. Room - temperature antiferromagnetic tunnelling anisotropic magnetoresistance. *SPIN*, 03(01):1350005, 2013.

[32] D. Petti, E. Albisetti, H. Reichlova, J. Gazquez, M. Varela, M. Molina-Ruiz, A. F. Lopeandia, K. Olejnik, V. Novak, I. Fina, B. Dkhil, J. Hayakawa, X. Marti, J. Wunderlich, T. Jungwirth, and R. Bertacco. Storing magnetic information in $IrMn/MgO/Ta$ tunnel junctions via field-cooling. *Applied Physics Letters*, 102(19):192404, 2013.

[33] T. Jungwirth, V. Novák, X. Martí, M. Cukr, F. Máca, A. B. Shick, J. Mašek, P. Horodyská, P. Němec, V. Holý, J. Zemek, P. Kužel, I. Němec, B. L. Gallagher, R. P. Campion, C. T. Foxon, and J. Wunderlich. Demonstration of molecular beam epitaxy and a semiconducting band structure for I-Mn-V compounds. *Physical Review B*, 83:035321, 2011.

[34] Sadao Adachi. *Properties of semiconductor alloys: group-IV, III-V and II-VI semiconductors*, volume 28. John Wiley & Sons, 2009.

[35] J. Mašek, J. Kudrnovský, F. Máca, B. L. Gallagher, R. P. Campion, D. H. Gregory, and T. Jungwirth. Dilute Moment *n*-Type Ferromagnetic Semiconductor Li(Zn,Mn)As. *Physical Review Letters*, 98:067202, 2007.

[36] A. P. Wijnheijmer, X. Martí, V. Holý, M. Cukr, V. Novák, T. Jungwirth, and P. M. Koenraad. Scanning tunneling microscopy reveals LiMnAs is a room temperature anti-ferromagnetic semiconductor. *Applied Physics Letters*, 100(11):112107, 2012.

[37] Joachim Mündelein and Hans-Uwe Schuster. Darstellung und Kristallstruktur der Verbindungen MnCuX (X = P, As, P_xAs_{1-x}) / Preparation and Crystal Structure of Compounds MnCuX (X = P, As, PxAs1-x). *Zeitschrift für Naturforschung B*, 47:925–928, 1992.

[38] F. Máca, J. Mašek, O. Stelmakhovych, X. Martí, H. Reichlová, K. Uhlířová, P. Beran, P. Wadley, V. Novák, and T. Jungwirth. Room-temperature antiferromagnetism in CuMnAs. *Journal of Magnetism and Magnetic Materials*, 324(8):1606 – 1612, 2012.

[39] P Wadley, V Novák, RP Campion, C Rinaldi, X Martí, H Reichlová, J Zeleznỳ, J Gazquez, MA Roldan, M Varela, et al. Tetragonal phase of epitaxial room-temperature antiferromagnet CuMnAs. *Nature communications*, 4, 2013.

[40] I. Vurgaftman, J. R. Meyer, and L. R. Ram-Mohan. Band parameters for III-V compound semiconductors and their alloys. *Journal of Applied Physics*, 89(11):5815–5875, 2001.

[41] R.H. Forster, G.B. Johnston, and D.A. Wheeler. Studies on the heusler alloys- III. The antiferro-magnetic phase in the Cu-Mn-Sb system. *Journal of Physics and Chemistry of Solids*, 29(5):855 – 861, 1968.

[42] T. Jeong, Ruben Weht, and W. E. Pickett. Semimetallic antiferromagnetism in the half-Heusler compound CuMnSb. *Physical Review B*, 71:184103, 2005.

[43] P. Mohn. *Magnetism in the Solid State*. Springer, 2006.

[44] J. F. Cooke. Heisenberg model and magnetic insulators. *Physical Review B*, 2:220–227, 1970.

[45] L. W. Shacklette. Specific heat and resistivity of iron near its Curie point. *Physical Review B*, 9:3789–3792, 1974.

[46] D. Kim, B. L. Zink, F. Hellman, S. McCall, G. Cao, and J. E. Crow. Mean-field behavior with Gaussian fluctuations at the ferromagnetic phase transition of $srruo_3$. *Physical Review B*, 67:100406, 2003.

[47] Paul P. Craig, Walter I. Goldburg, T. A. Kitchens, and J. I. Budnick. Transport Properties at Critical Points: The Resistivity of Nickel. *Physical Review Letters*, 19:1334–1337, 1967.

[48] V. Novák, K. Olejník, J. Wunderlich, M. Cukr, K. Výborný, A. W. Rushforth, K. W. Edmonds, R. P. Campion, B. L. Gallagher, Jairo Sinova, and T. Jungwirth. Curie Point Singularity in the Temperature Derivative of Resistivity in (Ga,Mn)As. *Physical Review Letters*, 101:077201, 2008.

[49] M. Wang, R. A. Marshall, K. W. Edmonds, A. W. Rushforth, R. P. Campion, and B. L. Gallagher. Determining Curie temperatures in dilute ferromagnetic semiconductors: High Curie temperature (Ga,Mn)As. *Applied Physics Letters*, 104(13), 2014.

[50] F. Matsukura, H. Ohno, A. Shen, and Y. Sugawara. Transport properties and origin of ferromagnetism in (Ga,Mn)As. *Physical Review B*, 57:R2037–R2040, 1998.

[51] K. Akabli, Y. Magnin, Masataka Oko, Isao Harada, and H. T. Diep. Theory and simulation of spin transport in antiferromagnetic semiconductors: Application to MnTe. *Physical Review B*, 84:024428, 2011.

[52] Robin Alexader Marshall. *Critical Behaviour and Quantum Properties in (Ga,Mn)As*. PhD thesis, School of Physics and Astronomy, The University of Nottingham, 2012.

[53] Tom Kuech. *Handbook of Crystal Growth: Thin Films and Epitaxy*. Elsevier, 2014.

[54] John R. Arthur. Molecular beam epitaxy. *Surface Science*, 500(1-3):189 – 217, 2002.

[55] M. Wang, R. P. Campion, A. W. Rushforth, K. W. Edmonds, C. T. Foxon, and B. L. Gallagher. Achieving high Curie temperature in (Ga,Mn)As. *Applied Physics Letters*, 93(13):132103, 2008.

[56] T. Jungwirth, Jairo Sinova, J. Mašek, J. Kucera, and A. H. MacDonald. Theory of ferromagnetic (III,Mn)V semiconductors. *Reviews of Modern Physics*, 78:809–864, 2006.

[57] Jan H Van Der Merwe. The role of lattice misfit in epitaxy. *Critical Reviews in Solid State and Material Sciences*, 7(3):209–231, 1978.

[58] Sadao Adachi. GaAs, AlAs, and $Al_xGa_{1-x}As$: Material parameters for use in research and device applications. *Journal of Applied Physics*, 58(3):R1–R29, 1985.

[59] Council Natl Res. *Frontiers in Crystalline Matter: From Discovery to Technology*. 2009.

[60] E. M. Kneedler, B. T. Jonker, P. M. Thibado, R. J. Wagner, B. V. Shanabrook, and L. J. Whitman. Influence of substrate surface reconstruction on the growth and magnetic properties of Fe on GaAs(001). *Physical Review B*, 56:8163–8168, 1997.

[61] J. J. Krebs, B. T. Jonker, and G. A. Prinz. Properties of Fe single-crystal films grown on (100)GaAs by molecular beam epitaxy. *Journal of Applied Physics*, 61(7):2596–2599, 1987.

[62] C A F Vaz, J A C Bland, and G Lauhoff. Magnetism in ultrathin film structures. *Reports on Progress in Physics*, 71(5):056501, 2008.

[63] Aidan T. Hindmarch. Interface magnetism in ferromagnetic metal-compound semiconductor hybrid structures. *SPIN*, 01(01):45–69, 2011.

[64] G. A. Prinz and J. J. Krebs. Molecular beam epitaxial growth of single-crystal Fe films on GaAs. *Applied Physics Letters*, 39(5):397–399, 1981.

[65] Y. B. Xu, E. T. M. Kernohan, D. J. Freeland, A. Ercole, M. Tselepi, and J. A. C. Bland. Evolution of the ferromagnetic phase of ultrathin Fe films grown on GaAs(100)-4×6. *Physics Review B*, 58:890–896, 1998.

[66] G. W. Anderson, M. C. Hanf, and P. R. Norton. Growth and Magnetic Properties of Epitaxial Fe(100) on S-Passivated GaAs(100). *Physical Review Letters*, 74:2764–2767, 1995.

[67] J. W. Matthews. Defects associated with the accommodation of misfit between crystals. *Journal of Vacuum Science & Technology*, 12(1):126–133, 1975.

[68] Roberto Fornari. 1 - Epitaxy for Energy Materials. In Thomas F. Kuech, editor, *Handbook of Crystal Growth (Second Edition)*, Handbook of Crystal Growth, pages 1 – 49. North-Holland, Boston, second edition edition, 2015.

[69] R. Jaszek. Carrier scattering by dislocations in semiconductors. *Journal of Materials Science: Materials in Electronics*, 12(1):1–9, 2001.

[70] P Sitch, R Jones, Sven Öberg, and MI Heggie. Structures of dislocations in GaAs and their modification by impurities. *Physical Review B*, 50(23):17717, 1994.

[71] G. Vanamu, A.K. Datye, and Saleem H. Zaidi. Heteroepitaxial growth on microscale patterned silicon structures. *Journal of Crystal Growth*, 280(1):66 – 74, 2005.

[72] C.T. Foxon. Three decades of molecular beam epitaxy. *Journal of Crystal Growth*, 251(1-4):1 – 8, 2003. Proceedings of the Twelfth International Conference on Molecular Beam Epitaxy.

[73] Alfred Cho, editor. *Molecular Beam Epitaxy*. Key Papers in Applied Physics. American Institute of Physics, 1994.

[74] Bruce A Joyce and Tim B Joyce. Basic studies of molecular beam epitaxy-past, present and some future directions. *Journal of crystal growth*, 264(4):605–619, 2004.

[75] Martin Heiß, Eva Riedlberger, Danče Spirkoska, Max Bichler, Gerhard Abstreiter, and Anna Fontcuberta i Morral. Growth mechanisms and optical properties of GaAs-based semiconductor microstructures by selective area epitaxy. *Journal of Crystal Growth*, 310(6):1049 – 1056, 2008.

[76] J. W. Ward, R. N. R. Mulford, and Milton Kahn. Study of Some of the Parameters Affecting Knudsen Effusion. I. Experimental Tests of the Validity of the Cosine Law as a Function of Cell and Sample Geometrics and Materials. *The Journal of Chemical Physics*, 47(5):1710–1717, 1967.

[77] Karl Jousten, editor. *Handbook of Vacuum Technology*. Wiley-VCH, 2008.

[78] A. J. SpringThorpe, S. J. Ingrey, B. Emmerstorfer, P. Mandeville, and W. T. Moore. Measurement of GaAs surface oxide desorption temperatures. *Applied Physics Letters*, 50(2):77–79, 1987.

[79] A. Y. Cho and I. Hayashi. P-N Junction Formation during Molecular-Beam Epitaxy of Ge-Doped GaAs. *Journal of Applied Physics*, 42(11):4422–4425, 1971.

[80] Robert K Willardson and Albert C Beer. *Semi-insulating GaAs*. Academic Press, 1984.

[81] R. P. Campion, C. T. Foxon, and R. C. Bresnahan. Modulated beam mass spectrometer studies of a Mark V Veeco cracker. *Journal of Vacuum Science & Technology B*, 28(3):C3F1–C3F4, 2010.

[82] C.T. Foxon, R.P. Campion, V.A. Grant, S.V. Novikov, J.J. Harris, R. Thomson, C. Taylor, and D. Barlett. Use of band-gap thermometry to investigate the growth of GaN on sapphire and GaAs. *Journal of Crystal Growth*, 301-302(0):482 – 485, 2007.

[83] R. N. Sacks, D. Barlett, C. A. Taylor, and J. Williams. Growth related interference effects in band edge thermometry of semiconductors. *Journal of Vacuum Science & Technology B*, 23(3):1247–1251, 2005.

[84] F. C. Frank and J. H. van der Merwe. One-Dimensional Dislocations. I. Static Theory. *Proceedings of the Royal Society of London. Series A, Mathematical and Physical Sciences*, 198(1053):pp. 205–216, 1949.

[85] M. Volmer and A. Weber. Germ-formation in oversaturated figures. *Zeitschrift Fur Physikalische Chemie–Stochiometrie Und Verwandtschaftslehre*, 119(3/4):277–301, 1926.

[86] Ivan N Stranski and Lubomir Krastanow. Zur Theorie der orientierten Ausscheidung von Ionenkristallen aufeinander. *Monatshefte für Chemie/Chemical Monthly*, 71(1):351–364, 1937.

[87] JH Neave, BA Joyce, PJ Dobson, and N Norton. Dynamics of film growth of gaas by mbe from rheed observations. *Applied Physics A*, 31(1):1–8, 1983.

[88] Colin EC Wood. RED intensity oscillations during MBE of GaAs. *Surface Science*, 108(2):L441–L443, 1981.

[89] S. Franchi, G. Trevisi, L. Seravalli, and P. Frigeri. Quantum dot nanostructures and molecular beam epitaxy. *Progress in Crystal Growth and Characterization of Materials*, 47(2-3):166 – 195, 2003. Vapour Growth of Bulk Crystals and Epitaxy: Part I, Vapour Growth of Bulk Crystals and Epitaxy: Part I.

[90] Lucy Elizabeth Goff. *Growth and Charecterisation of III-V Semiconductor Materials Grown Primarily by AME and PA-MBE*. PhD thesis, Univeristy of Nottingham, 2015.

[91] R. Dingle, H. L. Strŏmer, A. C. Gossard, and W. Wiegmann. Electron mobilities in modulation-doped semiconductor heterojunction superlattices. *Applied Physics Letters*, 33(7):665–667, 1978.

[92] Secondo Franchi. Chapter 1 - Molecular beam epitaxy: fundamentals, historical background and future prospects. In Mohamed Henini, editor, *Molecular Beam Epitaxy*, pages 1 – 46. Elsevier, Oxford, 2013.

[93] M. Ilegems. Beryllium doping and diffusion in molecular-beam epitaxy of GaAs and $Al_xGa_{1-x}As$. *Journal of Applied Physics*, 48(3):1278–1287, 1977.

[94] R. J. Malik, R. N. Nottenberg, E. F. Schubert, J. F. Walker, and R. W. Ryan. Carbon doping in molecular beam epitaxy of GaAs from a heated graphite filament. *Applied Physics Letters*, 53(26):2661–2663, 1988.

[95] A.Y. Cho and I. Hayashi. Epitaxy of silicon doped gallium arsenide by molecular beam method. *Metallurgical Transactions, Volume 2, Issue 3, pp.777-780*, 2:777–780, 1971.

[96] A. Y. Cho. Impurity profiles of GaAs epitaxial layers doped with Sn, Si, and Ge grown with molecular beam epitaxy. *Journal of Applied Physics*, 46(4):1733–1735, 1975.

[97] Jiang De-Sheng, Y. Makita, K. Ploog, and H. J. Queisser. Electrical properties and photoluminescence of Te doped GaAs grown by molecular beam epitaxy. *Journal of Applied Physics*, 53(2):999–1006, 1982.

[98] N. Sakamoto, K. Hirakawa, and T. Ikoma. Conduction type conversion in Si doped (311)A GaAs grown by molecular beam epitaxy. *Applied Physics Letters*, 67(10):1444–1446, 1995.

[99] E. A. Emelyanov, M. A. Putyato, B. R. Semyagin, D. F. Feklin, and V. V. Preobrazhensky. Molecular beam epitaxy of III-P_xAs_{1-x} solid solutions: Mechanism of composition formation in the sublattice of a group V element. *Semiconductors*, 49(2):157–165, 2015.

[100] Z.R. Wasilewski, M.M. Dion, D.J. Lockwood, P. Poole, R.W. Streater, and A.J. SpringThorpe. Determination of $Al_xGa_{1-x}As$ composition: the MBE perspective. *Journal of Crystal Growth*, 175-176, Part 1:238 – 243, 1997. Molecular Beam Epitaxy 1996.

[101] R Dingle, AC Gossard, and W Wiegmann. Direct observation of superlattice formation in a semiconductor heterostructure. *Physical Review Letters*, 34(21):1327, 1975.

[102] B. F. Levine. Quantum-well infrared photodetectors. *Journal of Applied Physics*, 74(8):R1–R81, 1993.

[103] J. Simon, S. Tomasulo, P. J. Simmonds, M. Romero, and M. L. Lee. Metamorphic GaAsP buffers for growth of wide-bandgap InGaP solar cells. *Journal of Applied Physics*, 109(1), 2011.

[104] Dr Paul Gates. http://www.bris.ac.uk/nerclsmsf/techniques/gcms.html, 2016.

[105] R.F.C. Farrow. *Molecular Beam Epitaxy - Applications to Key Materials*. William Andrew Publishing/Noyes, 1995.

[106] Aaron J. Ptak. 4 - principles of molecular beam epitaxy. In Thomas F. Kuech, editor, *Handbook of Crystal Growth (Second Edition)*, Handbook of Crystal Growth, pages 161 – 192. North-Holland, Boston, second edition edition, 2015.

[107] R. N. Peacock, N. T. Peacock, and D. S. Hauschulz. Comparison of hot cathode and cold cathode ionization gauges. *Journal of Vacuum Science & Technology A*, 9(3):1977–1985, 1991.

[108] JH Singleton. Practical guide to the use of bayard - alpert ionization gauges. *Journal of Vacuum Science & Technology A*, 19(4):1712–1719, 2001.

[109] Christopher Hammond and Christopher Hammond. *The basics of crystallography and diffraction*, volume 12. Oxford University Press Oxford, 2009.

[110] ISIS. Isis home page. http://www.isis.stfc.ac.uk, 2016.

[111] D Duxbury, D Khalyavin, P Manuel, D Raspino, N Rhodes, E Schooneveld, and E Spill. Operational performance characteristics of the WISH detector array on the ISIS spallation neutron source. *Journal of Instrumentation*, 9(12):C12008, 2014.

[112] Institut Laue-Langevin. D10 - Four-circle diffractometer with three-axis energy analysis. http://www.ill.eu/instruments-support/instruments-groups/instruments/d10/description/general-view-of-the-instrument/, 2016.

[113] ISIS. Wish beamline diagram - isis. http://www.isis.stfc.ac.uk/instruments/wish/science/wish-schematic-drawing11555.jpg, 2016.

[114] P Wadley, V Hills, MR Shahedkhah, KW Edmonds, RP Campion, V Novák, B Ouladdiaf, D Khalyavin, S Langridge, V Saidl, et al. Antiferromagnetic structure in tetragonal CuMnAs thin films. *Scientific Reports*, 5, 2015.

[115] R. L. Fagaly. Superconducting quantum interference device instruments and applications. *Review of Scientific Instruments*, 77(10), 2006.

[116] Quantum Design. Squid application note 1052 - 202a, 2001.

[117] Naoto Nagaosa, Jairo Sinova, Shigeki Onoda, A. H. MacDonald, and N. P. Ong. Anomalous Hall effect. *Review Modern Physics*, 82:1539–1592, 2010.

[118] T. Jungwirth, Qian Niu, and A. H. MacDonald. Anomalous Hall Effect in Ferromagnetic Semiconductors. *Physical Review Letters*, 88:207208, 2002.

[119] Michalski L., Eckersdorf K., Kucharski J., and McGhee J., editors. *Temperature Measurement*. Wiley, 2nd edition, 2001.

[120] Ricardo García and Rubèn Pèrez. Dynamic atomic force microscopy methods. *Surface Science Reports*, 47(6-8):197 – 301, 2002.

[121] Andrew Stannard. *Pattern Formation in Nanostructured Systems*. PhD thesis, University of Nottingham, 2009.

[122] David Necas and Petr Klapetek. Gwyddion: an open-source software for SPM data analysis. *Central European Journal of Physics*, 10:181–188, 2012.

[123] U. Hartmann. Magnetic force microscopy. *Annual Review of Materials Science*, 29(1):53–87, 1999.

[124] S. Rumyantsev M. Levinshtein and M. Shur, editors. *Handbook Series on Semiconductor Parameters*, volume 1. World Scientific, 1996.

[125] M Wang, RA Marshall, KW Edmonds, AW Rushforth, RP Campion, and BL Gallagher. Three-dimensional heisenberg critical behavior in the highly disordered dilute ferromagnetic semiconductor (ga, mn) as. *Physical Review B*, 93(18):184417, 2016.

[126] Massimo Campostrini, Martin Hasenbusch, Andrea Pelissetto, Paolo Rossi, and Ettore Vicari. Critical exponents and equation of state of the three-dimensional heisenberg universality class. *Physical Review B*, 65:144520, 2002.

[127] J. J. Berry, S. J. Potashnik, S. H. Chun, K. C. Ku, P. Schiffer, and N. Samarth. Two-carrier transport in epitaxially grown MnAs. *Physical Review B*, 64:052408, 2001.

[128] H-A Krug von Nidda, T Kurz, A Loidl, Th Hartmann, P J Klar, W Heimbrodt, M Lampalzer, K Volz, and W Stolz. Tuning the magnetic properties of GaAs:Mn/MnAs hybrids via the MnAs cluster shape. *Journal of Physics: Condensed Matter*, 18(26):6071, 2006.

[129] S. Ye, P. J. Klar, Th. Hartmann, W. Heimbrodt, M. Lampalzer, S. Nau, T. Torunski, W. Stolz, T. Kurz, H.-A. Krug von Nidda, and A. Loidl. Anisotropy of the magnetotransport in (Ga,Mn)As/MnAs paramagnetic-ferromagnetic hybrid structures. *Applied Physics Letters*, 83(19):3927–3929, 2003.

[130] A. Kwiatkowski, D. Wasik, M. Kaminska, R. Bozek, J. Szczytko, A. Twardowski, J. Borysiuk, J. Sadowski, and J. Gosk. Structure and magnetism of MnAs nanocrystals embedded in GaAs as a function of post-growth annealing temperature. *Journal of Applied Physics*, 101(11):113912, 2007.

[131] Dillip Kumar Satapathy. *Molecular-beam epitaxy growth and structural characterization of semiconductor-ferromagnet heterostructures by grazing incidence x-ray diffraction*. PhD thesis, Mathematisch-Naturwissenschaftlichen Fakultät I Humboldt-Universität zu Berlin, 2005.

[132] F. Schippan, G. Behme, L. Däweritz, K. H. Ploog, B. Dennis, K.-U. Neumann, and K. R. A. Ziebeck. Magnetic structure of epitaxially grown MnAs on GaAs(001). *Journal of Applied Physics*, 88(5):2766–2770, 2000.

[133] J.L. Hall, A.J. Kent, C.T. Foxon, and R.P. Campion. Temperature effects during the growth of $In_xGa_{1-x}N$ films through the whole compositional range by plasma-assisted molecular beam epitaxy. *Journal of Crystal Growth*, 312(14):2083 – 2088, 2010.

[134] V. Novák, K. Olejník, M. Cukr, L. Smrcka, Z. Remeš, and J. Oswald. Substrate temperature changes during molecular beam epitaxy growth of GaMnAs. *Journal of Applied Physics*, 102(8), 2007.

[135] Laurent C. Chapon, Pascal Manuel, Paolo G. Radaelli, Chris Benson, Leigh Perrott, Stuart Ansell, Nigel J. Rhodes, Davide Raspino, D. Duxbury, E. Spill, and Julian Norris. Wish: The New Powder and Single Crystal Magnetic Diffractometer on the Second Target Station. *Neutron News*, 22(2):22–25, 2011.

[136] J. Singh. *Semiconductor Devices - Basic Principles*. John Wiley & Sons, Inc., 2001.

[137] F. J. Di Salvo, D. E. Moncton, and J. V. Waszczak. Electronic properties and superlattice formation in the semimetal $tise_2$. *Physical Review B*, 14:4321–4328, 1976.

[138] A. H. Thompson. Electron-electron scattering in tis_2. *Physical Review Letters*, 35:1786–1789, 1975.

[139] J.R. Hook and H.E. Hall. *Solid State Physics*. Manchester Physics Series. Wiley, 2013.

[140] David Ferry. *Semiconductor transport*. CRC Press, 2000.

[141] M. Spangenberg, J.R. Neal, T.-H. Shen, S.A. Morton, J.G. Tobin, G.D. Waddill, J.A.D. Matthew, D. Greig, A.E.R. Malins, E.A. Seddon, and M. Hopkinson. Observation of a low Curie temperature ferromagnetic phase of ultrathin epitaxial Fe films on GaAs(0 0 1). *Journal of Magnetism and Magnetic Materials*, 292:241 – 247, 2005.

[142] Keizo Endo, Tetuo Ohoyama, and Ren'iti Kimura. Antiferromagnetism of CuMnSb. *Journal of the Physical Society of Japan*, 25(3):907–908, 1968.

[143] Mu Wang. *Studies of III-V ferromagnetic semiconductors*. PhD thesis, University of Nottingham, Nottingham, 2012.

[144] X Sheng, W Song, and W Song. *Essentials of Computational Electromagnetics*. WILEY-IEEE press, 2012.

[145] Lawrence N Dworsky. *Introduction to Numerical Electrostatics Using MATLAB*. John Wiley & Sons, Inc., 2014.

[146] J Heremans. Solid state magnetic field sensors and applications. *Journal of Physics D: Applied Physics*, 26(8):1149, 1993.

[147] V. Hills, P. Wadley, R. P. Campion, V. Novak, R. Beardsley, K. W. Edmonds, B. L. Gallagher, B. Ouladdiaf, and T. Jungwirth. Paramagnetic to antiferromagnetic transition in epitaxial tetragonal CuMnAs (invited). *Journal of Applied Physics*, 117(17), 2015.